Distributed Photomixers

by

Erik Kurt Duerr

Submitted to the Department of Electrical Engineering and Computer Science
in partial fulfillment of the requirements for the degree of

Doctor of Philosophy in Computer Science and Engineering

at the

MASSACHUSETTS INSTITUTE OF TECHNOLOGY

September 2002

Author .....
Department of Electrical Engineering and Computer Science
August 30, 2002

Certified by .....
Qing Hu
Professor
Thesis Supervisor

Accepted by .....
Arthur C. Smith
Chairman, Department Committee on Graduate Students

Distributed Photomixers

by

Erik Kurt Duerr

Submitted to the Department of Electrical Engineering and Computer Science
on August 30, 2002, in partial fulfillment of the
requirements for the degree of
Doctor of Philosophy in Computer Science and Engineering

Abstract

Although the terahertz domain has been explored scientifically, components, especially sources, are needed to enable further exploration of the frequency range. A photomixer generates coherent THz radiation through optical heterodyne down-conversion. A terahertz-frequency beat signal on an optical carrier illuminates an ultrafast photoconductor, modulating the conductance. The time-varying conductance together with a constant voltage bias generates time-varying current at the beat frequency. Low-temperature-grown gallium arsenide (LTG-GaAs) is the photoconductive material of choice, because its short carrier lifetime allows the conductance to be efficiently modulated at THz frequencies.

The distributed photomixer described in this thesis is a new style of LTG-GaAs photomixer which uses an optical waveguide to couple the beat signal to an active area which is large relative to the terahertz wavelength. This large, traveling-wave mode active area distributes the heat load from absorbed optical power and ohmic heating from photocurrent and avoids the RC rolloff associated with a lumped-element photomixer's intrinsic capacitance and the load resistance. The distributed photomixer structure consists of coplanar strips (CPS) fabricated on top of a dielectric strip-loaded waveguide that guides the optical beat. The conductance of a thin layer of LTG-GaAs between the CPS and optical guide is modulated by the weakly coupled optical signal. The THz conductance wave between the dc-biased CPS creates a THz electromagnetic wave which propagates along the CPS. To velocity match the THz and optical waves, the CPS are periodically loaded with thin electrodes that add a small shunt capacitance to the line. The CPS are terminated in a planar antenna that radiates the THz wave.

This thesis describes the design, fabrication, and testing of waveguide-coupled distributed photomixers. The photomixers demonstrated in this thesis operated in traveling-wave mode and produced 100 nW of power at 0.3 THz and the power output rolled off at 6 dB/octave until 1.4 THz. A model which qualitatively and quantitatively predicts the device performance as a function of frequency, illumination and voltage bias is developed. A general design methodology, detailed discussion of fabrication steps and possible methods to increase output power are also presented.

Thesis Supervisor: Qing Hu

Title: Professor

Acknowledgments

I first want to express my gratitude to my advisor, Professor Qing Hu. Thank you for giving me the opportunity to come to MIT and embark on this fantastic journey. Thank you also for supervising me closely on my Masters work and being my advisor for my PhD work at Lincoln Lab.

Thank you to Simon Verghese for giving me the opportunity to work at MIT Lincoln Laboratory and for being a great mentor. Many thanks are also due Alex McIntosh for all the prodding on project management and for the exceptional assistance in experimental technique. Thank you to both Simon and Alex for providing guidance and being patient while I learned the ins and outs of becoming an experimentalist simultaneously in the optical and far-infrared domains. Many thanks to other folks at Lincoln . . . to Len Mahoney and Karen Molvar for all the fabrication work . . . to Steve Calawa for the wafer growth . . . to Joe Donnelly who knew the answer to any device question I ever asked him . . . to everyone in the group office, Jon, George, Paula, and Mary for making sure that both technical expertise and funding was available.

I also owe my gratitude to Qing for assembling a dynamic, intelligent research group. Ben Williams and I spent many hours discussing physics, history, politics, philosophy, and current events. Many other former and current members of Qing's group have provided me with both useful and enjoyable conversations: Dr. Ir. Gert de Lange, Noah Zamdmer, Kostas Konistis, Farhan Rana, Hans Callebaut, Juan Montoya, Arif Rahman, Bin Xu, Brian Riely, and Ilya Lyubomirsky.

Thank you to "the boys", Adam, Amit, Constantine, Dave, Luc, and Zolti, my connection to the Aero/Astro, Computer Science, and Nuclear departments as well as to many good times. You are all inspirations to me as researchers and friends.

Thank you to "Coach" Garcia for all the advice on training, racing, car repair, home improvement and so on and also to Joe and Mark for their advice and abuse over the thousands of miles we all ran together.

I owe my thanks also to many non-terahertz folks . . . to the family members and family friends who have prayed for me, especially, Grandmother Duerr, Jane, Rosemary, Cindy,

Marty, Tweedie, Brenda, Julie, Glenda, Nancy . . . to all my friends at Park Street . . . to the Cafe team who always supported me . . . to my small groups who did the same . . . to Ken and to Norris who said little but meant much . . . to Chris Sherwood for all the advice . . . to Julie, Amy, Eva, and Toni for faithfully praying for so long . . . to Victoria & Michael and Sean & Charlene for the same . . . to Lee, who always checked up on me and made sure I had a little fun . . . to Johnny, who always understood . . . to Alex, who also always understood but for different reasons . . . to Chris, who is much of a kindred spirit even though we are also so different . . . to Jonathan, who also always understood for yet different reasons and with whom I have shared much . . . and to Tom, whom I have known lo these many years of grad school and from whom I have learned so much about friendship and faith. These few words seem so inadequate, and I have neglected to mention so many people, but I have greatly appreciated and benefited from all of the friendships have developed during the past 7 years in Boston.

Mom and Dad, I cannot possibly express the depth of my gratitude to you. You gave me a firm foundation and loving home, read *Make Way for Ducklings* and *From Atoms to Quarks* to me, and sent me off to become my own person. Anything I have accomplished in life is because of the support and love that you have always given me unconditionally.

Finally, to the One who is the Alpha and Omega, my faithful Savior, Jesus Christ . . .

Soli Deo Gloria

To my parents

who always had faith

Contents

List of Figures

List of Tables

Chapter 1

Introduction

In the broadest definition, the terahertz (1 THz = 10^{12} Hz) domain refers to the portion of the electromagnetic spectrum corresponding to photon frequencies between 0.1 THz and 10 THz; however, the most common usage of terahertz refers to frequencies between 0.3 THz and 3 THz [1]. Although the terahertz domain, also known as the submillimeter-wave region, has been explored scientifically, it has been largely unexploited commercially, due to the lack of low-cost components operating at terahertz frequencies.

A relatively new terahertz source is the photomixer, which generates coherent THz radiation through optical heterodyne down-conversion [2, 3, 4, 5]. A terahertz-frequency beat signal on an optical carrier illuminates an ultrafast photoconductor, modulating the conductance. The time-varying conductance together with a constant voltage bias generates time-varying current at the beat frequency, as long as the photoconductor can respond on the time scale of the beat. Low-temperature-grown gallium arsenide (LTG-GaAs) is the photoconductive material of choice in terahertz photomixing, because its short carrier lifetime (~ 200 fs) allows the conductance to be effectively modulated at THz frequencies[1]. The distributed photomixer described in this thesis is a new style of LTG-GaAs photomixer which uses an optical waveguide to couple the beat signal to an active area which is large relative to the terahertz wavelength and thus operates in the traveling-wave mode.

In the first section of this chapter, I mention some of the driving applications for tera-

[1]The advantage of materials with short carrier lifetime is discussed in Section 1.3.2

hertz technology, focusing on those relevant to distributed photomixer development. The following section contains an overview of terahertz components related to distributed photomixers, and the chapter concludes with an introduction to photomixer theory.

1.1 Applications of Terahertz Technology

Existing applications of terahertz technology fall into two broad categories, imaging and spectroscopy. Imaging systems generate THz radiation and then record the transmitted or reflected images of an object to deduce either its shape or composition. Terahertz spectroscopic applications are divided into transmit/receive and receive-only techniques, depending on whether the system generates and detects the THz signal or only detects it, as in a heterodyne receiver.

While imaging has been performed with coherent, continuous-wave (cw) sources [6], the majority of terahertz imaging systems use terahertz-bandwidth electromagnetic pulses generated by ultrashort-laser-pulse excitation of nonlinear crystals or polymers [7]. The success of this electro-optic technique suggests that imaging will likely remain in the realm of pulsed, time-domain systems.

Coherent sources play a critical role in either type of spectroscopy system, as narrowband emitters or as local oscillators (LOs) in heterodyne receivers. Spectroscopy is of particular interest in the terahertz, because a number of important light molecules, including H_2O, O_3, HNO_3, N_2O, HCl, ClO, NH_3, SO_2, and OH, either absorb terahertz frequency photons through excitation of rotational and vibrational modes or re-radiation of absorbed, higher-frequency energy in the terahertz. Therefore, observation of absorption or emission spectra yields information about the composition of the dust or gas being monitored.

Spectroscopy involving both transmission and reception of THz radiation has traditionally been the domain of incoherent sources and Fourier transform spectroscopy (FTS) [1]. The drawback to the FTS technique is that high-resolution spectroscopy ($\sim$ MHz) requires an instrument with tens of meters of travel and liquid-helium cooled detectors. Development of the photomixer has created the option of a compact, tunable, narrowband source, and a number of groups have demonstrated photomixing as a viable option for labora-

tory molecular spectroscopy [8, 9, 10, 11]. Most experiments have used a helium-cooled bolometer as the detector [8, 10], but a transmit-and-receive configuration comprised of two identical photomixers has achieved phase-sensitive detection of radiation through the technique of homodyne down conversion [12]. While very high atmospheric absorption in the terahertz makes long-distance versions of this type of spectroscopy unlikely, small systems for point-detection of chemical and biological agents are actively being pursued. As a stand-alone systems or in conjunction with sensors at other wavelengths, these "sniffers" would monitor local air content by continual measurement of absorption spectra and comparison to known spectra.

The development of heterodyne receivers has been the dominant driver in terahertz technology. By down-converting a portion of the THz spectrum to an intermediate frequency (IF) where it can be processed by low-noise amplifiers and correlators, heterodyne receivers allow measurement with high frequency-resolution of signals which cannot be amplified and processed directly. The primary applications of terahertz heterodyne receivers are in: plasma fusion diagnostics, in which the position-dependent electron temperature within the plasma can be inferred from the electron-cyclotron-emission spectrum; atmospheric monitoring, either of Earth or extraterrestrial bodies; and observation of interstellar dust and gas emission and absorption [1].

The astronomy applications [13] are those most relevant for photomixers, because they require compact, tunable LOs, and antenna-coupled photomixers have been demonstrated as LOs up to 630 GHz [14]. A sampling of planned and operating land and space-based missions provides a flavor of the scope of terahertz astronomy. Launched in 1998, the Submillimeter Wave Astronomy Satellite (SWAS), has been successfully observing interstellar clouds and star formation by recording lines of water, oxygen, carbon monoxide and other molecules in the frequency bands: 487–493 GHz and 547–557 GHz [15]. With its 3.5-meter primary mirror, the telescope for the European Space Agency's Herschel (formerly FIRST, Far InfraRed Space Telescope) mission will enable unprecedented observation from 480 GHz to 5 THz for investigation of interstellar dust, star-forming regions, extreme redshifted emissions from galaxies, and possibly even atmospheric composition of comets and extrasolar plants [16]. Scheduled for a 2007 launch, the Heterodyne Instrument for the Far

Infrared (HIFI) unit for Herschel completely covers 480 GHz to 1.25 THz in five bands and 1.41 THz to 1.91 THz in two bands. The HIFI unit will provide frequency resolution from 0.1–1.0 MHz with a 4 GHz IF bandwidth and receiver noise temperatures of 3–5 hf/k_B [17].

In addition to peering deep into the universe, space-based observatories monitor the chemistry of the Earth's atmosphere. Scheduled for a 2003 launch, the Earth Observing System (EOS) Aura mission [18] will contain a microwave limb sounder (MLS) for detecting chemicals in the upper atmosphere, especially those related to ozone depletion. Aura continues the work of the 1991-launched Upper Atmosphere Research Satellite (UARS) [19] and extends observation to higher frequencies including the OH line at 2.52 THz through the use of a compact methanol laser pumped by a CO_2 laser producing 30 mW of THz LO power to pump a Schottky-diode receiver [20].

Ground-based terahertz astronomy has been demonstrated since 1988 at the Caltech Submillimeter Observatory (CSO), a single 10.4-meter telescope operating on Mauna Kea, Hawaii. Operating frequencies of the heterodyne receivers at the CSO range from 300 GHz to 1 THz [21]. One of the most ambitious Earth-based astronomy projects ever attempted, the Atacama Large Millimeter Array (ALMA) will offer significant opportunities for terahertz technology development during its implementation and for terahertz astronomy during its operation. Planned for a 5000 m plateau in Chile, ALMA consists of a reconfigurable array of sixty-four 12-meter-dish telescopes covering all atmospheric transmission windows from 30 GHz to 850 GHz [22]. In a configuration spanning kilometers, the array will provide high angular resolution, while in a compact configuration, the telescopes act like a single enormous dish and can observe very faint objects. In either configuration, the local oscillator signal must be distributed to all of the telescopes. Distributing the LO directly is prohibitively expensive, so the current plan is for photonic distribution, i.e. the same LO signal is encoded in an optical signal which is split and propagates via optical fiber to each telescope where it is converted back to RF[2]. Photonic LO distribution for THz

[2]Even though it is a misnomer, the signal and LO frequencies in a THz heterodyne receiver are called RF, which stands for radio frequency, a holdover from the days when heterodyne receivers were used primarily in radio astronomy.

phased arrays is a natural application for photomixers because a photomixer is designed specifically to produce a terahertz signal from an optical signal.

1.2 Enabling Terahertz Technology

Terahertz systems require various quasioptical elements (lenses, mirrors, polarizers, etc.), waveguides, and signal processing techniques. The key enabling technologies, however, are the sources and detectors. Detectors fall into two broad categories: mixers which can be used for heterodyne detection and direct detectors which measure incident power [23]. Source technologies are varied since the terahertz frequency range falls in between the regime of transit-time-based classical devices (e.g. diodes and transistors) and quantum-transition-based devices (e.g. lasers).

1.2.1 Detectors

The three most successful types of terahertz heterodyne mixers are based on Schottky diodes, superconductor-insulator-superconductor (SIS) junctions, and hot-electron bolometers (HEBs). Each of these mixer technologies has been used or will be used on space-based and ground-based observatories.

Schottky mixers generate mixing products through either the nonlinear capacitive or resistive characteristic of a Schottky barrier formed at the interface of a metal and semiconductor (usually doped GaAs) [24]. Maturing from whisker-contacted devices to planar devices has improved reliability, durability, and reproducibility. These mixers operate at room temperature or cooled, have noise temperatures (T_n) in the range of 2000–5000 K, and require LO power of a few milliwatts [1, 25].

SIS devices operate at cryogenic temperatures but have a very nonlinear current-voltage characteristic which results in near-quantum-limited mixer noise temperatures of $\sim 5hf/k_B$ (which yields $T_n = 250$ K at 1 THz) [1, 26]. Because the LO-pumped current-voltage relationship is caused by photon-assisted tunneling of quasi-particles across the insulator barrier, SIS devices have a maximum operating frequency corresponding to twice the superconducting gap (Δ), which is proportional to the superconductor's critical temperature

(T_c), i.e. $2\Delta \sim 3.5 k_B T_c$ [1, 27]. Niobium, the most successful superconductor for SIS junctions has a $T_c = 9.3\,\mathrm{K}$ and therefore a maximum frequency of 1.4 THz. Higher T_c superconductors have been used for SIS mixers but the maximum operating frequency remains $< 2\,\mathrm{THz}$ for good noise performance. The LO power requirement for optimum operation is a few microwatts.

The most recently added member of the terahertz mixer family is the hot-electron bolometer, a resistive mixer which relies on the heating of an electron gas by absorption of terahertz photons [26, 28, 29, 30]. The HEB is effective as a mixer because the sub-micron-sized active area is cooled quickly enough to produce an IF signal up to several GHz. While HEBs theoretically need much less than 100 nW of LO power for good performance ($T_{\mathrm{mix}} \sim 10hf/k$), the few successful tests with well-calibrated low-power sources indicate that they need at least $0.5\,\mu$W of LO power at the dewar window for frequencies near 2 THz [31, 32]. The LO power requirement depends on the bolometer material, and new materials (aluminum, niobium, tantalum) promise lower required LO power than the proven niobium nitride HEBs but have yet to be consistently demonstrated in practical mixers.

Direct detectors have been used in lab settings for spectroscopy or component characterization and have been deployed for astronomical and atmospheric observations [1]. Uncooled detectors tend to be slow and low sensitivity, but can be useful at higher power where cooled bolometers saturate. Cooled (< 5 K) detectors, such as silicon or indium antiminide composite bolometers have much higher sensitivity but have the drawback of requiring cryogenic cooling. A detector operating at 50 mK based on single electron transistor has recently shown single photon sensitivity from 1.4 to 1.7 THz, but the device has a very large impedance [33].

1.2.2 Sources

Development of the coherent sources needed for operation of these heterodyne receivers has lagged behind detector development. I will mention the major technologies, including gas lasers, vacuum tube devices, quantum cascade lasers, three-wave mixing, Schottky-

diode multipliers, and photonic downconverters. In the terahertz frequency regime, transit time devices have decreasing performance with increasing frequency, while photonic, or quantum-transition, based devices have improving performance with increasing frequency.

The highest power terahertz sources of any reasonable size (i.e. neglecting gyrotrons and free-electron lasers) are molecular gas lasers. These optically-pumped lasers produce tens to hundreds of milliwatts at discrete frequencies up to several terahertz. While gas lasers tend to be fragile and bulky, CO_2-pumped methanol lasers at 2.52 THz are planned for both ground-based and space-based observatories [20, 34].

Vacuum tube devices, such as backward-wave oscillators (BWOs) and klystrons, supply milliwatt power levels to nearly 1 THz [35]. However, these tubes are available almost exclusively from Russia, require kilovolt power supplies and generally have short operating lifetimes. A number of groups are working on miniature vacuum electronics for oscillators, but no practical sources have been produced.

Quantum-cascade lasers (QCLs) based on intersubband transitions have been actively investigated as a means of extending laser operating frequencies from optical and near-infrared frequencies to longer wavelengths, especially the far-infrared [36, 37, 38, 39]. With the recent demonstration of a QCL operating at cryogenic temperatures producing a few milliwatts at 4.4 THz [40], QCLs have moved from the mid and long-wave infrared to the far-infrared with a projected lower frequency bound of 2 THz [41]. Though a number of issues such as frequency stability need to be addressed before a successful LO is created, the technology shows great potential as a compact, high-power, high-efficiency, coherent solid-state terahertz source.

The other solid-state photonic technique that is used in terahertz generation is $\chi^{(2)}$ mixing in nonlinear optical materials, such as $LiNbO_3$, KTP, and DAST. Nonlinear optical mixing is generally used in time-domain (i.e. short pulses with terahertz bandwidth) experiments but the technique has been successfully used for cw terahertz generation [42, 43]. Because of the Manley-Rowe limit, efficiency improves with increasing frequency.

Schottky multiplier chains generate terahertz radiation by upconverting a lower frequency (10–100 GHz) fundamental source, such as transistor or Gunn oscillators, through a series of frequency doublers and/or triplers [44, 45]. The same nonlinear capacitive or re-

sistive characteristic used in mixing an RF and LO signal to produce an IF signal generates harmonics of a pump signal. Multiplier chains have produced 14 mW at 400 GHz [32], 3 mW at 600 GHz [46], 2 mW at 800 GHz [47], 100 μW at 1.2 THz [46], and 45 μW at 1.5 THz [32]. Extensive fabrication and modeling work allow accurate production of diodes for fixed-tuned waveguide designs on the first fabrication run, and multiplier-chain operation up to 2 THz with power levels adequate for an LO in an HEB heterodyne mixer is projected in the near future [32]. The drawback of multiplier chains is the narrow tuning range ($\sim 10\%$). Nonetheless, mixers with Schottky-diode-based LOs have been demonstrated [48, 49] and multipliers are the baseline LO in Herschel [16].

Photomixers that generate coherent radiation through the downconversion of an optical beat signal have only recently been used for the generation of terahertz radiation [2, 4], though the photomixing effect itself has been investigated since the 1950's and can even be traced as far back as 1883 [50]. The key advantages of photomixers as terahertz sources are that they operate at room temperature, can be made compactly from all-solid-state components, and are frequency-agile. The main deficiency is that the output power is low (a few microwatts up to ~ 1.5 THz) because of low external quantum efficiency. Because photomixers are the subject of this thesis, I will discuss them in more depth below.

1.3 Photomixers

1.3.1 Photomixing Theory

Assuming photon absorption by an ideal photodetector, two monochromatic plane waves produce a count rate, or carrier generation rate,

$$R \propto I_1 + I_2 + 2\sqrt{mI_1I_2}\cos(\omega_1 - \omega_2)t \ , \tag{1.1}$$

where I and ω are the intensity and radial frequency, respectively, of the two fields and m is a positive number less than one which describes the degree of spatial overlap and copolarization [3]. Assuming incident photons generate free carriers which can be collected

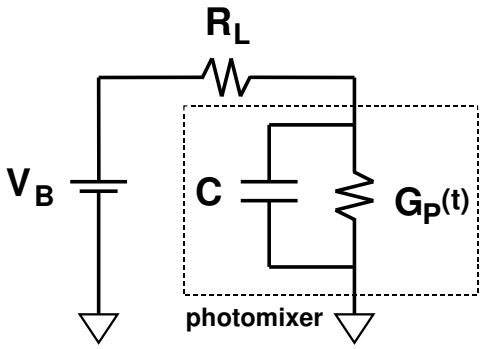

Figure 1-1: Equivalent circuit model for a lumped-element photomixer system.

with some non-zero probability, the current is given by

$$i = \frac{q\eta_e}{\hbar\omega}\left(P_1 + P_2 + 2\sqrt{mP_1P_2}\cos(\omega_1 - \omega_2)t\right) \ , \tag{1.2}$$

where η_e is the external quantum efficiency into which is lumped all carrier creation and collection effects and P is the power incident on the detector area. The quantum efficiency which gives the fraction of incident photons that induce an electron in the circuit depends on the specifics of the photodetector design and involves effects such as the carrier lifetime, transit time, applied electric field, and mobility. The photodetector responsivity can be written in terms of η_e as

$$S = \eta_e \frac{q}{\hbar\omega} \ . \tag{1.3}$$

The quantum efficiency and responsivity are discussed in greater detail in Section 4.3.

The photodetector type used almost exclusively in terahertz generation is the photoconductive small-area, or lumped-element, photomixer which has the simple equivalent circuit shown in Figure 1-1. The time-varying carrier generation is modeled as a time-varying conductance. The applied dc-voltage induces time varying currents which couple to the load (an antenna for quasioptical output or a coplanar waveguide for on-chip propagation) but are partially shunted by the photomixer's intrinsic capacitance. The frequency performance of the system depends on two factors: the $R_L\,C$ product and the intrinsic frequency response of the modulated conductance term, $G_P(t)$. The photoconductance can be written

as

$$G_P(t) = G_0(1 + \beta \sin \omega t) \ , \tag{1.4}$$

where G_0 is the dc-photoconductance, ω is the copolarized optical beat frequency $|\omega_1 - \omega_2|$ from equation (1.2), and β is the frequency-dependent modulation depth given by

$$\beta = \frac{2\sqrt{mP_1P_2}}{(P_1 + P_2)\sqrt{1 + \omega^2\tau^2}} \ , \tag{1.5}$$

where τ is the carrier lifetime [51]. β behaves as expected physically. For equal power in the optical beams and perfect overlap and copolarization, the modulation depth is maximized for a given difference frequency. The $\sqrt{1 + \omega^2\tau^2}^{-1}$ term models the effect that at frequencies near or above the reciprocal of the carrier lifetime, the photoconductor fails to "turn off and on" completely. At low power levels where saturation is not an issue, G_0 is given by

$$G_0 = \frac{SP_{\text{abs}}}{V_B} \ , \tag{1.6}$$

where S is the responsivity in amps per watt and P_{abs} is the absorbed optical power [51]. Equation (1.4) illustrates one of the great advantages of photomixing for RF generation: the current and power modulation frequency is set by the difference frequency between two lasers. Even terahertz frequencies are a small fraction of an optical laser's frequency, so the photomixer's frequency can be quickly and easily tuned over a bandwidth of a few THz by frequency tuning the optical pump lasers. This frequency-agility makes photomixers attractive for spectroscopy applications.

In the small-signal approximation, i.e. when $G_0R_L \ll 1$ and the photomixer looks like a current source, the power delivered to the load is given by

$$P_\omega = \frac{1}{2}\frac{\left(V_BG_0\right)^2 R_L}{(1 + \omega^2\tau^2)\left(1 + \left(\omega R_L C\right)^2\right)} \ , \tag{1.7}$$

where the modulation depth is assumed to be maximized for the given frequency, ω [51]. At low frequencies, equation (1.7) reduces to the expected dc result of $\frac{1}{2}(V_BG_0)^2R_L$, while

at high frequencies, the expression becomes

$$P_\omega \sim \frac{1}{2}\frac{(V_B G_0)^2 R_L}{\omega^4 (\tau R_L C)^2} \ . \tag{1.8}$$

The next section describes material considerations and device designs to maximize this terahertz power, including the distributed photomixer idea.

1.3.2 Terahertz Photomixers

For the generation of millimeter-wave and terahertz radiation, most photomixer designs have been metal-semiconductor-metal (MSM) devices with the semiconductor being low-temperature-grown gallium arsenide (LTG-GaAs) [5]. Interdigitated metal electrodes provide the dc voltage bias and collect the photocurrent and couple it to an antenna also deposited on the LTG-GaAs. When GaAs is grown by molecular beam epitaxy (MBE) at low substrate temperatures ($\sim 250^{\circ}C$) and with As overpressure, excess (up to 1%) arsenic is incorporated, creating a nonstoichiometric material with a large number of defects ($10^{20}\,\mathrm{cm}^{-3}$, mostly arsenic antisites) [52]. This as-grown material has a very low resistivity (tens of $\Omega\,\mathrm{cm}$) and fast electron and hole trapping times [53]. Annealing ($\sim 600^{\circ}C$ for 10 minutes) reduces the number of defects to $\sim 10^{19}\,\mathrm{cm}^{-3}$ through the formation of As precipitates [54] which increases the resistivity dramatically to 10^6–$10^7\ \Omega\,\mathrm{cm}$ [52] while slightly increasing the electron capture time ($\sim 250\,\mathrm{fs}$ [55]) and the electron mobility (reported values vary between $160\,\mathrm{cm}^2/\mathrm{Vs}$ [56] and $2000\,\mathrm{cm}^2/\mathrm{Vs}$ [51]). Electrons are the dominant carrier in annealed LTG-GaAs, so discussion centers on their properties. The defects in both as-grown and annealed LTG-GaAs have energy near midgap [52] pinning the Fermi level there and allowing many as-deposited metals to form ohmic contacts. These material characteristics, along with a high electric breakdown field ($\sim 1 \times 10^6 \mathrm{V/\,cm}$), make LTG-GaAs an ideal material for photoconductive mixing of optical signals with photons above the 1.42 eV ($\lambda = 873\,\mathrm{nm}$) bandgap.

Early work on LTG-GaAs photomixers focused on reducing the electron lifetime to reduce the τ-dependent high-frequency roll-off term in equation (1.7) [55]. Even though the output power for photomixers operating at frequencies for which $\omega\tau \gg 1$ does not

depend on carrier lifetime, shorter lifetimes lead to improved device performance due to higher efficiency modulation of the LTG-GaAs conductance [5]. Two photomixers with different τ but the same illumination will produce the same THz power as long as the operating frequency is beyond the "knee" of the lifetime response, i.e. $\omega\tau \gg 1$; however, the total dc photocurrent will be higher in the longer lifetime material by the ratio of the lifetimes. Higher dc photocurrent leads to a higher heat load and device failure at lower THz output power (compared to the short lifetime material which generates less dc photocurrent for the same THz power). In most LTG-GaAs photomixer work, carrier transit times are neglected because the transit time even for electrode gaps $\sim 1\,\mu$m are much larger than the carrier lifetime. This difference means that the LTG-GaAs photomixer is a lifetime dominated device and also leads to very low photoconductive gain (typically < 0.01).

Because the failure mode of photomixers has been burnout due to heating from a combination of absorbed optical power and ohmic heating, continuing material work includes the growth of LTG-GaAs on silicon for better thermal conductivity [3] and the growth of high-thermal-conductivity layers (e.g. AlAs) beneath the LTG-GaAs layer [57]. Jackson quantified the importance of thermal considerations by demonstrating that the maximum output power at a certain frequency and given a circuit design and carrier lifetime is

$$P_{\max} \propto \frac{\eta_e^2}{\theta^2 \left(A + V_B \eta_e (q/\hbar\omega)\right)^2} \,, \tag{1.9}$$

where θ is the thermal impedance, A is the device area, and the terms in the denominator account for conduction of the optical-power-induced heating and ohmic heating, respectively [57]. The work of Jackson emphasizes the importance of photomixer designs which both increase η_e and distribute the optical and ohmic heat load. A technique which increases η_e by increasing carrier collection efficiency is the use of Bragg reflectors beneath the LTG-GaAs to create a multiple-pass cavity [58]. The applied electric field which collects photo-generated carriers decreases with depth into the LTG-GaAs, so even though a thick LTG-GaAs layer will absorb all optical power, collection is not efficient deep within the LTG-GaAs. For a thin layer backed by a mirror, higher responsivity is achieved for the same absorbed power. The field dependence of carrier collection efficiency is dis-

cussed in more detail in Section 4.3. In a material technique that is a slight departure from LTG-GaAs, self-assembled erbium arsenide (ErAs) islands grown in GaAs act in a manner similar to the As precipitates, and the GaAs:ErAs material has been used as the photoconductor in THz generation [59]. The advantage of this technique is that the size and density of the ErAs islands can be controlled; however, the material has not yet shown improvement over LTG-GaAs. Finally, the work of Zamdmer, *et al.* demonstrated that the electron lifetime increases with applied electric field, which is important because it means that there is a maximum operating V_B for a given frequency [56]. This electron-lifetime effect is discussed in more detail in Section 4.1.2.

In addition to material improvements, new device and circuit configurations seek to optimize C, R_L, and G_0 from the standpoint of the metal structure deposited on the LTG-GaAs. From equation (1.8), high-frequency photomixer operation is improved by minimizing the photomixer capacitance (to avoid the $(\omega R_L C)^{-2}$ pole) and maximizing G_0 (to increase the power at all frequencies). Minimizing C and maximizing G_0, however, are generally competing goals for a lumped-element photomixer, because both are proportional to the device area. A larger area means not only a larger area over which to distribute optical power absorption but also more capacitance between the electrodes which collect the current. Reducing the electrode width and the distance between electrodes does allow an increase G_0 without a corresponding penalty in C; however, a lower limit to electrode width of $0.2\,\mu$m determined by fabrication practicality sets a corresponding limit on the extent to which this tradeoff can be made [58]. A successful technique for avoiding the $R_L C$ pole has been the design of antennas with inductive elements to resonate out the photomixer intrinsic capacitance and allow the benefits of a higher R_L to be realized over a narrow frequency band [60]. Dipole, double dipole, and double slot antennas have been designed using this technique [57, 60].

While resonant antennas with inductive tuning elements achieve narrowband elimination of C, these designs sacrifice one of the major benefits of photomixing, the frequency agility. By creating a photomixer for which the active area is large relative to the THz frequency and operates in the traveling-wave mode, the $(\omega R_L C)^{-2}$ pole can be eliminated over the entire operating range. In the resonant-tuning picture, the distributed inductance

of a traveling-wave structure exactly resonates out the distributed capacitance leading to the well-known result that a transmission line has a frequency independent impedance. In addition to eliminating the deleterious effect of intrinsic capacitance, a distributed structure allows for higher G_0 because the maximum optical power that can be absorbed before device failure is increased by distributing the optical and ohmic heat load over a larger area/volume. A surface-illuminated traveling-wave photomixer has been demonstrated by Matsuura, *et al.* and it produced 200 nW at 2.5 THz [61]. The drawback of this surface-illuminated design is that the optical signal must be free-space coupled because the traveling wave of photogenerated carriers is tuned by varying the incidence angles of the two lasers. In this thesis, I describe the design, fabrication and characterization of a waveguide-coupled distributed photomixer. In a waveguide-coupled distributed photomixer, the optical beat signal is guided by an optical waveguide and coupled weakly to a terahertz waveguide by a LTG-GaAs absorber layer [62]. Power is gradually converted from the optical beat signal through generation of a conductance wave which leads to a current wave and an electromagnetic (THz) wave at the beat frequency. The terahertz power can be confined on-chip or radiated for quasi-optical propagation and collection by a receiver. In addressing a number of concerns related to traveling-wave photodetectors, I draw on extensive work done on traveling-wave photodetectors designed for lower frequency operation [63, 64, 65, 66, 67, 68, 69].

A few comments on traveling-wave photodetector theory provide insight into the operation of these devices and the design considerations involved. For the purposes of considering a distributed photomixer, the two main effects of operating in traveling-wave mode are: 1) the 6 dB reduction in RF power compared to a lumped-element device with the same photocurrent and 2) the need to match the optical and THz (RF) wave velocities. To understand the 6 dB reduction in power for a device in traveling-wave mode, consider a photomixer which consists of an active area modeled as a current source delivering power to a load. When the optical beat frequency is small compared to the size (length) of the active area, all of the current produced will be in phase. Thus, if we neglect carrier lifetime effects, all of the RF current generated delivers RF power to the load. Once the beat frequency becomes comparable to the length of the active area, the current source becomes

distributed. Half of the current produced at any point along the active area flows toward the load, and half flows in the opposite direction. The portion of current that flows toward the load combines in phase with other current produced (by absorption of the propagating optical beat) in the active area and delivers RF power to the load. Current flowing in the opposite direction; however, is completely out of phase with the counter-propagating optical beat signal and thus is not phase matched and generates no RF power. Therefore, with half of the current delivered to the load, one quarter (-6 dB) of the power is delivered.

From an intuitive perspective, the need for velocity match can be understood by considering co-propagating optical and RF waves. The photomixing process can be considered as a transfer of power from the optical to the RF, as in $\chi^{(2)}$ mixing. Power transfer will be more efficient the closer the waves are velocity matched. The aspect of this velocity matching that is less clear is which velocities need to be matched. The fundamental requirement that must be met is the phase matching condition,

$$k_{o1} - k_{o2} = k_{RF}\,, \tag{1.10}$$

where k_{o1} and k_{o2} are the optical propagation constants and k_{RF} is the RF propagation constant. Dividing this equation by the optical difference frequency, which is also the RF frequency yields

$$\frac{k_{o1} - k_{o2}}{\omega_{RF}} = \frac{k_{RF}}{\omega_{RF}}\,, \tag{1.11}$$

where ω_{RF} is the optical beat and RF frequency. If the dispersion relation of the optical waveguide is well behaved (linear over the frequency range between the two optical frequencies), the relation becomes

$$\frac{\Delta k_o}{\Delta \omega_o} = \frac{1}{\mathrm{d}\omega/\mathrm{d}k} = \frac{k_{RF}}{\omega_{RF}}\,, \tag{1.12}$$

which reduces to

$$(v_{o,g})^{-1} = (v_{RF,ph})^{-1}\,, \tag{1.13}$$

where $v_{o,g}$ is the optical group velocity and $v_{RF,ph}$ is the RF phase velocity.

Figure 1-2 illustrates these two effects. The 6 dB roll-off occurs at a frequency cor-

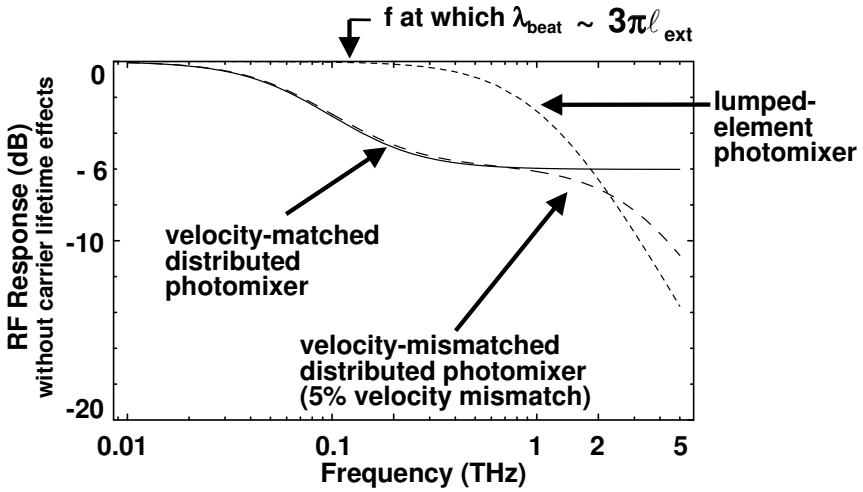

Figure 1-2: Bandwidth plots of lumped-element and distributed (both velocity-matched and velocity-mismatched) photomixers operating at the same photocurrent and neglecting carrier lifetime and parasitic (e.g. ohmic) losses.

responding to a optical beat wavelength (in the dielectric) of approximately $3\pi\ell_{\rm ext}$, where $\ell_{\rm ext}$ is the extinction length of the optical mode. The relevant length is $\ell_{\rm ext}$ and not $\ell_{\rm phys}$ (the physical device length) because the extinction length sets the effective device length, or interaction length. Note that most sources which discuss traveling-wave photodetector theory (e.g. [64, 68]) incorrectly describe this frequency as the 3 dB bandwidth set by velocity mismatch. This roll-off has nothing to do with velocity-mismatch and is simply due to the device entering traveling-wave mode. Velocity-mismatch does have a role and is considered next.

By considering various combinations of device length and extinction length, a number of aspects of traveling-wave photodetector theory can be elucidated. Using the formulation of Chiu [70] given in [68] as

$$I_f(\omega) = e^{-\gamma_m l}\left(\frac{1-\exp(-(\gamma_o-\gamma_m)l)}{\gamma_o-\gamma_m}+\frac{1-\exp(-(\gamma_o+\gamma_m)l)}{\gamma_o+\gamma_m}\right), \qquad (1.14)$$

where γ_m is the microwave (RF) propagation constant ($\gamma_m = j\omega\sqrt{\epsilon_{\rm re}}/c$ for a quasi-TEM mode), γ_o is the optical propagation constant ($\gamma_o = \Gamma\alpha_o + j\omega/v_o$ where $\Gamma\alpha_o = 1/\ell_{\rm ext}$ and v_o is the optical group velocity) and $l = \ell_{\rm phys}$, the RF response of traveling-wave

photodetectors can be predicted for combinations of $\ell_{\rm ext}$ and $\ell_{\rm phys}$. Figure 1-3 shows three combinations. Note that even though absolute frequency is given as the x axis, the plots can be scaled. For example, increasing the extinction length by a factor of 10, scales all the frequencies down by a factor of 10. In the figures, velocity mismatch has been defined as $1 - v_o/v_e$. Figure 1-3(a) shows the response of a device for which $\ell_{\rm phys} \sim \ell_{\rm ext}$. The smooth curves are for a device for infinite $\ell_{\rm phys}$ and are provided to show the asymptotic behavior of the response. The small scale ripples are due to reflections from the un-terminated input port of the RF waveguide. In understanding the other features, it is helpful to rewrite the expression of Chiu describing the magnitude of the forward going current wave as

$$\frac{1 - \exp(-2\Gamma\alpha_o l) - 2\exp(-\Gamma\alpha_o l)\cos(\Delta k l)}{(1/\ell_{\rm ext})^2 + (\Delta k)^2}, \tag{1.15}$$

where I have used $\Delta k = \omega(v_o^{-1} - v_e^{-1})$ to denote to the phase mismatch. The larger scale ripples occur as $\cos(\Delta k l)$ and correspond to the fact that even as phase mismatch accumulates, there are discrete frequencies for which the accumulated mismatch will be destructive or constructive for a finite length device. These cases correspond to having accumulated either π or 2π phase mismatch over the length of the device. The velocity mismatch roll-off has an onset at $\Delta k \ell_{\rm ext} = 1$ because this is the point at which appreciable phase mismatch accumulates by the effecitive end of the device (rather than the physical end of the device). Figure 1-3(a) shows the response of a device for the same $\ell_{\rm ext}$ but longer $\ell_{\rm phys}$, while Figure 1-3(c) shows the response of a device for the same $\ell_{\rm phys}$ (as Figure 1-3(a)) but shorter $\ell_{\rm ext}$. These figures show the asymptotic behavior of devices as $\ell_{\rm phys}$ becomes long relative to $\ell_{\rm ext}$.

The basic photomixing effect is the same for a distributed photomixer as for a lumped-element photomixer. The equivalent circuit, however, is completely different. In Figure 1-4, a differential element of the distributed photomixer equivalent circuit is shown. An optical waveguide (transmission line) guides the optical signal which is coupled to the THz waveguide through the current source which models the photoconductive element. The other two lumped elements R_{pc} and C_{elec} model the photoconductor series resistance and the distributed capacitance of the electrodes which collect the photocurrent and are

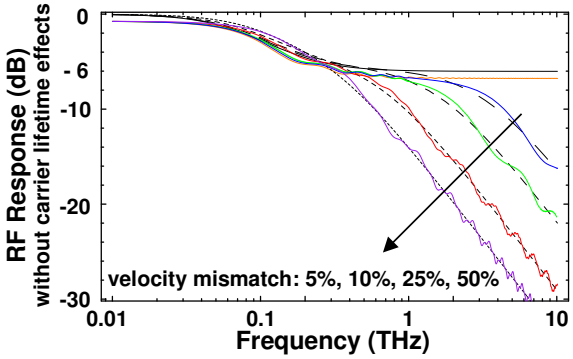

(a) $\ell_{\text{phys}} = 150\,\mu\text{m}$. $\ell_{\text{ext}} = 90\,\mu\text{m}$.

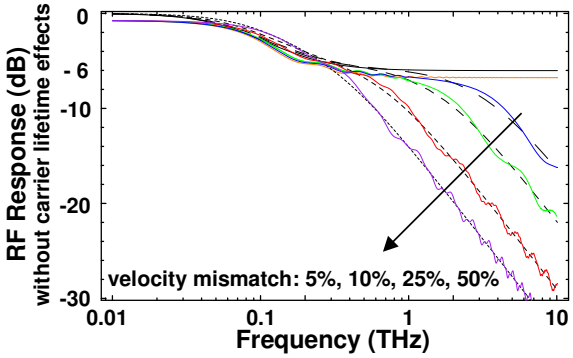

(b) $\ell_{\text{phys}} = 225\,\mu\text{m}$. $\ell_{\text{ext}} = 90\,\mu\text{m}$.

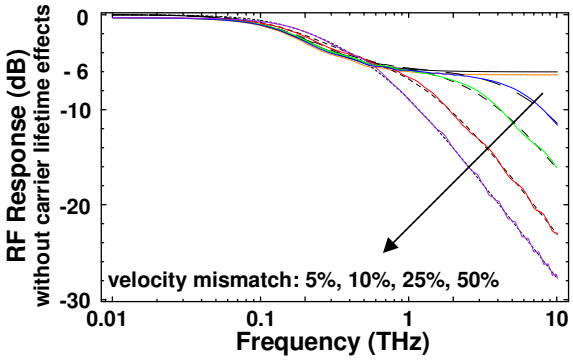

(c) $\ell_{\text{phys}} = 150\,\mu\text{m}$. $\ell_{\text{ext}} = 45\,\mu\text{m}$.

Figure 1-3: Response of traveling-wave photomixers with different ℓ_{ext} and ℓ_{phys} values. The smooth (dashed) lines represent the response of an infinitely long device and are provided as symptotes for the behavior of the finite length devices.

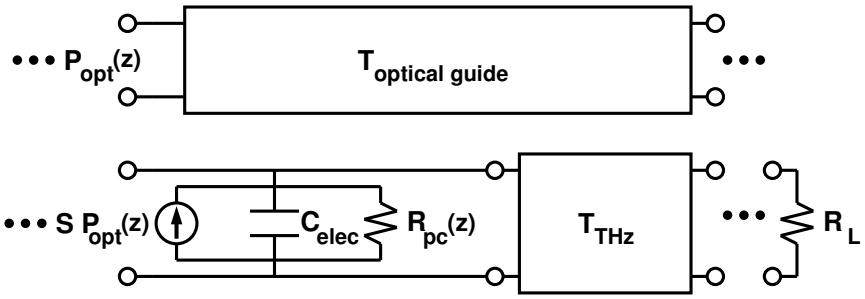

Figure 1-4: Equivalent circuit model for a distributed photomixer system.

explained in Section 2.2. A SPICE circuit using this differential element model for the distributed photomixer is explained in Section 5.1. The traveling-wave nature of the active area is accounted for in the SPICE model accounts. If this velocity-match problem is addressed and other losses are low, the distributed photomixer's bandwidth is set solely by the LTG-GaAs carrier lifetime, which means this distributed design has the largest possible bandwidth for a photomixer. If the optical and terahertz waveguides are coupled properly to achieve efficient conversion of optical to terahertz power, the distributed photomixer can also produce high power over this bandwidth.

This thesis describes waveguide-coupled distributed photomixers designed to capture the benefits of the distributed photomixing idea for coherent terahertz generation. In Chapter 2, I discuss the design trade-offs involved in the design of the optical waveguide, terahertz waveguide and radiating element. I present a general methodology through development of a specific design which, together with the details in Appendix A, allows others to understand and use the design process. Chapter 3 contains fabrication and post-processing steps for making distributed photomixers. Again, I provide general considerations as well as specific recipes for fabrication steps. In Chapter 4, I describe a number of different measurements which characterize various aspects of the distributed photomixer. Because distributed photomixer performance depends on many different material and device characteristics, I measure as many as possible to be able to accurately model and predict device performance. In Chapter 5, the results from Chapter 4 are used to predict the distributed photomixer performance, which is compared with THz photomixing measurements.

Chapter 2

Distributed Photomixer Design

This chapter contains the design of each of the three major components of the distributed photomixer structure. The structure consists of a waveguide to confine the optical beat signal and couple it to the absorber, a waveguide to guide the terahertz (THz) signal, and a radiating element to couple the THz power off of the chip. For each component, I describe performance considerations, design methodology, and analysis techniques.

In order to provide a complete, self-contained explanation of the design process, I present the design flow with as few preconceived assumptions or constraints as possible; however, some external influences are inevitable and desirable. Some design choices are informed by other work in the field, and some choices are informed by our own previous experience. In addition, certain design choices are shown to be reasonable only in an *a posteriori* sense — either from simulation or device testing — but are presented in the flow of the design and not afterwards for the sake of the chapter's coherence and usefulness.

2.1 Optical Waveguide Design

Three primary considerations influence the design of the optical waveguide for a distributed photomixer. The optical beat signal needs to:

a) be coupled into the waveguide efficiently and over as large an area as possible,

b) be coupled to the absorbing, photomixing material sufficiently to give the de-

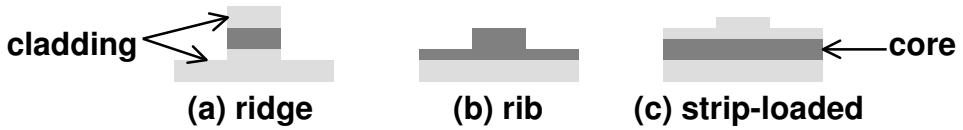

Figure 2-1: Schematics of etched dielectric waveguides.

sired mode extinction length (the distance a mode propagates before its power is e^{-1} of its original value), and

c) propagate in a single mode so that it can be described by a single phase velocity.

After choosing a general type of optical waveguide, I use these design considerations to specify a specific geometry.

The absorption of the optical beat signal and resulting photomixing occurs in a low-temperature-grown gallium arsenide (LTG-GaAs) layer; therefore, the optical waveguide must be compatible with growth and fabrication of LTG-GaAs. The natural choice for the waveguide, then, is a dielectric waveguide composed of layers of aluminum gallium arsenide ($Al_xGa_{1-x}As$) grown on GaAs. Choosing a large enough aluminum fraction, x, of the $Al_xGa_{1-x}As$ layers prevents absorption of the optical pump signal in any layer but the LTG-GaAs absorber. The index-of-refraction contrast between low index cladding layers and a higher index core layer provides confinement of the optical mode in the vertical (growth) direction, and patterning of the layers provides confinement in the lateral direction.

Several different etched layer geometries, including ridge, rib, and strip-loaded guides, provide lateral confinement. In a ridge waveguide (Figure 2-1(a)), cladding layers provide vertical confinement while the index contrast between the core region and air provides horizontal confinement. A rib waveguide (Figure 2-1(b)) is similar to a ridge waveguide, but the upper cladding layer is not present and the guide layer is not usually etched completely. In a strip-loaded waveguide (Figure 2-1(c)), patterning of the upper cladding layer laterally from a central strip confines the mode. In the ridge and rib waveguide designs, the high index contrast between the core region and air provides strong confinement, meaning that the core region must be narrow laterally to ensure single mode operation. This narrowness

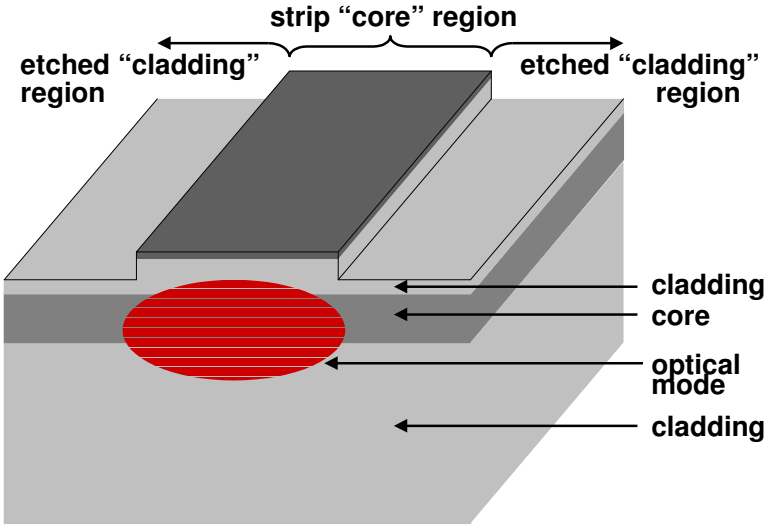

Figure 2-2: Schematic of strip-loaded waveguide.

means that comparatively little optical signal can be coupled into the guide for a given power density, dictated by the facet damage threshold. The strong confinement also results in high optical field strength on the etched sidewalls, which leads to loss. Creating a buried ridge waveguide through regrowth after etching eliminates the problems associated with high index contrast in the ridge and rib waveguide geometries; however, a regrowth step adds complication to the fabrication process without any gains for this particular application. Therefore, we choose a strip-loaded dielectric waveguide as the optical waveguide, as depicted in Figure 2-2. While the LTG-GaAs layer could theoretically be grown at any position in the layer stack, for ease of integration with the THz waveguide, the LTG-GaAs layer is grown on top.

2.1.1 Optical Waveguide Modeling

To analyze and design specific waveguide structures, I wrote codes to calculate dielectric waveguide modes based on the method of field shadows [71]. This technique uses a combination of one-dimensional (1-D) multilayer dielectric stack analysis and the effective index method to calculate the fields in a two-dimensional (2-D) dielectric waveguide. The method of field shadows accurately predicts the lowest order modes in a variety of

waveguides when the mode is far from cutoff [71]. In Section 2.1.2, I provide comparison between my code and a commercial full-wave analysis package for two-dimensional waveguides. Appendix A contains the detailed equations for my formalism. By writing my own code, I have access to the material parameters as well as the the equations for the mode profile. This access gives the abilities to change the material parameters arbitrarily and to perform calculations directly on the mode, such as finding the waist and finding the coupling to a circular Gaussian beam.

Enforcing the boundary conditions on the electric and magnetic fields at the layer boundaries gives exact solutions to the modes in a one-dimensional multilayer dielectric slab waveguide. For a strip-loaded guide, one of the layers which has a higher index of refraction than the surrounding layers is the core and contains most of the optical mode. The surrounding, lower-index layers function as cladding. Solving the coupled linear equations that enforce the boundary conditions yields the mode profile as well as propagation constant of the mode. The propagation constant is related to the *effective index* for the mode, using the following relations

$$v = \frac{c}{n_{\text{eff}}} \quad \text{and} \quad \beta = k_0 n_{\text{eff}} \ , \tag{2.1}$$

where c is the speed of light, $k_0 = \frac{2\pi f}{c}$, f is the optical frequency, and n_{eff} is the effective index. To solve the two-dimensional problem, the effective index method treats the central, strip region as a 1-D slab waveguide (in the z direction) and solves for an effective index. The lateral, etched regions are also solved as slab waveguides with corresponding effective indices. As shown in Figure 2-3, the effective indices of the strip and etched regions form an effective dielectric stack in the direction orthogonal to growth (the x direction). Solving this 1-D dielectric stack yields the effective index for the two-dimensional mode as well as the lateral mode profile. The group velocity of the optical wave can be found by solving for the effective index over a range of frequencies and then taking $(\mathrm{d}k/\mathrm{d}\omega)^{-1}$. The final 2-D mode field profile is a product of the fields in the orthogonal directions. The power distribution of the mode is calculated as explained in Appendix A. The fill factor, or fraction of the total power in a certain portion of the waveguide is calculated from the power distribution. For

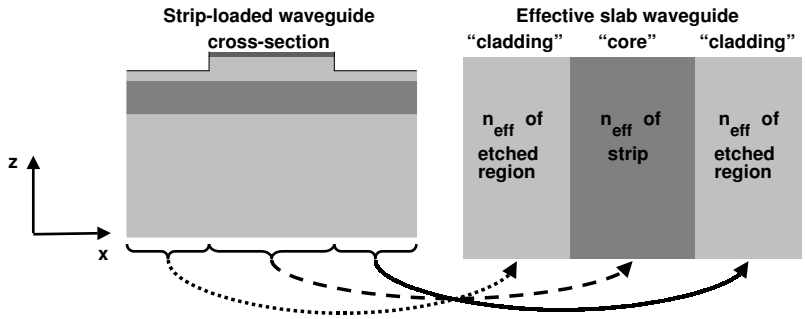

Figure 2-3: Schematic showing the treatment of a two-dimensional waveguide as the combination of orthogonal one-dimensional waveguides using the effective index method. Propagation in the strip-loaded waveguide is in the y direction.

a detailed discussion of this procedure, see Appendix A.

2.1.2 Comparison of Modeling Techniques

To estimate the accuracy of my effective index code, I compared the effective index and fill factor calculations for a nominal structure with calculations of the same structure analyzed with a commercial full-wave analysis code for dielectric waveguides, FIMMWAVE [72]. The structure analyzed supports two TE and two TM modes. The effective indices of the modes are compared in Table 2.1, which shows that my code predicts the effective index of each mode quite accurately. As expected, the effective index method is more accurate for the lower order modes. Fill factor calculations for the absorber layer and for the core of the strip-loaded waveguide are compared. The results of the absorber fill factor comparison are tabulated in Table 2.2, while the core fill factor results are shown in Table 2.3. As explained in Section 2.1.3, the more important factor of these two is the absorber fill factor, which the effective index method calculates to within about ten percent accuracy for all of the modes considered.

Because measured dielectric constants are not available for all $Al_xGa_{1-x}As$ compositions at all wavelengths, we must employ an interpolation or modeling to fill in missing data. Thus, in addition to differences arising from the choice of numerical technique, this

Table 2.1: Comparison of modeling techniques: effective index

Strip-Loaded Waveguide Mode Effective Index Calculation					
Waveguide Mode			Technique		Fractional Difference
			Field Shadows	FIMMWAVE	
TE	1^{st}	order	3.42961	3.42939	6.4×10^{-5}
TE	2^{nd}	order	3.42503	3.42424	2.3×10^{-4}
TM	1^{st}	order	3.42784	3.42767	5.0×10^{-5}
TM	2^{nd}	order	3.42296	3.42232	1.9×10^{-4}

Table 2.2: Comparison of modeling techniques: absorber fill factor

Strip-Loaded Waveguide Absorber Fill Factor Calculation					
Waveguide Mode			Technique		Fractional Difference
			Field Shadows	FIMMWAVE	
TE	1^{st}	order	0.005862	0.005713	0.026
TE	2^{nd}	order	0.005336	0.004683	0.14
TM	1^{st}	order	0.002086	0.002281	0.085
TM	2^{nd}	order	0.001954	0.001995	0.021

Table 2.3: Comparison of modeling techniques: core fill factor

Strip-Loaded Waveguide Core Fill Factor Calculation					
Waveguide Mode			Technique		Fractional Difference
			Field Shadows	FIMMWAVE	
TE	1^{st}	order	0.8012	0.7998	0.0018
TE	2^{nd}	order	0.7293	0.7375	0.011
TM	1^{st}	order	0.8126	0.8083	0.0053
TM	2^{nd}	order	0.7649	0.7608	0.0054

model choice affects the mode calculation. A simple interpolation for the real part of the the dielectric function of $Al_xGa_{1-x}As$ is the Sellmeier equation[1],

$$n^2(x,\lambda) = 10.906 - 2.92x + \frac{0.97501}{\lambda^2 - C} - 0.002467(1.41x + 1)\lambda^2 \ , \tag{2.2}$$

where

$$C = (0.52886 - 0.735x)^2 \ \text{for}\, x \leq 0.36 \tag{2.3}$$

$$C = (0.30386 - 0.105x)^2 \ \text{for}\, x \geq 0.36 \ , \tag{2.4}$$

and where n is the index of refraction, x is the aluminum mole fraction, and λ is the wavelength in microns $(0.69 < \lambda < 1.0)$ [73]. Another commonly used set of relations is the semi-analytical model proposed by Adachi [74]. These relations are given as

$$\epsilon_1(\omega) = A_0 \left\{ f(\chi) + \frac{1}{2}\left[\frac{E_0}{E_0 + \Delta_0}\right]^{3/2} f(\chi_{so}) \right\} + B_0 \tag{2.5}$$

$$f(\chi) = \chi^{-2}\left[2 - (1+\chi)^{1/2} - (1-\chi)^{1/2}\right] \tag{2.6}$$

$$\chi = \frac{\hbar\omega}{E_0} \tag{2.7}$$

$$\chi_{so} = \frac{\hbar\omega}{E_0 + \Delta_0} \ , \tag{2.8}$$

where A_0 and B_0 are fitting parameters, E_0 is the lowest direct gap energy, and $\hbar\omega$ is the photon energy. By fitting to data, Adachi arrived at the expressions

$$A_0(x) = 6.3 + 19.0x \tag{2.9}$$

$$B_0(x) = 9.4 - 10.2x \ , \tag{2.10}$$

where x is the aluminum fraction. Djurišić, *et al.* proposed an extension to Adachi's model which retains some of the simplicity but improves agreement with measurement [75]. The model only applies, however, over the range from 1.5 to 6.0 eV.

For $Al_xGa_{1-x}As$ compositions with $x < 0.40$ and in the wavelength range 840 nm $<$

[1]Note that the denominator is incorrectly written as $\lambda^2 + C$ in [71].

Table 2.4: Indices of refraction for $Al_xGa_{1-x}As$ with $x < 0.40$ and index contrasts for selected core and cladding layers according to the Sellmeier equation and at $\lambda = 850$ nm.

Al fraction	Index
0.00	3.620
0.05	3.576
0.10	3.536
0.15	3.500
0.20	3.466
0.25	3.434
0.30	3.403
0.35	3.374
0.40	3.351

(a) Index of $Al_xGa_{1-x}As$ compositions at $\lambda = 850$ nm.

Core Al fraction	Cladding Al fraction	Δn
0.30	0.35	0.029
0.20	0.25	0.032
0.10	0.15	0.037
0.30	0.40	0.053
0.20	0.30	0.062
0.10	0.20	0.071
0.20	0.35	0.092
0.20	0.40	0.115
0.10	0.30	0.133
0.10	0.35	0.162
0.10	0.40	0.186

(b) Index contrasts (Δn) between layers with different $Al_xGa_{1-x}As$ compositions at $\lambda = 850$ nm.

$\lambda < 860$ nm, the Sellmeier and Adachi expressions vary on the order of a percent. While the effective index of the mode varies by a correspondingly small amount, the absorber fill factor and mode extinction length can vary by up to 30%. As evidenced by the degree of agreement between my code and FIMMWAVE, that package must use the Sellmeier equation. To duplicate the results of Lin, *et al.* [66], I used Adachi's expressions for the $Al_xGa_{1-x}As$ (and the non-standard value of $\epsilon_1 = 12.91$ for GaAs at $\lambda = 860$ nm.) Thus, prior work indicates evidence of dielectric waveguide design using both formulations. The values predicted by Sellmeier agree better with the data [76] at 1.5 eV, while Adachi's formulation agrees more closely with the data at 1.4 eV. Because my design wavelength, 850 nm, is slightly closer to 1.5 eV, the Sellmeier equation is appropriate. Table 2.4(a) contains indices of refraction for different Al fractions in $Al_xGa_{1-x}As$ at $\lambda = 850$ nm using the Sellmeier equation.

2.1.3 Dielectric Waveguide Design

Based on the performance considerations described in Section 2.1 and the analysis tool and material data described in Sections 2.1.1 and 2.1.2, I present the design methodology for the distributed photomixer optical waveguide. The three primary design considerations for the design of the optical waveguide are that the optical power be coupled into the waveguide efficiently over a relatively large area, that the power then be coupled to the absorber, and that the waveguide support a single mode. Each of these design considerations can be linked both to a performance metric and a characteristic of the waveguide. The input coupling determines the amount of power that can be coupled into the guide for a given power density threshold and is determined by the mode shape. The coupling of the guided mode to the absorber layer determines the length of guide along which the optical power will be absorbed and thus the area over which photomixing occurs. This coupling to the absorber depends primarily on the thickness of the upper cladding layer. Finally, a good velocity match between the terahertz and optical signals can only be achieved if the optical signal propagates with a single phase velocity, i.e. in a single mode. The single mode nature of the guide depends on the thickness of the core, width of the strip as well as the strength of confinement in both the vertical and lateral directions. In addition to the primary considerations, a wider strip will give more absorber area (and therefore volume) over which to distribute the heat load from optical power and ohmic heating in the photoconductor. This constraint is not independent of the input coupling efficiency consideration. Finally, the only absorption of the optical power should occur in the absorber layer. This requirement maximizes device efficiency and constrains the possible aluminum fractions for the $Al_xGa_{1-x}As$ layers and requires the lower cladding to prevent interaction of the mode with the absorbing GaAs substrate. Thus, four layers are required: lower cladding, core, upper cladding, and absorber.

A schematic cross-section of the strip-loaded waveguide with the design variables is shown in Figure 2-4. The variables are the height (or thickness) of the lower cladding, core, upper cladding, and absorber layers, the aluminum fraction in the core and cladding regions, the strip width and the etch depth. With only four independent constraints or

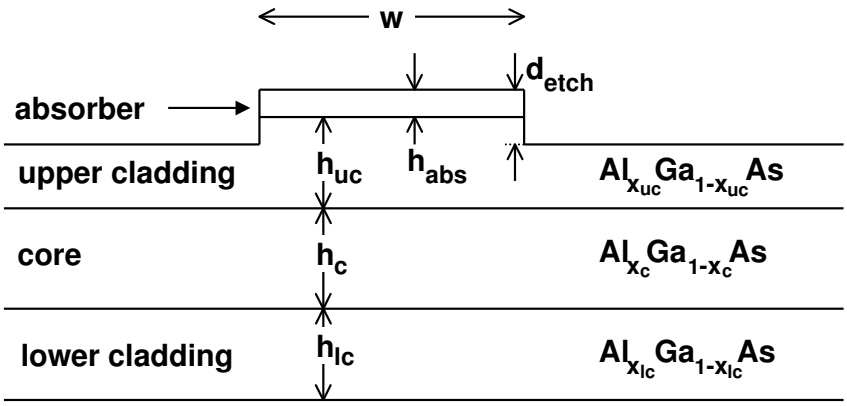

Figure 2-4: Cross-section of a distributed ridge waveguide showing the design variables.

performance metrics and nine design variables, a rigorous mathematical optimization procedure cannot be performed. However, by making an investigation of the design space, a heuristic approach gives reasonable results and allows one to focus on the physics of the device operation.

A few initial design choices need to be made to reduce the number of degrees of freedom so that the design space is manageable. The requirement for all absorption to occur in the absorber layer means that the lower cladding layer must be sufficiently thick to prevent interaction of the mode with the substrate. For modeling purposes, then, the lower cladding layer is assumed to be effectively infinitely thick. In practice, a lower cladding layer with thickness of $3\,\mu$m effectively isolates the mode from the substrate. The other layer-thickness assumption is that the LTG-GaAs absorber layer should be thin ($\sim 0.1\,\mu$m). This assumption is partly based on other work with traveling-wave photodetectors [65] and partly on the fact that the responsivity of LTG-GaAs photomixers is larger per unit length for thin LTG-GaAs layers because the carrier collection efficiency decreases (approximately exponentially) with depth into the LTG-GaAs [57, 58]. The final designs iterate over the LTG-GaAs layer thickness to bracket the desired extinction length.

Simplifications and constraints are also made concerning the layers' compositions. The absorption requirement sets a minimum Al fraction in the waveguide layers to prevent band-to-band absorption from tails of the band edge. The band gap of $Al_{0.10}Ga_{0.90}As$

corresponds to a photon wavelength of 800 nm, which is far enough from the operating wavelength of 850 nm that absorption is negligible over the millimeter lengths of waveguide involved in this device. Therefore, ten percent (10%) will be a lower limit on the Al concentration in core and cladding layers. No design requirement sets an upper limit on Al concentration; however, higher Al concentration alloys oxidize more and are less desirable from a device lifetime perspective. Also, any desirable index contrast can be achieved with Al fractions limited to less than 0.4. No compelling reason exists to choose different Al fractions for the upper and lower cladding, and choosing the cladding indices to be the same simplifies the analysis and make the guide easier to understand. Finally, the three variables related to Al fraction can be collapsed into one variable, because simulations indicate that the mode profile depends on the index contrast between the core and the cladding and not the absolute indices of the layers. The index contrast is given by

$$\Delta n = n_c - n_{lc} = n_c - n_{uc} \ , \tag{2.11}$$

where n_c, n_{lc}, and n_{uc} are in the indices of refraction of the core, lower cladding and upper cladding, respectively. The mode depends only on Δn, because it is contained almost entirely in the core and cladding layers, i.e. different index steps between the upper cladding layer and the absorber and/or air do not affect the mode profile.

The design variables and initial constraints are given in Table 2.5. The method of field shadows requires analysis of the vertical (growth) direction first; therefore, I explore that portion of the design space before the design space of two variables related to the lateral behavior of the guide.

Design in Vertical Dimension

Pairs of core and cladding indices which sample the achievable index contrasts within the constraints are given in Table 2.4(b) along with the corresponding index contrasts. For each value of index contrast, I calculate the mode waist and absorber fill factor for a matrix of core and upper cladding thicknesses. Keeping the guide single mode sets the upper limit on core thickness, and requiring the mode to be "well confined," which I have chosen

Table 2.5: Dielectric waveguide design variables with initial constraints.

Description	Variable	Constraints
Lower cladding thickness	$\mathrm{h_{lc}}$	effectively infinite
Core thickness	$\mathrm{h_c}$	none
Upper cladding thickness	$\mathrm{h_{uc}}$	none
Absorber thickness	$\mathrm{h_{abs}}$	$\sim 0.1\ \mu$m
Core/cladding	$\Delta n(\mathrm{x_c}, \mathrm{x_{lc}}, \mathrm{x_{uc}})$	$\mathrm{x_{lc}} = \mathrm{x_{uc}}$
index contrast		$0.1 < \mathrm{x_c} < \mathrm{x_{uc,lc}} < 0.4$
Strip width	w	none
Etch depth	$\mathrm{d_{etch}}$	none

to mean more than approximately sixty percent of the power in the core layer, sets the lower limit. The constraints on the cladding thickness are somewhat more arbitrary. A minimum $0.1\ \mu$m thickness was shown to allow any desired absorber fill factor, and below that thickness, fill factor varies quickly, making those designs more sensitive to growth tolerances. The maximum cladding thickness was that which gave an absorber fill factor of 0.002 or less, which was smaller than needed for any device design.

As explained in Appendix Section A.2, the absorber fill factor, ζ, calculated using real dielectric constants for all layers provides a good approximation for the mode absorption length by multiplying the fill factor by the bulk absorption coefficient of the absorbing material. The absorber fill factor calculated with one-dimensional analysis is always an upper limit on the achievable fill factor in a complete strip-loaded waveguide structure for a given stack of dielectric layers. This limiting nature arises because etching a strip in the top of the stack will cause the mode to curve downward thereby "pushing" part of the mode out of the absorber. As discussed in Section 4.1.1, the reported values for the absorption coefficient of LTG-GaAs, $\alpha_{\mathrm{LTG-GaAs}}$, vary from $1 \times 10^4 \mathrm{cm}^{-1}$ to $2 \times 10^4 \mathrm{cm}^{-1}$. At the outset of this thesis, the latter value was assumed; therefore, discussion in this chapter focuses on designs for which that assumption is made. Designing a waveguide for a different $\alpha_{\mathrm{LTG-GaAs}}$ requires simply using the same design curves to choose an alternate absorber fill factor.

The mode waist in the growth direction is the waist of the best-fit Gaussian to a mode's field profile. The Gaussicity, or normalized overlap between the field and its best-fit Gaus-

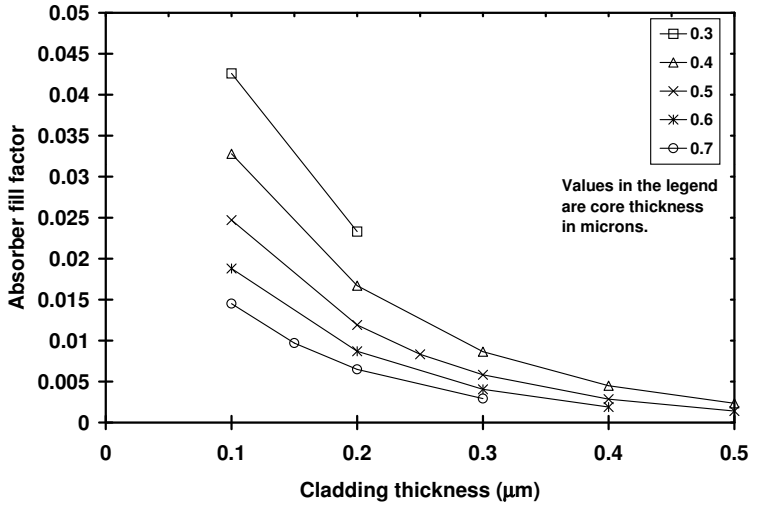

Figure 2-5: Absorber fill factor for core of $Al_{0.20}Ga_{0.80}As$ and cladding of $Al_{0.30}Ga_{0.70}As$ yielding $\Delta n = 0.062$.

sian, is defined by

$$\sqrt{G} = \frac{\left| \int_{-\infty}^{\infty} \exp\left(-\frac{(z-z_o)^2}{w^2}\right) E^*(z)\, \mathrm{d}z \right|}{\left(\frac{\pi w^2}{2}\right)^{-1/4} \sqrt{\int_{-\infty}^{\infty} |E(z)|^2 \, \mathrm{d}z}} \,, \tag{2.12}$$

where z_o is the mode center and w is the waist. While the modes' shapes are not exactly Gaussian, the Gaussicity for all the designs presented is greater than 0.986.

Simulation results of absorber fill factor as a function of upper cladding thickness parameterized by core thickness are presented in Appendix A in Figures A-5, A-6, and A-7. An representative plot is given in Figure 2-5 for a slab waveguide with core of $Al_{0.20}Ga_{0.80}As$ and cladding of $Al_{0.35}Ga_{0.65}As$. Absorber fill factors up to a few percent can be achieved for many different index contrast and thickness values. The design space itself can be more easily visualized in Figure 2-6, which presents the mode waist as a function of core thickness, parameterized by index contrast. Upper cladding thickness is not included in this plot because mode waist is almost invariant with respect to it. The regions of the design space for which the guide is either multimode or poorly confined are noted in the figure. As expected, smaller index contrasts allow thicker core layers before the guide goes multimode. Interestingly and counter-intuitively, mode waist varies quite slowly with core layer thickness. The physical reason behind this effect is that the curvature of the mode

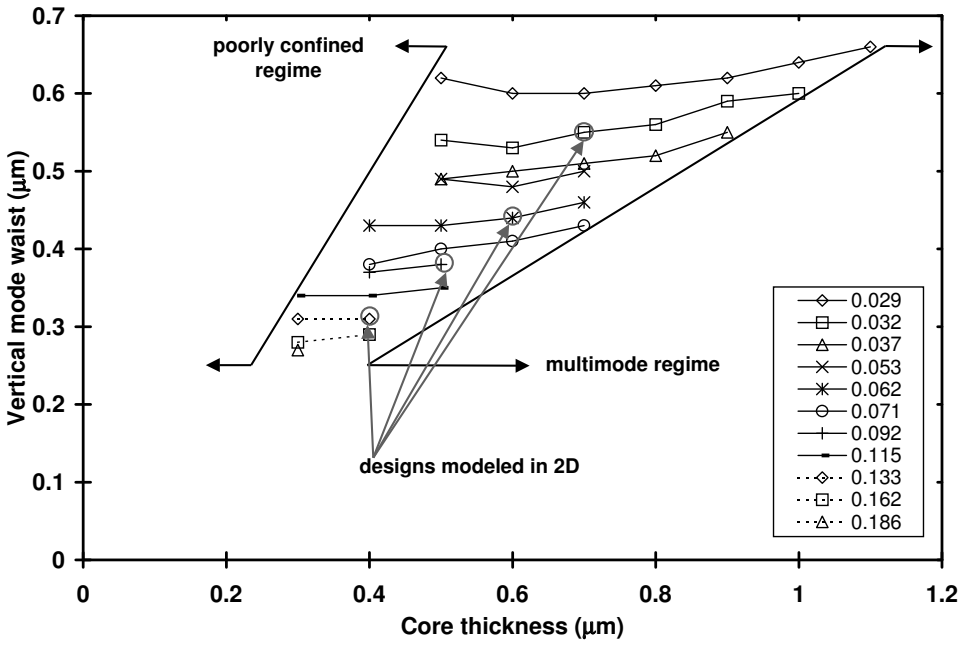

Figure 2-6: Mode waist as a function of core layer thickness parameterized by Δn between the core and cladding layers.

is set primarily by the index contrast between the core and cladding layers. The boundary conditions which require the slope of the field profile to be continuous for TE modes determine the mode shape. Thus, if the mode is well-confined, the width of the mode is relatively invariant to the distance between the core/cladding boundaries. The value that changes is the fraction of the mode in the core layer.

Of the approximately 40 combinations of Δn and core thickness, the four noted in Figure 2-6 bracket both degrees of freedom. The fraction of optical power absorbed is given by

$$A = 1 - e^{-\frac{\ell_{\text{active}}}{\ell_{\text{ext}}}} , \tag{2.13}$$

where ℓ_{active} is the length of the active area and ℓ_{ext} is the mode extinction length. Therefore, for a 150-μm-long active area, $\ell_{\text{ext}} = 90\,\mu$m is a good compromise between high efficiency and distributing the power absorption over a large area. Assuming $\alpha_{\text{LTG-GaAs}} = 2 \times 10^4 cm^{-1}$, an absorber fill factor of ~ 0.005 yields the desired mode extinction length of as calculated by equation (A.37). For each Δn and $\mathrm{h_c}$ combination, I choose the $\mathrm{h_{uc}}$

Table 2.6: Designs modeled as full two-dimensional strip-loaded waveguides.

Δn	x_c	x_{uc}	h_c	h_{uc}	1-D ζ	n_{eff}
0.032	0.20	0.25	0.7	0.25	0.00649	3.45041
0.062	0.20	0.30	0.6	0.25	0.00593	3.44174
0.092	0.20	0.35	0.5	0.25	0.00600	3.43120
0.133	0.10	0.30	0.4	0.22	0.00571	3.48461

value from Figure A-5(b), A-6(a), A-6(c), or A-7(a) which corresponds to and absorber fill factor slightly larger than that which is ultimately desired. These four designs are detailed in Table 2.6.

Design in Lateral Dimension

For each one-dimensional dielectric stack design in Table 2.6, a matrix of etch depths and strip widths are chosen. The mode waist in the lateral direction is calculated for each design. The absorber fill factor is not calculated, because the computation time is long and the 1-D fill factor will be a good approximation, especially for wider strips. The lateral mode waist values are shown in Figure 2-7.

From the designs in Figure 2-7, I simulate — in 2-D and with a complex dielectric constant for the absorber — the designs which allow the widest single mode strip for each Δn. A wider strip permits both more power coupled into the guide and a larger absorber region which distributes the thermal load in the absorber. For the full simulations, the Sellmeier equation gives the AlGaAs indices, while for LTG-GaAs, $\epsilon_r = 13.22 + j0.984$, where 13.22 is the accepted value for ϵ_1 of GaAs and $\epsilon_2 = 0.984$ yields the assumed bulk absorption coefficient of $\alpha = 2 \times 10^4\,\mathrm{cm}^{-1}$. Achieving the desired extinction length for the complete structure requires tweaking of the upper cladding thicknesses for a couple of the designs. The dimensions and characteristics of the final designs are presented in Table 2.8. The $\Delta n = 0.133$ design is less desirable than the others, because the fabrication tolerances are higher with a $200\,\text{Å}$ etch into the upper cladding versus a $500\,\text{Å}$ etch. The other designs are essentially equivalent with the same extinction lengths and similar mode sizes. The $\Delta n = 0.092$ design was grown and fabricated as described in Chapter 3. The

Table 2.7: Δn_{eff}'s for varying etch depths.

Δn	$\mathrm{d_{etch}}$(Å)	Δn_{eff}
0.032	500	0.00227
0.062	500	0.00238
0.133	200	0.00243
0.092	500	0.00258
0.032	1000	0.00311
0.133	500	0.00330
0.062	1000	0.00348
0.092	1000	0.00393
0.032	1500	0.00419
0.062	1500	0.00508
0.032	2000	0.00554
0.133	1000	0.00563
0.092	1500	0.00610
0.032	2500	0.00713
0.062	2000	0.00736
0.092	2000	0.00948
0.133	1500	0.00971
0.062	2500	0.01040
0.092	2500	0.01445
0.133	2000	0.01662

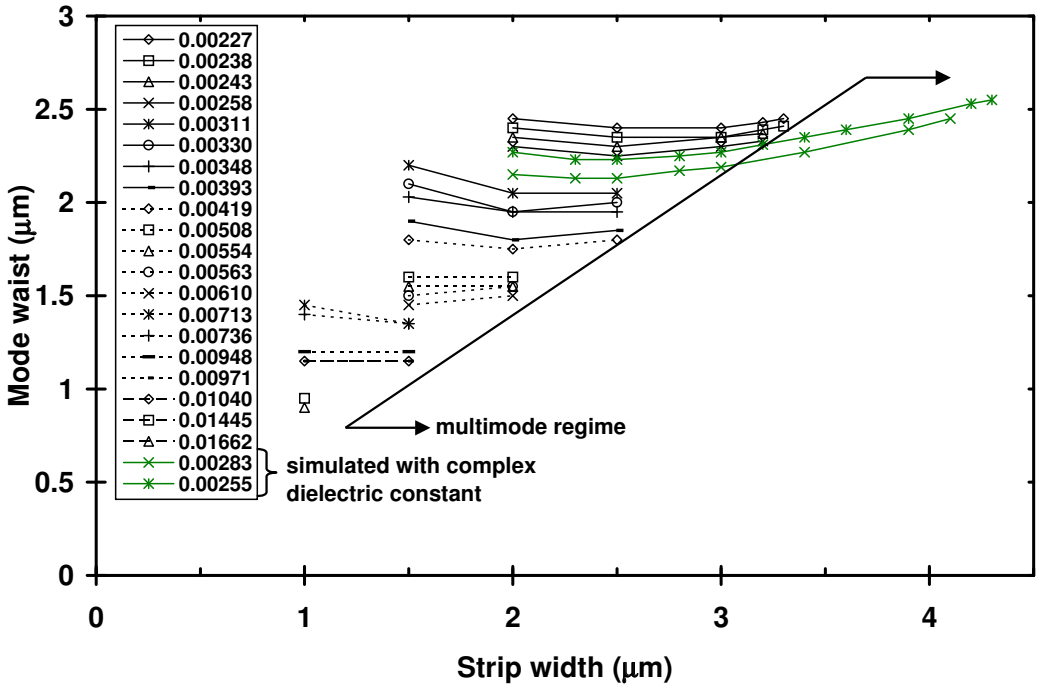

Figure 2-7: Mode waist as a function of strip width parameterized by Δn_{eff} between the strip and etched sides.

Table 2.8: Dielectric waveguide designs: structure and characteristics.

Δn	x_c	x_{uc}	h_c (μm)	h_{uc} (μm)	h_{lc} (μm)	w (μm)	d_{etch} (Å)
0.032	0.20	0.25	0.7	0.23	3	3	500
0.062	0.20	0.30	0.6	0.23	3	3	500
0.092	0.20	0.35	0.5	0.24	3	3	500
0.133	0.10	0.30	0.4	0.21	3	3	200

(a) Dielectric waveguide designs: structure.

Δn	Δn_{eff}	Vert. w_0 (μm)	Lateral w_0 (μm)	ζ	ℓ_{ext} (μm)	N_{eff}
0.032	0.00217	0.55	2.41	0.00513	92	3.44907
0.062	0.00247	0.44	2.29	0.00517	91	3.44046
0.092	0.00255	0.38	2.27	0.00500	94	3.42995
0.133	0.00252	0.31	2.27	0.00509	94	3.48346

(b) Dielectric waveguide designs: characteristics.

higher index contrast between layers allows slightly more leeway in growth, i.e. the closer the Al fractions in the core and cladding are, the more sensitive the confinement will be to variations in the fraction of one or the other. By decreasing the LTG-GaAs layer thickness to $0.08\,\mu$m, the extinction length is almost doubled to $168\,\mu$m, and by increasing the thickness to $0.13\,\mu$m, ℓ_{ext} is halved to $47\,\mu$m. A contour plot of the power distribution in a waveguide with this design is given in Figure 2-8. The 3.2-μm width of the design in the contour plot is the widest strip that supports a single mode.

Before investigating the terahertz waveguide design, a few comments on the dependence of mode extinction length on AlGaAs indices, $\epsilon_{\text{LTG-GaAs}}$, and strip width are in order. Using the Adachi expression for AlGaAs indices on the nominal $\Delta n = 0.032$ structure yields a 26% increase in extinction length relative to the same structure modeled using Sellmeier, because the absorber fill factor decreases by a corresponding amount. The extinction length is most sensitive to the value of ϵ_1 used for LTG-GaAs. A change from 13.11 given by Sellmeier to the 13.22 literature value for GaAs (a change of only 0.8%) leads to a 13% change in the extinction length. This sensitivity is understood heuristically

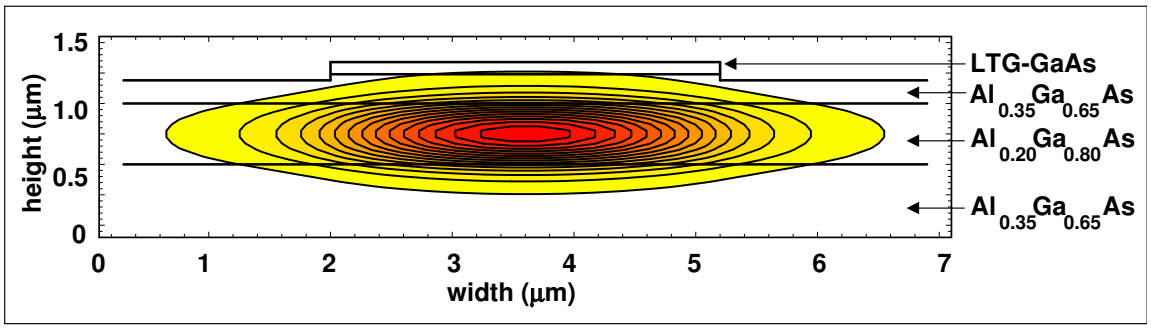

Figure 2-8: Mode in $\Delta n = 0.092$ and $\Delta n_{\text{eff}} = 0.00255$ waveguide.

as the higher index of the LTG-GaAs layer drawing the mode into the absorber layer. Because only the tail of the mode couples into the absorber, a small shift of the mode "up" leads to a large fractional change in the absorber fill factor. This change in ζ produces a change in ℓ_{ext} of the same magnitude. The ϵ_2 value for LTG-GaAs has a more intuitive effect on ℓ_{ext}, in that a change in ϵ_2 produces almost exactly the same fractional change in ℓ_{ext}. The change is not exactly the same because ϵ_2 does affect the mode profile. Finally, the absorber fill factor increases as the strip width is increased, asymptotically approaching the 1-D value.

All of these effects are illustrated in Figure 2-9. The nominal $\Delta n = 0.092$ design was simulated for different values of $\epsilon_{\text{LTG-GaAs}}$ and the mode extinction length and absorber fill factor plotted. The lateral mode waist values from these simulations are included in Figure 2-7. Note that the Δn_{eff} values of these two designs analyzed with complex dielectric constants in Figure 2-7 are different even though the ϵ_1 values are the same. The square root relationship between ϵ and $\tilde{n}$ means that changes in ϵ_2 affect n as well as k.

2.2 Terahertz Waveguide Design

The choice and design of terahertz (THz) waveguide is much simpler than for the optical waveguide. Metal is the waveguiding material of choice in the millimeter and THz regimes. If the waveguide is metal, it can also apply the dc-bias to the absorbing, photomixing layer. In order to confine the THz signal close to the substrate and maximize coupling

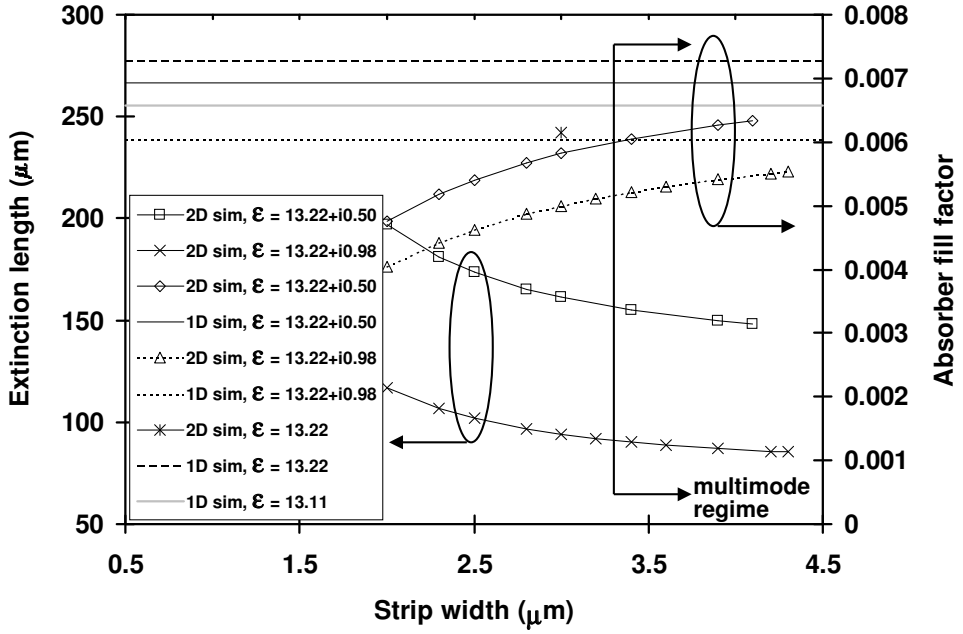

Figure 2-9: Absorber fill factor and mode extinction length as a function of strip width for simulations with different relative ϵ_2 values for LTG-GaAs but with the same geometry and same ϵ_1. Absorber fill factors calculated from a one-dimensional analysis of the strip are shown for comparison. Extinction length curves use the left axis, while absorber fill factor curves use the right.

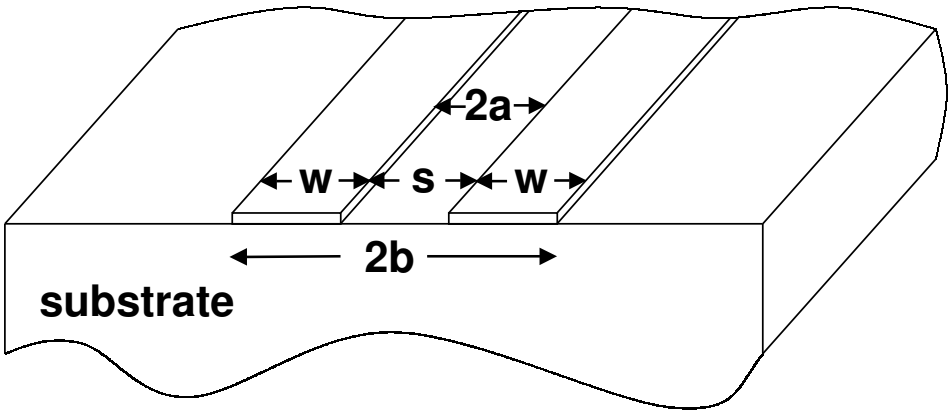

Figure 2-10: Schematic of coplanar strips with infinite substrate.

to the photomixing layer, the waveguide should be coplanar. Of the three most common coplanar metal waveguides, coplanar strips, coplanar waveguide, and slotline; coplanar strips (CPS) and coplanar waveguide (CPW) have much lower dispersion than slotline for similar dimensions and frequencies. Traveling-wave photodetectors have been reported in which the photo-excited layer is under the central strip of CPW [63, 64]. In these designs, based on *p-i-n* diodes, the entire optical mode is contained in the diode layer under the central CPW strip. A conducting layer under the diode allows the photocurrent to flow to the finite ground planes. For a photoconducting detector with an absorbing layer weakly coupled to the optical mode, this geometry is not appropriate. Therefore, CPS are used to guide the THz signal. The CPS can be ignored in modeling the optical mode because the optical intensity is very small ($\ll 0.01$) at the top of the dielectric waveguide where the CPS are fabricated.

2.2.1 Coplanar Strips

The design variables for CPS are the gap between the strips, s, and the width of the strips, w, as shown in Figure 2-10, and the overall length of the active area. Coplanar strips have been extensively studied and characterized, and for the relative dimensions in the distributed photomixer, quasi-static models work well. Because the distributed photomixer will be mounted on a Si hyperhemispherical lens, the substrate can be assumed to be infinitely

thick. For symmetric CPS on an infinitely thick substrate, the impedance is given by

$$Z_{0,\mathrm{cps}} = \frac{120\pi}{\sqrt{\epsilon_{\mathrm{re}}}} \frac{K(k_1)}{K'(k_1)} \ , \tag{2.14}$$

where

$$\epsilon_{\mathrm{re}} = \frac{\epsilon_{\mathrm{r}} + 1}{2} \tag{2.15}$$

$$k_1 = \frac{s}{s + 2w} = \frac{a}{b} \ , \tag{2.16}$$

where ϵ_{r} is the relative dielectric constant of the substrate and $K()$ and $K'()$ are the complete and complementary complete elliptic integrals of the first kind, respectively [77]. Because the LTG-GaAs is very high impedance under constant wave (cw) illumination, the photoconductor can be considered a current source. Therefore, the power developed on the CPS is linearly related to the CPS impedance. However, for high values of CPS impedance the lines become very narrow, which means their current carrying capacity decreases and ohmic loss increases. Figure 2-11 shows the variation of CPS impedance with structure parameter as given by equation (2.14).

The width of the absorber on top of the strip of the optical waveguide dictates the choice of CPS gap, s. For a s narrower than the strip, the absorber collection area is less than the maximum available. Even though a value of s wider than the strip can be used as long as dc-bias is applied to the photomixing layer, no compelling reason exists to do so. Therefore, a CPS gap of 3 μm is reasonable. This width will put the inside edges of the coplanar strips on top of the raised strip of the optical waveguide. This geometry makes the fabrication of the CPS easier because the thin electrode described in Section 2.2.2 will lie completely on top of the strip.

Literature describing propagation of THz signals on CPS and CPW focuses a lot of attention on radiation loss [78, 79, 80, 81]. However, the radiation loss is only high in these structures because the dimensions of the waveguide are so large compared to the wavelength of the THz radiation and the substrates are so small compared to the wavelength. Using the semiempirical formulation of Frankel, *et al.*, I plot in Figure 2-12 the radiation

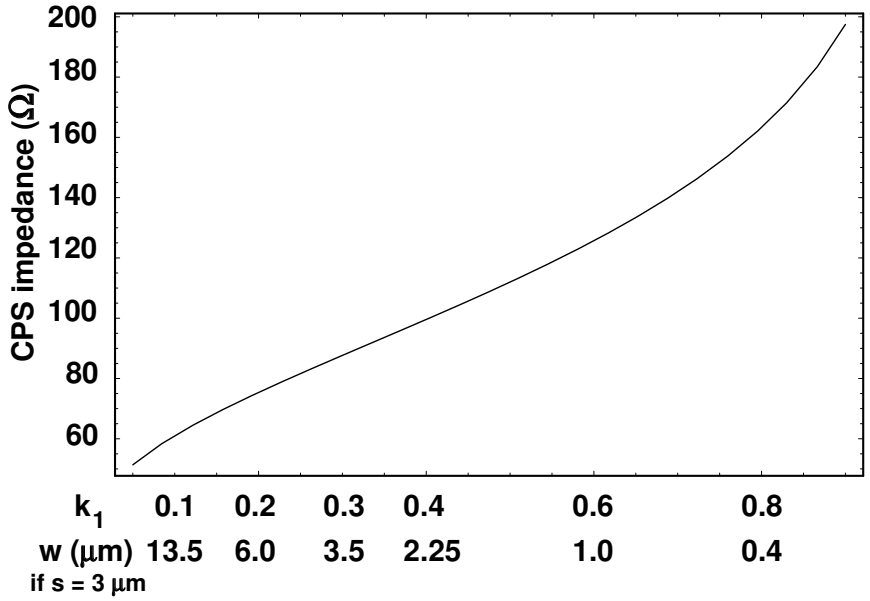

Figure 2-11: CPS impedance as a function of structure parameter. Impedance is also shown for a gap of $3\,\mu$m.

loss as a function of frequency for CPS with a gap of $3\,\mu$m for different strip widths [82]. Even for widths up to $10\,\mu$m the total radiation loss at 3 THz is relatively low for a 150-μm-long active area. A width near $3\,\mu$m, however, is a good compromise between narrow strips with their higher impedance and lower radiation loss and wider strips with their larger current capacity. From Figure 2-11, a width of $3.2\,\mu$m yields an impedance of $90\,\Omega$.

2.2.2 Quasistatic Calculation for Electrode Design

The quasi-TEM mode propagating on the CPS sees an effective index given by $n_{THz} = \sqrt{\epsilon_{\rm re}} = \sqrt{(\epsilon_{\rm r}+1)/2}$, where $\epsilon_{\rm r}$ is the relative dielectric constant of the substrate at THz frequencies ($\epsilon_{\rm r} \sim 12.9$). As previously discussed, the optical beat signal propagates at a group velocity for which the group index is approximately the effective index of the guide ($n_{o,g} \sim n_{\rm eff} \sim \sqrt{\epsilon_{r,o}}$), where $\epsilon_{r,o}$ is the relative dielectric constant of the waveguide material at optical frequencies ($\epsilon_{r,o} \sim 3.3 - 3.6$ for $\mathrm{Al}_x\mathrm{Ga}_{1-x}\mathrm{As}$ with $0.1 < x < 0.35$). Therefore, because the velocity of the THz signal is higher than the velocity of the optical signal, the CPS must be modified to slow the THz signal and velocity match it to the optical signal for

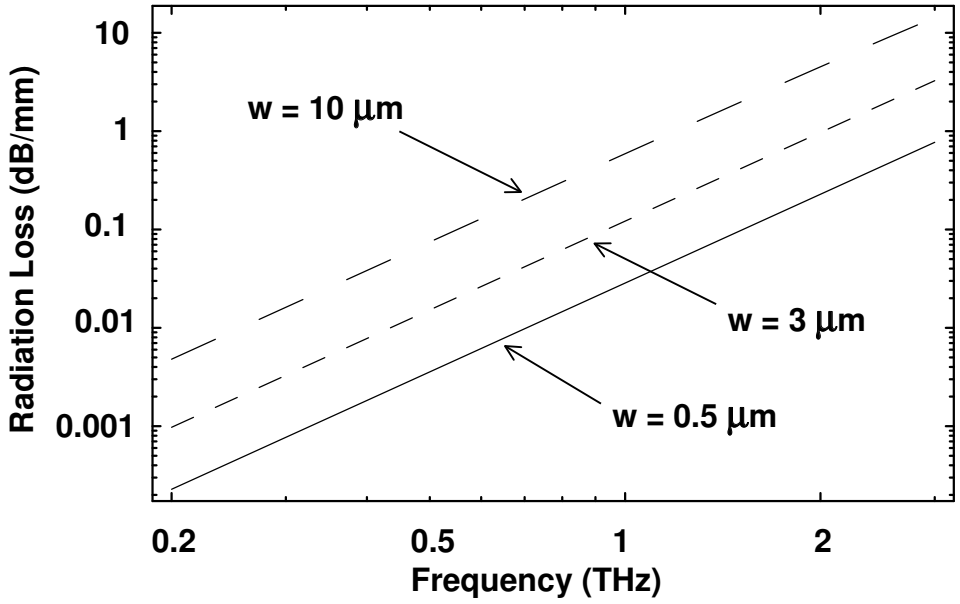

Figure 2-12: Radiation loss for different CPS strip widths.

optimum power transfer. The velocity of the THz wave on the CPS is given by

$$v_{\mathrm{THz}} = \left(\sqrt{L_{\mathrm{cps}} C_{\mathrm{cps}}}\right)^{-1} , \tag{2.17}$$

where L_{cps} and C_{cps} are the intrinsic, distributed inductance and capacitance, respectively, of the CPS. The velocity on the CPS is reduced when capacitance is added, and this is the most straightforward and common way of achieving velocity match. Solving

$$v_{\mathrm{opt}} = v_{\mathrm{THz}} = \left(\sqrt{L_{\mathrm{cps}}(C_{\mathrm{cps}} + C_{\mathrm{add}})}\right)^{-1} \tag{2.18}$$

for C_{add}, the added, distributed capacitance yields the required capacitance to match the velocity of the THz wave to the optical wave. Note that the units of C_{add} are F/m, so that if the capacitance is added in lumped amounts the added capacitance should be averaged over the pitch of the lumped capacitors. Adding thin electrodes that bridge part of the gap between the coplanar strips will add a small amount of capacitance, forming what is called a balanced interdigital line, as shown in Figure 2-13. Lim and Moore [83] calculate the capacitance between electrodes in a series of equally-spaced, infinitely-long, thin elec-

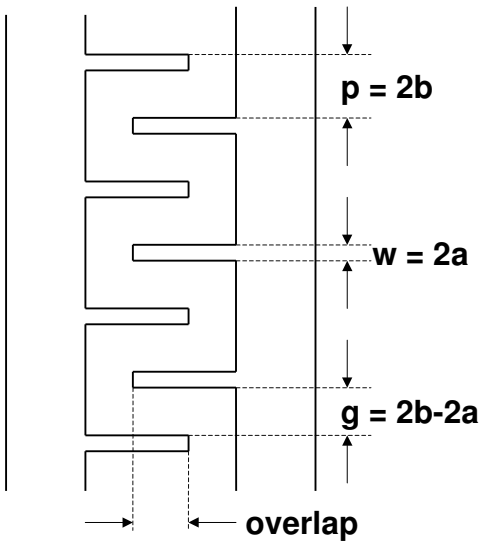

Figure 2-13: Schematic of interdigitated electrodes periodically loading CPS.

trodes. Through a series of conformal mappings, they calculate the capacitance between two electrodes to be

$$C = \frac{\epsilon_0(1+\epsilon_\mathrm{r})K(k)}{K'(k)} \ , \tag{2.19}$$

where $K()$ and $K'()$ are the complete and complementary complete elliptic integrals of the first kind, where

$$k = \tan^2 \frac{a\pi}{4b} \ , \tag{2.20}$$

and where a and b defined as in Figure 2-13. The capacitance calculated using equation (2.19) is per unit length but the length is the length by which two electrodes overlap as in Figure 2-13. While the electrodes periodically loading the CPS are neither infinitely long nor thin (relative to their width), this expression gives a good starting point for choosing electrode geometries to simulate in Momentum [84], as explained in Section 2.2.3. These electrodes are similar to those used in the standard lumped-element photomixers developed at MIT Lincoln Laboratory [60], and they have been shown to efficiently collect THz current.

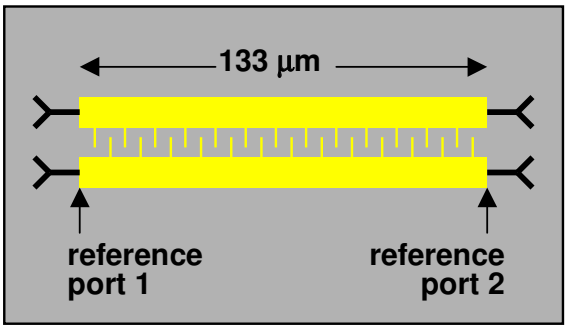

Figure 2-14: Schematic of loaded CPS circuit modeled in Momentum.

2.2.3 Method-of-Moments Calculation for Electrode Design

Using Hewlett Packard's method-of-moments electromagnetic field solver for planar circuits, Momentum, the phase velocity of the THz signal, impedance of the CPS, and radiation loss can all be accurately calculated. Method-of-moments codes solve the integral form of Maxwell's equations by solving for a Green's function for the current. This type of code is much efficient for planar structures than for three-dimensional structures. The circuit modeled in Momentum is shown in schematic in Figure 2-14. All of the simulations assume 0.2-μm-wide electrodes, because this width is the standard photomixer electrode width and is achievable using the electron-beam lithography equipment at Lincoln Lab. Momentum assumes the metal lines are perfect conductors. Impedance and phase velocity is extracted from the S_{11} values returned by Momentum. The impedance looking into reference port 1 is given by

$$Z_{1,\text{in}} = Z_{\text{line}} \frac{Z_{\text{port}} + jZ_{\text{line}} \tan(k\ell)}{Z_{\text{line}} + jZ_{\text{port}} \tan(k\ell)} \ , \tag{2.21}$$

where Z_{line} and Z_{port} are the impedances of the line and port, respectively, k is the propagation constant of the signal on the CPS, and ℓ is the physical length. For $k\ell \rightarrow \frac{\pi}{2} + N\pi$, $\tan(k\ell) \rightarrow \infty$ and therefore,

$$Z_{1,\text{in}} \rightarrow \frac{Z_{\text{line}}^2}{Z_{\text{port}}} \ . \tag{2.22}$$

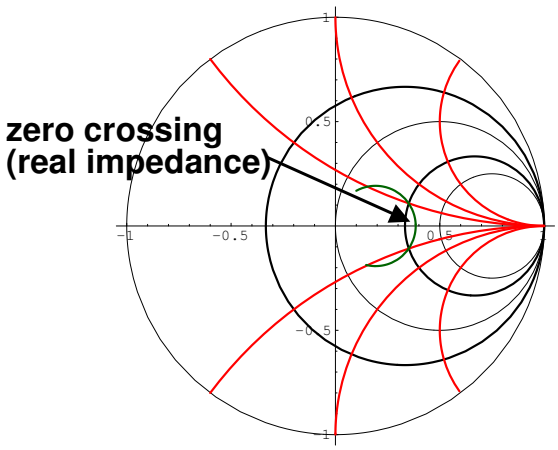

Figure 2-15: Smith chart showing zero-crossing for a through line.

For this value of $k\ell$, the propagation constant, or effective index, can be calculated by

$$k\ell = \frac{\pi}{2} + N\pi = \frac{2\pi n f}{c}\ell \ , \tag{2.23}$$

where f is the frequency for which this occurs. Thus, by finding the frequency for which a given length of line has a real input impedance — equivalently S_{11} crosses the real axis on a Smith chart as in Figure 2-15 — Z_{line} can be computed from equation (2.22), while $v_{\text{THz}} = c/n$ can be computed from equation (2.23). The added capacitance of the electrodes can then be deduced using equation (2.18). The impedance of the CPS is slightly higher than predicted from

$$Z'_{\text{cps}} = \sqrt{\frac{L_{\text{cps}}}{C_{\text{cps}} + C_{\text{add}}}} \ , \tag{2.24}$$

because the electrodes add a small amount of inductance as well. For the $90-\Omega$ CPS described in Section 2.2.1, a gap between electrodes of $0.8\,\mu$m and an overlap of $1.0\,\mu$m adds enough capacitance to slow the THz wave to match the optical signal. The quasi-static calculations predicted a gap of $0.63\,\mu$m and overlap of $1.2\,\mu$m. The results of a number of simulations are plotted in Figure 2-16 along with the quasi-static prediction of Lim and Moore from Section 2.2.2. The capacitance added to the line for a given electrode structure is generally $\sim 50\%$ higher than predicted by quasi-static analysis. This underestimate is expected, because fringing fields off the end of the electrodes make them effectively longer

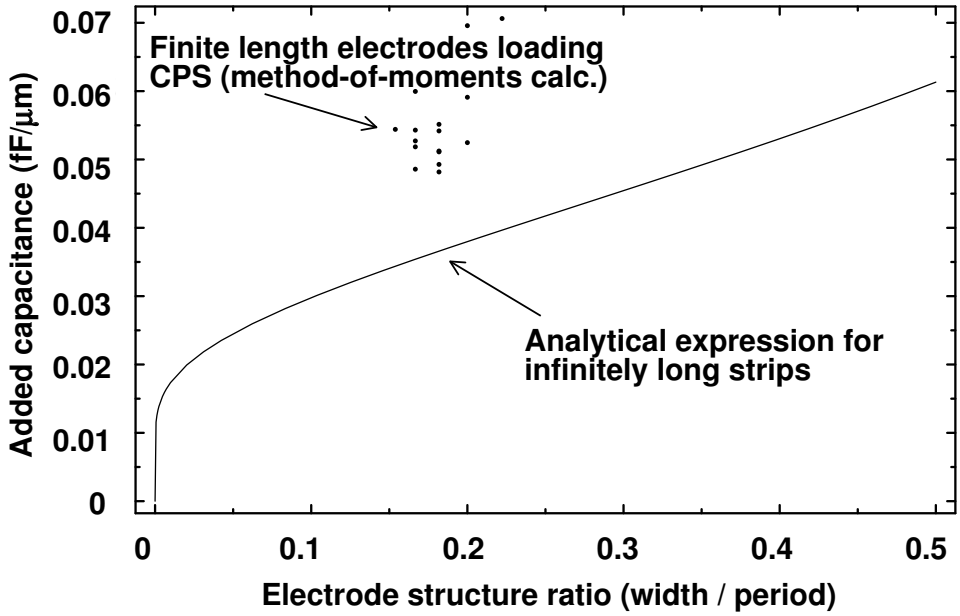

Figure 2-16: Capacitance added per length of overlap between the electrodes.

than they are physically.

To calculate the radiation loss, the structure depicted in Figure 2-14 is considered in two different representations, using voltage waves and S-parameters, as shown in Figure 2-17. The radiation loss is extracted by considering the fraction of power lost from both perspectives. In terms of voltage waves, the power at the input port is given by

$$\begin{aligned} P(-\ell) &= \frac{1}{2}\Re\left\{V(-\ell)I^*(-\ell)\right\} \\ &= \frac{1}{2}\Re\left\{\left(V_0^+e^{\gamma\ell}+V_0^-e^{-\gamma\ell}\right)\left(\frac{(V_0^+)^*}{Z_{\text{line}}^*}e^{\gamma^*\ell}-\frac{(V_0^-)^*}{Z_{\text{line}}^*}e^{-\gamma^*\ell}\right)\right\} \\ &= \frac{1}{2}\Re\left\{\frac{|V_0^+|^2}{Z_{\text{line}}^*}e^{2\alpha\ell}+\frac{(V_0^+)^*V_0^-}{Z_{\text{line}}^*}e^{-j2\beta\ell}-\frac{V_0^+(V_0^-)^*}{Z_{\text{line}}^*}e^{j2\beta\ell}-\frac{|V_0^-|^2}{Z_{\text{line}}^*}e^{-2\alpha\ell}\right\} \\ &= \frac{1}{2}\frac{|V_0^+|^2}{\Re\{Z_{\text{line}}^*\}}\left(e^{2\alpha\ell}-|\Gamma_0|^2e^{-2\alpha\ell}\right)\ , \end{aligned} \tag{2.25}$$

where the propagation constant is $\gamma=\alpha+j\beta$ and Γ_0, the reflection coefficient at port 2, is given by

$$\Gamma_0=\frac{Z_{\text{port}}-Z_{\text{line}}}{Z_{\text{port}}+Z_{\text{line}}}\ . \tag{2.26}$$

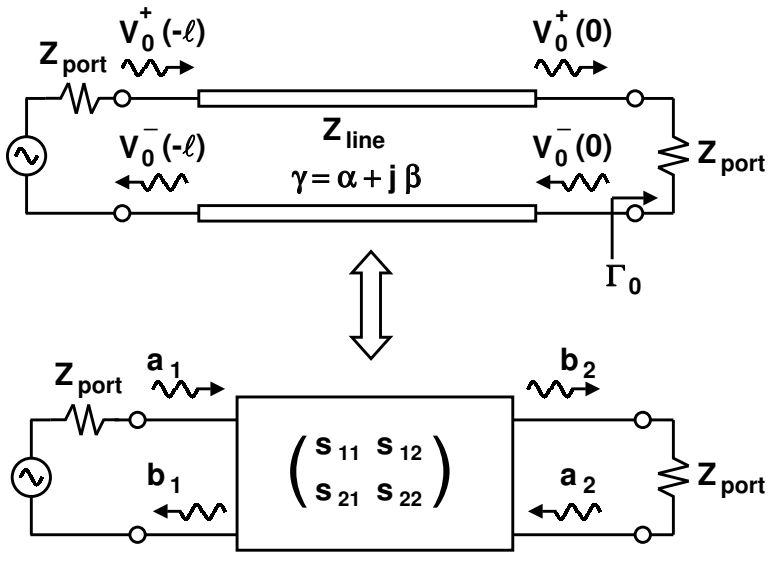

Figure 2-17: Equivalent wave and S-parameter representations of transmission line modeled in Momentum.

The power at the load (port 2) is given by

$$\begin{aligned} P(0) &= \frac{1}{2}\Re\left\{V(0)I^*(0)\right\} \\ &= \frac{1}{2}\frac{|V_0^+|^2}{\Re\{Z_{\text{line}}^*\}}\left(1-|\Gamma_0|^2\right) \ . \end{aligned} \tag{2.27}$$

Therefore, the power lost on the line is given by

$$P_{\text{lost}} = \frac{1}{2}\frac{|V_0^+|^2}{\Re\{Z_{\text{line}}^*\}}\left((e^{2\alpha\ell}-1)+|\Gamma_0|^2(1-e^{-2\alpha\ell})\right) \ . \tag{2.28}$$

The CPS is low loss enough that Z_{line} can be used for $\Re\{Z_{\text{line}}^*\}$. The fraction of power lost, L, is the ratio of P_{lost} to the power at the input, $P(-\ell)$, i.e.

$$L = \frac{(e^{2\alpha\ell}-1)+|\Gamma_0|^2(1-e^{-2\alpha\ell})}{e^{2\alpha\ell}-|\Gamma_0|^2e^{-2\alpha\ell}} \ . \tag{2.29}$$

From a scattering matrix perspective, the fraction of power lost is the fraction that is not

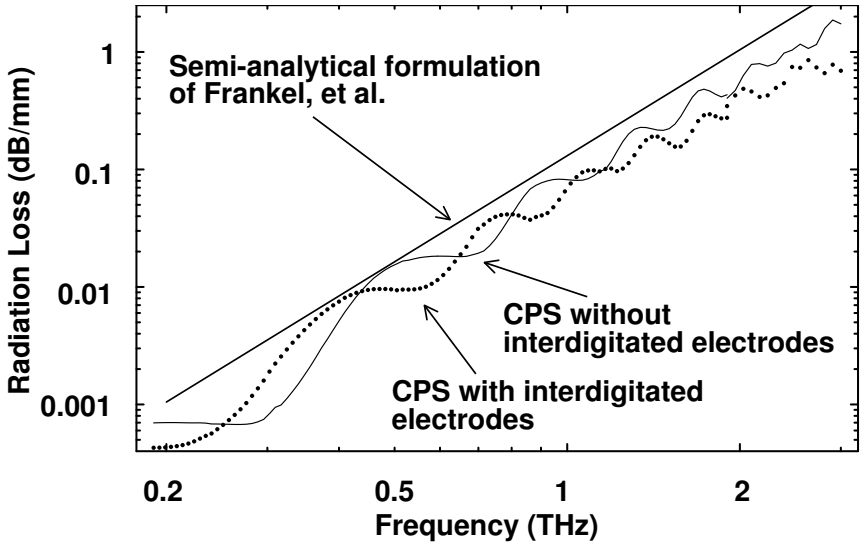

Figure 2-18: Calculated radiation loss for CPS with and without interdigitated electrodes.

either reflected back to port 1 or transmitted to port 2, i.e.

$$L = 1 - |S_{11}|^2 - |S_{21}|^2 \ . \tag{2.30}$$

Equating the two expressions for L, using the S_{11} and S_{21} values from Momentum, and solving the transcendental equation for α yields the radiation loss of the CPS. The results for an unloaded CPS line and for a CPS line loaded with electrodes for velocity matching are shown in Figure 2-18. The radiation loss remains less than 2 dB/mm up to 3 THz and is cubic with frequency, agreeing quite closely to the semiempirical prediction of Frankel, *et al.* [82]. The interdigitated electrodes do not introduce significant loss. Oscillations in the data can be attributed to standing wave effects that are significant in the short length of line used in the calculations.

2.3 Antenna Design

The final component of the distributed photomixer is the radiating element. After the optical signal has been absorbed, generating a conductance wave, which gives rise to a THz electromagnetic wave guided by the CPS, the THz signal must be coupled off of the chip. A frequency independent antenna preserves the frequency dependence of the transmission line. A narrowband antenna such as a dipole produces a pure polarization state, which is needed for some applications.

2.3.1 Bowtie Antenna

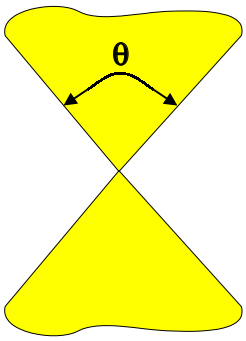

Figure 2-19: Bow-tie antenna schematic.

The standard frequency-independent antenna for photomixers has been the log-spiral [2], but that geometry is not compatible with the large active area of the distributed photomixer. A log-periodic antenna is a commonly used self-complementary antenna, but it is not truly frequency independent, only periodic, as its name implies. The bowtie antenna which is a projection of a biconical antenna [85], is commonly used in millimeter and sub-millimeter wave applications. The drawbacks of the bowtie are the lack of polarization purity and the a multiple lobed far-field pattern at high frequencies (relative to the bow-length) [85, 86]. For coupling power to a bolometer, these deficiencies can be overcome through proper choice of focusing elements. Compton, *et al.* [86] give the radiation resistance of a bowtie antenna on a substrate as

$$R_{\text{bowtie}} = \frac{Z_0}{\sqrt{\epsilon_{\text{r}}}} \frac{K(k)}{K'(k)} \ , \tag{2.31}$$

where Z_0 is the impedance of vacuum, ϵ_{r} is the dielectric constant of the substrate, $K()$ and $K'()$ are the complete and complementary complete elliptic integrals of the first kind, and k is given by[2]

$$k = \tan^2\left(45^{\text{o}} - \frac{\theta}{4}\right) \ , \tag{2.32}$$

[2]Note that the definition of k is incorrectly listed as $\tan\left(45^{\text{o}} - \frac{\theta}{4}\right)$ in [78].

where θ is the bow angle as indicated in Figure 2-19. This structure is too large to simulate in Momentum in a reasonable amount of time. The bow angle of 83° yields an impedance of $76\,\Omega$ to match the loaded CPS impedance. A bowtie terminated at an arm length $2\lambda_d$, where λ_d is the wavelength in the dielectric substrate of the lowest frequency of interest, has an impedance which is not frequency dependent [78]. A bow arm length of $750\ \mu$m corresponds to a minimum frequency of 62 GHz, according to this convention, which allows some margin below the minimum desired frequency of operation of $\sim$200 GHz.

2.3.2 Dipole Antennas

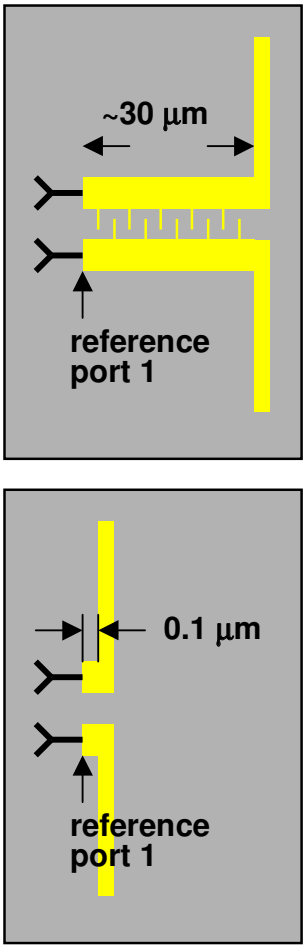

Figure 2-20: Dipole modeling in Momentum.

Printed dipoles on substrates have been extensively studied. In a standard reference, Kominami, *et al.* analyze printed dipoles and slots on a semi-infinite substrate [87]. The moment method they use does not produce closed form expressions for dipole impedance. However, they do give an expression for first resonance length of $\frac{\ell_{\rm res}}{\lambda_0} = \frac{1}{\epsilon_{\rm re}} 0.48 \left(1 + \frac{W}{L}\right)^{-1}$, where $\epsilon_{\rm re} = 0.5(\epsilon_{\rm r} + 1)$, λ_0 is the wavelength in vacuum, and W and L are the width and length, respectively, of the dipole. They assumed a delta gap excitation and no feed structure, but the work of Carver and Mink [88] suggests that as long as the excitation gap is less than $0.1\lambda_0$ the dipole behavior is not significantly affected. Momentum has accurately predicted the center frequency and bandwidth of photomixer antenna designs in the past [60]; therefore, as with design of the CPS, Momentum is used to refine the initial designs. I consider three dipole designs, resonant at 850 GHz, 1.6 THz, and 2.5 THz. Using a structure like that in the upper portion of Figure 2-20, the dipoles are modeled in a similar way to the CPS modeling in Section 2.2.3, using equations (2.21), (2.22), and (2.23), except that $Z_{\rm port}$ is replaced by $Z_{\rm ant}$, the dipole impedance to be calculated. Alternately, the length of

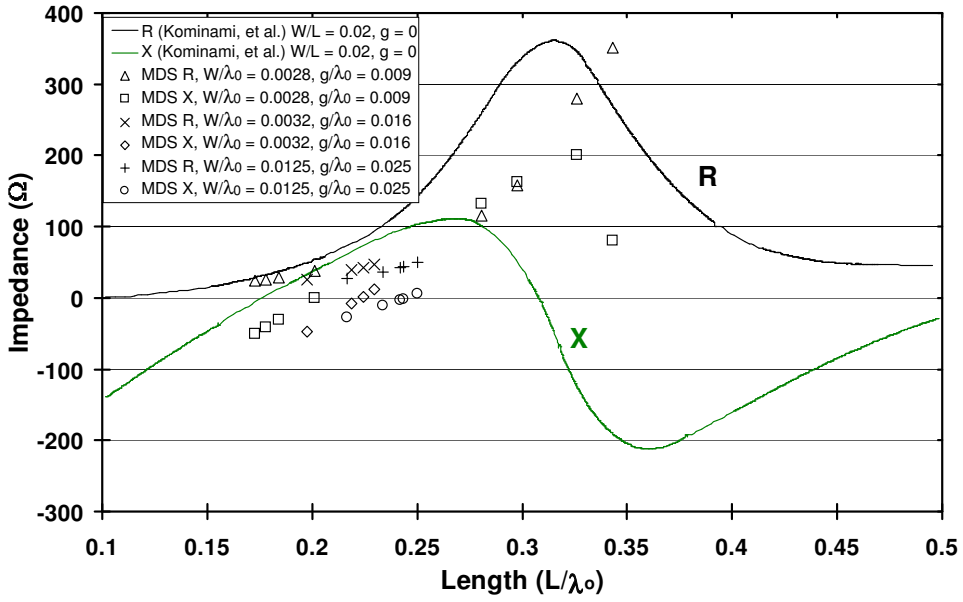

Figure 2-21: Variation of dipole impedance with dipole length. Solid curves from Kominami, *et al.*

CPS can be dispensed with as shown in the lower part of Figure 2-20, and $Z_{\rm ant}$ can be found directly from the Momentum-calculated S_{11} values. The dipole impedance for various lengths for each design frequency are plotted in Figure 2-21. The prediction of Kominami, *et al.* are shown for comparison, and excitation gap makes a noticeable difference. The real part of the impedance varies in a manner similar to that described by Zhu and Wu [89]. Final dimensions are in Table 2.9.

In this chapter, I presented accurate modeling techniques and a design procedure for each of the 3 major components of the distributed photomixer: optical waveguide, terahertz waveguide, and antenna. Specific designs have been detailed, and these designs were fabricated as described in Chapter 3. The design methodology, design curves and data are general, however, and allow the design of other distributed photomixers with different characteristics.

Table 2.9: Dipole designs.

Design f (THz)	Full length (L) (μm)	Width (W) (μm)
0.85	70.0	2.0
1.6	41.0	1.5
2.5	29.2	1.5

Chapter 3

Distributed Photomixer Fabrication

This chapter describes the fabrication of the distributed photomixer, including mask design, growth, and processing for the the optical waveguide, terahertz waveguide, and radiating element. The aluminum gallium arsenide (AlGaAs) and low-temperature-grown gallium arsenide (LTG-GaAs) layers for the optical waveguide are grown using Molecular Beam Epitaxy (MBE). A combination of optical and electron-beam (e-beam) lithography define features for etching and metal deposition. Partial etching of the top AlGaAs layer creates the strip for the strip-loaded waveguide, while metal evaporation and liftoff produce the terahertz waveguide and antenna. Section 3.1 details design of the masks for both optical and e-beam lithography. Section 3.2.1 contains layer growth parameters, and Section 3.2.2 includes processing steps for photolithography, etching and metal deposition. Section 3.3 provides photographs and micrographs of fabricated devices.

3.1 Mask Design

Lithography defines features on the surface of a wafer by patterning a coating of photoresist, a photosensitive polymer, using a mask which causes parts of the photoresist to be exposed while protecting other portions. Depending on the polarity of the resist, development removes the exposed (positive) or unexposed (negative) photoresist, which allows selective processing of the now uncovered portions of the wafer. For optical lithography, or photolithography, masks are physical objects made from transparent and opaque materials,

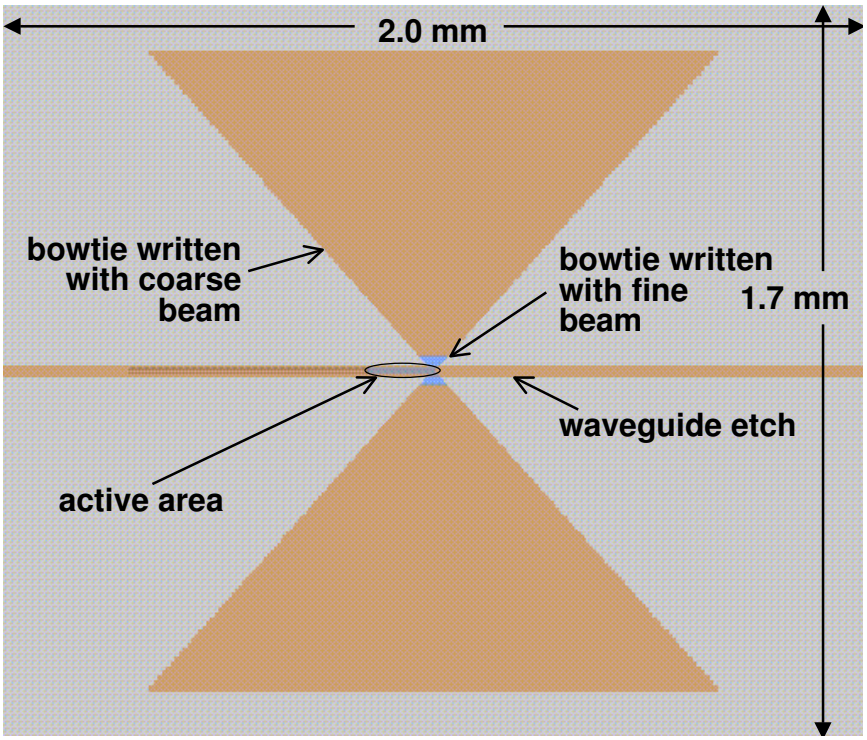

Figure 3-1: Bowtie-coupled photomixer SEBL masks. The etch and metal deposition masks are superimposed. A wire bond to the middle of the antenna provides bias contact to the bowtie-coupled devices. Different colors denote different e-beam doses.

which allow light to pass unimpeded in certain areas while occluding other areas. For scanning electron-beam lithography (SEBL), the mask is a series of commands that move an electron beam across the surface of the photoresist-coated wafer. Distributed photomixer processing requires design of both types of masks.

The obvious requirements of mask design are accurate definition of the features of interest and proper registration of patterns from one processing step to the next. For a new type of device, a mask allows parameterization of particular design features to bracket design choices in order to account for unknowns and verify models. The distributed photomixer masks accomplish these goals as well as defining a manageable device chip size and providing test structures for independent measurement of various device characteristics.

Except for the bowtie antennas ($\sim$ 1300 μm by $\sim$ 1500 μm), the distributed photomixer designs from Chapter 2 fit in an area approximately 150 μm by 75 μm. On its own

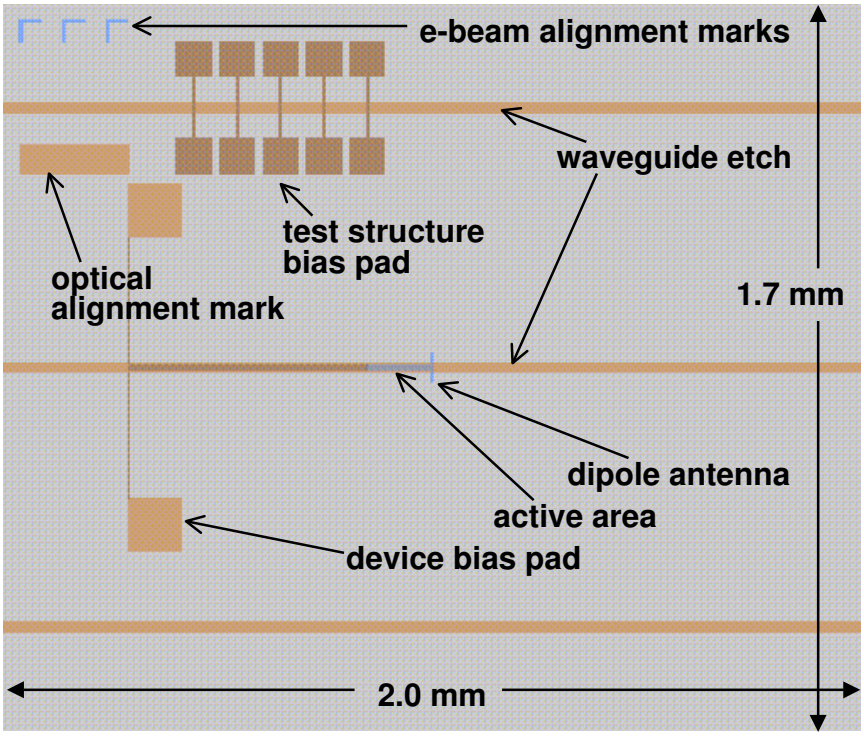

Figure 3-2: Dipole-coupled distributed photomixer SEBL masks. The e-beam alignment mark, etch, and metal deposition masks are all superimposed. Different colors denote different e-beam doses.

merit, the benefit of a standard chip size dictates a larger chip for all the distributed photomixer designs. A large chip also allows test structures with dc-bias pads large enough for wire-bonding and allows for manageable handling. A chip size of $2.0\,\text{mm}$ by $1.7\,\text{mm}$ accomplishes these objectives. Centering the active area avoids damage to the active area resulting from handling near the edges of the wafer. The SEBL masks which define the bowtie-coupled distributed photomixer are shown in Figure 3-1.

Distributed photomixer processing involves a minimum of two processing steps, etching to define the strip-loaded dielectric waveguide and metal deposition to create the terahertz waveguide and antenna. Because the 0.2-μm-wide electrodes that periodically load the coplanar strips (CPS) are narrower than achievable using standard optical photolithography, patterning of the CPS requires e-beam lithography. The use of SEBL requires an initial e-beam mask for alignment marks, which are used for all subsequent SEBL steps and are shown in Figure 3-4. The critical alignment of the CPS to the dielectric strip is

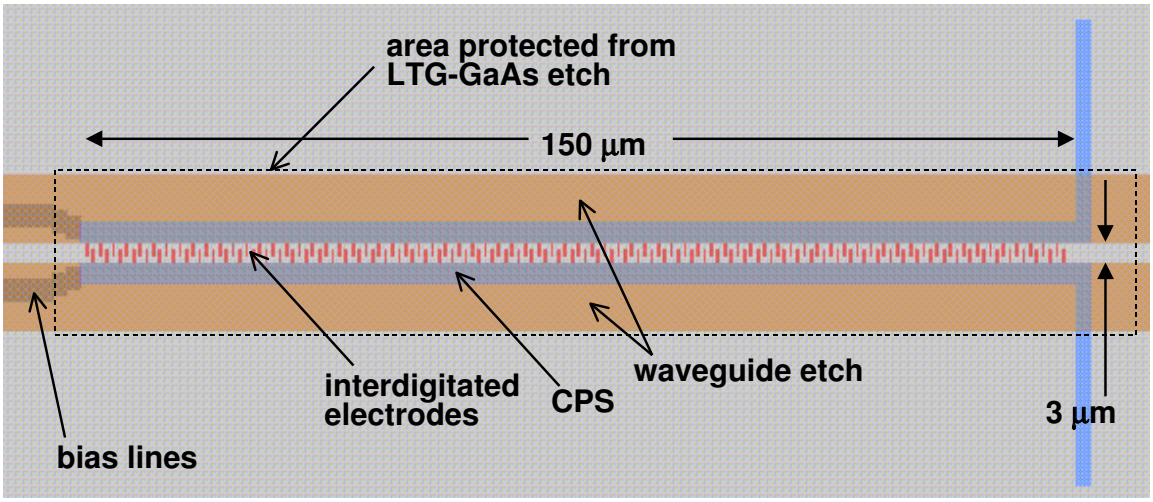

Figure 3-3: Detail of the device active area in SEBL masks. The etch and metal deposition masks are superimposed. Different colors denote different doses.

more accurate and reliable if both processing steps use e-beam lithography, because the SEBL alignment marks are more easily located in subsequent processing steps [90]. Thus, SEBL defines the optical waveguide, even though the dimensional tolerances on the strip itself do not require it. Because the active area is ~ 1 mm from the input facet, the LTG-GaAs layer must be etched from the majority of the chip to prevent the optical signal from being absorbed before it reaches the active area. The alignment and dimensional tolerances are large enough that an optical mask is sufficient. The waveguide etch and metal deposition masks for the active area of a dipole-coupled photomixer are shown in Figure 3-3. The active area protected during the field etch of LTG-GaAs is noted in Figure 3-3. Alignment marks for this step are written during the waveguide etch step, and an example is shown in Figure 3-4.

Different electrode lengths and spacings on the CPS bracket added capacitance which determines the velocity of the terahertz signal. Together with the frequency-independent bowtie antenna, active areas with different added capacitance are used to investigate the effect of velocity match between the optical and terahertz signals. The design electrode gap[1] of $0.8\,\mu$m and overlap of $1.0\,\mu$m adds $0.06\,\mathrm{fF}/\mu\mathrm{m}$. For greater capacitance, a $0.4\,\mu$m

[1]For definition of the dimension terms, see Figure 2-13.

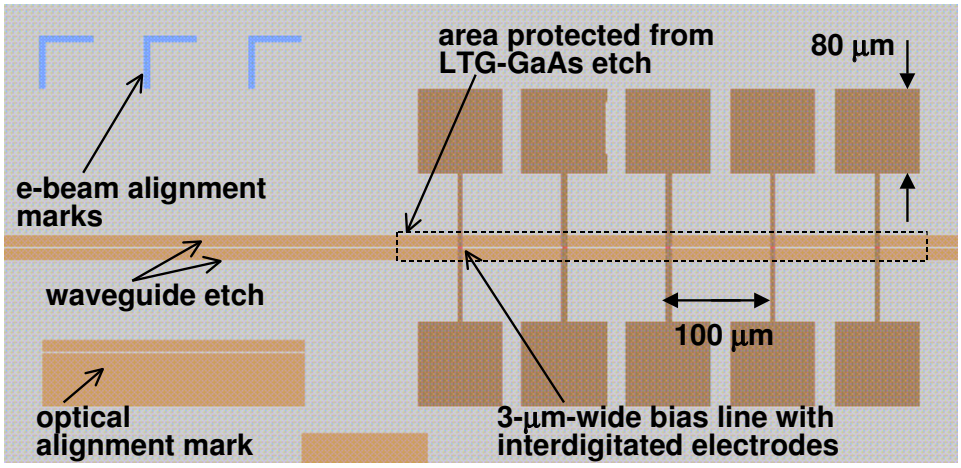

Figure 3-4: Detail of test structure area in SEBL masks. The e-beam alignment mark, etch, and metal deposition masks are all superimposed. Different colors denote different doses.

gap and $1.6\,\mu$m overlap adds $0.20\,\mathrm{fF}/\mu\mathrm{m}$, when accounting for the $0.15\,\mu$m height of the electrodes by modeling them as zero height electrodes with width $0.24\,\mu$m [91]. For lower added capacitance, the gap is increased; however, the electrode overlap must be reduced as the gap is increased to keep the distance between the end of an electrode and the CPS greater than the gap. Fields are higher at the tip of the electrode, so the distance between the end of the electrode and opposite coplanar strip must be greater than the inter-electrode gap to prevent unwanted breakdown. Thus, the only practical design with capacitance lower than the design electrode geometry is one with no interdigitated electrodes. For the dipole-coupled distributed photomixers, instead of varying the electrode geometry, the three antenna designs from Section 2.3.2 vary the resonant frequency of the dipole.

In addition to the distributed photomixer device, the masks contain test structures which allow independent measurement of the LTG-GaAs responsivity, the carrier lifetime in the LTG-GaAs, and the optical mode's coupling to the LTG-GaAs layer. A dielectric waveguide, which is identical to the one used for the device, guides the optical beat signal; however, instead of CPS along the length of the active region, 3-μm-wide taps provide bias to five discrete points along the waveguide. The photocurrent at these points measures the optical intensity at the point along the optical waveguide. The SEBL masks for defining the test structures are shown in Figure 3-4. By surface illuminating these structures in-

stead of waveguide coupling, these test structures can be used for measuring responsivity or carrier lifetime. Continuous-wave (cw) illumination and measurement of the resulting dc photocurrent determines the LTG-GaAs responsivity. Using an ultrafast pulsed laser and an autocorrelation technique [92], the carrier lifetime in the LTG-GaAs layer is measured.

3.2 Fabrication

3.2.1 Layer Growth

The LTG-GaAs and AlGaAs layers comprising the dielectric guide are grown using Molecular Beam Epitaxy (MBE) with a Intevac Modular Gen II solid source MBE reactor on a semi-insulating GaAs substrate. Surface quality and layer growth are monitored using Reflection High Energy Electron Diffraction (RHEED), in which a high-energy electron beam is bounced off the surface of the sample at a grazing angle. Diffraction of the electrons by the sample's lattice creates a series of streaks, the sharpness of which indicate the surface's flatness. A RHEED oscillation, or the change from a sharp pattern to diffuse and back to sharp, occurs as growth progresses from a completed layer to an incomplete monolayer with islands and back to a completed surface and thus marks the growth of a layer. The RHEED patterns for all layers up to the LTG-GaAs were good on all the growth runs indicating high quality layers. RHEED oscillations are not seen when growing LTG-GaAs because even though crystalline material is grown, the surface never forms perfectly flat sheets due to the reduced surface mobility of the constituent atoms at low temperatures. The epitaxial layers are given in Table 3.1, while a not-to-scale schematic of the layers is shown in Figure 3-5. The same schematic convention is used in Section 3.2.2: Figure 3-7 for detailing the processing steps. All $Al_xGa_{1-x}As$ layers as well as the buffer GaAs layer are grown at a substrate temperature of 800^{o} C. The LTG-GaAs is grown at a substrate temperature of 240^{o} C and then annealed for 10 minutes at 580^{o} C, because these conditions have produced short carrier lifetimes [55].

Table 3.1: Epitaxial layer structure.

Thickness	Material	Doping
~ 1000 Å	LTG-GaAs	undoped
2500 Å	$Al_{0.35}Ga_{0.65}As$	undoped
5000 Å	$Al_{0.20}Ga_{0.80}As$	undoped
$3.0\,\mu$m	$Al_{0.35}Ga_{0.65}As$	undoped
1000 Å	GaAs	undoped
SI-GaAs substrate		

Figure 3-5: Schematic of the distributed photomixer epitaxial layer structure.

3.2.2 Processing

Processing of the distributed photomixer comprises four steps: SEBL alignment mark definition, waveguide etch, device metal deposition, field etch of LTG-GaAs. Each step uses the appropriate mask described in Section 3.1.

The SEBL system requires cross-shaped wafer level alignment marks as well as the L-shaped die alignment marks shown in Figure 3-4. The standard SEBL photoresist, ZEP 520, is spun on at 4000 revolutions per minute (4k rpm) to a thickness of $\sim$ 3600 Å ($\sim$ 3.6 kÅ). After a 15 minute pre-bake at 110^{o} C, the photoresist is exposed and developed for 30 seconds in n-butyl acetate. The wafer is ashed in a LFE-118 plasma asher with a helium-oxygen (HeO_2) plasma at fifty watts (50 W) and one torr for 30 seconds to ensure that the exposed wafer surface is free of organics. Four-hundred angstroms (400 Å) of titanium (Ti) are evaporated followed by 1100 Å of gold (Au) in an Airco electron-beam evaporator. The metal layer is this thin because a liftoff must be performed and the e-beam resist is thin. Subsequent rinses of acetone and chlorobenzene dissolves the remaining photoresist and lifts off any metal not on the wafer surface. A final ashing at 100 W for 1 minute cleans the wafer surface. The key steps in this process are illustrated in Figure 3-7(a).

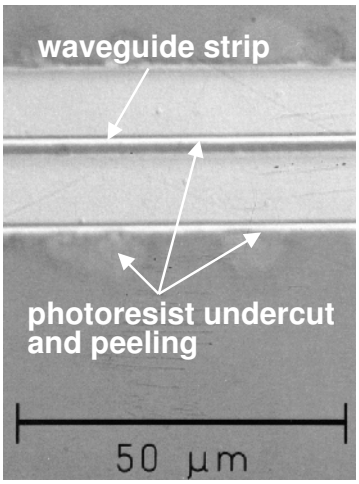

(a) Undercut during PA-11 etching as a result of ZEP 520 peeling.

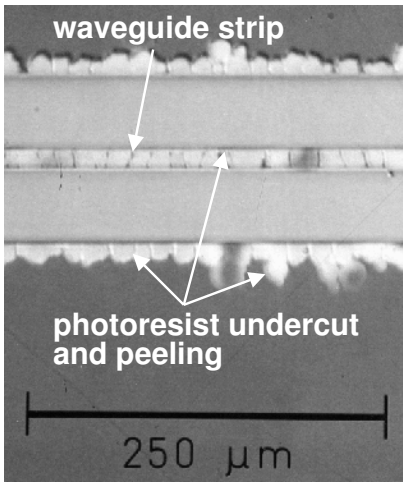

(b) Undercut during PA-11 etching as a result of SEBL developer interaction with PPAP.

Figure 3-6: Photographs of undercut during PA-11 etching.

For the waveguide etch, the standard SEBL photoresist, does not adhere to the wafer during a wet etch of $\sim$ 60 seconds using PA-11 and either allows the etchant to undercut the pattern or lifts off the wafer entirely as shown in Figure 3-6(a). A thin layer of PPAP applied to the wafer before coating allows the photoresist to maintain adhesion, but the standard SEBL developer (n-butyl acetate) reacts with the PPAP causing undercut as shown in Figure 3-6(b). The developer, MIBK, however, does not react with the PPAP. The etch rate of LTG-GaAs using PA-11 varied between 31 Å/sec and 37 Å/sec, while the etch rate of the $Al_{0.35}Ga_{0.65}As$ varied between 56 Å/sec and 62 Å/sec. Etch depths are measured with a Tencor Instruments Dectak. Table 3.2 details the successful waveguide etching process flow, while Figure 3-7(b) illustrates the major steps.

The process steps for device metal are nearly identical to the steps for the SEBL alignment mark deposition. The lithography is more difficult on this step, because of the small dimensions of the electrodes ($\sim$ 0.2 μm). The dose levels for each feature are set separately to avoid over-exposure from scattered electrons (the proximity effect). A two-step process in which the fine features are written in one run and the large features written in a subsequent run after increasing the diameter of the electron beam reduces e-beam write

Table 3.2: Process steps for waveguide etch.

Step	Processing
1.	Spin PPAP (diluted 35:1 with 1512 thinner) at 3k rpm.
2.	Bake at 180° C for 30 minutes.
3.	Apply $\sim$ 3.6 kÅ ZEP 520 by spinning at 3.6k rpm.
4.	Bake at 110° C for 15 minutes.
5.	Expose and develop using MIBK for 45 seconds.
6.	Bake at 110° C for 2 minutes.
7.	Ash for $\sim$ 30 seconds at 100 W to remove PPAP.
8.	Etch using PA-11.

time but increases total processing time because it requires two complete lithography and liftoff steps. Adjusting the beam characteristics and dose levels "on-the-fly" and writing the entire three inch wafer at one time results in a twenty-two hour write time but only one lithography and liftoff step, as described at the beginning of Section 3.2.2. Figure 3-7(c) shows a cross-section view of the key steps of this processing. As a result of the end-on perspective, the gold is shown both on top of the photoresist and on top of the LTG-GaAs layer. The gold of the electrodes directly contacts the LTG-GaAs layer, but between the electrodes, the gold is on top of the photoresist.

Etching of the LTG-GaAs from most of the wafer is the final processing step. Figure 3-4 and Figure 3-3 note the relevant area where LTG-GaAs is not etched away. The alignment mark for this layer is shown in Figure 3-4 and is defined during the waveguide etch. Dimensions and tolerances for this step allow the use of optical lithography. For the positive resists that we use, etch masks are bright field, meaning that the areas to be etched are transparent on the mask. A C-shaped feature on the optical photomask abuts one end of the strip alignment mark providing alignment in both directions. AZ photoresist 1512 is spun on the wafer at 4k rpm and baked at 70° C for 20 minutes. Exposure using a Karl Suss MJB-3 contact aligner is for 0.6 minutes and is followed by a 5 second develop in Microposite 303A developer diluted 9:1 with de-ionized water. The wafer with the remaining resist is baked for 30 minutes at 120° C and then ashed for 30 seconds at 100 W. Etching and step height measurement proceeds as in the waveguide etch processing using PA-11. The standard AZ photoresist used in the optical lithography does not delaminate in etching.

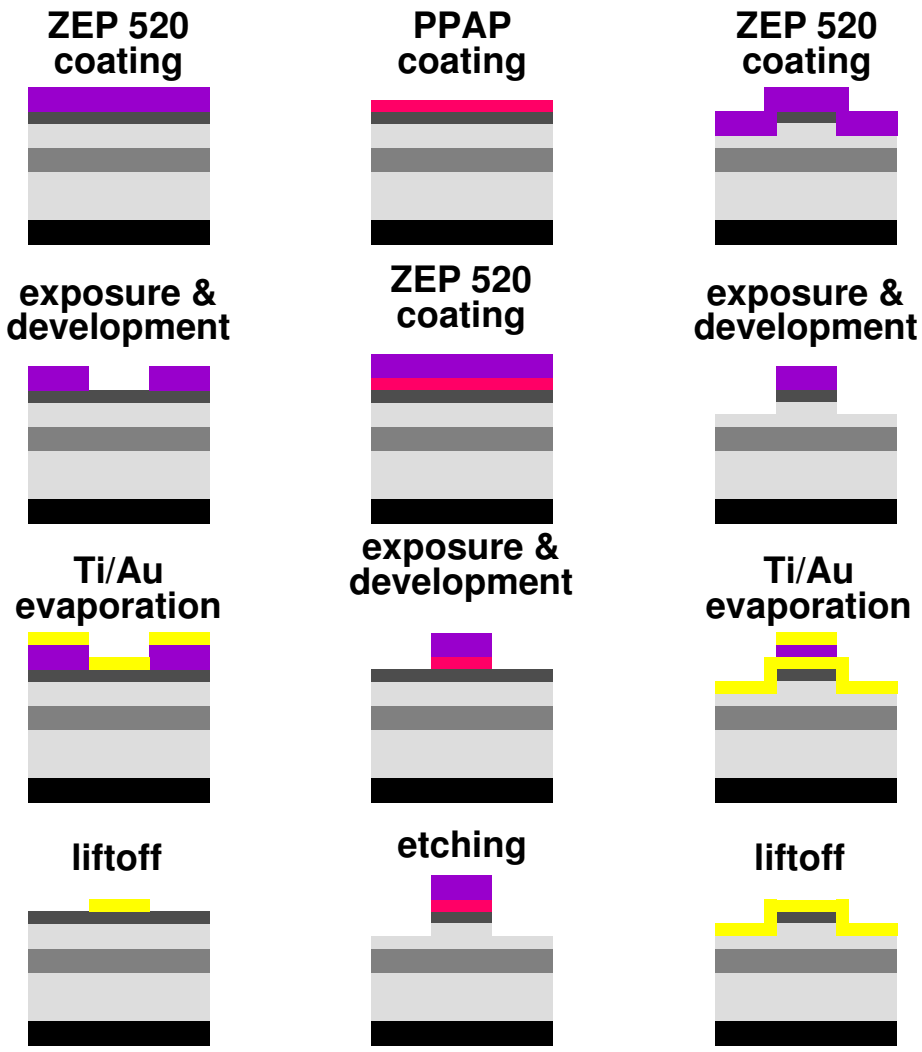

(a) Processing steps for e-beam alignment marks.

(b) Processing steps for waveguide etch.

(c) Processing steps for terahertz waveguide and antenna metal deposition.

Figure 3-7: Distributed photomixer processing steps.

3.2.3 Post-Processing

After processing, the distributed photomixer wafers undergo an optional passivation step to prevent further oxidation of the exposed $Al_{0.35}Ga_{0.65}As$ layer and a mandatory scribe and cleave step to create individual device chips. Either silicon nitride or polyimide passivates the surface. The silicon nitride is deposited using a Plasmatherm nitride deposition system. The polyimide is spun at 6000 rpm to create a ~ 4000 Å layer and then soft-baked. For either passivation, an optical lithography step opens access to the bias pads by patterning 1512 photoresist. The optical photomask for this step contains squares for every bias pad. The silicon nitride layer is etched with a Semi-Group reactive ion etcher (RIE) using CF_4. For the polyimide, the photoresist developer removes the exposed polyimide as well as the developed photoresist. The remaining resist is removed with acetone, and the polyimide is hard-baked at 180^o C for one hour. Cleaving for an optical-quality facet requires that the wafers be thinned and polished. The wafers are lapped and polished to a maximum thickness of 7 mils (175 μm) and minimum of 4 mils (100 μm). Wafer thickness greater than 7 mils makes an optical-quality facet difficult to achieve, while thickness less than 4 mils causes the wafers to be very difficult to handle. The standard procedures for the scribing and cleaving the distributed photomixer chips are detailed in Appendix B. For cleaving a large number of devices at once, standard scribing and cleaving is performed along the planes of the facets, while long scribes are made along the orthogonal direction. In long-scribe mode, the scribe tip drags along the surface of the wafer scoring the entire length. Cleaving is performed for the optical facets first, then the wafer is rotated 90^o and cleaved along the other scribes.

3.3 Photographs and Micrographs

This section contains photographs and micrographs from a scanning electron microscope (SEM) of fabricated distributed photomixers. The view of a bowtie-coupled photomixer in Figure 3-8 includes the entire active area as well as the bowtie antenna and the dc-bias lines. The interdigitated electrodes can barely be resolved in this micrograph. Figure 3-9 shows a close-up of part of a dipole-coupled distributed photomixer's active area, including

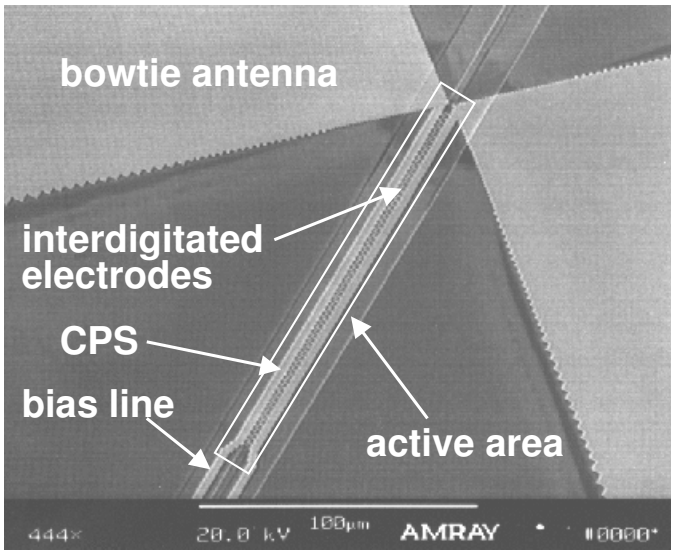

Figure 3-8: SEM micrograph of bowtie-coupled distributed photomixer showing the active area, bias lines, and bowtie antenna.

the top of the strip-loaded waveguide, the coplanar strips with interdigitated electrodes and the dipole antenna. Figure 3-10 provides an oblique view of the same portion of the active area including the LTG-GaAs field etch step. Figure 3-11 includes SEM micrographs of the strip-loaded waveguide overlayed with CPS and interdigitated electrodes of $0.4\ \mu$m and $0.8\ \mu$m gaps.

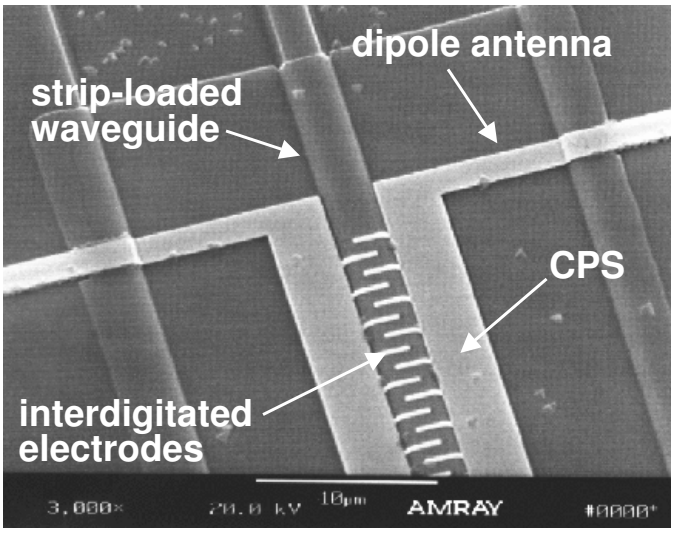

Figure 3-9: SEM micrograph of end of the active area of a dipole-coupled distributed photomixer. The strips in the dielectric away from the CPS are the edges of the region from which LTG-GaAs has been preserved.

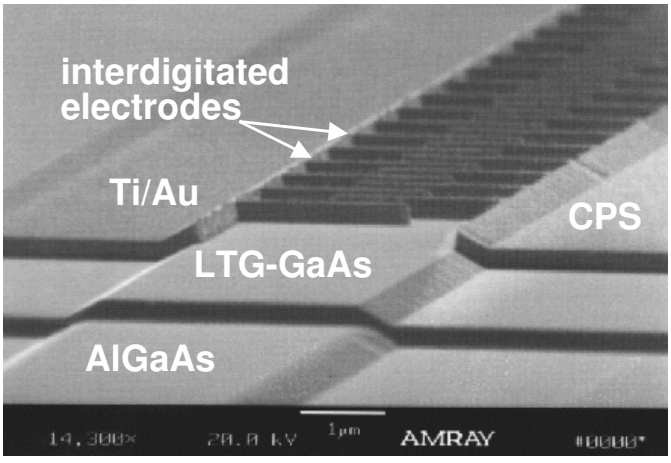

Figure 3-10: SEM micrograph at an oblique angle of a distributed photomixer's active area.

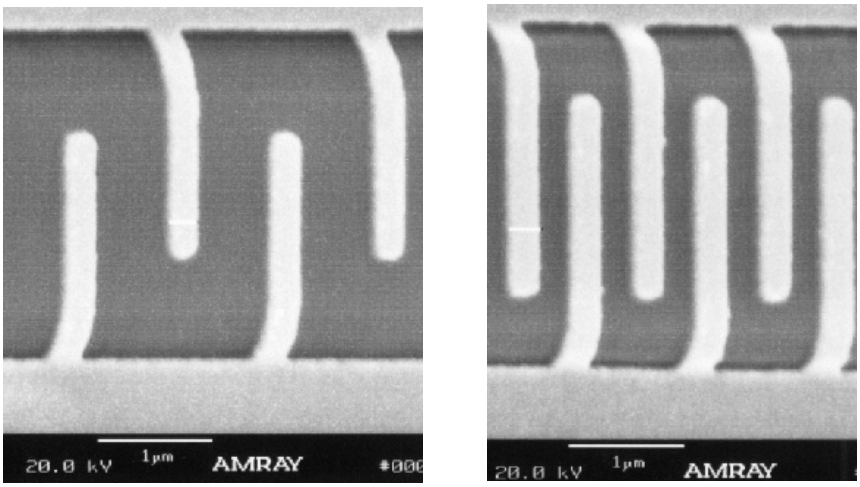

(a) Interdigitated electrodes with design gap of $0.8\ \mu$m.

(b) Interdigitated electrodes with $0.4\ \mu$m gap.

Figure 3-11: Distributed photomixer interdigitated electrode SEM micrographs.

Chapter 4

Device and Material Characterization

This chapter describes the measurement and analysis of the material and device parameters that determine distributed photomixer performance. Accurately predicting and understanding the terahertz performance of the photomixers requires the independent measurement of the low-temperature-grown gallium arsenide (LTG-GaAs) absorption coefficient and carrier lifetime, the extinction length in the optical waveguide, and the responsivity of the electrode geometries. The test structures described in Section 3.1 allow for experiments measuring the LTG-GaAs carrier lifetime, the mode extinction length and responsivity. The results of these measurements are compared with theory and physical intuition and the impact on device performance is considered.

4.1 LTG-GaAs Characterization

4.1.1 Absorption Coefficient Measurement

A material's bulk absorption coefficient, α, describes the power decay with propagation of an electromagnetic plane wave in the material according to $P \propto e^{-\alpha y}$. For the distributed photomixers, the bulk absorption coefficient of the LTG-GaAs in the absorber layer together with the fraction of the optical mode in the absorber determine the mode extinction length as explained in Section A.2. A few measurements of $\alpha_{\mathrm{LTG-GaAs}}$ have been published, but the data is scattered between 1.0×10^4 cm^{-1} and 2.0×10^4 cm^{-1} at my oper-

ating wavelength of 850 nm [93, 94, 95, 96, 97]. Studies indicate that $\alpha_{\mathrm{LTG-GaAs}}$ is system and growth dependent. Absorption coefficient measurement is performed therefore on the specific device wafers. Conceptually, the most straightforward method of determining the absorption, or loss, is to measure the fraction of incident power reflected and transmitted through the layer. With appropriate data analysis, this method yields $\alpha_{\mathrm{LTG-GaAs}}$ as described below. Two other methods, reflectometry and ellipsometry, were attempted for measuring the absorption coefficient. These measurements were not successful, and their limitations are discussed.

Transmission/Reflection Measurement

Incident power that is neither reflected from nor transmitted through a sample must be absorbed; therefore, the absorption coefficient is calculated by solving $L = e^{-\alpha \ell_{\mathrm{prop}}}$, where L is the fraction of absorbed power and ℓ_{prop} is the the total propagation distance. Given the distributed photomixer samples' optical waveguide structure, several factors complicate this technique for the measurement of $\alpha_{\mathrm{LTG-GaAs}}$. The GaAs substrate has optical properties very similar to LTG-GaAs, i.e. it is highly absorbing at the wavelength of interest, $\lambda = 850\,\mathrm{nm}$, so characterization of the thin LTG-GaAs layer requires removal of the substrate. Though the LTG-GaAs layer is too thin ($\sim 1000\,\text{Å}$) to be free standing, the AlGaAs layers ($\sim 4\,\mu$m) form a membrane strong enough to be free standing over several millimeters and can support the LTG-GaAs layer. In addition to providing support for the LTG-GaAs layer, the AlGaAs layers form a resonator. While this resonator complicates the analysis of the transmission and reflection coefficients, it allows for more accurate determination of the absorption coefficient. Even though LTG-GaAs is strongly absorbing at these wavelengths, the thinness of the layer makes it a weak absorber. A standard technique for accurately measuring weak absorbers is to place them in a resonant cavity, and the AlGaAs layers create this type of environment.

To prepare a sample for measurement, a device wafer piece is mounted with LTG-GaAs and AlGaAs layers down on a glass slide with black wax and fast etched with a 50:50 mixture of ammonium hydroxide and hydrogen peroxide (NH_4OH and H_2O_2) to within 50 μm of the bottom $Al_{0.35}Ga_{0.65}As$ layer. A selective etch, citric acid ($C_6H_8O_7$), which

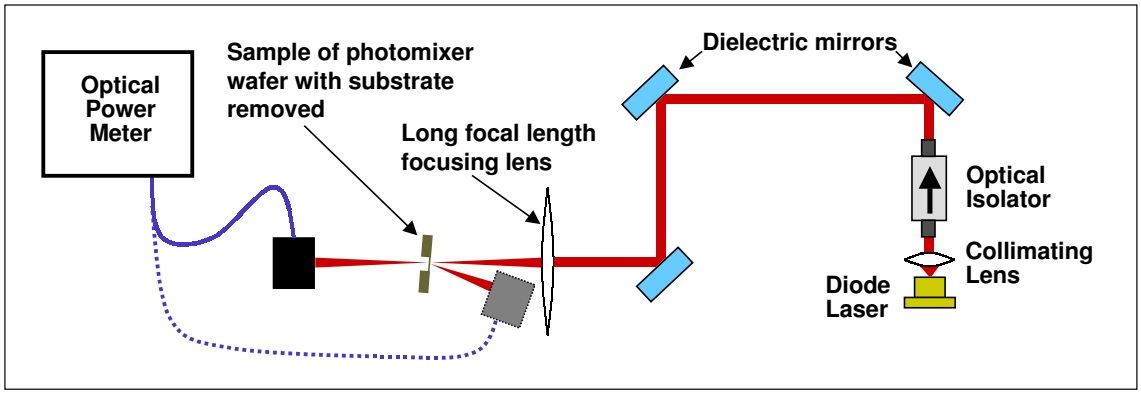

Figure 4-1: Transmission and reflection experimental setup.

etches GaAs preferentially over AlGaAs is subsequently used to remove the remainder of the substrate and leave the AlGaAs and LTG-GaAs membrane. The selectivity of this etch is approximately 30:1. The membrane is fragile but remains intact with careful handling.

Resonator response can be measured using an incoherent technique such as a transmission spectrometer or a coherent technique such as transmission/reflection measurement using laser sources. While an incoherent technique gives a good indication of the variation of absorption with wavelength and is immune to standing-wave issues, it is often difficult to determine accurately the absolute value of the absorption at any given wavelength. I am more confident of accurately coupling and collecting all of the light from laser sources; therefore, I chose to measure the transmission and reflection of light from diode lasers. The lasing wavelength of these lasers can be temperature tuned to cover a total range of approximately 7 nm. The experimental setup for the measurement is shown in Figure 4-1. Mounted on a translation stage (not shown in the figure), the etched sample is moved in the beam path of diode lasers such as those used to perform the terahertz device testing. Four different lasers can be switched into the beam path using beamsplitters and moveable mirrors. A long-working-distance lens focuses the beam into a spot on the sample. (Specifics of the lens are contained later in the paragraph.) The profile of the input beam taken with a 5-μm pinhole before the lens is shown in Figure 4-2. The profile was taken by moving the pinhole through the beam path and recording the transmitted power. Fitting the data to

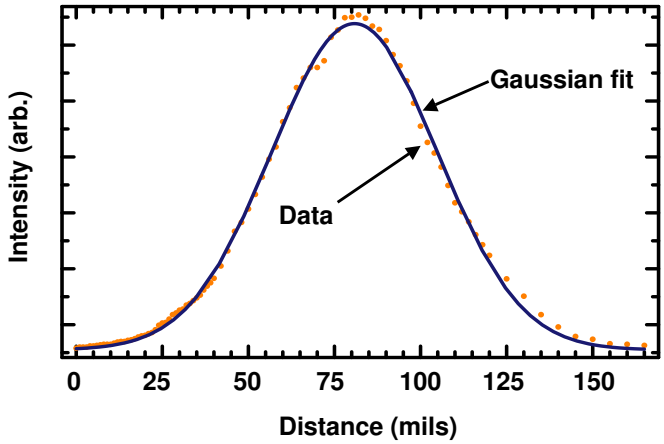

Figure 4-2: Beam profile from Transmission/Reflection experiment taken with 5- μm pinhole mounted on translation stage.

a function of the form

$$I(x) = I_{\text{bg}} + I_0 e^{-\frac{(x-x_0)^2}{2w_0^2}}, \tag{4.1}$$

where I is light intensity, I_{bg} is the background intensity from scattered light, and w_0 is the waist yields $w_0 = 48.1$ mils $= 1.22$ mm. Therefore, the beam diameter is $2w_0 = 2.44$ mm, which together with the 116 mm focal length, F, of the focusing lens gives a system *f-number* of $F/D = 47.5$. The waist diameter on the wafer is then $2w_{0,new} = \frac{4\lambda}{\pi}(f\text{-}\#) = 51$ μm. While the membrane exhibits some warping, this size spot fits on one of the smooth sections of the sample. The focused spot is aligned by observing the reflected light and finding a clean reflected beam. By making the beam incident on the sample at a slight angle, the reflected beam can be measured before it passes back through the focusing lens.

A Newport Power Meter [98] records the optical power levels. An optical isolator prevents power fluctuations due to feedback into the laser diodes. Standing waves in the power meter, however, cause interference with the measurement. To account for this effect, the power head is mounted on a miniature rotation stage and rotated through small angles to trace out the ripple in measured power. The peak value in this ripple is recorded for each measurement condition.

Extracting $\alpha_{\text{LTG-GaAs}}$ from the data requires modeling the dielectric resonator structure formed by the AlGaAs layers. The transmission matrix technique of propagating a plane

wave through dielectric layers described in Appendix A describes the interaction of the incident optical field and the dielectric stack. In Appendix A, the normalization condition which leads to a solution is the exponential decay of the fields in the uppermost and lowermost layers, as given in equations (A.17) and (A.18). In the present case, the equation analogous to (A.17) is

$$\begin{bmatrix} t \\ 0 \end{bmatrix} = \begin{bmatrix} M_{11} & M_{12} \\ M_{21} & M_{22} \end{bmatrix} \begin{bmatrix} 1 \\ r \end{bmatrix} , \tag{4.2}$$

where M is the composite transmission matrix and r and t are the field reflection and transmission coefficients. In terms of the measured quantities, the two equations to be solved are

$$R = r^2 = \frac{P_r}{P_{\text{tot}}} = \left(-\frac{M_{21}}{M_{22}}\right)^2 \quad \text{and} \tag{4.3}$$

$$T = t^2 = \frac{P_t}{P_{\text{tot}}} = \left(M_{11} - \frac{M_{21}}{M_{22}} M_{12}\right)^2 , \tag{4.4}$$

where P_r, P_t, and P_{tot} are the reflected, transmitted, and total powers, respectively. These two equations are solved for the two unknowns, the real and imaginary parts of the relative dielectric constant of LTG-GaAs.

Solving these equations for $\epsilon_{r,\text{LTG-GaAs}} = \epsilon_1 + j\epsilon_2$, however, requires knowing the dielectric function of the $Al_xGa_{1-x}As$ layers over the wavelength range of the measurements and the thickness of each layer. The Sellmeier equation discussed in Section 2.1.2 gives the index of refraction for the $Al_xGa_{1-x}As$ layers. The extinction coefficient for $Al_{0.20}Ga_{0.80}As$ and $Al_{0.35}Ga_{0.65}As$ is negligible at the wavelengths of interest [76]. The thickness of layers grown using Molecular Beam Epitaxy can be predicted from the growth parameters and are shown in Table 3.1. Non-physical values for $\epsilon_{r,\text{LTG-GaAs}}$ are extracted at the exact predicted thickness because the actual thickness is not precisely this value. In order to duplicate the actual resonator response which depends on the effective thickness, i.e. the ϵ_1-physical thickness product, the error in physical thickness is transferred to an error in ϵ_1. By stepping through actual thickness values within a narrow range of the expected thickness and solving for $\epsilon_{r,\text{LTG-GaAs}}$ at each point, I conclude that the most plausible thickness for the dielectric stack is $99.69\% \pm 0.06\%$ of the expected thickness. Using this thickness

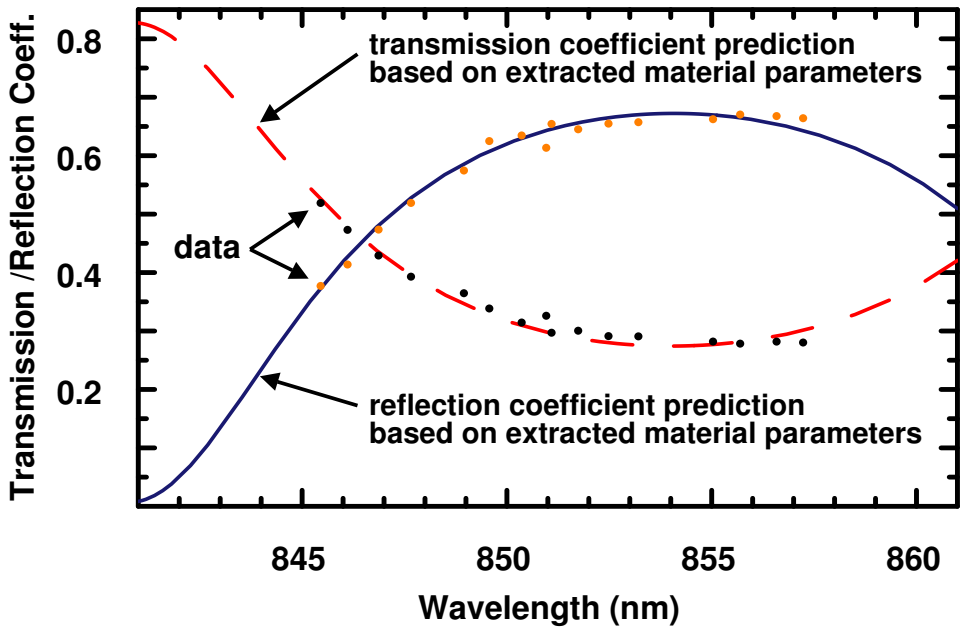

Figure 4-3: Transmission and reflection coefficient of dielectric stack.

fraction and the extracted $\epsilon_{r,\mathrm{LTG-GaAs}}$ values, the transmitted and reflected power for the dielectric stack are calculated and shown in Figure 4-3 along with the data. The close fit between the calculation and measurement indicates that the extracted $\epsilon_{r,\mathrm{LTG-GaAs}}$ values correspond to the actual values of the layer.

The sensitivity to experimental uncertainties is investigated next. In Figure 4-4, the extracted ϵ_1 and ϵ_2 values are shown for each measured wavelength along with the linear fit to the extracted points, which are given by

$$\epsilon_1 = 13.89 \tag{4.5}$$

$$\epsilon_2 = 0.556 - 0.0061(\lambda - 840)\ , \tag{4.6}$$

where λ is the wavelength in nm and $(840 < \lambda < 860)$. The figure also shows the the uncertainty in ϵ values that the uncertainties in physical thickness and measured power produce. The thickness uncertainty ($\pm 0.06\%$) leads to variation primarily in the extracted ϵ_1's, because ϵ_1 determines the effective thickness of the resonator. Uncertainty in measured power levels affects the extracted ϵ_2 and is estimated at two percent for *each* power.

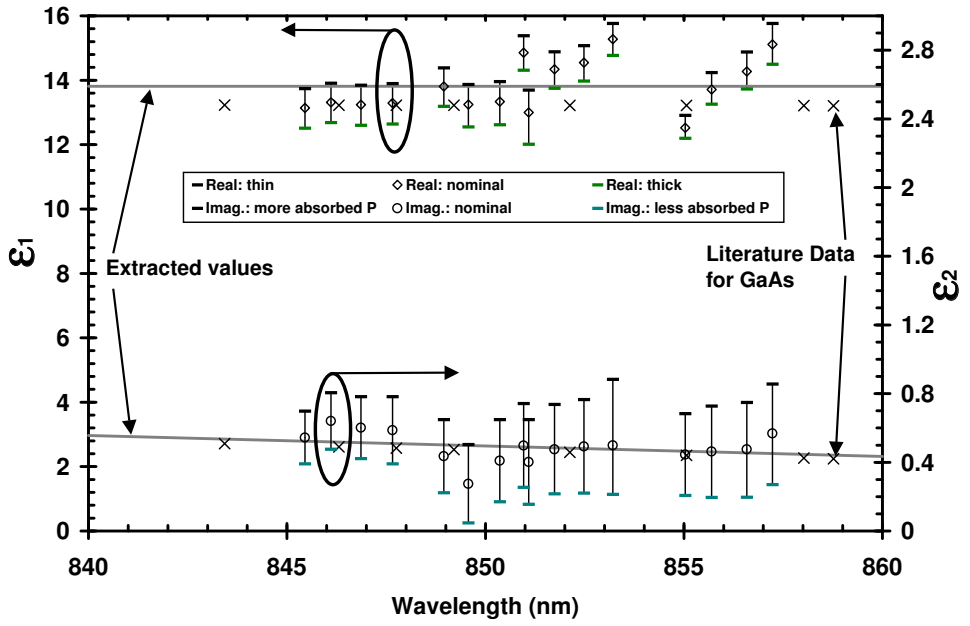

Figure 4-4: Extracted ϵ_r values showing the effect of an uncertainty in thickness on ϵ_1 and an uncertainty in measured power on ϵ_2.

I verify that the measurement is sensitive to the LTG-GaAs material parameters by comparing absorbed power data to predictions based on different $\epsilon_{r,\mathrm{LTG-GaAs}}$ values. As expected, this transmission and reflection measurement is sensitive to ϵ_2 of the LTG-GaAs layer as demonstrated in Figure 4-5. Even with scatter in the data, the value for ϵ_2 can be predicted within thirty percent. However, this measurement is not sensitive to ϵ_1 of the LTG-GaAs layer, because the AlGaAs layers dominate the cavity's effective length, i.e. the resonant period. Small variations in ϵ_1 of LTG-GaAs produce unnoticeable changes in the transmitted, reflected, and absorbed powers. This insensitivity combined with the large scatter in the extracted values for ϵ_1 and the fact that the average extracted value is so much higher than the literature values, I decided it was more prudent to use the literature values for ϵ_1 in the optical waveguide modeling.

The absorption coefficient is calculated by

$$\alpha_{\mathrm{LTG-GaAs}} = \frac{4\pi}{\lambda}\left(-\frac{\epsilon_1}{2} + \frac{1}{2}\sqrt{\epsilon_1^2 + \epsilon_2^2}\right)^{\frac{1}{2}} . \tag{4.7}$$

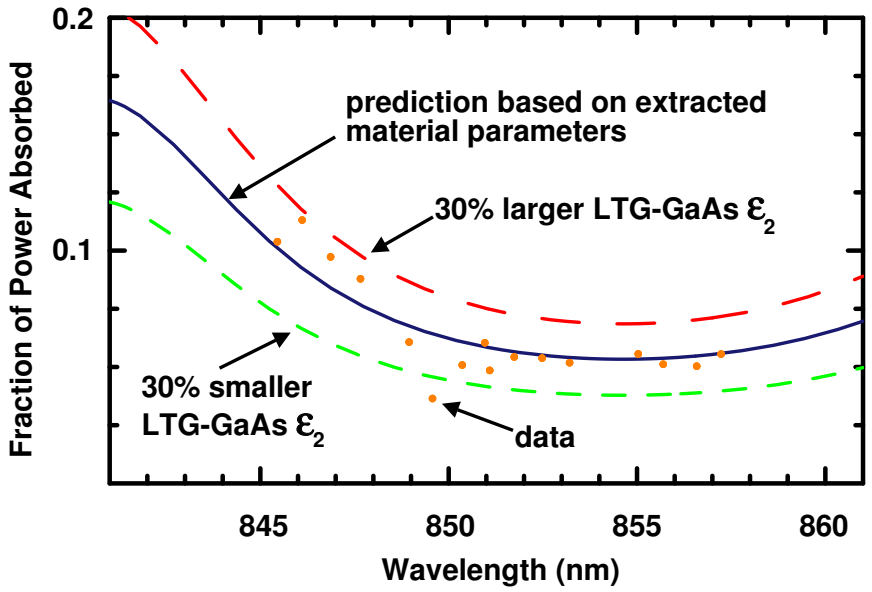

Figure 4-5: Fraction of power absorbed in dielectric stack.

For the design wavelength of 850 nm, $\alpha_{\mathrm{LTG-GaAs}} = 1.0 \times 10^4\,\mathrm{cm}^{-1}$ which is within the range of reported absorption coefficients. Therefore, the transmission/reflection measurement successfully accomplished goal of determining $\alpha_{\mathrm{LTG-GaAs}}$. Interpreting the data requires careful consideration of the unknowns and their effect on the extracted material parameters.

Ellipsometry

The standard technique for characterizing thin films on the top of a wafer is ellipsometry. While there are several different flavors of ellipsometry, the basic principle is that the amplitude and phase of an incident TE (s, or perpendicular to the plane of incidence) and TM (p, or parallel to the place of incidence) wave are compared and used to calculate the characteristics of the material under test. The ratio of the complex reflectances is

$$\rho = \frac{R_p}{R_s} = \frac{|R_p|}{|R_s|} e^{i(\delta_p - \delta_s)} = \tan(\Psi) e^{i\Delta} \ , \tag{4.8}$$

where $\tan(\Psi)$ is the amplitude ratio and Δ is the phase difference. With two measured quantities, two material unknowns can be calculated. For example, for a bare substrate, the

real and imaginary part of the dielectric constant can be found. For a thin film on top of a known substrate, the thickness and ϵ_1 can be calculated, or if the thickness is known, ϵ_1 and ϵ_2 can be found.

Using a Gaertner Scientific Variable Angle Ellipsometer, I measured Ψ and Δ at $\lambda = 830\,\text{nm}$ for device wafers as well as test wafers of a GaAs substrate with a thick layer of LTG-GaAs grown on top. With the best guess for the $Al_xGa_{1-x}As$ and LTG-GaAs indices of refraction, the extracted thickness and absorption coefficient of the LTG-GaAs layer on the device wafer are not reasonable, e.g. $t = 500\,\text{Å}$ and $k = 0.4$. While extracted properties of the LTG-GaAs layer on the device wafer depends on characteristics of the $Al_xGa_{1-x}As$ layers underneath which are not known with great certainty, characterization of the test substrates indicates similar non-physical behavior, e.g. an extracted index of refraction of 2.7 for a thick layer of LTG-GaAs on GaAs. A Brewster's angle measurement, however, yields a Brewster's angle of 75^{o}, which corresponds to an index of refraction of 3.7 which is expected.

Physically, the discrepancy arises because ellipsometry is very sensitive to thin layers on the surface of the layer in question; whereas, the Brewster's angle measurement is not. The origin of this sensitivity is the dependence on the phase of the reflected waves. The most plausible explanation is that an oxide of gallium oxide and aluminum oxide of unknown thickness grows on the surface of the LTG-GaAs after being exposed to atmosphere. Sources report oxide thicknesses from $15\,\text{Å}$ to $100\,\text{Å}$ [99, 100]. Therefore, ellipsometry is unsuited to characterize the LTG-GaAs layer on top of the optical waveguide, because the method is too sensitive to parameters that are not known with great accuracy

Spectroscopic Reflectance

Spectroscopic reflectance is a thin film measurement technique that is less sensitive than ellipsometry to very thin films on the surface of the sample under test. The reflectance of a sample is measured over a broad wavelength range, e.g. 200 nm to 1020 nm, and matched to a predicted reflectance spectrum generated with models of the materials' optical constants which have a small number of adjustable parameters [75]. Both the index of refraction, n, and the extinction coefficient, k, can be extracted from a reflectance-only measurement

through the use of the Kramers-Kronig relations. A Filmetrics F20 Fixed Czerny-Turner spectrometer is used for the reflectance data acquisition, but the data analysis software is not sufficiently adaptable to model the complicated dielectric stack on the distributed photomixer device wafers. With code similar to that which I wrote for the transmission/reflection measurement, the reflectance of the dielectric stack can be predicted over a wide range of wavelengths using a model for the optical constant of LTG-GaAs which includes adjustable parameters. However, the spectroscopic reflectance technique is ultimately unsuited to characterization of the LTG-GaAs layer because it is not sensitive enough to thin films if the index contrast is very small. Changes in the characteristics of the LTG-GaAs layer do not measurably affect the reflectance spectrum given the accuracy with which the measurement can be made. Also, because the substrate has very similar optical properties to the thin film, separating the effects of the substrate and film is not possible.

4.1.2 Carrier Lifetime Measurement

The ultrashort ($\sim$ 200 fs) carrier lifetime in LTG-GaAs is one of the material properties that make it popular for use in terahertz frequency devices. Photomixer performance depends on carrier lifetime because the photocurrent must be able to follow the optical beat signal, i.e. the photoconductor must turn on and off along with the optical signal. As explained in Section 1.3, small-signal optical heterodyne theory predicts

$$P_{\mathrm{THz}} \propto \frac{1}{1+(\omega\tau_e)^2} \ . \tag{4.9}$$

The carrier lifetime in LTG-GaAs films is typically characterized through an optical reflectance technique [55] or an optoelectronic autocorrelation technique [92]. The optoelectronic autocorrelation technique uses the fact that the photocurrent produced by two cross-polarized pulses is nonlinear in illumination intensity, because $i_{\mathrm{pc}}(t) = V_{\mathrm{bias}}/(Z_0 + G(t)^{-1})$, where V_{bias} is the constant bias voltage, Z_0 is the embedding impedance of the photoconductor, and $G(t)^{-1}$ is the photoconductance of the illuminated photoconductor. The second-order nonlinear term gives rise to a contribution to the time-averaged photocurrent which depends on the delay, τ, between the pulses. If the photoconductor is fast

enough to follow the optical pulse, then the contribution is

$$\langle i_{pc}(\tau)\rangle_t = 2S_I^{(2)}\langle I(t)I(t+\tau)\rangle_t + \text{constant} , \tag{4.10}$$

where $S_I^{(2)}$ is the second-order responsivity, $I()$ denotes the intensity of an optical pulse, and the subscript t denotes a time average. If the response of the photoconductor is slow compared to the duration of the optical pulse, e.g. for a photoconductor with a long carrier lifetime, then the photocurrent is given by

$$\langle i_{pc}(\tau)\rangle_t = A\langle i(t)i(t+\tau)\rangle_t + \text{constant} , \tag{4.11}$$

where $A \propto S_I^{(2)}$, $i(t) \propto E_p e^{-t/\tau_e}$, E_p is the optical pulse energy, and τ_e is the carrier[1] lifetime. In the limit of the optical pulse much shorter than the carrier lifetime, $i()$ is the current impulse response of the photoconductor; therefore, measuring the delay-dependent term in the photocurrent yields the autocorrelation of the impulse response. The width of the autocorrelation is determined by the carrier lifetime. Test structures described in Section 3.1 allow for this autocorrelation measurement of carrier lifetimes.

Experimental Setup

Generating cross-polarized, ultrashort ($\sim$ 100 fs) optical pulses is the key to the autocorrelation measurement. As shown in Figure 4-6, a Tsunami Argon-Ion laser pumps a Schwartz Electro-Optics Titan-ML self-modelocked titanium:sapphire laser. In the self-modelocked regime, the pulses from the Ti:sapph are 80–100 fs long. This pulsed beam is split and sent to two corner cube reflectors. One corner cube reflector is mounted on a computer controlled translation stage, while the other is mounted at the center of an audio speaker. The computer-controlled translation stage is adjusted so that the lengths of the two legs are approximately equal. By driving the speaker, the time delay provided by this leg of the autocorrelator is dithered sweeping out the zero path difference (ZPD) point in distance. A half-wave plate rotates the polarization of one of the beams by 90°, and polarizers are used

[1] In the case of LTG-GaAs, electrons are the dominant charge carrier, hence the subscript e.

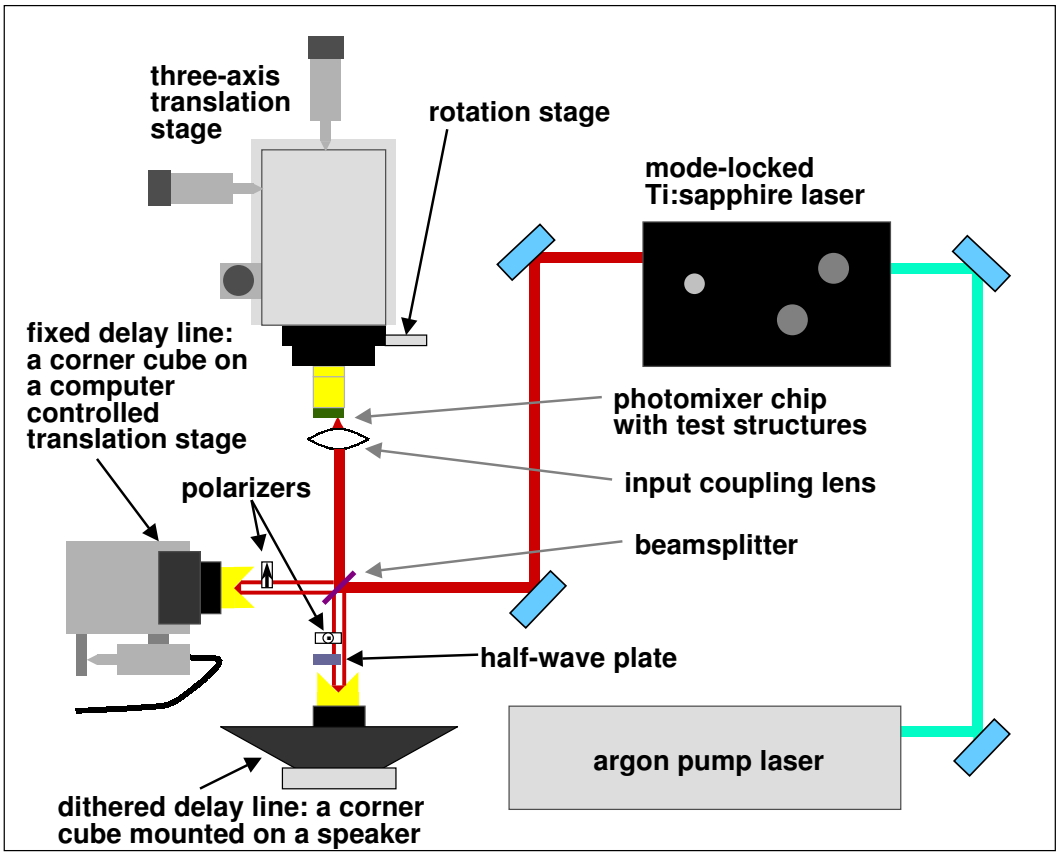

Figure 4-6: Experimental setup for autocorrelation lifetime measurement.

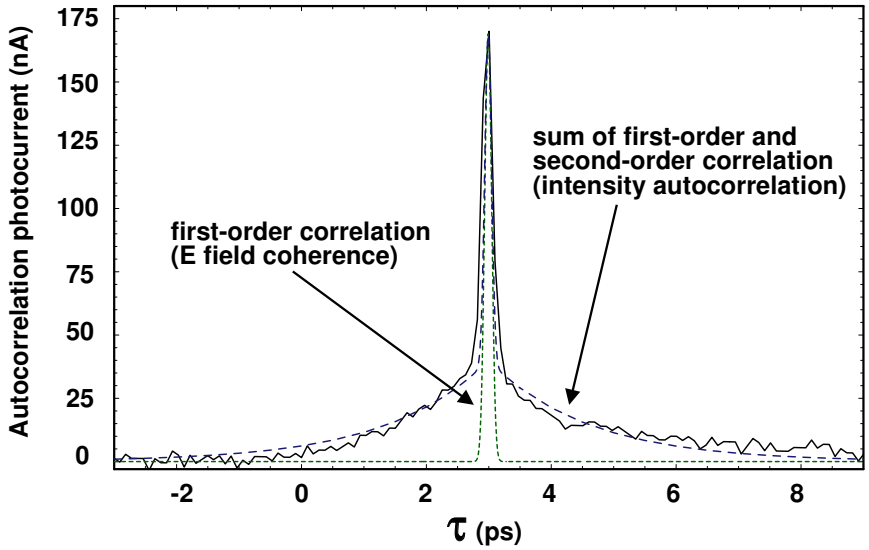

Figure 4-7: Autocorrelation trace with fit.

to clean up the polarization states of the two beams to reduce their co-polarization at the sample. A high numerical aperture lens (NA ~ 0.5) focuses the combined beams onto the sample. An oscilloscope triggered by the speaker drive displays the photocurrent from the test structure induced by the pulse trains. When the translation stage is adjusted correctly, the oscilloscope trace includes the delay-dependent autocorrelation signal.

Measurements

An example autocorrelation measurement is shown in Figure 4-7. The time base is true time delay, τ, calculated by taking consecutive traces before and after moving the fixed delay line a known distance. Knowing the time of flight difference between the two fixed delay leg lengths, the time base on the oscilloscope is calibrated. The trace is the result of averaging 256 scans on the digital oscilloscope (~ 60 seconds).

Post-collection data processing occasionally includes subtraction of a sine wave "base-line" that is locked to the speaker frequency but does not change with a change in length of the fixed delay line. A slight change in beam position with motion of the speaker causes this background. Off-normal incidence of the beam on the speaker-mounted corner cube will cause the beam to translate slightly changing the overlap with the translation-stage-

mounted corner cube beam on the sample. This variation in overlap results in a variation of background photocurrent. I used optical autocorrelation in a nonlinear crystal to measure the laser pulse width. The same laser pulse train used for the optoelectronic autocorrelation is diverted to a nonlinear crystal in which pulses overlapping in time undergo $\chi^{(2)}$ mixing. The same type of Michelson interferometer setup shown in Figure 4-6 is used to vary the arrival of the pulses at the crystal, resulting in output pulses with duration equal to the convolved width of the laser pulses. Assuming a sech^2 shape and the resulting deconvolution factor of 0.648, the deconvolved laser pulse width is 100 ps.

Distinguishing between the first-order correlation, or electric field coherence, and the second-order correlation, or intensity autocorrelation, signals is difficult for short carrier lifetimes. Even with the cross-polar power down by $\sim$ 30 dB, the coherence signal can have magnitude comparable to the intensity autocorrelation signal. The intensity correlation signal is proportional to the product of the intensities of the incident optical pulses, while the first-order correlation is proportional to the product of the electric fields of the optical pulses. Therefore, it is tempting to use the power dependence of the pulse height to discriminate between intensity and electric field correlation. However, as noted by Verghese, *et al.* in [92] the coherence peak measured in this type of autocorrelation experiment is proportional to the square of the first-order correlation function. Thus, the electric field coherence signal and the intensity autocorrelation both depend quadratically on the incident optical power. Another technique for detecting coherence is to resolve the individual coherence fringes, which have a period corresponding to the wavelength of the optical radiation. By reducing the speaker throw and oscilloscope sampling window, these fringes can be resolved. Care must be taken, however, that the frequency of these photocurrent fringes is within the passband of the transimpedance amplifier feeding the oscilloscope. Finally, the shape and width of the coherence peak is determined by the optical spectrum. Using an optical spectrum analyzer, the optical spectrum shown in Figure 4-8 is measured and fit to

$$F(\omega) = Ae^{-\frac{(\omega-\omega_0)^2}{2\delta^2}} \ , \tag{4.12}$$

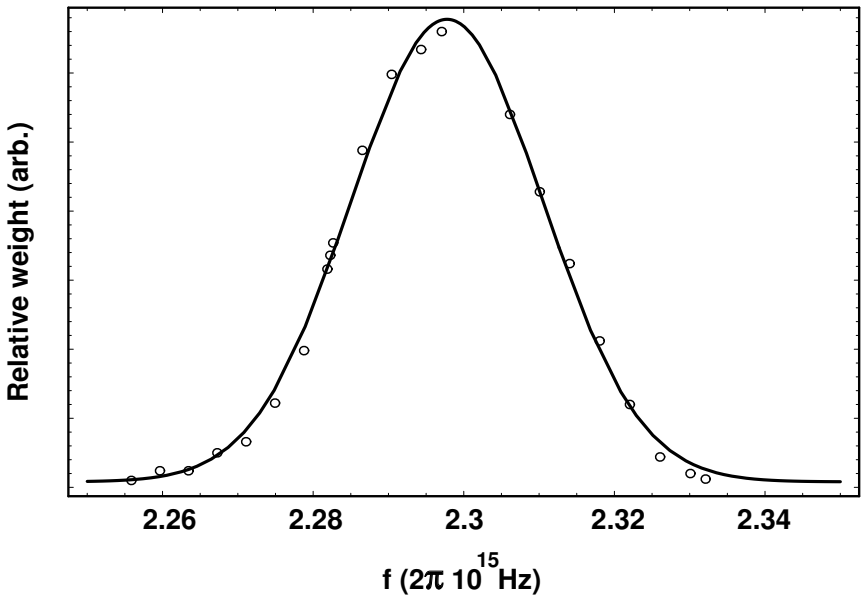

Figure 4-8: Optical spectrum of self-modelocked Ti:sapphire laser with Gaussian lineshape fit.

which corresponds to a first-order correlation function of the form [101]

$$g^{(1)}(\tau) = Be^{-\frac{1}{2}\delta^2\tau^2} \ . \tag{4.13}$$

The extracted coherence peak shape is shown in Figure 4-7 along with the intensity autocorrelation signal in a regime in which the two are easily distinguishable.

Zamdmer, *et al.* demonstrated an increase in carrier lifetime with applied electric field by measuring autocorrelation signals at different applied bias voltages. This effect is significant for the performance of photomixers, because photomixers are often operated at relatively high voltages to increase photocurrent and terahertz power. However, an increase in carrier lifetime with field causes a corresponding decrease in terahertz power as given by equation (4.9).

The mechanism proposed by Zamdmer, *et al.* is Coulomb barrier lowering of deep donor states that act as electron capture sites [56, 102]. As the applied field is increased, the effective capture cross-section is reduced as illustrated in a one-dimensional (1-D) sim-

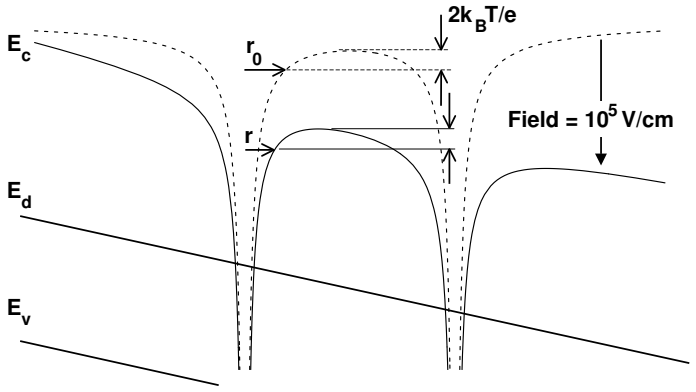

Figure 4-9: One-dimensional illustration showing the effect of applied electric field on the capture cross-section of a Coulomb well. The well to the right models the effect of the nearest neighbor and is a distance z_0 from the donor site in question.

plification in Figure 4-9. The capture radius is defined as the radius, $r = z$, which satisfies

$$V_{\max} - \frac{2k_BT}{e} = \frac{-e}{4\pi\epsilon|z|} - Ez - \frac{e}{4\pi\epsilon|z - z_0|} \ , \tag{4.14}$$

where $V_{\max}$ is the peak voltage between the wells, z_0 is the distance between the wells, and ϵ is the static dielectric constant of the material. Using this 1-D model and a model for electron heating of $T_e = T + \lambda Ee/k_B$, where λ is the optical phonon mean free path, they obtain good agreement with autocorrelation measured carrier lifetime and the dc current-voltage characteristic[2] by using z_0 and λ as fitting parameters. The field-dependent electron lifetime is then given by

$$\tau_e(E) = \tau_e(E=0) \times \left(\frac{T_e}{T}\right)^{1.5} \times \left(\frac{r(E=0)}{r(E)}\right)^3 \ . \tag{4.15}$$

Carrier lifetime values are extracted from autocorrelation measurements performed on distributed photomixer test structures. The data are shown in Figure 4-10 along with a fit using the electric-field-dependent carrier lifetime. The fitting parameters, $z_0 = 6.0\,\text{nm}$, $\lambda = 0.7\,\text{nm}$, and $\tau_e(E=0) = 160\,\text{fs}$ are comparable to those used by Zamdmer, *et al.* These lifetime values are used in Section 4.3.2 in modeling the dc responsivity and in

[2]The current-voltage characteristic of LTG-GaAs devices is discussed in Section 4.3.

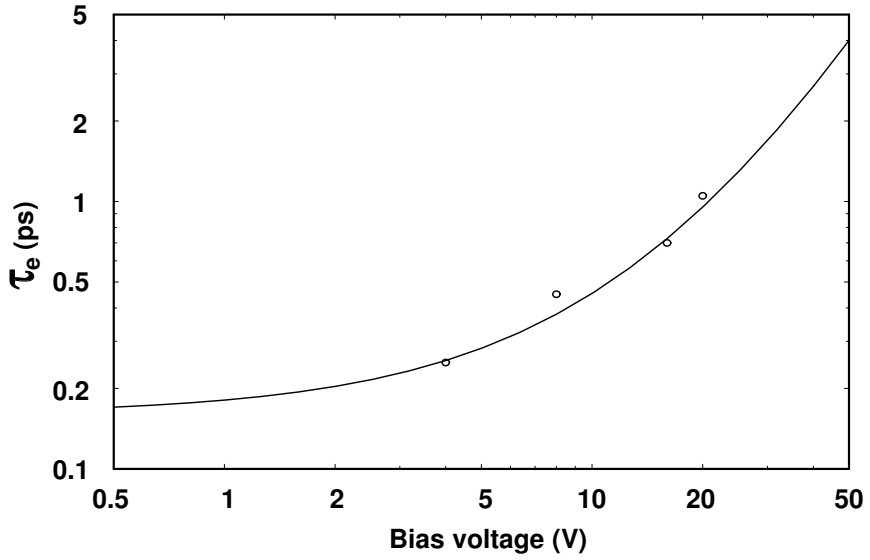

Figure 4-10: Electron lifetime extracted for autocorrelation experiment for a device with $0.8\ \mu$m electrode gap.

Section 5.1 in modeling the distributed photomixer terahertz performance.

4.2 Dielectric Waveguide Characterization

In addition to characterizing the material composing the distributed photomixers, the device structures themselves are characterized. As described in Chapter 2, the dielectric waveguide is a very important component of the distributed photomixer. Dielectric waveguide characterization comprises two steps: verifying that the optical signal can be coupled into the waveguide and measuring the mode extinction length in the waveguide. The mode extinction length, which determines the propagation distance over which the optical signal is absorbed, is a key feature of the dielectric waveguide design discussed in Section 2.1.3. If the extinction length is too short, the optical signal is absorbed in a small distance and the heat load is not effectively distributed. If the extinction length is too long, then the quantum efficiency of the photomixer is lowered because a small fraction of the power is absorbed and transformed to photocurrent. Test structures (discussed in Section 3.1 and shown in Figure 3-4) allow the measurement of the extinction length. A schematic of the extinc-

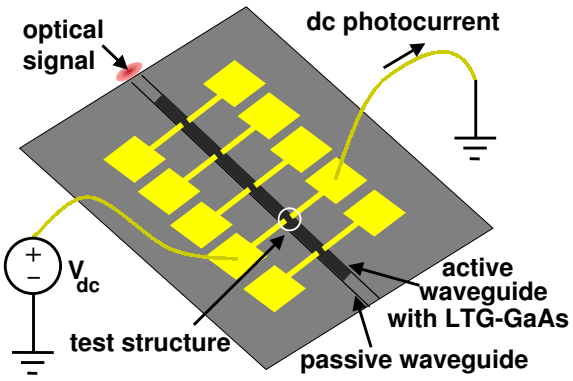

Figure 4-11: Schematic of test structure measurement.

tion length measurement is shown in Figure 4-11. The optical signal is coupled into the waveguide, and the test structures provide bias to the photoconductor at five discrete points along the waveguide. Assuming a linear current-power relationship, the dc photocurrent at each test structure, or tap, is a measurement of the relative optical intensity at that point in the waveguide. Fitting an exponential to these current values yields the extinction length.

4.2.1 Experimental Setup

The experimental apparatus for waveguide measurements is shown in Figure 4-12. Coupling into the waveguide is achieved with a 8 mm focal length lens with a numerical aperture of 0.5. Because of the small size of the waveguide mode ($\sim$ 3 μm^2 as calculated from the mode waists in Section 2.1.3) and focused laser spot, coupling in the waveguide is difficult and highly sensitive to the position and orientation of the photomixer chip. A Newport ULTRAlign three-axis translation stage [98] provides translational positioning, while a rotation stage and two crossed-axis goniometers provide rotational positioning. The goniometers and rotation stage are chosen and positioned such that the center of rotation for all three axes is at the photomixer chip.

The output coupling lens is a 19 mm focal length lens with a numerical aperture of 0.56 (Newport part number KBX043), chosen to collect $>$ 80% of the light exiting the waveguide. The other two lenses in the telescope have 100 mm focal length (NA = 0.126)

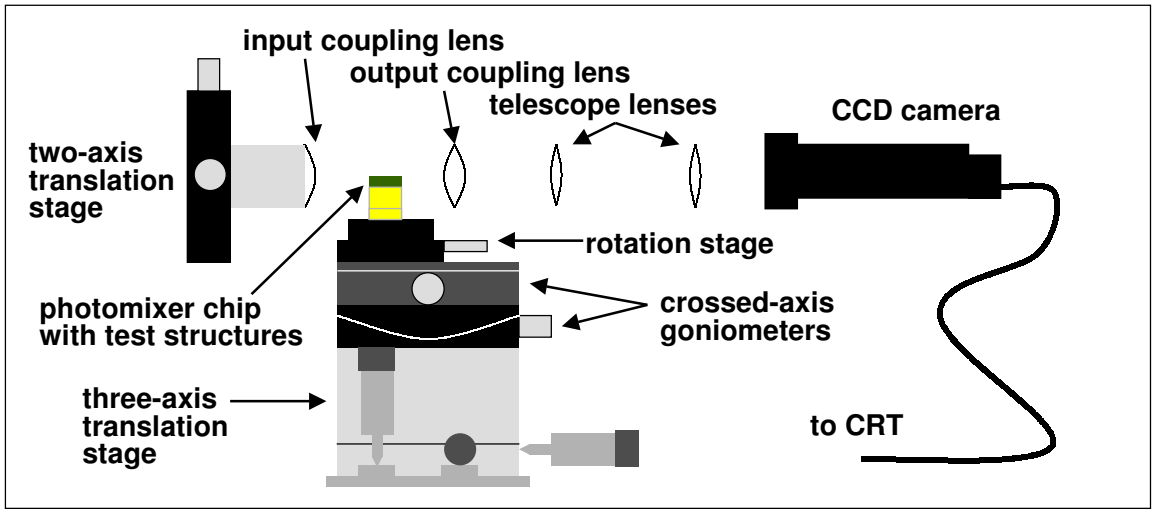

Figure 4-12: Waveguide coupling experimental setup.

and 25.4 mm focal length ($\mathrm{NA} = 0.45$) (Newport part numbers KBX064 and KBX046, respectively) and are placed ~ 130 mm apart, while the 25.4 mm lens is ~ 30 mm from the focal plane of the CCD camera. Gaussian beam analysis of the system indicates a system magnification of ~ 30.

4.2.2 Measurements

The initial challenge of waveguide measurements involves coupling the invisible optical signal into the optical waveguide. Examining the chip and optical beam using an infrared viewer allows for rough positioning of the chip using the translation stage. A glass slide is used to couple white light into the telescope beam path so that the reflection off the back of the chip is seen on the CCD camera. This reflected image and the optical beam imaged on the CCD camera allow for precise positioning. For each measurement, the rotational degrees of freedom are set followed by the translation degrees of freedom. Defined relative to the axis of propagation of the optical signal, the pitch and yaw of the photomixer chip are usually set by eye. The roll is set by observing the spillover optical input on the CCD while translating the chip horizontal to the optical table top. The position of the chip relative to the focus of the input beam is set by translating the chip in the direction of the input lens

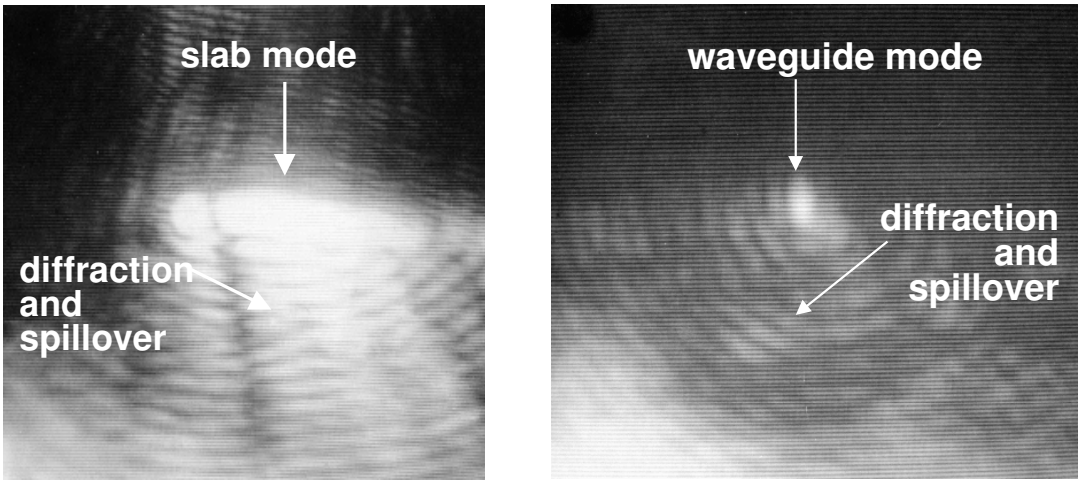

(a) Slab mode photograph.

(b) Waveguide mode photograph.

Figure 4-13: Photographs of a slab mode and waveguide mode from distributed photomixer chips.

while slowly dithering the chip's vertical position. The waist is at the smallest height off the table for which there is a minimum in spillover. When a slab guided mode can be observed, as in Figure 4-13(a), the chip can be translated laterally to find a waveguide mode as shown in Figure 4-13(b)[3].

In order for the test structure extinction length to provide meaningful information, the photocurrent must be linear in absorbed optical power. At low illumination levels, some evidence exists of photovoltaic behavior [3]. Also, no one has ever used an optical waveguide to couple the optical signal to a photomixer, so this measurement verifies that a waveguide-coupled photomixer acts as a photoconductor. Photocurrent as a function of voltage for different input optical power levels is shown in Figure 4-14. The photocurrent is nearly linear over an order of magnitude in incident optical power. Therefore, we conclude that the photocurrent is photoconductive in origin and thus is an accurate measure of the optical intensity at a given point along the optical waveguide. Discussion of the current-voltage characteristic and further examination of the optical power dependence of the photocurrent is contained in Section 4.3.

[3]The horizontal striations in Figure 4-13(b) are a Moiré pattern from the interference between the lines on the CRT that was photographed and the digital sampling in scanning.

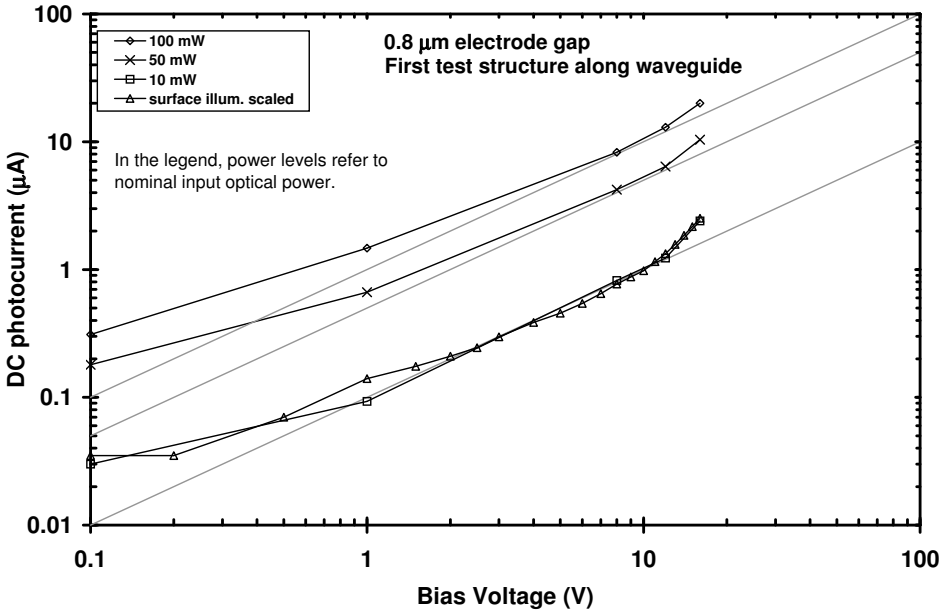

Figure 4-14: IV curve of waveguide-coupled test structure with $0.8\,\mu$m gap at different input optical power levels.

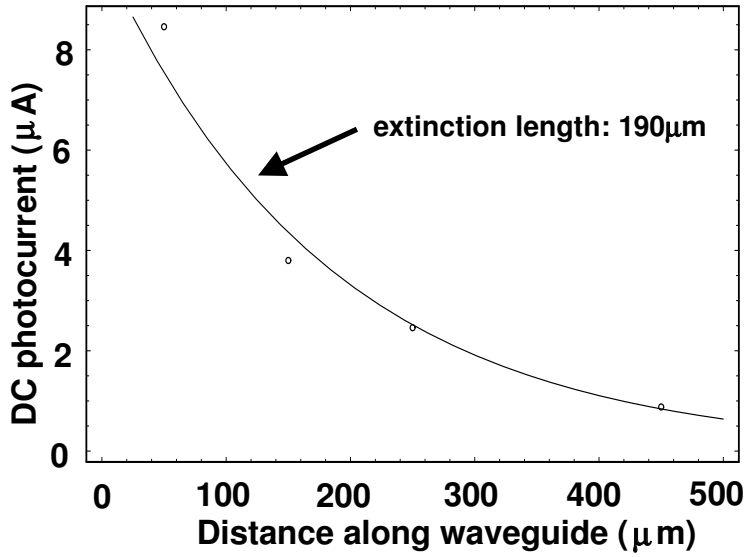

Figure 4-15: Example fit to photocurrent in extinction length measurement.

The data from an extinction length measurement are shown in Figure 4-15. The photocurrent in each test structure is associated with a distance down the waveguide from the beginning of the absorber layer. The nonlinear fit routine in *Mathematica* is used to fit an exponential to the data, and that fit is also shown in Figure 4-15. The extinction length for the devices with a $1000\,$Å LTG-GaAs absorber layer are centered at $240\,\mu$m with a scatter of $\sim \pm 60\,\mu$m for different devices, different bias voltages, and different illumination conditions. The devices from the wafer with a $800\,$Å LTG-GaAs layer exhibit extinction lengths centered at $210\,\mu$m with a variation of $\sim \pm 30\,\mu$m.

The scatter in the fits is likely due to a fabrication variations. For example, slight changes in electrode width change the field in the LTG-GaAs for a given applied voltage. A representative sampling of test structure responsivities for different chips, different test structures on a chip and different measurement conditions of the same test structure is shown in Figure 4-18(b). While any one test structure is linear in power, structure to structure responsivity variations exist. The sensitivity of the fit to variations in the photocurrent values is consistent with this variation in device responsivity.

For the as-fabricated structure with a $1000\,$Å absorber layer and measured $\alpha_{\mathrm{LTG-GaAs}}$, the extinction length is expected to be $\sim 150\,\mu$m, while for the as-fabricated structure with $800\,$Å absorber layer, the length is expected to be $\sim 250\,\mu$m. This value is not quite double the extinction length of the thicker LTG-GaAs structure, because of surface passivation with silicon nitride, SiN. The higher index (than air) of the nitride pulls the mode up into the absorber slightly thereby reducing the extinction length by $\sim 15\%$. Both extinction lengths are longer than the design value, because the measured value of $\alpha_{\mathrm{LTG-GaAs}}$ for the device wafers is different from that assumed during the design.

4.3 Responsivity

The terahertz output power of a photomixer given in equation (1.7) depends quadratically on the photoconductance, G_0. This photoconductance can be thought of in terms of the responsivity, S, of the photomixer as in equation (1.6) or equivalently in terms of the external quantum efficiency, $\eta_e = S\hbar\omega/q$. At $\lambda = 850\,$nm, $\eta_e = 1.459S$. Physically, η_e can be

thought of as a product of the carrier collection efficiency ($\eta_{\rm elec}$) and the photon absorption efficiency ($\eta_{\rm opt}$).

For a photoconductive device, $\eta_{\rm elec}$ is more frequently called the photoconductive gain (g) and for a semiconductor device, is expressed as

$$g = \frac{\tau_e}{t_e} + \frac{\tau_h}{t_h} \tag{4.16}$$

$$= \frac{v_e \tau_e}{l} + \frac{v_h \tau_h}{l} \ , \tag{4.17}$$

where τ is the carrier lifetime, t is the transit time, v is the velocity, l is the path length, and the subscripts e and h refer to electrons and holes, respectively. From equation (4.16), a photoconductor with a carrier lifetime longer than the transit time can exhibit photoconductive gain, in which a single photo-generated carrier can induce multiple carriers in the external circuit. For LTG-GaAs the carrier lifetime is so short that even for submicron electrode gaps $g \ll 1$. In the most general terms, $\eta_{\rm opt}$ and g are both position dependent within the photoconductor so the expression for S should be an integral over the photoconductor volume

$$S = \frac{q}{\hbar\omega}\frac{T}{A}\int_V \alpha e^{-\alpha z} g \, {\rm d}v \ . \tag{4.18}$$

As discussed in Section 4.3.2, the terms in g given in equation (4.17) are electric field dependent, so inasmuch as the field varies with depth, carriers created at different locations within the active area have different contributions to the responsivity. For my photomixer structure, I treat g as constant over the volume of the device, because the LTG-GaAs layer is so thin. The field does not drop much by the bottom of the active volume, unlike in lumped-element photomixers. This high level of electric field throughout the active volume means that the carrier collection efficiency is higher on average than it is for devices with thicker LTG-GaAs layers.

The photon absorption efficiency simply quantifies the fraction of the incident photons which produce photogenerated carriers. For lumped-element photomixers and for my responsivity measurements, the active area is surface-illuminated; therefore, $\eta_{\rm opt}$ includes reflection at the dielectric interface, shadowing/diffraction from metal electrodes, and bulk

absorption of the optical signal that enters the photoconductor. For a material characterized by a bulk absorption coefficient α and for an optical signal propagating in the z direction, the amount of power absorbed in an incremental δz is

$$I\,\mathrm{d}A\alpha\,\delta z = I\alpha\,\mathrm{d}V = I_0 e^{-\alpha z}\alpha \mathrm{d}V\ ,$$

where I is the optical intensity *at* z and I_0 is the initial ($z = 0$) intensity. If all transmission effects are lumped into T, the expression for η_{opt} becomes

$$\eta_{\mathrm{opt}} = T\frac{\alpha I_0 e^{-\alpha z}}{P_0} = T\frac{\alpha e^{-\alpha z}}{A}\ , \tag{4.19}$$

where P_0 is the incident power and A is the detector active area.

The bulk absorption coefficient of LTG-GaAs was measured in Section 4.1.1, but the missing piece of η_{opt} is T, the coupling of the optical signal into the LTG-GaAs for the case of surface illumination. Calculating T requires modeling of the interaction of the incident field with the interdigitated electrodes that are part of the test structure and form a grating on the surface of the wafer. Marcuvitz [103] proposed treating gratings in free space as lumped circuit elements with transmission lines on either side with $Z_0 = \sqrt{\mu_0/\epsilon_0}$. If the electric field is perpendicular to the thin grating strips, the grid is modeled as a shunt capacitances because the stored energy is electric. For a parallel electric field, the effect of stored magnetic energy is modeled as an inductance. Gratings which are thick compared to the wavelength are modeled as T or π combinations of inductors and capacitors.

Blanco, *et al.* treat thick gratings near resonance with a circuit model by introducing a dissipative component to the impedance of the lumped elements representing the grid [104]. The power dissipation models power converted from the zero-order mode to higher order modes beginning at the first Wood's anomaly, which occurs at $\frac{\lambda}{p} = 1$ in free space, where p is the period of the grating.[4] The treatment is verified by comparison to measurement and to full-wave analysis [105]. For my structure, however, the grating behavior is affected by a substrate [106, 107]. The capacitive part impedance is modified by

[4]The regime $\lambda < p$ is typically called the non-diffraction regime, though that term is somewhat misleading since even the zero-order mode is a diffracted mode [105].

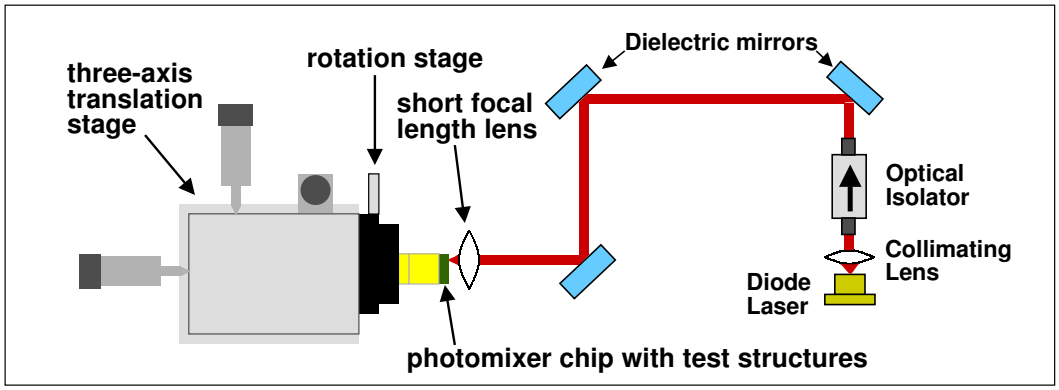

Figure 4-16: Experimental setup for responsivity measurement.

the average dielectric constant (i.e. $1/2\,(n_1^2 + n_2^2)$) as in quasi-static analysis. The inductive component of the grating reactance is not affected by the presence of the substrate, because the stored energy is magnetic and thus not affected by the dielectric constant. We make these enhancements to the model of Blanco and derive an expression for reflection. We present them in Appendix C along with an alternate expression for transmission which is algebraically equivalent to that used by Blanco, *et al.* but involves an order of magnitude fewer terms.

4.3.1 Experimental Setup

A schematic of the responsivity experimental apparatus is shown in Figure 4-16. The setup is a combination of the laser system used for the transmission/reflection measurement and the chip mounting and positioning system used for the autocorrelation measurement. The important feature of the apparatus is that the optical signal is coupled in a known manner into the test structure area. For the input beam diameter of 3 mm, the 0.5-NA input coupling lens focuses the beam to a diameter of $2.8\ \mu$m, which fills the $3\ \mu\text{m} \times 3.2\ \mu$m test structure active area. The sensitivity of the photocurrent to chip position is consistent with this calculation.

4.3.2 Voltage Dependence

While a number of mechanisms (space-charge effects, avalanche, etc.) have been proposed [108] to explain the super-linear current-voltage characteristic of LTG-GaAs at high fields, Zamdmer, *et al.* convincingly demonstrated that electron lifetime increase is the most plausible explanation [56, 109]. Because the capture sites for holes (filled donor states) are neutral and thus not associated with Coulombic potentials, their lifetime does not increase in the same field-dependent manner described in Section 4.1.2 that τ_e does. With this model, the current in an LTG-GaAs photoconductor under a given electric field, E, and illumination power, P, is given

$$i_{pc}(P,E) = T\frac{P}{V_{\text{act}}}\frac{q}{\hbar\omega}(\tau_e(E)v_e(E) + \tau_h\mu_h E)wd \ , \tag{4.20}$$

where P is the optical power incident on the photomixer, V_{act} is the volume of the active area, ω is the radial frequency of the optical signal, $\tau_e(E)$ and $v_e(E)$ are respectively the field-dependent electron lifetime and velocity, τ_h and μ_h are the hole lifetime and mobility, w is the width of the device[5] and d is the depth of the absorber. Electron velocity saturation is modeled as

$$v_e(E) = \frac{v_{\text{sat,e}}}{1 + \frac{v_{\text{sat,e}}}{\mu_e E}} \ . \tag{4.21}$$

The field-dependent electron lifetime is as described in Section 4.1.2.

Sublinear behavior at low fields is attributed to velocity saturation of the electrons. The hole mobility ($\sim 5\,\text{cm}^2/Vs$) in LTG-GaAs is so much lower than that for electrons ($\sim 200\,\text{cm}^2/Vs$) that they do not contribute appreciably to the current [109].

Using this grating model for coupling of the optical signal into the LTG-GaAs, we calculate η_{opt}. Using equation (4.20), the current is calculated for four different cases: uncoated test structure with $0.8\,\mu$m gap between the interdigitated electrodes, uncoated test structure with $0.4\,\mu$m gap, and versions of both with a $2500\,$Å silicon nitride passivation coating. The close match between prediction and model for three of the four cases suggests

[5]For my device with interdigitated electrodes, the width is more easily thought of as the length of the meander gap.

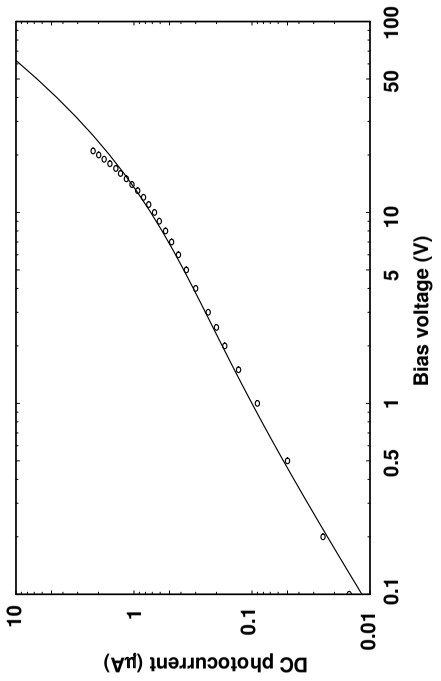

(a) 0.8 μm electrode gap.

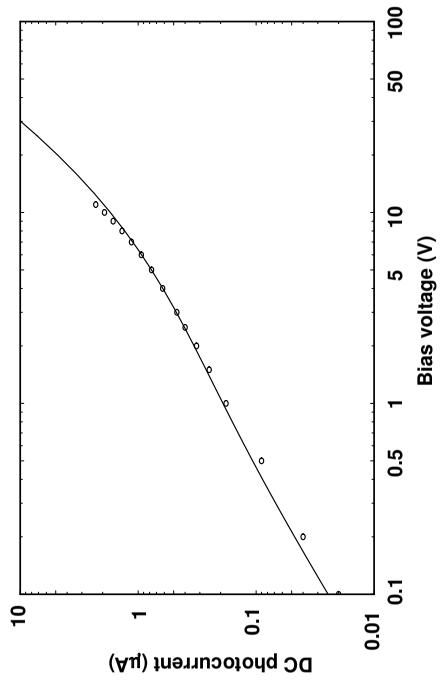

(b) 0.4 μm electrode gap.

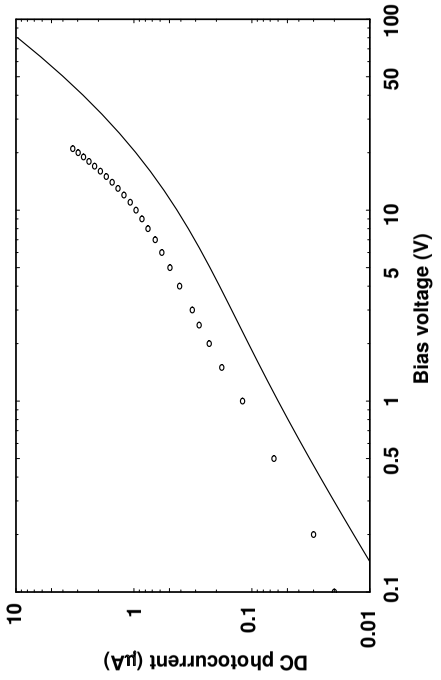

(c) 0.8 μm electrode gap. SiN coating.

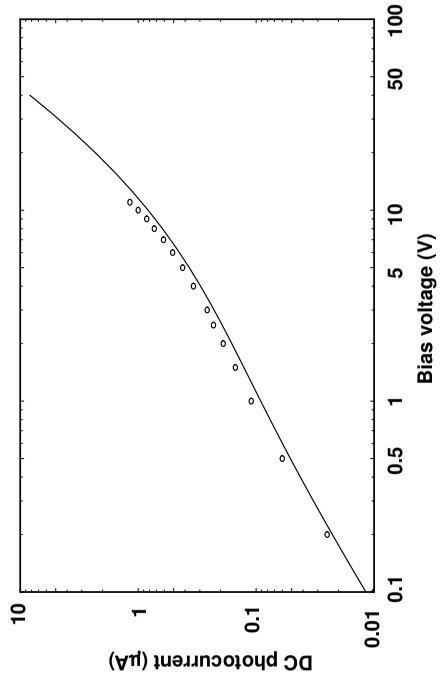

(d) 0.4 μm electrode gap. SiN coating.

Figure 4-17: Surface-illuminated test structure current-voltage characteristics. Solid lines are model and circles are data.

that not only is the current model correct, but the grating coupling calculation is accurate as well. The values for mobility and lifetime are comparable to those used by Zamdmer, *et al.* : $v_{\mathrm{sat,e}} = 5.0 \times 10^6\,\mathrm{cm/s}$, $\mu_e = 200\,\mathrm{cm^2/Vs}$, $\mu_h = 10 cm^2/\mathrm{Vs}$, $\tau_e(0) = 160\,\mathrm{fs}$, and $\tau_h = 700\,\mathrm{fs}$. With these same models, absolute responsivities are calculated for the test structures as shown in Figure 4-18 and compared with the prediction of the model described in Section 4.3. The absolute value of responsivity agrees well with the work of Jackson [57] and Brown [58]. The higher responsivity of the coated $0.8\,\mu$m-gap device is consistent with Figure 4-17(c) and almost certainly indicates an improperly predicted value of T. This discrepancy is to be expected because the coating is not modeled rigorously, as explained in Appendix C. This approximation of treating it as a modification to the effective dielectric constant is more valid for the $0.4\,\mu$m-gap devices where the fields are confined more to the area of the electrodes. Thus, we have verified that the responsivity model can be used in calculating the photoconductance G_0 according to equation (1.6) and then the terahertz power according to the traveling-wave analog of equation (1.7).

4.3.3 Optical Power Dependence

LTG-GaAs has been observed to be a photoconductor in previous work, so linearity in optical power is expected. Also, in these distributed photomixer devices, linearity in optical power was demonstrated in waveguide-coupled test structures in Section 4.2. For the sake of completeness, the linearity of photocurrent with optical power (a constant responsivity) is verified for surface illumination and the results presented in Figure 4-19. The measurement conditions including alignment were the same for each power level. The optical power was measured at the same place in the beam path.

The slight nonlinearity ($\sim 25\%$ over more than an order of magnitude in optical power) is attributed to the existence of a small number of long-lived states [3]. At low absorbed powers, however, electrons with long τ_e can measurably affect the current even if there are relatively few states, because the $v_e\tau_e$ product will be so large. At high illumination levels, however, the behavior of the LTG-GaAs photoconductor is dominated by electrons with short lifetime, because so many more of these states are excited.

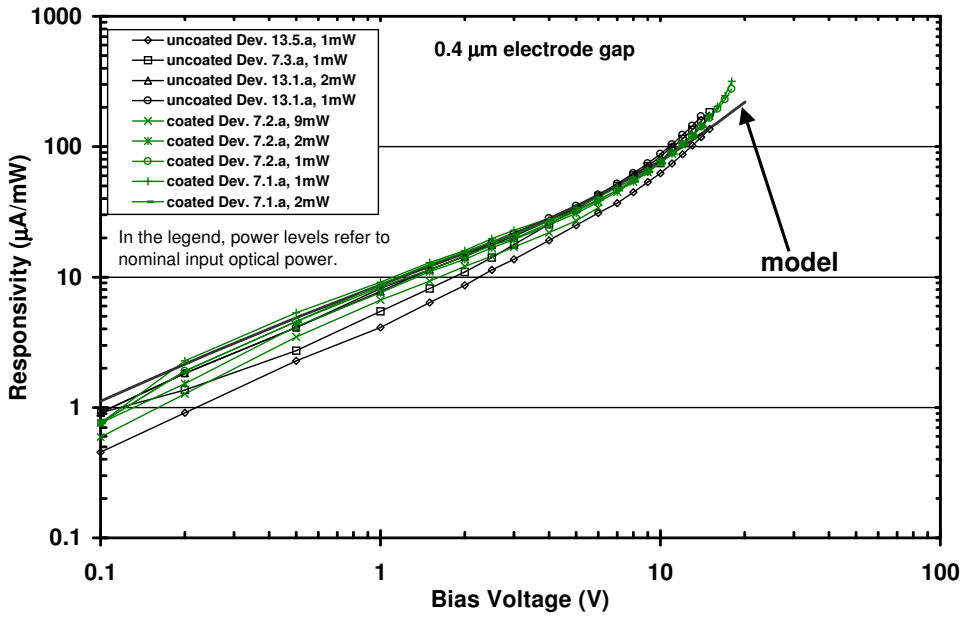

(a) Responsivity of $0.4\,\mu$m gap test structure with E field perpendicular to the electrodes.

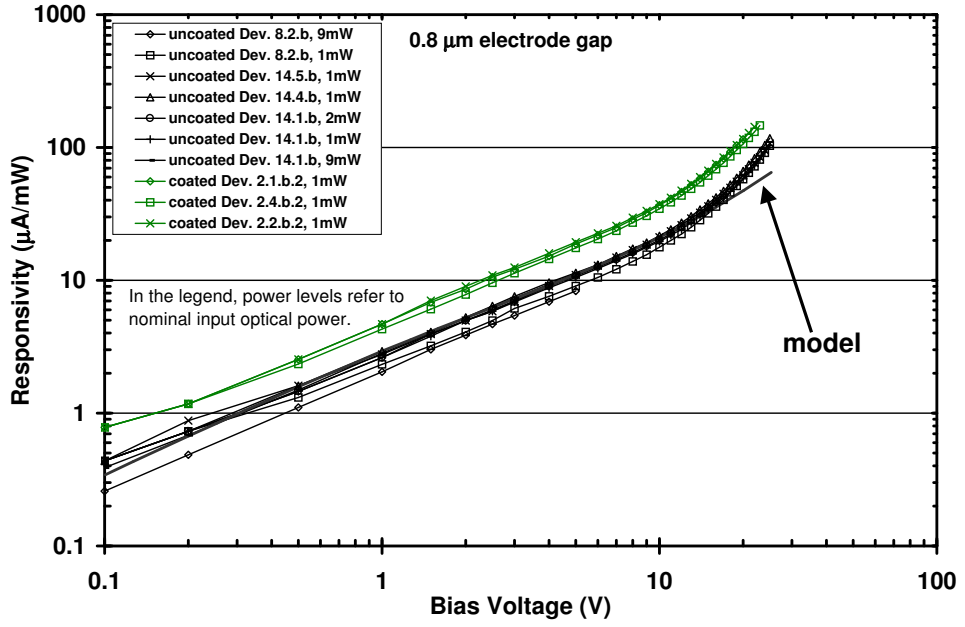

(b) Responsivity of $0.8\,\mu$m gap test structure with E field perpendicular to the electrodes.

Figure 4-18: Responsivity of test structures for E field perpendicular to the interdigitated electrodes.

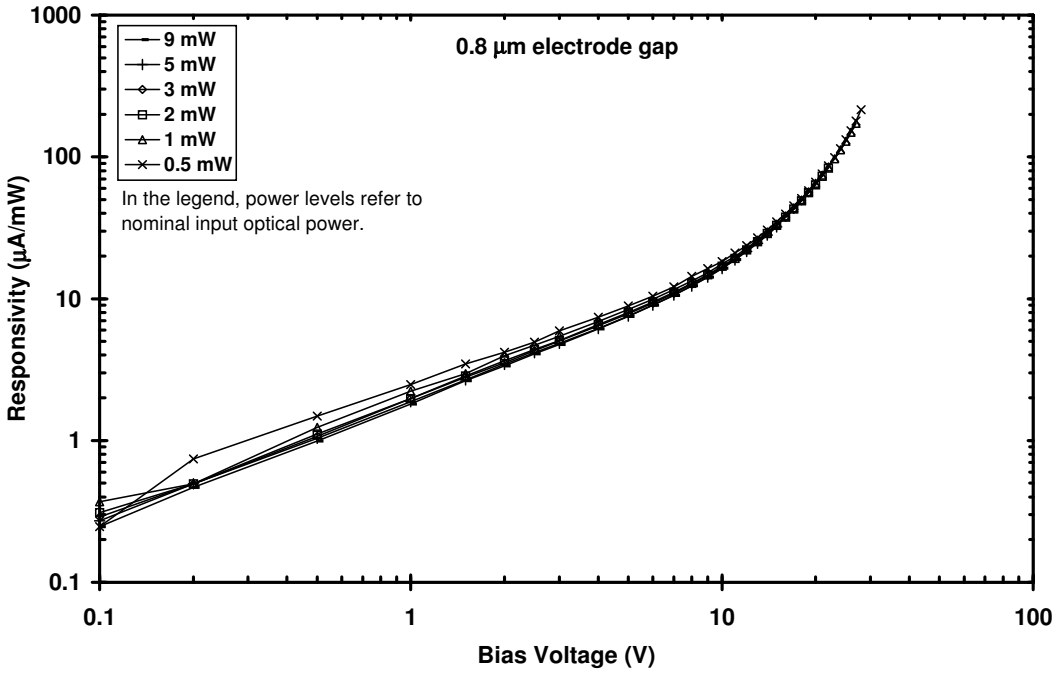

Figure 4-19: IV curves for a surface-illuminated test structure for different incident power levels.

4.3.4 Polarization Dependence

In measuring the device responsivity, I varied the polarization of the electric field of the incident optical field. The photocurrent varied with polarization of the optical field. Part of this variation is understood as polarization-dependent coupling through the grating as discussed in Section 4.3.2 and Appendix C. However, as demonstrated in Section 4.3.3, the photocurrent is linear in absorbed power. Therefore, even if the grating calculations did not predict the correct absorbed power and lead to a discrepancy in responsivity between two nominally identical designs, the offset should be constant with voltage as in Figure 4-18(b). Plotting the ratio of the responsivity for optical field perpendicular and parallel to the electrodes (grating) reveals the voltage dependence shown in Figure 4-20.

The most plausible explanation for this voltage dependence is that carriers are not generated uniformly across the electrode gap. This non-uniform carrier generation leads to a voltage dependent responsivity, because the assumption that the electric field and therefore the carrier velocity are constant across the width of the electrode gap is an oversimplifica-

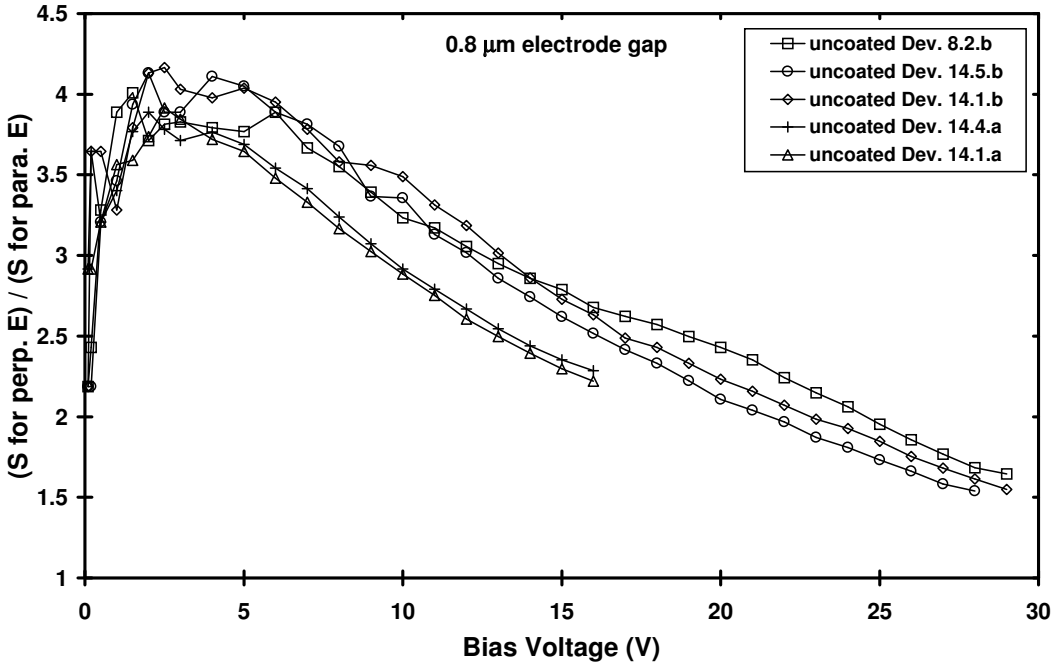

Figure 4-20: Responsivity ratio for a $0.8\,\mu$m-gap test structure.

tion [57, 58]. The electric field is higher near the electrodes, so the carriers created near the electrodes contribute more to the current than carriers created midway between the electrodes [57]. There are two physical reasons for the field nonuniformity. The first and simplest reason is that the interdigitated electrodes do not form a parallel plate configuration. Therefore, the field is higher near the edge of the electrode. The second reason for this field non-uniformity is that LTG-GaAs is a highly compensated material and thus much of the field drops at the contacts due to screening by charged trap sites. As the applied field increases, the high field region near the electrodes grows toward the opposite electrode.

Photo-excited carriers will be generated where there is incident optical power. Therefore, because the optical field has to obey boundary conditions at the metal electrodes, the power density profile at the LTG-GaAs surface will be different depending on the orientation of the optical electric field relative to the electrodes. In a simple approximation, the interaction can be modeled as a parallel plate waveguide as shown in Figure 4-21. The power in a parallel plate waveguide is $\propto \cos \frac{n\pi y}{d}^2$ for a TM mode with n = 0 being the TEM case and for a TE mode, the power is $\propto \sin \frac{n\pi y}{d}^2$. While this model is an oversimplification,

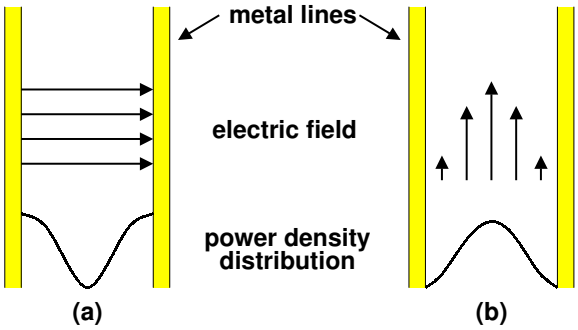

Figure 4-21: Depiction of electric field and power distribution between parallel plates.

it is illustrative of the situation and consistent with the observations. For the electric field parallel to the electrodes (TE mode), the photo-excited carriers have the highest density midway between the electrodes where the electric field is weakest. Thus, higher voltages are needed to reach the same responsivity as for a perpendicular electric field (TM mode) for which the carrier are created preferentially where the field is high. This explanation is consistent with the fact that the responsivity ratio of the test structures with $0.4\,\mu$m gap varies little with applied bias.

Many of the photomixer's material and device characteristics have been independently measured and analyzed. The LTG-GaAs absorption coefficient was a factor of two lower than was assumed in the design process but is within the range of previously reported values. The other material characteristics are also consistent with previous photomixer work. The mode extinction length is measured to be slightly longer than predicted by this measured value of $\alpha_{\mathrm{LTG-GaAs}}$, and the difference is attributed to fabrication tolerances. The dc responsivity of the structures is consistent with the relatively new theory of Zamdmer, *et al.* In Chapter 5, I use the device and material measurements and analysis from this chapter to formulate a predictive model for the distributed photomixer's performance.

Chapter 5

Photomixing Performance

This chapter contains a detailed model for distributed photomixer terahertz performance as well as measurements which characterize the terahertz operation of these photomixers. By combining the results of the measurements and analyses in Chapter 4 into an equivalent circuit model and accounting for sources of loss and coupling efficiencies, the distributed photomixer's terahertz performance is quantitatively predicted. I describe the design and analysis of an experimental apparatus for photomixing measurements. Measurements of the output power of the photomixers as a function of frequency, optical illumination and applied bias voltage are compared to theory. In the final section, I consider the distributed photomixer's performance in light of other photomixers and delineate the technical challenges that would need to be overcome to produce higher power from this type of device.

5.1 Performance Estimation

Terahertz power generation in the distributed photomixer's active area is modeled in a SPICE circuit. The predictions of the circuit model are modified using estimations of loss mechanisms and coupling efficiencies.

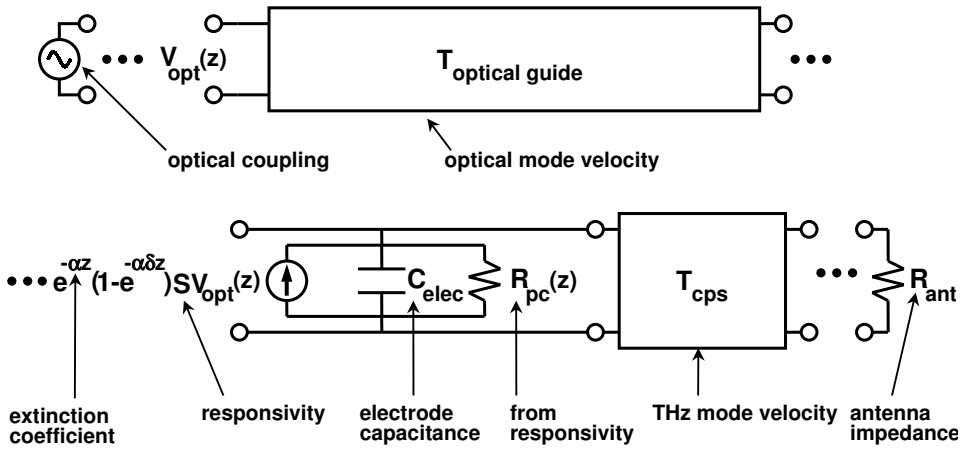

Figure 5-1: One segment of a SPICE circuit model for the distributed photomixer. The upper section is the optical guide model. The lower section is the THz CPS model.

5.1.1 Distributed Photomixer Circuit Model

In Chapter 1, I presented an equivalent circuit model for a distributed photomixer in Figure 1-4. The measurements of Chapter 4 allow the elements of that general model to be quantified. A SPICE circuit model is created in which the optical and terahertz waveguides are represented in a discretized manner. Each segment in the discrete circuit represents an incremental distance along the distributed photomixer active area. Figure 5-1 shows a segment in this model along with the measurement and analysis that enables the prediction of a given circuit element. The optical waveguide is modeled by a lossless transmission line where the voltage on the line corresponds to the optical power in the dielectric waveguide. Each segment of the terahertz guide consists of: a transmission line segment to model the coplanar strips (CPS), a lumped capacitor to model the interdigitated electrodes, a resistor to model resistive losses in the photoconductor, and a voltage-dependent current source to model the current generated by the biased LTG-GaAs photoconductor. The current source depends on the voltage at the corresponding segment on the model of the optical guide. Therefore, the current source couples the two waveguides in the circuit model as the LTG-GaAs layer couples the waveguides in the device.

In each segment of the circuit model, the transmission line for the optical waveguide is longer than the transmission line for the CPS to account for the higher velocity of the

THz wave on an unloaded CPS. The ratio of the lengths is the inverse of the ratio of the velocities, where $v_{\rm opt} = c/3.43$ and $v_{\rm THz} = c/2.64$. The slowing of the terahertz wave by the interdigitated electrodes is modeled in the capacitance, $C_{\rm elec}$, where the value is computed as in Section 2.2.3 for a given electrode geometry. These two transmission lines and the lumped capacitance together predict the quality of velocity match between the optical wave and the terahertz wave and determine the efficiency of power transfer from the optical to the terahertz.

The generation of the terahertz current wave is governed by the dependent current source. The responsivity for a given electrode geometry measured in Section 4.3 is multiplied by the optical power absorbed in the segment. The power in the $N^{\rm th}$ segment of the optical guide is $e^{-\alpha z}V_{\rm opt}(z)$, where $\alpha = \ell_{\rm ext}^{-1}$, $\ell_{\rm ext}$ is the measured extinction length, z is the position of the segment along the active guide given by $(N-1)\delta z$, and δz is the incremental length of one segment. The fraction of that power absorbed in the segment is $\left(1 - e^{-\alpha \delta z}\right)$. The shunt resistor $R_{\rm pc}$ models ohmic loss in the on-state of the LTG-GaAs layer.

A number of loss mechanisms and practical power coupling issues are not included in this model and are considered in the next section.

5.1.2 Loss and Coupling Efficiencies

The intrinsic loss mechanisms associated with distributed photomixer's active area are: conductor loss in the CPS, radiation loss of the propagating terahertz wave, and dielectric loss in the substrate. The coupling efficiencies I take into account are coupling of the optical signal into the dielectric waveguide and coupling of the terahertz signal off chip.

The most significant loss associated with the distributed photomixer active area is ohmic loss in the metal coplanar strips. Gupta, *et al.* provide expressions for conductor loss in CPS [77]. The most accurate closed form expression for conductor loss is given in dB per unit length by

$$\alpha_c^{\rm cps} = \frac{8.68 R_s \sqrt{\epsilon_{\rm re}}}{480\pi K(k_1)K'(k_1)\left(1-k_1^2\right)} \times$$

$$\left[\frac{1}{a}\left(\pi+\ln\frac{8\pi a(1-k_1)}{t(1+k_1)}\right)+\frac{1}{b}\left(\pi+\ln\frac{8\pi b(1-k_1)}{t(1+k_1)}\right)\right] , \qquad (5.1)$$

where R_s is the surface resistivity, a and b are defined as in Figure 2-10, k_1 is given in equation (2.16), $\epsilon_{\rm re}$ is the effective relative dielectric constant given in equation (2.15), t is the thickness of the CPS, and $K()$ and $K'()$ are the complete and complementary complete elliptic integrals of the first kind, respectively [77]. The surface resistivity due to the normal skin effect is given by

$$R_s = \frac{1}{\sigma\delta} = \sqrt{\frac{\omega\mu}{2\sigma}} , \qquad (5.2)$$

where δ is the skin depth, σ is the material's electrical conductivity, $\omega = 2\pi f$ is the radial frequency of the radiation, and μ is the material's permeability [110]. The CPS in my distributed photomixer structures are 1500–2000 Å thick, consisting of 400 Å of titanium (Ti) and the remainder of the thickness gold (Au). An effective conductivity is estimated by $\sigma_{\rm eff} = (f_{\rm Au})\sigma_{\rm Au} + (1 - f_{\rm Au})\sigma_{\rm Ti}$, where $f_{\rm Au}$ is the fraction of the CPS thickness that is Au, $\sigma_{\rm Au}$ is the conductivity of Au, $4.5 \times 10^7(\Omega m)^{-1}$, and $\sigma_{\rm Ti}$ is the conductivity of titanium, $2.4 \times 10^6(\Omega m)^{-1}$. The calculation with a linear combination of conductivities predicts a conductor loss of $10.2\sqrt{f}$ dB/mm, where f is in THz, which is very close to the $8.8\sqrt{f}$ dB/mm for the same structure made entirely of Au. However, if the current crowds along the bottom of the CPS [111], the loss would be higher.

The radiation loss of the CPS with and without interdigitated electrodes was calculated in Section 2.2.3. As shown in Figure 2-18, the radiation loss for either type of structure is approximately $0.13f^3$ dB/mm, where f is in THz.

The final source of loss in the active area is absorption of the terahertz wave in the dielectric waveguide. In the parlance of the microwave engineer, this effect is related to the loss tangent of the dielectric, while for the optical engineer, it's simply the bulk absorption coefficient. Reported loss values for semi-insulating GaAs in the frequency range of interest are 4.5–5 $\rm cm^{-1}$ at 3 THz, 2.4–2.7 $\rm cm^{-1}$ at 2 THz, and 0.5–1.5 $\rm cm^{-1}$ at 1 THz [61, 112, 113]. Absorption values in undoped $\rm Al_xGa_{1-x}As$ compounds are available down to 3 THz. While the loss in AlAs is lower than that in GaAs at 3 THz, the loss in $\rm Al_{0.18}Ga_{0.82}As$ and $\rm Al_{0.36}Ga_{0.64}As$ (the closest compositions to my layers for which data

are available) are significantly higher, 24 cm^{-1} and 30 cm^{-1}, respectively [114]. In the absence of data below 3 THz, I make the reasonable assumption that these coefficients have similar variation with decreasing frequency. Exact calculation of the absorption involves integration of the half of the THz field in the dielectric waveguide and substrate over the GaAs and $\text{Al}_x\text{Ga}_{1-x}\text{As}$ layers. The uncertainty in absorption coefficients does not warrant this sort of calculation, so the fraction of the mode in each layer is estimated. For CPS with a gap $s \ll \lambda$, the fields extend a distance from the strips approximately equal to s [77]. Thus, I estimate the dielectric loss as a linear combination of the losses for the $\text{Al}_x\text{Ga}_{1-x}\text{As}$ layers with a quarter of the mode in $\text{Al}_{0.20}\text{Ga}_{0.80}\text{As}$ and the rest in $\text{Al}_{0.35}\text{Ga}_{0.65}\text{As}$. These assumptions lead to a dielectric loss that varies from $6\,\text{cm}^{-1} = 2.6\,\text{dB/ mm}$ at 1 THz to $28\,\text{cm}^{-1} = 12\,\text{dB/ mm}$ at 3 THz.

Calculating the coupling efficiency of the optical signal involves calculating the fraction of the free-space input optical signal that is coupled into the active area of the device. I estimate the coupling efficiency of the free-space signal into the passive dielectric waveguide facet and of the passive waveguide mode to the active waveguide mode. Coupling into the facet is calculated as $T_{\text{facet}} = T_{\text{mode}} T_{\text{dielec}}$, where T_{mode} is the power coupling due to overlap of the free-space optical mode and the waveguide mode, and T_{dielec} is the transmission of a plane wave into a dielectric. Because the waveguide mode and optical signal are both Gaussian to a very good approximation, the total overlap can be performed as the product of two one-dimensional integrals, i.e. ,

$$T_{\text{mode}} = \frac{\left|\int_{-\infty}^{\infty} E_{fs}(x) E_{wg}^{*}(x)\,\mathrm{d}x\right|^2}{\left|\int_{-\infty}^{\infty} E_{fs}(x)\,\mathrm{d}x\right|^2 \left|\int_{-\infty}^{\infty} E_{wg}(x)\,\mathrm{d}x\right|^2} \cdot \frac{\left|\int_{-\infty}^{\infty} E_{fs}(z) E_{wg}^{*}(z)\,\mathrm{d}z\right|^2}{\left|\int_{-\infty}^{\infty} E_{fs}(z)\,\mathrm{d}z\right|^2 \left|\int_{-\infty}^{\infty} E_{wg}(z)\,\mathrm{d}z\right|^2}\ , \quad (5.3)$$

where fs and wg denote the free-space and waveguide modes, respectively. The component of the electric field used in the integration depends on the polarization of the incident field and the type of waveguide mode. For the TE modes used in my structures and appropriate linear polarization of the incident field, this corresponds to the $\hat{x}$ component, in the formalism of Appendix A. Considering the total transmission as a product of the mode overlap and dielectric transmission of a plane wave is an approximation, but it gives accurate results [115]. For typical test conditions (a 3-mm-width collimated laser spot focused

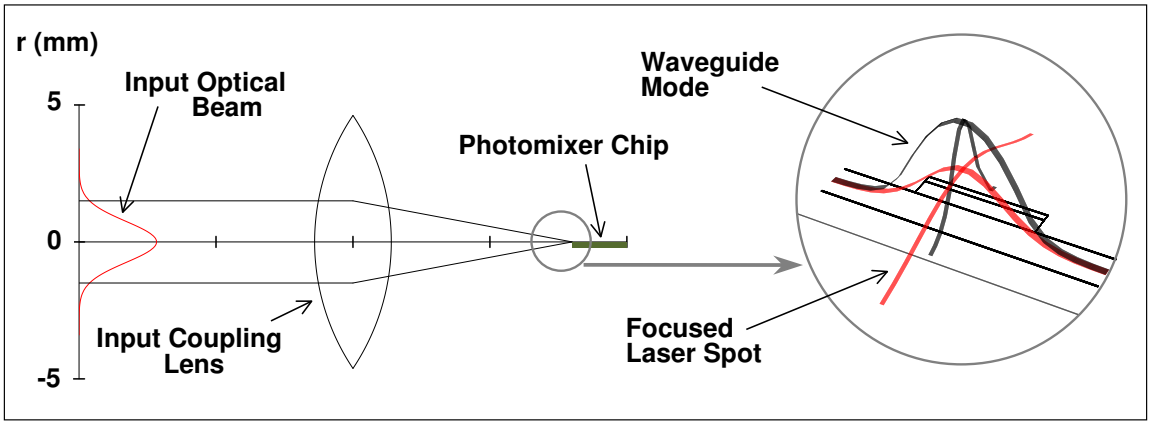

Figure 5-2: Illustration of coupling the optical signal into the distributed photomixer dielectric waveguide.

by a 0.5-NA lens), the overlap with a waveguide mode in one of my distributed structures is 0.5. This case is illustrated in Figure 5-2, where the calculated x and z slices of the two modes are shown in the inset, superimposed on the dielectric waveguide structure. T_{dielec} is given by the well-known formula

$$T_{\text{dielec}} = 1 - \left(\frac{n_2 - 1}{n_2 + 1}\right)^2 \tag{5.4}$$

where n_2 is the index of refraction of the dielectric. For my structures, $n_2 = 3.43$ which yields $T_{\text{dielec}} = 0.7$. Propagation of the optical signal from the facet to the active portion of the device is assumed to be lossless since the photon energy is far below the bandgap of any of the $\text{Al}_x\text{Ga}_{1-x}\text{As}$ layers and the mode is tightly confined enough to be isolated from the substrate. The step in strip height from the passive to active guide caused by the presence of the LTG-GaAs layer results in a very small loss of optical power due to reflection and conversion to higher order modes. The mode overlap between the passive and active guides results in greater than 95% power transfer for all the designs. Thus, the total optical coupling efficiency is approximately 0.33.

Finally, the coupling efficiency of terahertz power off-chip involves both loss mechanisms and quasioptical coupling efficiency. One of the primary means of coupling power off-chip at millimeter and terahertz (submillimeter) frequencies is through the use of a pla-

nar antenna and dielectric lens attached the the substrate [78, 116]. By using a low-loss dielectric with index close to that of the substrate, much of the terahertz power can be coupled into free-space. Silicon is the typical dielectric lens material of choice for GaAs-based devices. The radiation pattern for an antenna on a hemisphere is the same as for an antenna on a dielectric half space. As the hemisphere is extended to the synthesized ellipse position (moving the antenna back from the hemisphere plane), the lens narrows the pattern. Thus, the radiation pattern can be matched to a collimated or diverging beam through appropriate choice of extension length [117]. My specific lens design is discussed in more detailed in Section 5.2.1. For the purposes of this section, I consider four sources of loss in the planar antenna and silicon lens system: backside loss, absorption loss in the Si, reflection loss, and Gaussicity [118]. Planar antennas on a dielectric radiate more power into the substrate than into the air [78]. For the $\epsilon_{\mathrm{r}} \sim 12$ appropriate for the GaAs substrate and Si lens, this effect results in 90% of the power being radiated into the lens, and only 10% backside loss [118]. For float-zone high-resistivity silicon, absorption loss is measured to be 0.20 dB/mm from approximately 0.5 to 2 THz [112], which results in 0.8 dB loss for the 4 mm lens designed in Section 5.2.1. Calculated using equation (5.4), transmission through the Si-air interface is 0.67. Gaussicity quantifies how well the antenna pattern couples to a Gaussian beam at the aperture of the lens. For my lens design, a Gaussicity of 0.9 is predicted for a variety of planar antenna designs [117]. The performance of the specific antennas I used will be discussed in Section 5.2.2 as will the coupling of this Gaussian beam into a detector. The total quasioptical coupling efficiency to the exit aperture of the dielectric lens is 0.46.

5.1.3 Performance Prediction

Using the SPICE model of Section 5.1.1 and the loss calculations of Section 5.1.2, the terahertz power at the aperture of the dielectric lens is predicted. The two distributed photomixer structures modeled are: the structure for which the interdigitated electrodes should add an amount of distributed capacitance sufficient to match the terahertz and optical velocities (0.8-μm gap), and the structure for which the electrodes should add slightly more capacitance (0.4-μm gap) making the THz wave slower than the optical. For typical mea-

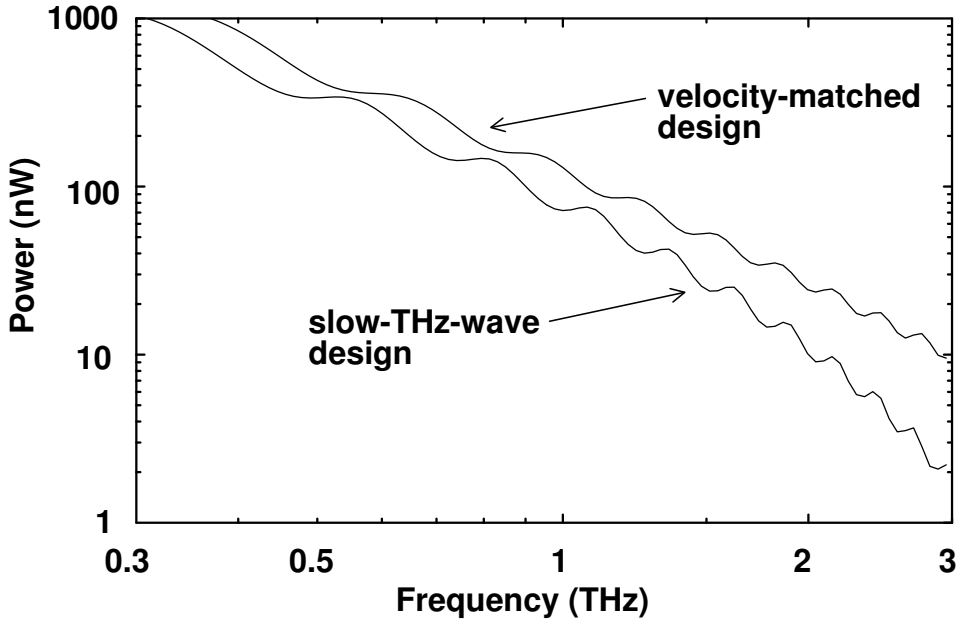

Figure 5-3: Bandwidth comparison between a distributed photomixer with velocity match between THz and optical wave and distributed photomixer with a THz wave slower than the optical. See text for comparison with lumped-element photomixers.

surement conditions (bias field of 2×10^5 V/cm and optical power of 160 mW), the predicted power-bandwidth curves are shown in Figure 5-3. The total predicted dc-photocurrent for each design is 0.9 mA. The roll-off in the velocity-match design's power is primarily due to carrier lifetime effect discussed in Sections 1.3 and 4.1.2. The oscillation in the prediction is due to reflections from the open input end of the CPS. For comparison, lumped-element photomixers using resonant have produced 2 μW at 1 THz, 0.9 μW at 1.7 THz, and $\sim$ 0.2 μW at 2.5 THz over $\sim$ 20% bandwidths. The following section describes an apparatus to measure the terahertz performance.

5.2 Terahertz Characterization

5.2.1 Experimental Setup

The experimental apparatus for distributed photomixer testing must couple the optical beat signal to the photomixer and couple the terahertz beam to a detector. The main compo-

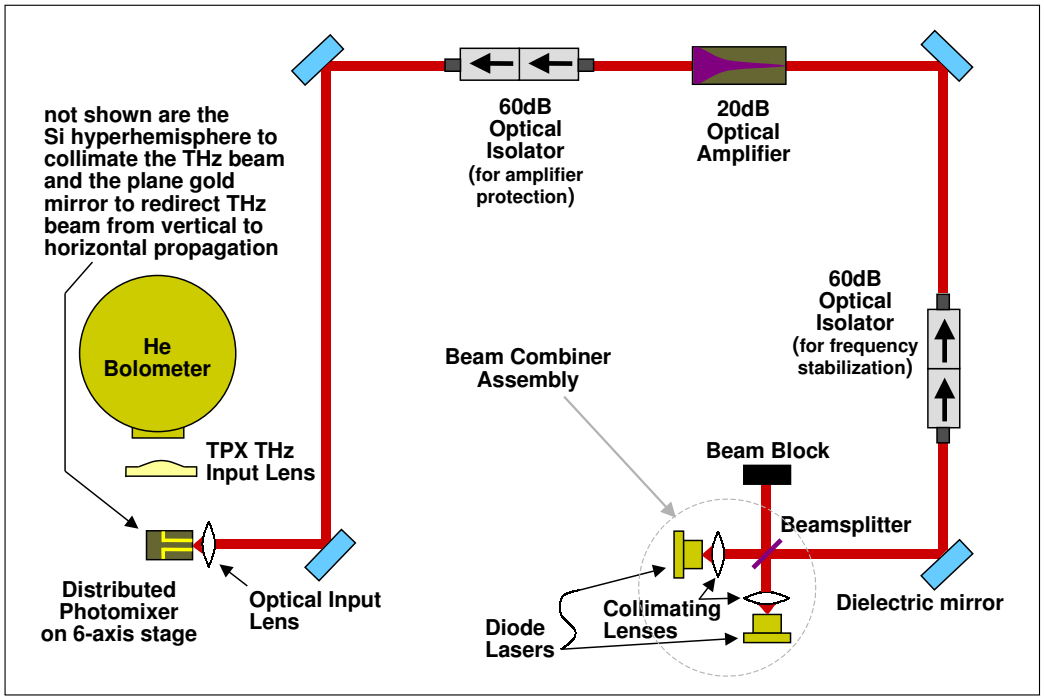

Figure 5-4: THz experimental setup cartoon.

nents of this apparatus are shown in a schematic in Figure 5-4. Two diode lasers generate an optical beat signal by combining on a beamsplitter. This beat signal passes through an optical isolator which prevents feedback into the laser cavities and then through a semiconductor optical amplifier which provides 20 dB of gain up to $\sim$ 400 mW. The amplified signal passes through another isolation stage and then is coupled into the optical waveguide of the photomixer. The terahertz signal is radiated by the planar antenna at the end of the active area, focused by the Si and TPX lenses, and detected in a helium-cooled bolometer. This technique of amplifying a reference signal is known as MOPA (master-oscillator power-amplifier) and has been used for photomixing [119, 120].

Two 850-nm distributed-Bragg-reflector laser diodes are used to generate the optical beat signal. By temperature or current tuning these seed lasers, the frequency of the beat signal (the difference between the lasing frequencies) can be varied from 0 to 1.9 THz. Changing the laser temperature changes the cavity length by a small amount which changes the lasing frequency. Temperature-tuning changes the lasing frequency by approximately

30 GHz/^{o}C. Fine tuning of the frequency is achieved through current-tuning at the rate of approximately 1 GHz/mA. Temperature and current control are provided by an ILX Lightwave LDC-3900 Modular Laser Diode Controller.

Beam-combining occurs between the two free-space-propagating beams incident on the beamsplitter. The reflected light from one of the seed lasers combines with the transmitted light from the other laser. The beat signal is tuned by tuning either laser. The laser spots must be coincident not only on the beamsplitter but also at some point in the far field. Therefore, efficient beam-combining requires the ability to position the collimated output of the diodes precisely on the beamsplitter and the ability to precisely control the orientation of the beamsplitter. A rail system from ThorLabs, Inc. [121] (Ø6 mm rails (6 mm diameter) on 30 mm centers) provides stable, paraxial locating of optical components. Each leg of the rail system houses one laser with positioning hardware and collimating lens. These two legs meet at a right angle at a mounting cube which houses the beamsplitter. The entire assembled system is approximately $15\,\text{cm} \times 15\,\text{cm} \times 9\,\text{cm}$. An expanded view of the beam-combiner hardware is shown in Figure 5-5. The FL20B collimating lenses are from Newport Corporation [98]. The 07TRT504 rotation stage is from Melles Griot [122]. The 123-2450 goniometer is from OptoSigma [123]. The thin beamsplitter (suitable for use with femtosecond laser systems) is from CVI [124]. All other hardware with part numbers is from ThorLabs, Inc. I designed and drew all of the custom hardware, and technical drawings of these pieces are contained in Appendix D.

The beamsplitter positioning hardware consists of a rotation stage and goniometer which together provide the necessary two degrees of rotational freedom. The beamsplitter is mounted so that the axes of rotation of both stages coincide at its center. Two close-up views of this hardware in assembled configuration are contained in Figure 5-6. The three dimensional modeling allowed me to verify before fabrication that hardware was the proper size and shape.

The air-path optical isolators which prevent feedback to the seed lasers have an input polarizer and a powerful permanent magnet to provide 45^{o} of Faraday rotation to the input optical field. Reflected light is rotated another 45^{o} in the same direction and rejected on the input polarizer. Two consecutive isolators provide 60-dB of isolation and a linear polariza-

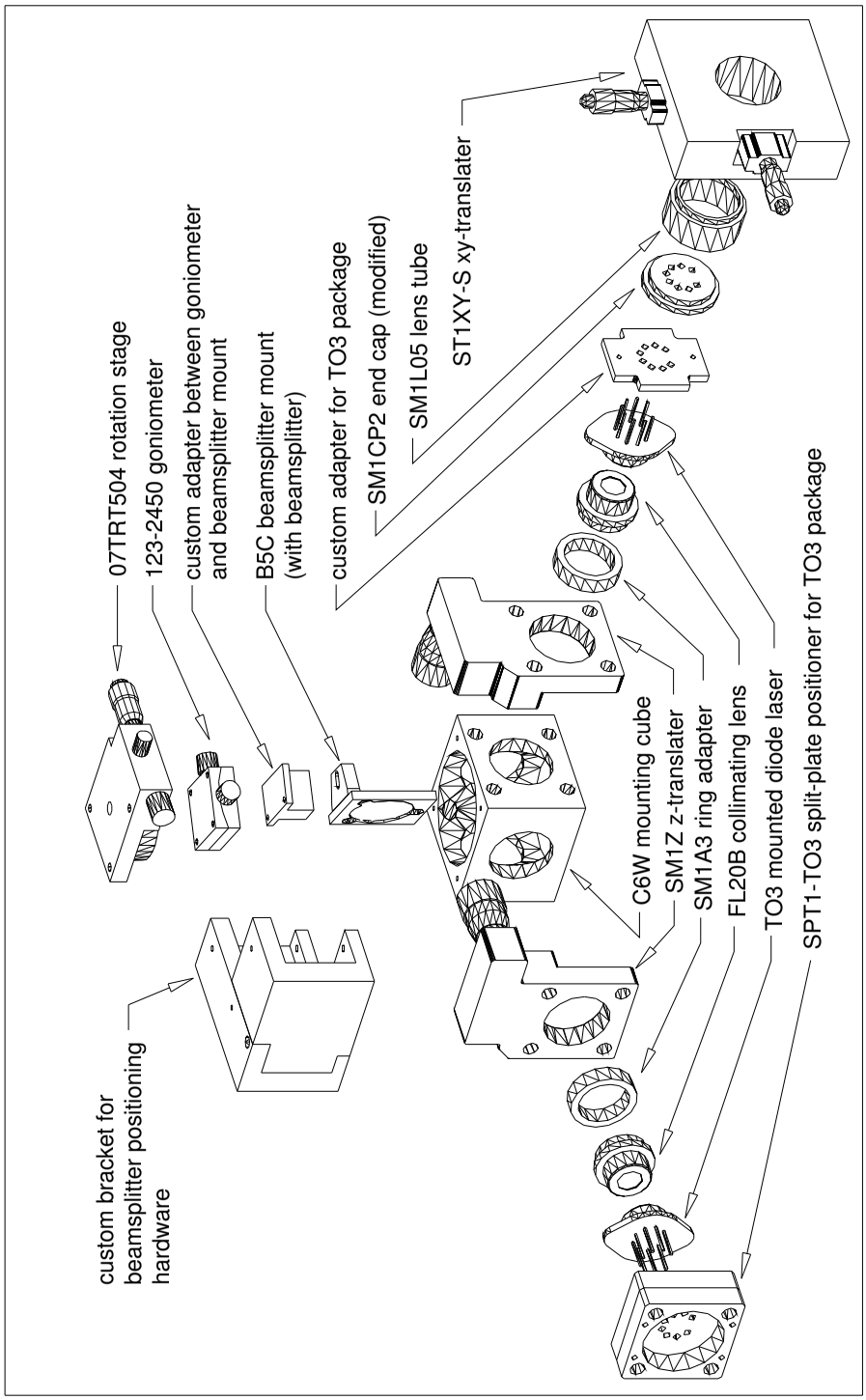

Figure 5-5: Expanded view of beam-combiner hardware. The rails are not shown.

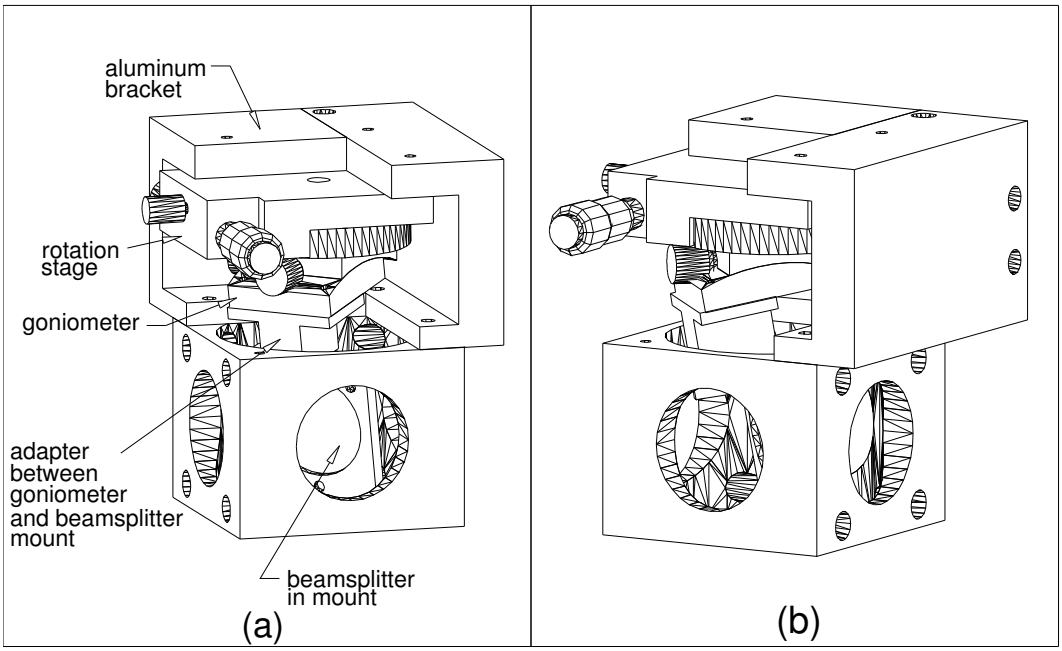

Figure 5-6: (a) View of beamsplitter positioning hardware. (b) View of positioning hardware with rotated goniometer.

tion 90^{o} from the initial polarization. Typically, photomixing experiments have used 30-dB of isolation, but with careful alignment of the 60 dB isolator, I achieved the best long-term frequency stability we have ever observed (50 MHz over 10 minutes) for temperature-tuned diode lasers without active optical-feedback control. The instantaneous linewidth of these lasers is on the order of 1 MHz, but significant effort is required to produce long-term linewidths on that order [120].

The optical amplifier is a Semiconductor Device Laboratories [125] SDL-8630 tunable cw laser diode, which has had the rear cavity assembly removed. With this modification the diode operates as a single pass optical amplifier providing approximately 20 dB of gain. In place of the external tuning cavity, a dielectric mirror directs the optical beat signal to a lens which focuses the light onto the anti-reflection-coated input facet. The amplifier chip has a tapered gain region that is much narrower at the input facet than the exit facet. This tapering allows the amplifier to produce high powers by reducing the power density at the exit facet, but it also means the amplifier can be easily damaged by optical feedback. The 60 dB of isolation after the amplifier provides this protection.

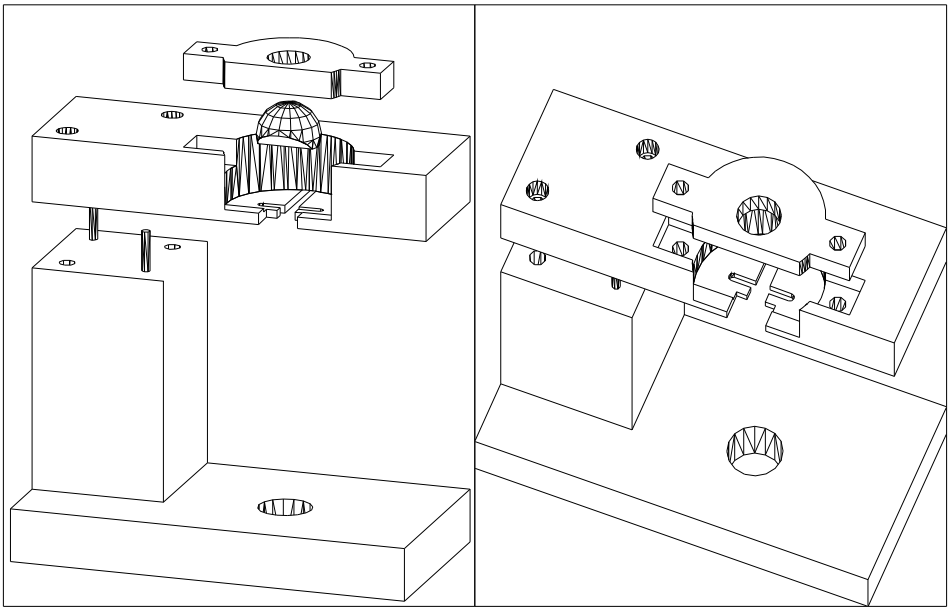

Figure 5-7: Views of hyperhemispherical lens mount. View on left includes 6 mm diameter extended hyperhemisphere lens with 40° flat.

The apparatus to couple the optical signal into the photomixer chip is similar to that shown in Figure 4-12. The mount for the photomixer chip is designed to allow for accurate placement of the chip relative to the Si extended hyperhemisphere lens. Because the photomixer chips are scribed and cleaved using the procedure described in Chapter 3 and Appendix B, the size of the chips is accurate and repeatable to within a few microns. By designing the lens and chip mount shown in Figure 5-7 so that the chip is constrained in the two lateral dimensions (i.e. by pushing it into a corner), the position relative to the lens is accurate and repeatable to within the machining tolerances as mentioned below. The radius of the extended hyperhemisphere ($R = 3\,\text{mm}$) used to collect the terahertz radiation from the photomixer was chosen so that the R/λ ratio provides a good compromise between a pattern that couples well to a Gaussian beam and a highly directive beam [117]. The extension length of the lens itself ($0.92\,\text{mm}$) was chosen so that with the 0.12-mm thick photomixer chip, the total extension length falls within the range ($0.32R$–$0.35R$) that also provides this compromise [117]. The antenna is centered on the cleaved photomixer chip, so the chip must be centered on the lens. Since the lens is larger than the chip, the Si lens

was ground and polished to provide optical access for the input laser signal. The calculated mode waist at the input facet of the distributed photomixer's strip-loaded waveguide predicts a mode exit/entrance half angle of 35^{o} in the vertical dimension. To provide tolerance, a 40^{o} flat was machined off the lens. The dimensioned lens is shown in Figure D-4. With a small radius lens, misalignments of the planar antenna from the center of the lens can lead to deteriorated beam patterns and quasioptical coupling. Therefore, the mount that holds the photomixer chip and lens needs to locate them accurately and repeatably. I designed a mount which constrains the lens and chip to within 0.001" in position. Two views of the mount, lens, and retaining ring are shown in Figure 5-7, while the dimensioned hardware drawings are in Figures D-5, D-6 and D-7.

A 5.7-cm-focal-length and 4.8-cm-diameter TPX lens provides additional focusing to couple the THz radiation into an Infrared Labs helium-cooled silicon-composite bolometer. This particular bolometer has been calibrated over a range of frequencies [3] including a calibration I performed at the Harvard-Smithsonian Center for Astrophysics at 1.26 THz. The bolometer signal was recorded for power coupled into the bolometer from a calibrated source (multiplied Gunn which had been calibrated using a Golay cell) at 1.26 THz. The fraction of power coupled into the bolometer was calculated using Gaussian beam optics. The responsivity from that calibration ($6\ V_{rms}/\ \mu$W) is used in these power measurements presented in the next section. The loss in the TPX lens of 0.37 was also verified during this calibration.

The final issue with the experimental apparatus is the analysis of the quasioptical coupling of the terahertz signal from the Si lens aperture into the bolometer element. This coupling involves focusing by the TPX lens through a 1.25-cm window into a 2-mm aperture in the bolometer cavity. An effective waist at the Si lens was deduced by measuring the Si lens, TPX lens and bolometer positions, which gave maximum power coupled to the bolometer at approximately 1 THz. Coupling was calculated using Gaussian beam analysis, and the beam waist at the Si lens was varied to achieve the maximum coupling case ($\sim\ 80\%$) shown in Figure 5-8. The waist for maximum coupling was 1.2 mm, and knowledge of this waist allows the calculation of frequency dependent coupling into the bolometer through Gaussian beam analysis [126].

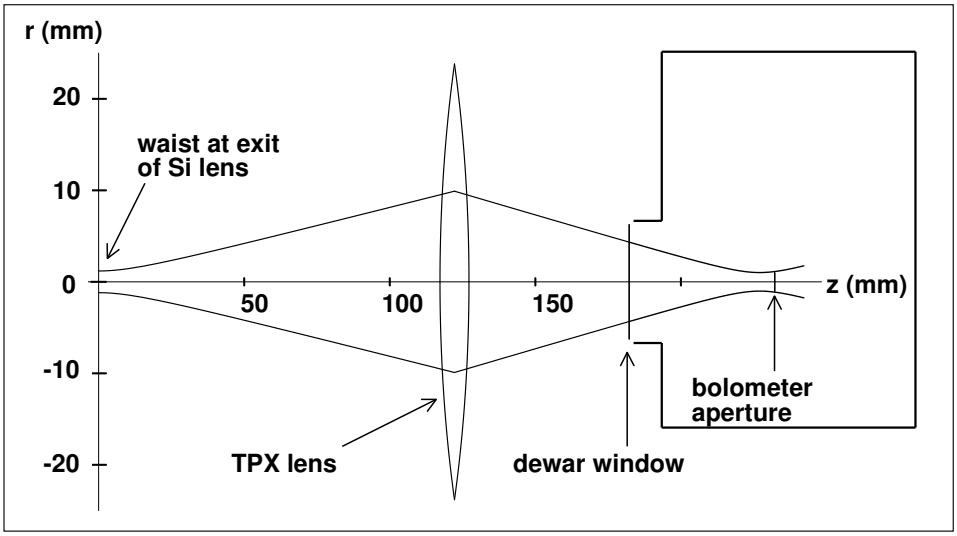

Figure 5-8: Illustration of coupling the terahertz signal into the bolometer.

5.2.2 Measurements

This section describes the measurement of the terahertz performance of the distributed photomixers. Specifically, I discuss the dependence of terahertz output power on frequency, input optical power, and bias voltage. Optical power and bias voltage are the two inputs that affect photomixer performance during testing. Therefore, it is important to verify that terahertz output power varies with these inputs as predicted by the distributed photomixer model.

Under typical test conditions, the voltage bias on the distributed photomixer was set so that the applied electric field was between 1.5 and 2.0×10^5 V/cm. An optical power of approximately 160 mW was incident on the waveguide facet. The CCD camera and telescope described in Section 4.2.1 were used to align the optical signal to the photomixer chip using a procedure similar to the one in that section. Once a waveguide mode was found, the photomixer chip position and orientation was optimized by maximizing the dc photocurrent. Typical photocurrent magnitudes were in the range of 350–550 μA. These values are 45–60% of the predicted photocurrent. Since the current model predicted the surface-illuminated test structure accurately, it is unlikely that there are significant errors in it. One plausible explanation for the discrepancy is that the predicted input optical coupling

efficiency is too high. The optical coupling efficiency calculated in Section 5.1.2 assumes a diffraction-limited laser spot and optics as well as perfect alignment of the signal to the waveguide facet. In talking with an experienced laser and waveguide designer, coupling better than 75% of the maximum is rarely achieved [115]. The source of the remainder of the discrepancy is not known, but it is plausibly due to a combination of device-to-device variations in responsivity and extinction length and small errors in the models for carrier lifetime and photocurrent.

For detection of terahertz power, the optical signal was chopped at $\sim$ 37 Hz with a mechanical chopper, and the bolometer voltage was amplified and detected on a EG&G Princeton Applied Research Model 5209 Lock-in Amplifier. The bolometer signal was maximized by moving the bolometer and micrometer-mounted TPX lens to increase coupling of the THz signal into the bolometer. By temperature tuning the seed lasers, the operating frequency of the photomixer was changed, and the corresponding bolometer voltage recorded. Usually, the laser pair is chosen so that at room temperature, the difference frequency is $\sim$ 0.9 THz, so that by tuning one laser to the hot extreme of its operating condition and the other to the cold extreme dc can be reached (as well as 1.8 THz by tuning the temperatures in the opposite sense.)

Examples of typical bandwidth plots for bowtie-coupled velocity-matched (0.8-μm electrode gap) and slow-THz-wave (0.4-μm electrode gap) distributed photomixers are given in Figure 5-9. For the purposes of comparison with predicted power, the bolometer voltage is scaled by the responsivity calibration from Section 5.2.1 and the Gaussian coupling efficiency discussed in the same section. The structure in the bandwidth plots is associated with atmospheric absorption as well as standing wave effects in the optical and terahertz systems. The output power is shown out to approximately 1.8 THz where the photomixer power dropped below the noise floor of the measurement system. The velocity-matched device shows the expected 6 dB/octave roll-off with frequency due to carrier lifetime up to ~ 1.4 THz, when the power drops by approximately 7 dB in 0.2 THz. The slow-THz-wave structure rolls off slightly faster than expected, so the drop in power from 1.4 to 1.6 THz is less obvious. The reason for this faster-than-expected roll-off is not known.

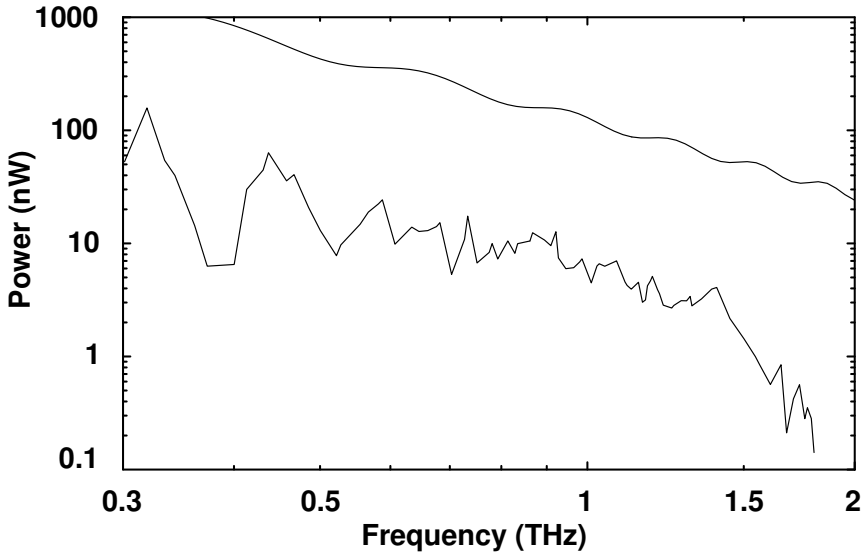

(a) Velocity-matched, bowtie-coupled distributed photomixer bandwidth compared to predicted performance.

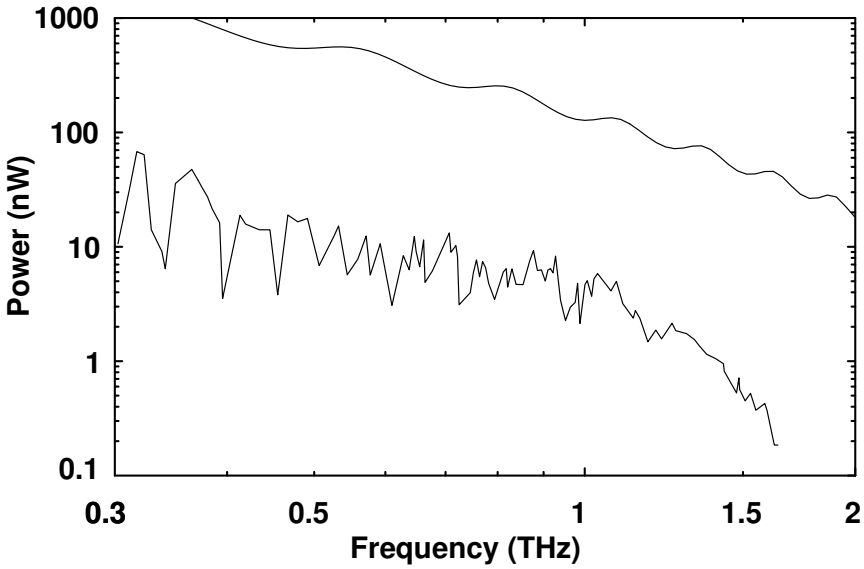

(b) Slow-THz-wave, bowtie-coupled distributed photomixer bandwidth compared to predicted performance.

Figure 5-9: Comparison of measured at predicted distributed photomixer bandwidth plots.

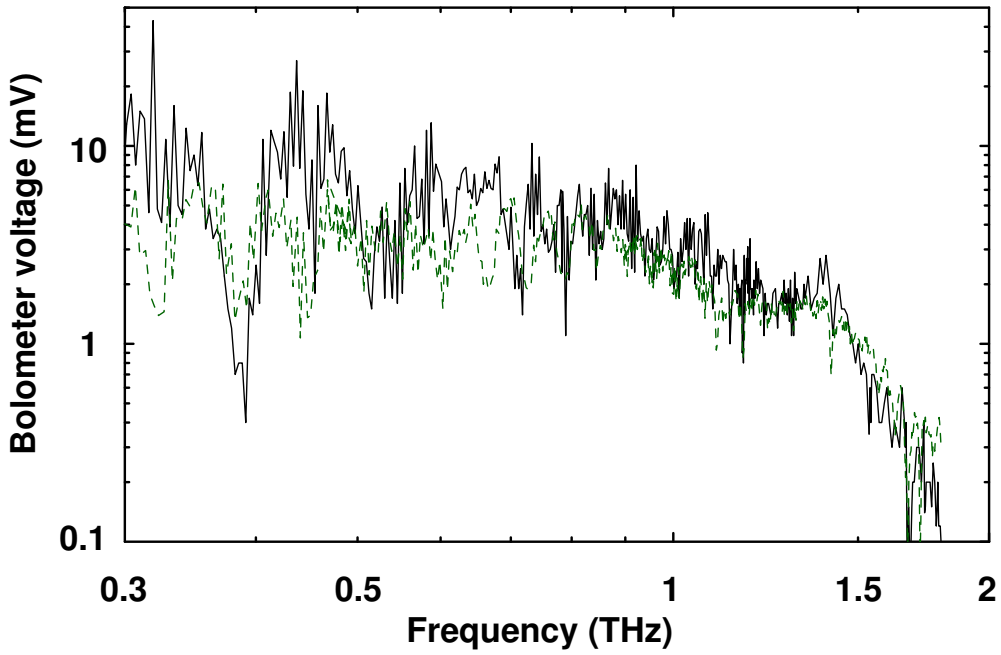

Figure 5-10: Bandwidth comparison between a bowtie-coupled distributed photomixer (—) and a log-spiral coupled lumped-element photomixer (- - -). The lumped-element photomixer data has been scaled down by about a factor of 50.

The absolute difference between predicted and measured terahertz power of approximately 10 dB is not surprising. The lower dc photocurrent mentioned earlier explains part of the discrepancy. The quasioptical coupling losses and a non-Gaussian antenna pattern are plausible explanations for the remainder of the discrepancy. The closest that lumped-element photomixer power predictions have ever been to measurements has been about 7 dB [127].

The dramatic drop in power near 1.4 THz can be understood by comparison with a scaled power-bandwidth curve of a log-spiral-coupled lumped-element photomixer. Figure 5-10 shows two high-frequency-resolution bandwidth curves for a bowtie-coupled and log-spiral coupled photomixer. Both photomixers show the same steep roll-off at that frequency. Therefore, I can rule out that it is intrinsic to either the distributed photomixer structure or the bowtie antenna. The only common elements between the two measurements are the bolometer and the TPX lens. Either element could plausibly have a frequency-dependent coupling or absorption characteristic.

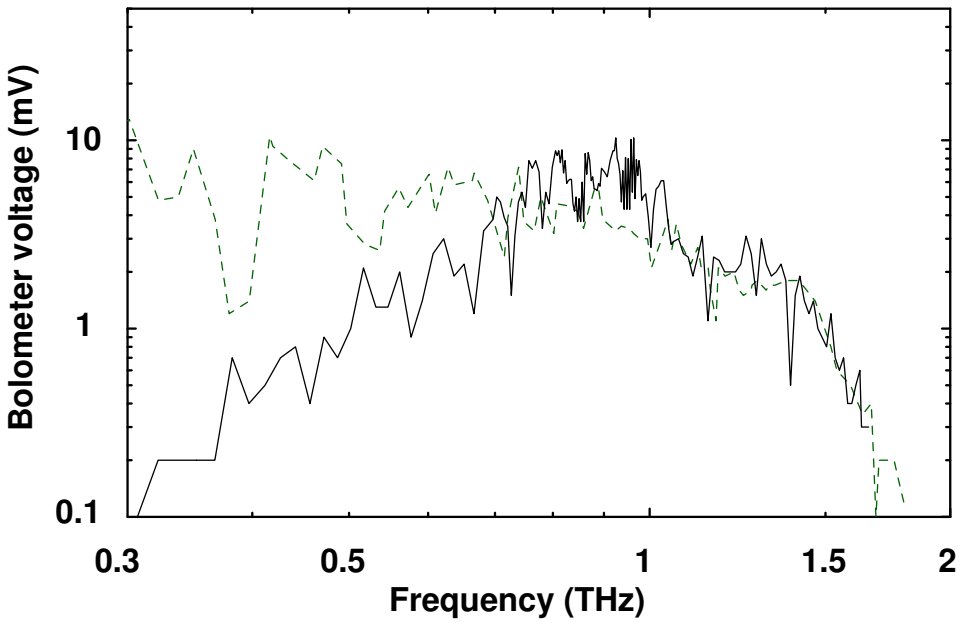

Figure 5-11: Bandwidth comparison between a dipole-coupled distributed photomixer (—) and a bowtie-coupled distributed photomixer (- - -).

The effect of antenna pattern on coupling to the bolometer is investigated through comparison of the bandwidth of a dipole-coupled and bowtie-coupled distributed photomixer. The dipole-coupled photomixer shows 3 to 5 dB higher power than the bowtie-coupled device near the half-wave resonant frequency of the dipole. For the bowtie antenna dimensions and frequencies of operation, the bowtie impedance is constant at $\sim 75\Omega$, which matches it to the impedance of the loaded CPS transmission line. Therefore, the higher power output is due to improved Gaussian coupling efficiency rather than improved impedance match (as is the case for lumped-element photomixers).

Having characterized the frequency performance of the distributed photomixer, the dependence on the control variable of optical power is investigated and compared with theory. According to the photomixer theory in Section 1.3, the dc-photocurrent should vary linearly with optical power as long as no saturation effects are seen. The terahertz power should increase quadratically with optical power. These assumptions are confirmed by Figure 5-12 which shows the photocurrent and bolometer voltage for a distributed photomixer operating at 0.3 THz. In addition to verifying the photoconductive nature of the LTG-GaAs, the

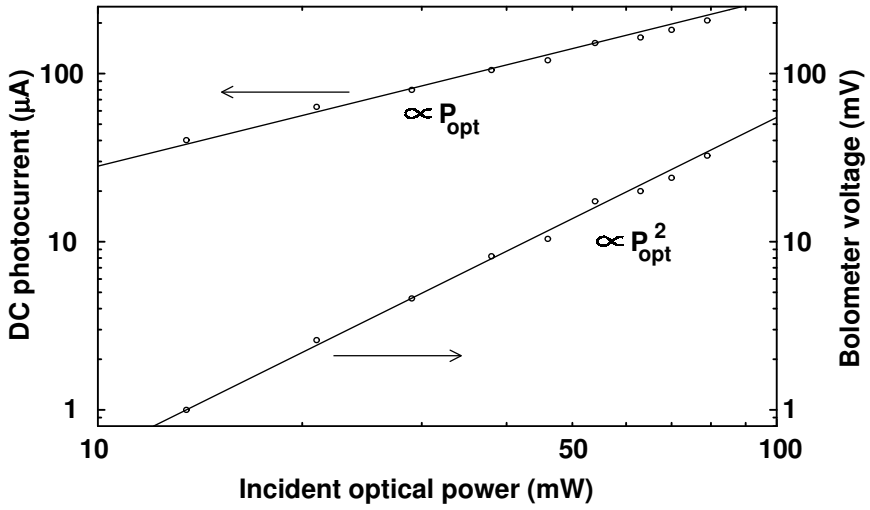

Figure 5-12: Distributed photomixer dc photocurrent and bolometer voltage as a function of incident optical power at constant bias voltage of 16 V across a 0.8-μm-gap. The optical signal was chopped for lock-in detection of the THz signal. Recorded optical power and photocurrent values are half their unchopped values.

measurement of current and terahertz power as a function of optical power also confirms that there are no coupling effects which depend on the magnitude of the optical signal up to incident powers which result in facet damage. Note that the optical power was chopped for terahertz measurements to permit lock-in detection of the bolometer voltage. Therefore, the power and photocurrent values are half of the constant illumination values discussed at the beginning of this section.

The second control for photomixer performance is applied bias voltage. As discussed in Section 4.3, a LTG-GaAs photomixer's responsivity increases with applied field; therefore, an accompanying increase in both photocurrent and terahertz power is expected. However, the carrier lifetime also increases with electric field so the terahertz power will not increase without bound. Distributed photomixer dc-photocurrent and bolometer signal as a function of applied electric field is shown in Figure 5-13 for operating frequencies of 0.3 THz, 0.6 THz, and 1.4 THz. For similar illumination and alignment conditions, the dc-photocurrent at any terahertz difference frequency should have the same voltage dependence as the current-voltage characteristic of the test structures in Section 4.3. The solid photocurrent line is predicted using equation (4.20), where T is the computed optical cou-

pling efficiency into the dielectric waveguide and an additional factor $\left(1 - e^{-\ell_{\text{active}}/\ell_{\text{ext}}}\right)$ is used to account for the fraction of optical power absorbed. The predicted IV curves required a scaling factor of approximately 0.6 to fit the data. This factor is consistent with the photocurrent discrepancy due to imperfect optical coupling mentioned previously. These measurements verify that the full 150-μm-long active area has the same dc current-voltage relationship as the surface and waveguide-illuminated test structures in Figures 4-14 and 4-17.

Figure 5-13 also demonstrates the dependence of distributed photomixer terahertz power on bias voltage. As expected, the terahertz power does not scale with the square of the dc-photocurrent at high bias. The full expression for predicted power differs functionally from the square of the photocurrent by a factor of $\left(1 + (\omega\tau(E))^2\right)^{-1}$, where τ is the carrier lifetime, which is a function of E the applied electric field. Therefore, this measurement is consistent with a carrier-lifetime increase with electric field. Thus, the increase in terahertz power with field is smaller as the operating frequency increases.

Distributed photomixer performance has been measured and compares well with the theory used to design the photomixers and predict their terahertz performance.

5.3 Discussion and Conclusions

Distributed photomixers operating at terahertz frequencies have been demonstrated. Qualitative and quantitative agreement between measured performance and predictions verify the distributed photomixer model. The output power of these distributed photomixers, however, is lower than that produced by lumped-element photomixers operating at the same frequency. Operation in traveling-wave mode incurs a fundamental 6-dB reduction in terahertz power over a lumped-element photomixer with the same dc-photocurrent. This loss can be understood phenomenologically by realizing that in traveling-wave mode, only half of the terahertz-frequency current (and thus one quarter of the power) generated at any point along the active area propagates in the direction of the antenna. This current does not contribute detrimentally to the performance of the device because no reverse-propagating current wave builds up because it is not phase-matched to the optical wave propagating

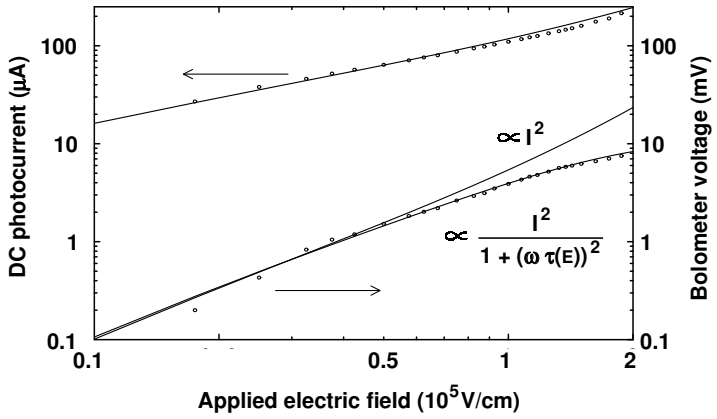

(a) Distributed photomixer operating at 0.3 THz.

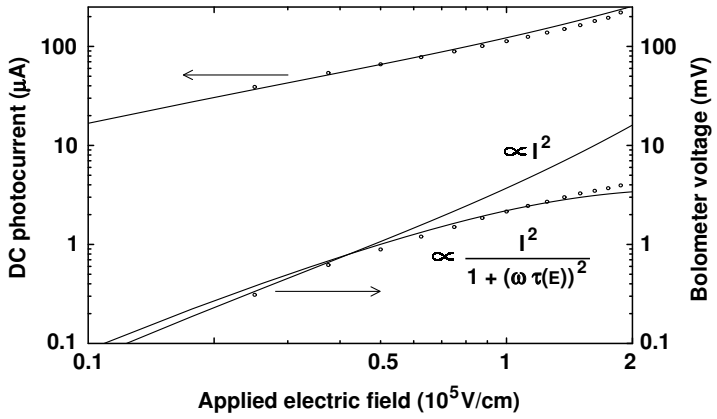

(b) Distributed photomixer operating at 0.6 THz.

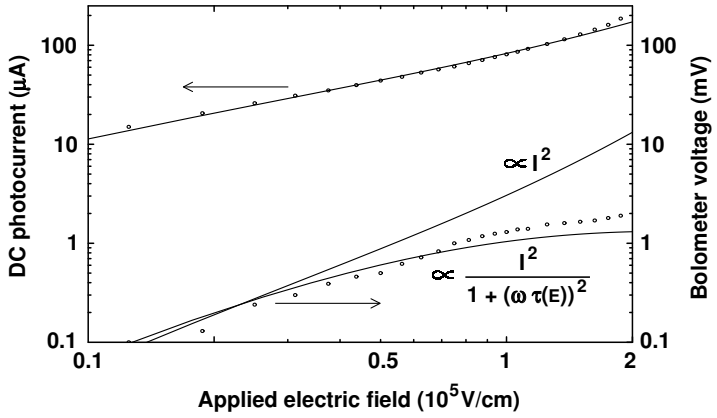

(c) Distributed photomixer operating at 1.4 THz.

Figure 5-13: Photomixer dc photocurrent and bolometer voltage illustrating the effect of field dependent carrier lifetime at different frequencies.

in the opposite direction. Thus, distributed photomixers are only expected to outperform lumped-element photomixers if they generate more than twice as much photocurrent or operate at frequencies far enough past the RC roll-off of lumped-element photomixers for their 6 dB/octave characteristic power roll-off to cross over the 12 dB/octave roll-off of lumped-element devices [65]. The devices tested in this thesis did not generate enough power to operate beyond this crossover frequency of ~ 2 THz. One of the primary reasons for the low output power is that insufficient optical power was absorbed in the active region. Facet failure typically occurred for incident power levels of about 180 mW. Runaway of dc-photocurrent accompanied by a corresponding drop in THz output power, a failure mode common to all LTG-GaAs photomixers, occurred for currents in the range of 0.8–0.9 mA. To reach the ~ 4 mA of photocurrent needed for 10–20 μW of power at 1 THz, the absorbed optical power and current-handling capability of the devices would need to be increased substantially. Additional measures for increasing THz power include the use of higher gain planar antennas and the deposition of thicker metal for the terahertz waveguide.

Three techniques could increase the amount of optical power absorbed in the active area: increasing the size of the optical waveguide mode at the input facet, increasing transmission into the waveguide, and increasing the fraction of power absorbed in the active region. High-power semiconductor lasers either employ wide, thin exit facets such as that used in the SDL tapered semiconductor optical amplifier in these experiments [125] or symmetrical exit facets which are a few microns in both width and height [128]. The thin, tapered waveguide design would greatly increase the required accuracy of alignment of the input beam to prevent excitation of higher order modes in the over-moded waveguide. Either design requires tight fabrication tolerances in order to produce a waveguide that only supports one mode. While these techniques are engineering challenges, they are not physical impossibilities and could result in devices which could handle 3–5 times more incident optical power. An antireflection (AR) coating would increase the fraction of that incident optical power transmitted into the dielectric waveguide. The difficulty in AR coating these $Al_xGa_{1-x}As$-based devices is that the coating must be non-oxidizing, stable, and capable of withstanding high power densities. Proprietary AR coatings have been developed for $Al_xGa_{1-x}As$ based lasers, but applying them is a very challenging engineering problem,

involving exotic surface treatments or cleaving and coating-deposition in vacuum. Increasing the fraction of the waveguide-coupled optical power which gets absorbed in the active waveguide involves either decreasing the extinction length or increasing the length of the active region in a predictable, repeatable way. The discrepancies between the desired, predicted, and measured values for extinction lengths in my structures are due to variations in growth and fabrication dependent material and geometry parameters. The associated technical challenge involves repeated growth and fabrication runs to determine and reduce the unknowns and variations in these parameters. The option of increasing the active region length is discussed in the next section.

Two proposed mechanisms for the thermal failure of LTG-GaAs photomixer structures are localized heating near the electrodes leading to stress-induced material failure and a thermally-induced increase of defects and dislocations in the LTG-GaAs. For either mechanism, increasing the maximum sustainable photocurrent requires the thermal load in the active area to be reduced, either by decreasing the active region's thermal impedance or increasing its volume. The $Al_{0.35}Ga_{0.65}As$ layer beneath the LTG-GaAs has a thermal conductivity approximately half that of annealed LTG-GaAs [57, 74]. The resulting decrease in heat-sinking capability depends on the exact details of the device geometry, but thermal modeling of lumped-element LTG-GaAs photomixers indicates that a decrease of $\sim 40\%$ would be expected [57]. This decrease corresponds roughly to the fact that the distributed photomixers failed at a current $\sim 20\%$ lower than that of a standard $8\,\mu\text{m} \times 6\,\mu\text{m}$ lumped-element photomixer, which has roughly the same active volume, i.e. $V_{\text{distrib}} = 150\,\mu\text{m} \times 3\,\mu\text{m} \times 0.1\,\mu\text{m} = 450\,\mu\text{m}^3$ and $V_{\text{lump}} = 8\,\mu\text{m} \times 6\,\mu\text{m} \times 1\,\mu\text{m} = 480\,\mu\text{m}^3$). A waveguide design with smaller aluminum fraction in the cladding would improve the thermal conductivity. (While very high Al fractions would also lead to higher thermal conductivity, device lifetime would suffer because of the rapid oxidation of high-Al-fraction $Al_xGa_{1-x}As$ layers.) The increase in thermal conductivity from $Al_{0.35}Ga_{0.65}As$ to $Al_{0.10}Ga_{0.90}As$ is a factor 2, which would not provide the necessary increase in current-handling. Therefore, in addition to a modification of the dielectric waveguide structure, the LTG-GaAs layer dimensions would need to be changed.

Increasing the active region volume involves either an increase in thickness or length.

(Figure 2-7 indicates that the 3-μm-width of the active area strip is near the limit for single mode optical waveguide operation.) The problems with a thicker LTG-GaAs layer are that it competes directly with the desire for a long extinction length and the desire for the higher photoconductive gain resulting from a thin LTG-GaAs layer. For a waveguide-coupled distributed photomixer, the optical intensity peaks at the bottom of the LTG-GaAs layer while the electric field is highest at the top where the electrodes are. The LTG-GaAs layers used in this thesis are thin enough that this effect was not significant; however, for layer thicknesses much greater than 0.2 μm, the effect would become important and detrimental. Also, if the more important thermal failure mechanism is localized heating near the electrodes, then increasing the length of the active region would be more effective than increasing the volume. Therefore, a longer active region would be preferred over a much thicker LTG-GaAs layer; however, that choice comes with its own difficulties. Longer active areas place more stringent limits on the quality of the velocity match between the optical and terahertz wave. Also, the conductor and dielectric loss mechanisms from Section 5.1.2 start to become important, especially at frequencies approaching 3 THz. Thicker metal could address both of these issues, but more accurate modeling would be required to determine the effect of metal thickness on CPS and electrode impedance and current distribution.

Finally, higher gain planar antenna structures could lead to an increase of 3 to 5 dB in coupled terahertz power. The bowtie coupling was similar to that of a dipole so it was not extremely poor; however, more directive antenna configurations such as double dipoles or endfire antennas would couple better than either of these designs.

Of these considerations, the primary challenges that must be met for distributed photomixers to outperform lumped-element photomixers are: 1) coupling more optical signal into the device and 2) handling more current. Both of these steps are required to increase the photocurrent to compensate for the 6 dB drop in THz power relative to lumped-element designs, for frequencies less than the $\sim$ 2 THz crossover.

In this thesis, I have described the design, fabrication, and characterization of LTG-GaAs waveguide-coupled distributed photomixers designed for terahertz operation. A design methodology and design curves were presented for all of the main elements of the distributed photomixer: the optical waveguide, the terahertz waveguide, and the radiating

element. The fabrication process was described. Material and device characteristics were independently measured, and used to create a model of the distributed photomixer performance at terahertz frequencies. Photomixing measurements verified that the model predicts with good accuracy the dependence of output power on frequency, optical power and applied voltage bias. I have discussed the limitations of the LTG-GaAs distributed photomixer design and possible routes to increasing its output power at terahertz frequencies.

Appendix A

Electromagnetic Model for the Dielectric Waveguide

A.1 Method of Field Shadows

An overview of the method of field shadows was given in Section 2.1.1. This appendix provides a more in-depth explanation and the details equations in the formalism I used.

Solving the electromagnetic modes in a one-dimensional slab waveguide is the initial and key component to the method of field shadows. The electromagnetic field in each layer of a slab waveguide can be represented as the sum of two counter-propagating plane waves with complex exponential spatial and temporal dependence. For a guided mode in the slab waveguide, the fields must be a real exponential in the topmost and bottommost layers, and for normalizability, the field magnitude must decay exponentially away from the topmost and bottommost boundary. The boundary conditions require continuous electric and magnetic fields tangential to all the boundaries. The technique is rigorously correct inasmuch as all the layers can be represented by scalar dielectric constants with abrupt junctions between layers. Benjamin Williams [41] suggested the use of the transmission matrix technique described in [129] for setting up and solving the boundary condition equations.

Consider a plane wave incident on the bottommost layer boundary as shown in Figure A-1. The reflection at the boundary can be described by a transmission matrix, relating the field magnitudes on one side of the boundary to those on the other. A propagation

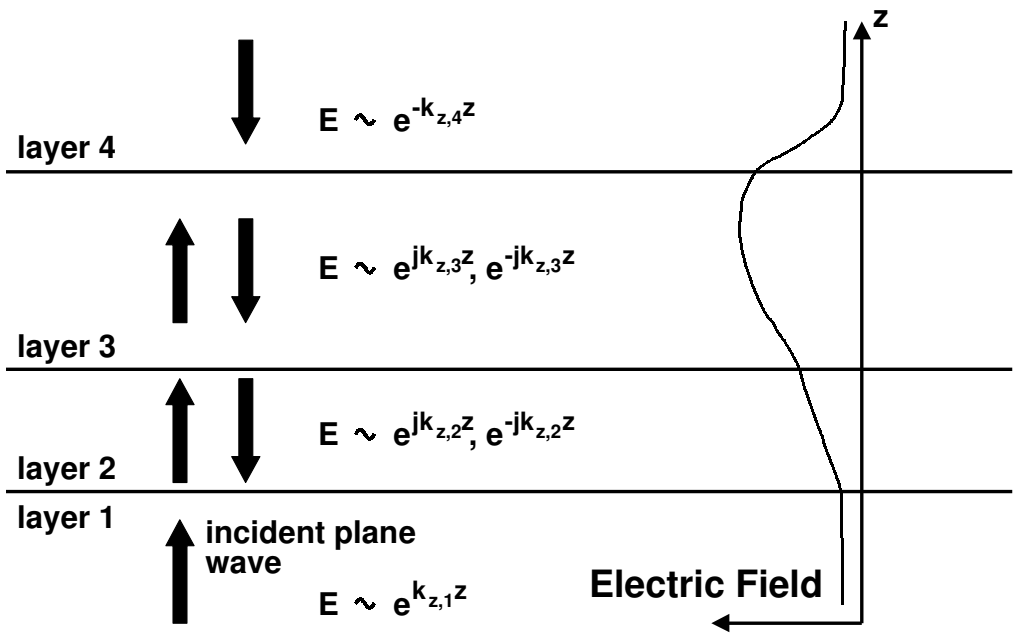

Figure A-1: Plane wave representation of a mode in a dielectric slab waveguide.

matrix can then account for the phase change of the fields propagating in the second layer. Another reflection matrix accounts for the next boundary and so on. Cascading reflection and propagation matrices provides a flexible way of modelling a slab waveguide with an arbitrary number of layers. The continuity equations determine the form of the reflection matrices, and the normalizability constraint requires that only one field component exists in the topmost and bottommost layers. An example profile of the tangential electric field is also shown in Figure A-1.

It should be noted that the propagation of the incident plane wave through the layers is not the propagation of the mode in the slab waveguide. This model simply provides a useful technique for determining the transverse dependence of the field in the waveguide. However, the effective index calulated by this technique is the index for the mode that would propagate in the slab waveguide. Figure A-2 illustrates the relationship between the slab waveguide and the plane wave reflection at a boundary. In this figure, the mode depicted is a transverse electric (TE) mode, and it propagates in the y direction. The electric field in the slab waveguide is x-directed and varies along the z direction. The electric

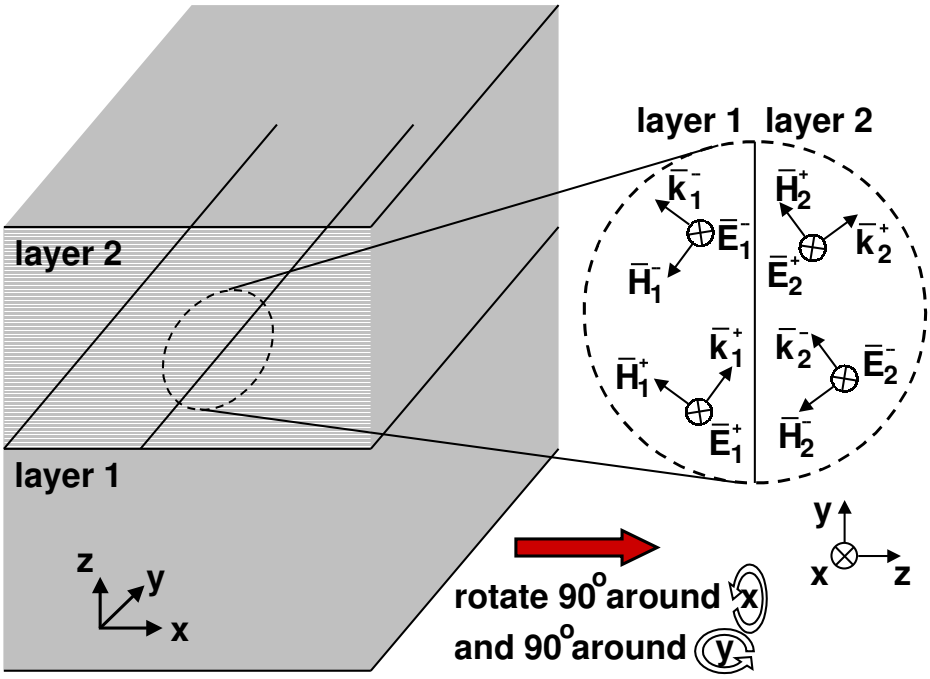

Figure A-2: TE mode in a dielectric waveguide views as a plane wave reflection at a boundary.

field in the effective slab waveguide of Figure 2-3 is also x-directed but varies along the x direction. Expressed in the sign and coordinate conventions of Figure A-2, field continuity requires

$$E_{x,1} = E_{x,2} \quad \text{and} \quad H_{y,1} = H_{y,2} \text{ , where} \tag{A.1}$$

$$E_{x,1} = E^{+}_{x,1} e^{-jk_{z,1}z} e^{-jk_{y,1}y} + E^{-}_{x,1} e^{jk_{z,1}z} e^{-jk_{y,1}y} \tag{A.2}$$

$$E_{x,2} = E^{+}_{x,2} e^{-jk_{z,2}z} e^{-jk_{y,2}y} + E^{-}_{x,2} e^{jk_{z,2}z} e^{-jk_{y,2}y} \tag{A.3}$$

and

$$H_{y,1} = (-j\omega\mu_1)^{-1} \frac{\partial E_{x,1}}{\partial z} = E^{+}_{x,1} e^{-jk_{z,1}z} e^{-jk_{y,1}y} + E^{-}_{x,1} e^{jk_{z,1}z} e^{-jk_{y,1}y} \tag{A.4}$$

$$H_{y,2} = (-j\omega\mu_2)^{-1} \frac{\partial E_{x,2}}{\partial z} = E^{+}_{x,2} e^{-jk_{z,2}z} e^{-jk_{y,2}y} + E^{-}_{x,2} e^{jk_{z,2}z} e^{-jk_{y,2}y} , \tag{A.5}$$

and where the superscript $+$ and $-$ refer to the field components traveling in the positive

and negative z directions, respectively. If the boundary conditions are enforced at $z = 0$ and $y = 0$, and impedances are defined as

$$Z_1^{\mathrm{TE}} = \frac{\omega\mu_1}{k_{z,1}} \quad \text{and} \quad Z_2^{\mathrm{TE}} = \frac{\omega\mu_2}{k_{z,2}}\,, \tag{A.6}$$

then the boundary condition equations can be written as

$$E_{x,1}^{+} + E_{x,1}^{-} = E_{x,2}^{+} + E_{x,2}^{-} \tag{A.7}$$

$$Z_2^{\mathrm{TE}} E_{x,1}^{+} - Z_2^{\mathrm{TE}} E_{x,1}^{-} = Z_1^{\mathrm{TE}} E_{x,2}^{+} - Z_1^{\mathrm{TE}} E_{x,2}^{-}\,. \tag{A.8}$$

These equations can be rewritten in a single matrix equation

$$\begin{bmatrix} E_{x,2}^{+} \\ E_{x,2}^{-} \end{bmatrix} = \underbrace{\frac{1}{2Z_1^{\mathrm{TE}}} \begin{bmatrix} \left(Z_1^{\mathrm{TE}} + Z_2^{\mathrm{TE}}\right) & \left(Z_1^{\mathrm{TE}} - Z_2^{\mathrm{TE}}\right) \\ \left(Z_1^{\mathrm{TE}} - Z_2^{\mathrm{TE}}\right) & \left(Z_1^{\mathrm{TE}} + Z_2^{\mathrm{TE}}\right) \end{bmatrix}}_{\overline{\overline{M}}_{\mathrm{refln}}^{\mathrm{TE}}} \begin{bmatrix} E_{x,1}^{+} \\ E_{x,1}^{-} \end{bmatrix}. \tag{A.9}$$

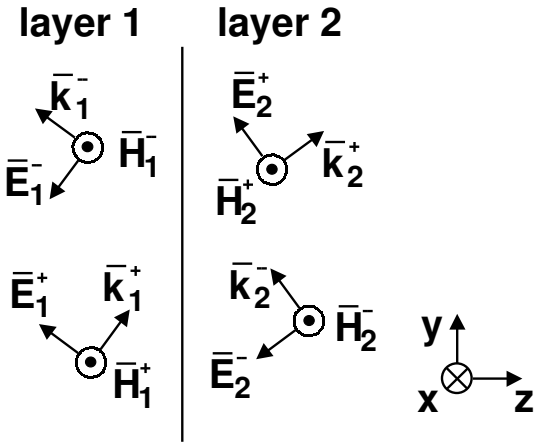

Figure A-3: TM reflection at a dielectric interface.

The sign convention and coordinate conventions for a transverse magnetic (TM) mode are shown in Figure A-3. As the TE mode does, the TM mode propagates in the y direction. The electric field in the slab waveguide has z and x-directed component and varies along the z direction. The electric field in the effective slab waveguide of Figure 2-3 also had z and x-directed components but varies along the x direction. The magnetic field of the TM mode is analogous to the electric field of the TE mode in terms of its vector component directions.

For a TM mode, the boundary condition equations are expressed more directly in terms

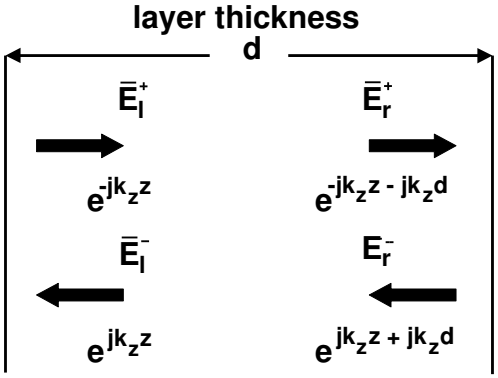

Figure A-4: Schematic showing the relationship between field components propagating through a layer of thickness, d.

of the magnetic field,

$$H_{x,1}^{+} + H_{x,1}^{-} = H_{x,2}^{+} + H_{x,2}^{-} \tag{A.10}$$

$$-Z_1^{\mathrm{TM}} H_{x,1}^{+} + Z_1^{\mathrm{TM}} H_{x,1}^{-} = -Z_2^{\mathrm{TM}} H_{x,2}^{+} + Z_2^{\mathrm{TM}} H_{x,2}^{-}, \tag{A.11}$$

which can be expressed in matrix form as

$$\begin{bmatrix} H_{x,2}^{+} \\ H_{x,2}^{-} \end{bmatrix} = \frac{1}{2Z_2^{\mathrm{TM}}} \begin{bmatrix} \left(Z_2^{\mathrm{TM}} + Z_1^{\mathrm{TM}}\right) & \left(Z_2^{\mathrm{TM}} - Z_1^{\mathrm{TM}}\right) \\ \left(Z_2^{\mathrm{TM}} - Z_1^{\mathrm{TM}}\right) & \left(Z_2^{\mathrm{TM}} + Z_1^{\mathrm{TM}}\right) \end{bmatrix} \begin{bmatrix} H_{x,1}^{+} \\ H_{x,1}^{-} \end{bmatrix}. \tag{A.12}$$

This matrix equation is converted to one relating the electric field components by observing from Figure A-3 that

$$\frac{H_{x,1}^{-}}{H_{x,1}^{+}} = -\frac{E_{y,1}^{-}}{E_{y,1}^{+}}. \tag{A.13}$$

The resulting matrix equation comparable to the TE equation is

$$\begin{bmatrix} E_{y,2}^{+} \\ E_{y,2}^{-} \end{bmatrix} = \underbrace{\frac{1}{2Z_2^{\mathrm{TM}}} \begin{bmatrix} \left(Z_1^{\mathrm{TM}} + Z_2^{\mathrm{TM}}\right) & \left(Z_1^{\mathrm{TM}} - Z_2^{\mathrm{TM}}\right) \\ \left(Z_1^{\mathrm{TM}} - Z_2^{\mathrm{TM}}\right) & \left(Z_1^{\mathrm{TM}} + Z_2^{\mathrm{TM}}\right) \end{bmatrix}}_{\overline{\overline{M}}_{\mathrm{refln}}^{\mathrm{TM}}} \begin{bmatrix} E_{y,1}^{+} \\ E_{y,1}^{-} \end{bmatrix}. \tag{A.14}$$

The translation, or propagation, matrix is common to both TE and TM modes. The

matrix can be formulated by inspection of Figure A-4. The matrix equation relating the fields on the left and right side of the layer is

$$\begin{bmatrix} E_r^+ \\ E_r^- \end{bmatrix} = \underbrace{\begin{bmatrix} e^{-jk_z d} & 0 \\ 0 & e^{jk_z d} \end{bmatrix}}_{\overline{\overline{M}}_{\text{prop}}} \begin{bmatrix} E_l^+ \\ E_l^- \end{bmatrix} . \tag{A.15}$$

To solve for the propagation constant, or effective index, of the mode of a slab waveguide, the appropriate reflection and propagation matrices need to be cascaded. For the four layer slab waveguide in Figure A-1, the complete matrix equation enforcing all of the boundary conditions is given by

$$\begin{bmatrix} 0 \\ E_4^- \end{bmatrix} = \overline{\overline{M}}_{\text{refln,3-4}} \overline{\overline{M}}_{\text{prop,3}} \overline{\overline{M}}_{\text{refln,2-3}} \overline{\overline{M}}_{\text{prop,2}} \overline{\overline{M}}_{\text{refln,1-2}} \begin{bmatrix} E_1^+ \\ 0 \end{bmatrix} , \tag{A.16}$$

where one field component in each outermost layer is not supported[1] as shown in Figure A-1. If the incident field is normalized to unit magnitude, then the matrix equation simplifies to

$$\begin{bmatrix} 0 \\ E_{x,4}^- \end{bmatrix} = \begin{bmatrix} M_{11} & M_{12} \\ M_{21} & M_{22} \end{bmatrix} \begin{bmatrix} 1 \\ 0 \end{bmatrix} . \tag{A.17}$$

Finally, the equation that must be solved to satisfy all the boundary conditions is simply

$$M_{11} = 0 . \tag{A.18}$$

As written, there are as many unknowns in equation (A.18) as there are layers, i.e. $k_{z,1}$,$k_{z,2}$, etc. However, by rewriting $k_z$as $k_z = \sqrt{k^2 - k_y^2}$, where $k^2 = \omega^2\mu\epsilon = \omega^2\mu_0\epsilon_0\mu_r\epsilon_r = k_0^2\mu_r\epsilon_r$ and μ_r and ϵ_r are the relative dielectric permeability and permittivity, respectively, the number of unknowns can be reduced to one. Phase matching requires k_y to be the same in all layers; therefore, the k_z's differ only in the material constants, μ and ϵ, which are known for each layer. Finally, a reduced, or relative, k_y can be defined $k_y' = \dfrac{k_y}{k_0}$, and

[1] Its magnitude is set to 0.

because the mode in the waveguide propagates in the y direction, $k_y' = \dfrac{\beta}{k_0}$ is **the effective index** of the slab waveguide mode. All of the elements of M_{11} can be rewritten using this notation

$$k_z = k_0\sqrt{\mu_r\epsilon_r - \left(k_y'\right)^2} \tag{A.19}$$

$$Z^{\mathrm{TE}} = Z_0\frac{\mu_r}{\sqrt{\mu_r\epsilon_r - \left(k_y'\right)^2}} \tag{A.20}$$

$$Z^{\mathrm{TM}} = Z_0\frac{\sqrt{\mu_r\epsilon_r - \left(k_y'\right)^2}}{\epsilon_r}, \tag{A.21}$$

where $Z_0 = \sqrt{\dfrac{\mu_0}{\epsilon_0}}$ is the impedance of free space, $\sim 377\Omega$. This effective index, k_y', becomes the single unknown in equation (A.18).

The effective index for the central strip region and the side etched regions are found by treating them as infinite slab waveguides and using the effective index technique described above. The etched regions will have lower effective indices than the strip region; therefore, they will act as cladding around a central core region. Thus, confinement, or guiding, is achieved in the lateral direction. Each of the three regions is treated as a material with

$$\mu_r \to 1 \quad \text{and} \quad \epsilon_r \to \left(k_y'\right)^2 , \tag{A.22}$$

where k_y' is the effective index, or reduced propagation constant, for the particular region. As shown in Figure 2-3, this treatment leads to a "sideways effective slab waveguide." If one is solving for a TE mode of the strip-loaded waveguide, then one first solves for a TE mode in the strip and etch regions and for a TM mode in the effective slab waveguide. This change is required because the effective slab waveguide is rotated ninety (90) degrees relative to the other slab waveguides.

After determining the effective index of the mode, the field and power profiles can be calculated using the now completely determined reflection and propagation matrices. For the example depicted in Figure A-1 and described by equation (A.16) and equation (A.17), the incident plane wave in layer 1 is normalized to unit magnitude, which means that for a

TE mode, the x component of the electric field in layer 1 evaluated at $y = 0$ is

$$E_{x,1} = E_{x,1}^{+} e^{-jk_{z,1}z} = e^{-jk_{z,1}z} \ , \tag{A.23}$$

where $k_z$can be determined using equation (A.19). The coefficient vector in equation A.16 and equation A.17 can therefore be interpreted as

$$\begin{bmatrix} E_{x,1}^{+} \\ E_{x,1}^{-} \end{bmatrix} = \begin{bmatrix} 1 \\ 0 \end{bmatrix} \ . \tag{A.24}$$

The implicit assumption is that $z = 0$ occurs at the layer 1-layer 2 boundary. The functional form of the electric field in layer 2 at an arbitrary y location is given in equation A.3. The coefficients can be determined by

$$\begin{bmatrix} E_{x,2}^{+} \\ E_{x,2}^{-} \end{bmatrix} = \overline{\overline{M}}_{\text{refln,1-2}} \begin{bmatrix} E_{x,1}^{+} \\ E_{x,1}^{-} \end{bmatrix} = \overline{\overline{M}}_{\text{refln,1-2}} \begin{bmatrix} 1 \\ 0 \end{bmatrix} \ . \tag{A.25}$$

Evaluating equation A.3 at $y = 0$ with the coefficients found above yield the field profile in layer 2. Using the next propagation matrix and reflection matrix, the coefficients for the next layer can be found. In this manner, the matrices transfer the initial field coefficients through all of the layers. As in calculating the effective index in the orthogonal direction, calculating the field profile in that direction involves the same procedure with material properties for the layers as in equation A.22. The total two-dimensional profiles are obtained by multiplying the field expressions with x and with z variation. For a TE mode, the x directed electric field is sought, while for a TM mode, the z directed electric field is sought.

The power profile, or distribution, of the mode is directly related to the electric field profile. By calculating the power distribution, the fill factor of the mode in the absorber layer can be calculated. For an electromagnetic wave, time averaged power flowing through a closed surface is [130]

$$P = \frac{1}{2} \Re \left\{ \oint_S \overline{E} \times \overline{H}^{*} \cdot \mathrm{d}\overline{S} \right\} \ , \tag{A.26}$$

where S is the surface in question and $\mathrm{d}\overline{S}$ is normal to that surface. For a TE mode, which in my formalism and coordinate convention only has components E_x, H_y, and H_z, the power expression becomes

$$P = \frac{1}{2}\Re\left\{\int\int_{\{x,z\}} -E_x H_z^* \,\mathrm{d}x\,\mathrm{d}z\right\} \ . \tag{A.27}$$

because the surface in question is the xz plane that represents a slice through the strip-loaded waveguide orthogonal to the direction of propagation of the mode. Recognizing that $H_z = -\dfrac{k_y}{\omega\mu}E_x$, the TE mode power expression can further be rewritten as

$$P = \Re\left\{\frac{k_y}{2\mu\omega}\right\}\int\int_{\{x,z\}} |E_x|^2 \,\mathrm{d}x\,\mathrm{d}z = \frac{1}{2Z_0}\Re\left\{\frac{k_y'}{\mu_r}\right\}\int\int_{\{x,z\}} |E_x|^2 \,\mathrm{d}x\,\mathrm{d}z \tag{A.28}$$

For a TM mode, equation A.26 reduces to

$$P = \frac{1}{2}\Re\left\{\int\int_{\{x,z\}} E_z H_x^* \,\mathrm{d}x\,\mathrm{d}z\right\} \tag{A.29}$$

Recognizing that for a TM mode, $E_z = \dfrac{k_y}{\omega\epsilon}H_x$, the expression can further be rewritten as

$$P = \Re\left\{\frac{k_y}{2\epsilon\omega}\right\}\int\int_{\{x,z\}} |H_x|^2 \,\mathrm{d}x\,\mathrm{d}z = \frac{Z_0}{2}\Re\left\{\frac{k_y'}{\epsilon_r}\right\}\int\int_{\{x,z\}} |H_x|^2 \,\mathrm{d}x\,\mathrm{d}z \tag{A.30}$$

A.2 Modeling Absorption

All of the dielectric layers are assumed to be lossless; therefore, they all have real permittivity, ϵ, and permeability, μ. The top LTG-GaAs absorber layer is lossy, but such a small fraction of the mode is coupled into that layer that it can be assumed lossless without affecting the calculations.

For a material with complex dielectric constant, the expression for power in a TE mode becomes

$$P = \frac{1}{2}\Re\left(\frac{k_y^*}{\omega\mu}\right) e^{2k_{y,i}y}\int\int_{\{x,z\}} |E_x|^2 \ \mathrm{d}x\,\mathrm{d}z \ , \tag{A.31}$$

where $k_{y,i} = \Im k_y$, the imaginary part of the reduced propagation constant, or effective

index. Therefore, the power absorption coefficient, α, is, as expected, double the field attentuation coefficient. At least two approaches exist to calculate $k_{y,i}$ for the strip-loaded waveguide structure. The more rigorous technique is to use an complex dielectric permittivity for the LTG-GaAs layer and solve the effective index problem with complex numbers. An interesting and general approximation is derived by considering the power in the different regions of the guide. For illustration, consider a mode propagating in the y direction and varying only in the x direction. The mode is partly in an absorbing region and partly in a (non-absorbing) guiding region. If the absorption is small (mathematically, $|k_i| \ll |k_r|$), the field propagates in the guide region according to $e^{-jk_r y}$ and in the absorbing region according to $e^{-jk_r y} e^{k_i y}$. Then, if $P(y)$ denotes the power at position y, ζ denotes the fraction of the total power in the absorbing region, and δy denotes a small increment of distance,

$$P_{\text{tot}}(y) = P_{\text{a}}(y) + P_{\text{g}}(y) \tag{A.32}$$

$$P_{\text{tot}}(y + \delta y) = \zeta P_{\text{tot}}(y) e^{-2|k_i|\delta y} + (1 - \zeta) P_{\text{tot}}(y) , \tag{A.33}$$

where the subscripts tot, a, and g label power in total, in the absorber and in the guide, respectively. Rearranging terms yields the difference equation,

$$\frac{P_{\text{tot}}(+\delta y) - P_{\text{tot}}(y)}{\delta y} = \zeta P_{\text{tot}}(y) \left(\frac{e^{-2|k_i|\delta y} - 1}{\delta y} \right) . \tag{A.34}$$

Taking the limit as $\delta y \to 0$ yields the differential equation,

$$\frac{dP_{\text{tot}}(y)}{dy} = -2 |k_i| \zeta P_{\text{tot}}(y) , \tag{A.35}$$

which assuming a known amount of total power at $y = 0$ yields

$$P_{\text{tot}}(y) = P_{\text{tot}}(0) e^{-2|k_i|\zeta y} . \tag{A.36}$$

Therefore, if a mode is partially an absorbing region, the mode absorption coefficient can be determined by multiplying the absorbing region's bulk absorption coefficient, $2|k_i|$, by the mode's fill factor in the absorber, ζ. The mode extinction length is the inverse of the

absorption coefficient and can then be calculated by

$$\ell_{\text{ext}} = \frac{1}{2|k_i|\zeta} = \left(\frac{4\pi f}{c} k\zeta\right)^{-1} \tag{A.37}$$

where due to an unfortunate overlap of naming conventions, k_i is the imaginary part of the mode propagation constant and k is the imaginary part of the complex index of refraction ($\tilde{n} = n + jk$). This approximation will hold as long as the mode distribution calculated assuming non-absorbing regions does not change when absorption is considered. This qualification is equivalent to the initial qualification that the absorption be slight. The practical meaning is that the mode profile can be calculated with all real dielectric coefficients and the extinction length can be approximated to good accuracy using the absorber fill factor. Finding real roots is much simpler and faster than finding complex roots, so this saves a lot of time when performing numerous iterations. For final refinement of a design, the full complex dielectric constant can be used. The quantitative difference between these approaches is discussed in Section 2.1.3.

A.3 Fill Factor Calculations using the Method of Shadows

Figures A-5, A-6, and A-7 present calculations of the fill factor in a 1000 Å LTG-GaAs absorber layer on top of a slab waveguide with given dimensions and layers compositions. These figures are mentioned in Section 2.1.3.

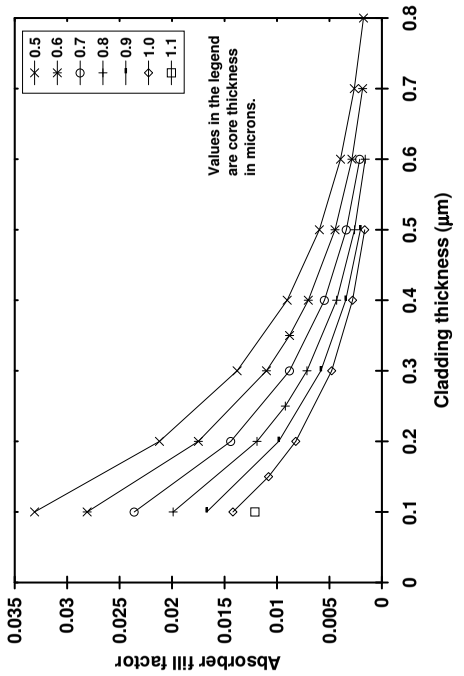

(a) $\Delta n = 0.029$.

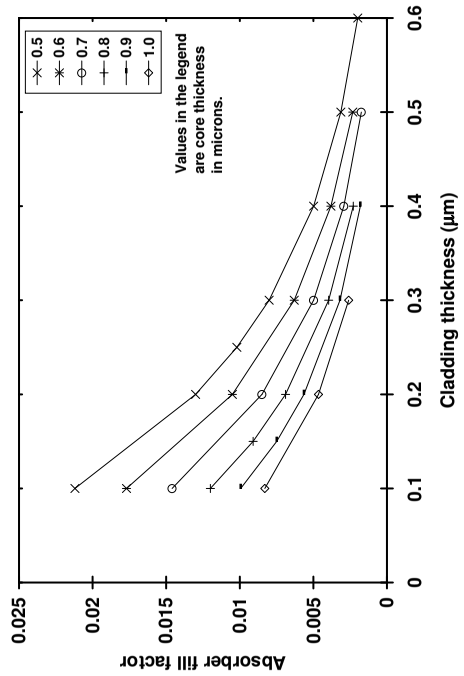

(b) $\Delta n = 0.032$.

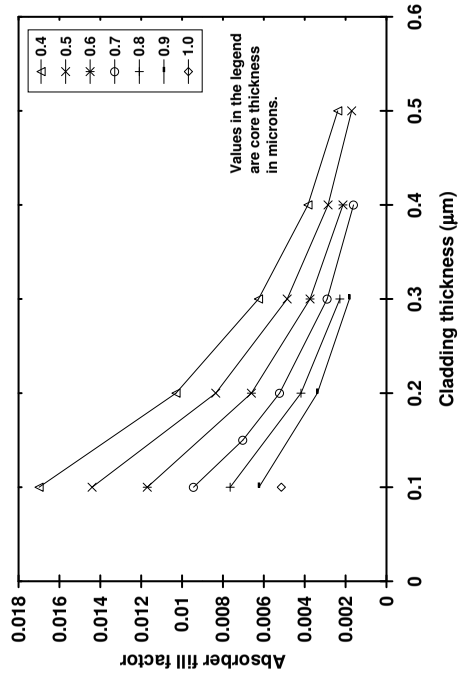

(c) $\Delta n = 0.037$.

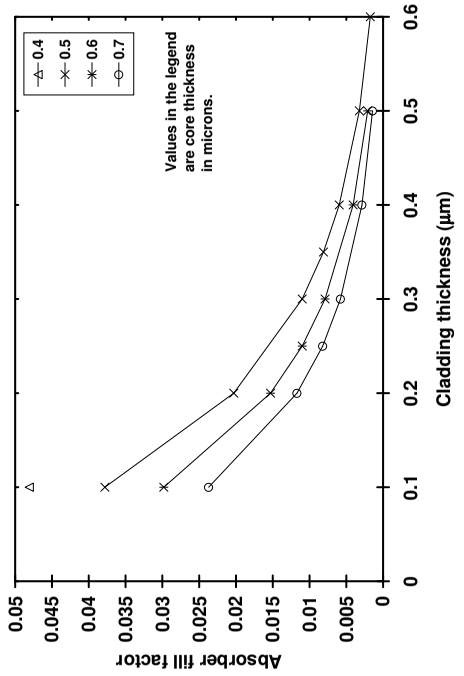

(d) $\Delta n = 0.053$.

Figure A-5: Absorber fill factor for core/cladding Al compositions of: a) 0.30/0.35, b) 0.20/0.25, c) 0.10/0.15, d) 0.30/0.40.

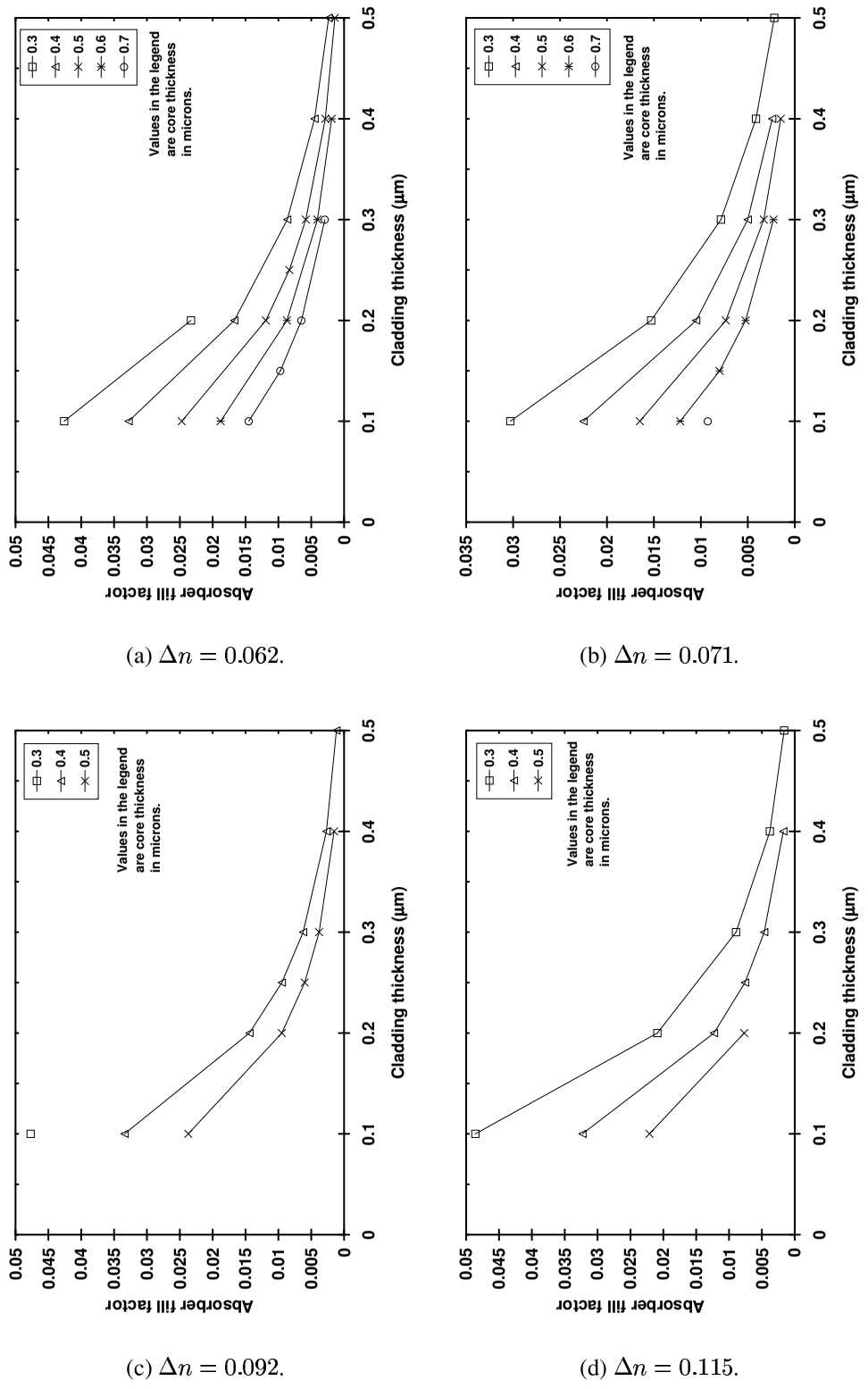

(a) $\Delta n = 0.062$.

(b) $\Delta n = 0.071$.

(c) $\Delta n = 0.092$.

(d) $\Delta n = 0.115$.

Figure A-6: Absorber fill factor for core/cladding Al compositions of: a) 0.20/0.30, b) 0.10/0.20, c) 0.20/0.35, d) 0.20/0.40.

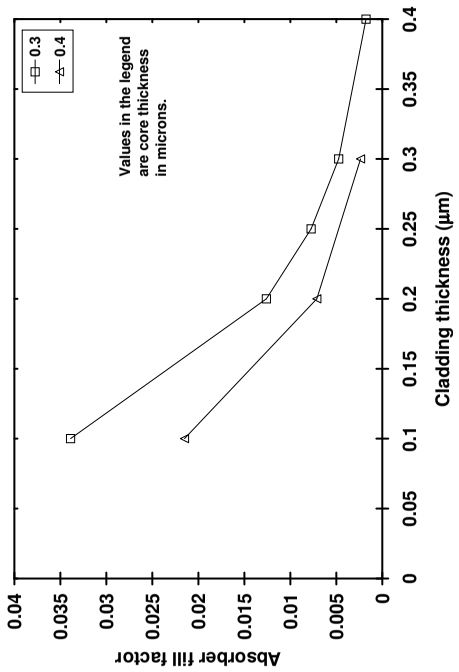

(a) $\Delta n = 0.133$.

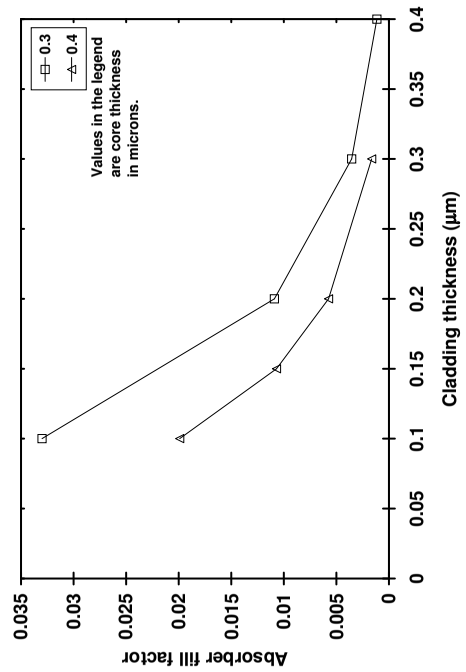

(b) $\Delta n = 0.162$.

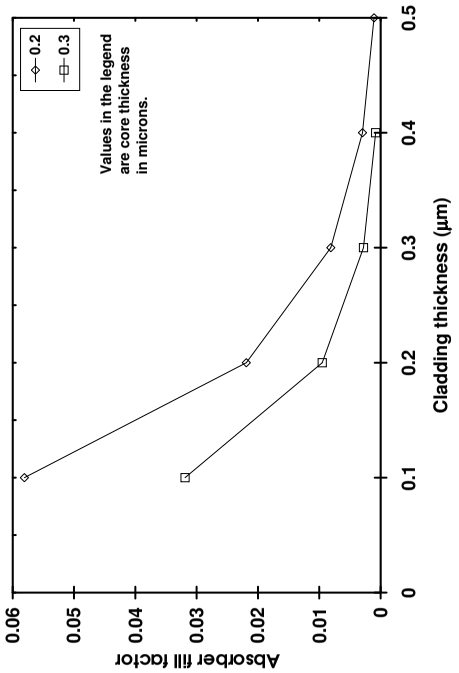

(c) $\Delta n = 0.186$.

Figure A-7: Absorber fill factor for core/cladding Al compositions of: a) 0.10/0.30, b) 0.10/0.35, c) 0.10/0.40.

Appendix B

Scriber Operation

This appendix contains operating procedures for the Loomis Scriber in C-400 of MIT Lincoln Laboratory.

B.1 Startup

These startup procedures are performed once per scribing session.

1. Turn on the air flow valve to 50 pounds per square inch (psi).

2. Turn on the vacuum pump used to hold samples to the vacuum stage.

3. Lower hook located near the back of the scribing mechanism (ram), and pull the ram forward to the end of its range of motion. Push the ram back to its original position and raise the hook.

4. Flip the power switch (labelled "MASTER") to the left. The scriber will run through a limit check in which it moves the ram and the vacuum stage. If the ram stops moving in the middle of this limit check and red LEDs flash, the hook has lost electrical contact with the metal cylinder it should be touching. Hold the hook to the cylinder and toggle the MASTER switch, while continuing to hold the hook to the cylinder.

B.2 Scriber Adjustment

These adjustment procedures are performed once per scribing session, unless the wafer height is changed in which case the ram height must be adjusted.

1. Place a piece of scrap wafer on the vacuum stage and turn on the vacuum, verifying that the gauge shows at least 20 inches of Hg.

2. Focus on the surface of the wafer using the metal knob at the bottom of the scope tube.

3. Make a test scribe by flipping the switch on the left of the scriber from INDEX to AUTO and then flipping the ACTUATE switch to the left or right. While the ram is in motion, return the switch from AUTO to INDEX so that only one scribe is made.

4. Set the force of the scribe on the pressure meter, which is above and to the left of the ram. The gauge should show ~ 14 as read on the inner dial. The knob near the gauge is used to adjust the pressure.

5. Set the air flow so that the meter reads between 2 and 3. Note that the setting of the air flow is coupled to the force of the ram so these two settings must be iterated.

6. Set the height of the ram so that the scribe is ~ 14 divisions long as seen through the scope. Turning the height adjustment knob counterclockwise raises the stage and makes the scribe shorter.

7. Move to a new spot on the wafer by flipping the switch on the left of the scriber from INDEX to TRAVEL. This mode allows the ACTUATE switch to move the vacuum stage freely left or right, while the switch on the separate control box moves the stage forwards and backwards.

8. Make another single scribe and adjust the cross-shaped reticle seen through the scope so that the scribe is centered left-to-right on it and the end of the

scribe is at the top of the cross. The small, vertically-mounted knob adjusts the stage forwards and backwards (up and down as seen through the scope) and the large, metallic, horizontally mounted knob adjusts the scope left and right. The small, anodized knob next to the left-right adjuster is a locking screw and should not be touched.

9. Move to a new place on the wafer and make a new scribe to verify that the scope placement settings are correct.

10. Move to a new place on the wafer and make a series of scribes by flipping the switch on the left from INDEX to AUTO and then flipping the ACTUATE switch to the left or right. The scriber will make scribes separated by the distance set by the thumb wheels on the front of the scriber until the switch is returned to INDEX. Verify that the scribes are uniform and evenly spaced.

B.3 Scribing and Cleaving the Device Wafer

After performing the steps in Section B.1 and Section B.2, the following steps are used to scribe the device wafer. After thinning and polishing, the edges of the wafer will be rounded, and an optical quality facet is not achievable. The facets of interest should be third-generation cleaves. The initial edge should be scribed and cleaved, yielding a sharp, but probably not flat edge. This new edge is scribed and cleaved, and then this second-generation edge is scribed for the device facets' cleaving. The steps in this section are generic for any of these scribe and cleave steps. For the initial scribe and cleave, the initial alignment will be more difficult because of the rounded edges, but it is also less critical. The initial cleave should be $\sim 500\,\mu$m from the edge, if possible. To perform multiple cleaves at the same time, use the AUTO/ACTUATE switch combination and set the increment distance using the thumbwheels as when using INDEX/ACTUATE. Stop the scriber by flipping the AUTO switch back to INDEX during the ram movement for the final scribe.

1. Place the wafer on the vacuum stage, and align the edge so that it is perpen-

dicular to the direction of the scribe. Rotating the vacuum stage by hand sets coarse angle before the vacuum is activated. For finer movements, the knob on the left side of the stage moves the stage left and right, while the knob on the right side rotates the stage. Alignment is determined by translating the wafer left and right (using the TRAVEL/ACTUATE switch combination) and watching it pass by a fixed spot on the scope reticle. Rotate the vacuum stage such that the entire edge of the wafer passes the same spot on the reticle as it moves from one extreme to the other.

2. Move the wafer so that the scribe will be the desired distance from the edge. The wafer can be translated by fixed amounts by setting the thumbwheels on the front of the scriber to the distance in microns and then using the INDEX/ACTUATE switch combination.

3. Align the reticle so that the horizontal part of the cross is centered on the wafer edge.

4. Make a single scribe mark or multiple scribe marks if multiple cleaves are to be performed simultaneously. If the edge is good, the scribe ends in a V-shaped notch at the edge of the wafer.

5. Turn off the vacuum by flipping the switch to the right.

6. Place the wafer scribed side up on the thin plastic available in a large roll near the scriber.

7. Cover the wafer with the square, thick "cleaving plastic," pressing the two pieces of plastic together firmly to ensure good adhesion.

8. The cleaving apparatus is simply a thick, wide piece of metal curved like a bow with a thinner aluminum sheet between the ends. The slight bowing in of this thin sheet allows the wafer to flex and the scribes to propagate. Align the wafer so that the scribes are parallel to the bowing of the aluminum sheet and facing down, into the sheet.

9. Roll a steel rod over the back of the wafer, guiding the rod either with a finger of another steel rod. The cracks as the wafer cleaves are audible.

10. Inspect the cleaved facets.

B.4 Turning off the Scriber

These shutdown procedures are performed once per scribing session.

1. Turn off the vacuum pump.

2. Turn off the air-flow valve.

3. Flip the MASTER power switch to the right.

Appendix C

Gratings near resonance

Modelling of gratings (periodic arrangements of infinitely-long metal structures) has been the subject of extensive work over many years [131]. To calculate accurately the optical power absorbed in my test structures which have parallel metal electrodes that form a grating, I need to calculate total power transmission through a grating on a substrate for which the wire diameter (d) and the grating period (p) are both comparable to a wavelength (λ) of the incident radiation. To my knowledge, a closed-form expression for this geometry does not exist.

Gratings for which $p \ll \lambda$ can be accurately and simply modeled using transmission line analysis with equivalent circuit models. A grating for which the incident electric field is perpendicular to the wires is modeled as a capacitive obstacle, because most of the stored energy is electric. Conversely, with electric field parallel to the wires, the obstacle is inductive. When the wires on the same order as the wavelength ($d \sim \lambda$), the model is modified to a Π or T circuit as in Figure C-1, where the new elements introduce reactance of the other type [104]. This modification can be understood by considering that for a capacitive grating with $d \sim \lambda$, inductive elements accounts for inductance arising from the field's traversing of the wire's diameter while passing throught the grating. Near resonance, where more than one mode is transmitted and reflected from the grating, these models break down because they are single mode by nature. To solve the problem of accounting for power lost to higher order modes, Blanco, *et al.* derived equivalent circuit models which incorporate resistive elements, thus reducing the transmission coefficient of the lowest order mode [104]. I

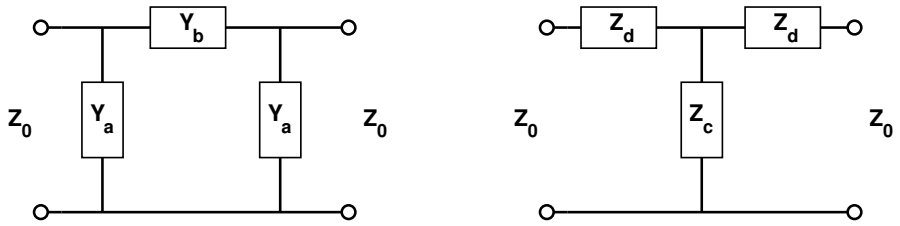

(a) Equivalent circuit for a capacitive grid, i.e. electric field perpendicular to the electrodes.

(b) Equivalent circuit for a inductive grid, i.e. electric field parallel to the electrodes.

Figure C-1: Equivalent circuits for gratings in free space.

present transmission coefficient expressions which are simpler but algebraically equivalent to theirs in Section C.2. I also present an expression for the reflection coefficient.

The final piece of this analysis is accounting for the effect of the substrate on the grating. From the work of [107], the effect of a substrate on the equivalent circuit of a grating is to scale the capacitive components by the average of the real part of the dielectric constant, i.e.

$$C' = \frac{n_1^2 + n_2^2}{2} C \text{ or } X_C' = \frac{2}{n_1^2 + n_2^2} X_C \ , \tag{C.1}$$

where n_1 and n_2 are the indices of refraction of the materials on either side of the grating and C denotes a capacitance in the free-space grating equivalent circuit, while X_C is the corresponding impedance. The capacitive parts of the circuits in Figure C-1 were modified accordingly. The model predictions shown in Figure C-2 and Figure C-3 for grating geometries that correspond to my test structure electrode geometries values of d/p. For my test structures, $\lambda = 0.8\,\mu$m, $d = 0.2\,\mu$m, and $p = 0.8\,\mu$m or $p = 0.4\,\mu$m.

C.1 Predictions of the Grating Circuit Model

The intermediate cases for which the grating and substrate are considered separately correspond to $T_{\text{tot}} = T_{\text{grating,fs}} T_{\text{subs}}$. The coating was accounted for by adjusting n_1. For the 0.4-μm-gap structure, $n_1 = 2.0$, while for the 0.8- μm-gap structure, $n_1 = 0.65(1) + 0.35(2.0)$.

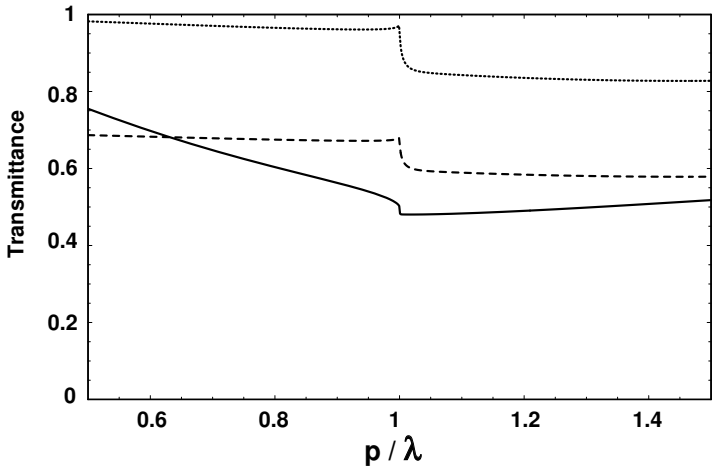

(a) $d/p = 0.2$.

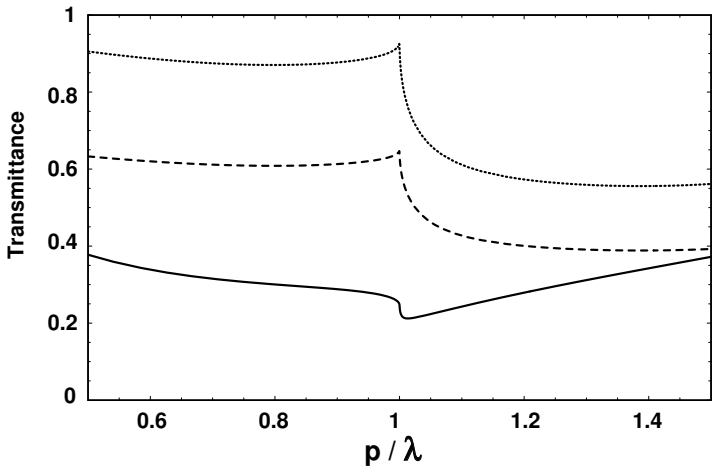

(b) $d/p = 1/3$.

Figure C-2: Transmission through a grating on a substrate with $n = 3.43$ as a function of the grating period to wavelength ratio. The traces are transmission through: the grid in free space ($\cdots$), a grid and into the substrate as separate effects ($- - -$), and the complete model of a grid modified by the substrate (—).

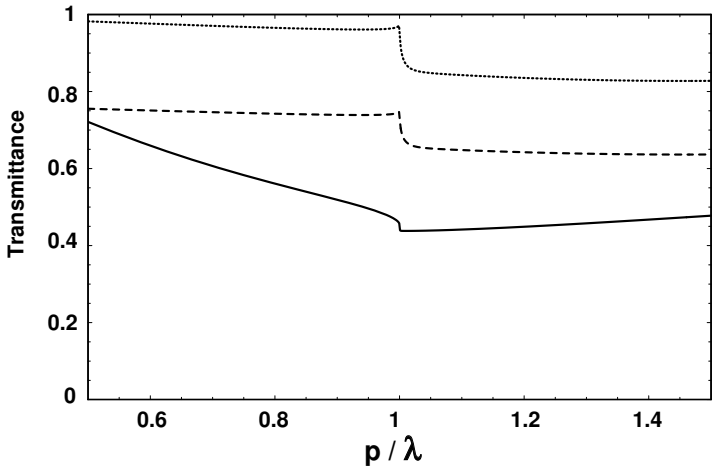

(a) $d/p = 0.2$.

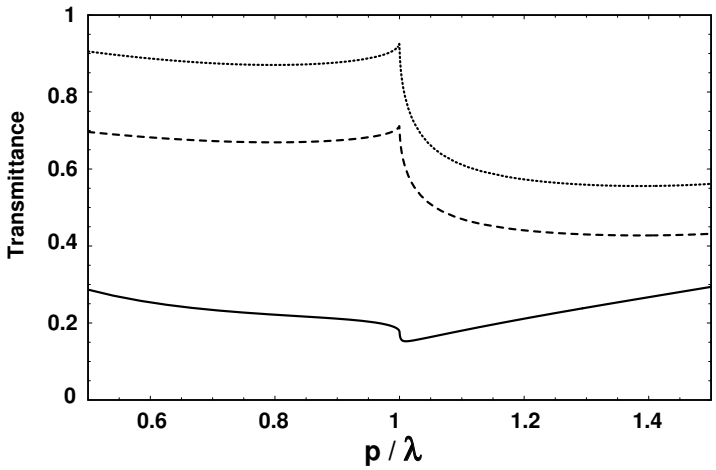

(b) $d/p = 1/3$.

Figure C-3: Transmission through a grating on a substrate with $n = 3.43$ and a coating with $n = 2$ as a function of the ratio the grating period to incident wavelength ratio. The traces are: transmission through: the grid in free space ($\cdots$), a grid and into the substrate as separate effects ($- - -$), and the complete model of a grid modified by the substrate (—).

C.2 Expressions for the Grating Circuit Model

The reflection (S_{11}) and transmission (S_{21}) coefficients for a capacitive grating modeled by Figure C-1(a) are given by

$$S_{11} = \frac{Y_0^2 - Y_a(Y_a + 2Y_b)}{(Y_0 + Y_a)(Y_0 + Y_a + 2Y_b)} \tag{C.2}$$

$$S_{21} = \frac{2Y_0 Y_b}{(Y_0 + Y_a)(Y_0 + Y_a + 2Y_b)}\,, \tag{C.3}$$

where in terms of quantities given in [104], $Y_0 = Z_0^{-1} = \sqrt{\epsilon/\mu}$, $Y_a = Z_a^{-1}$, and $Y_b = Z_b^{-1}$. The corresponding expression for the inductive grating in Figure C-1(b) are

$$S_{11} = \frac{-Z_0^2 + Z_d(Z_d + 2Z_c)}{(Z_0 + Z_d)(Z_0 + Z_d + 2Z_c)} \tag{C.4}$$

$$S_{21} = \frac{2Z_0 Z_c}{(Z_0 + Z_d)(Z_0 + Z_d + 2Z_c)}\,, \tag{C.5}$$

where in the impedances are all as given in [104]. The power reflection and transmission coefficients are $|S_{11}|^2$ and $|S_{21}|^2$, respectively.

As a convenience to the interested reader, the expressions for Z_a, Z_b, Z_c, and Z_d are reproduced here taken directly from Blanco, *et al.* [104].

$$\frac{Y_a}{Y_0} = \frac{Z_0}{Z_a} = i f_a(p, d, \lambda) \tag{C.6}$$

$$\frac{Y_b}{Y_0} = \frac{Z_0}{Z_b} = i f_b(p, d, \lambda) \tag{C.7}$$

$$f_a(p, d, \lambda) = \frac{p}{2\lambda}\left(\frac{\pi d}{p}\right)^2 \frac{1}{A_2} \tag{C.8}$$

$$f_b(p, d, \lambda) = \frac{2\lambda}{p}\left(\frac{p}{\pi d}\right)^2 A_1 - \frac{p}{4\lambda}\left(\frac{\pi d}{p}\right)^2 \frac{1}{A_2} \tag{C.9}$$

$$A_1 = 1 + \frac{1}{2}\left(\frac{\pi d}{\lambda}\right)^2 \left(\ln\frac{p}{\pi d} + \frac{3}{4}\right) + \frac{1}{2}\left(\frac{\pi}{d}\right)^2 \sum_{m=1}^{\infty}\left(\frac{1}{C_m} - \frac{1}{m}\right) \tag{C.10}$$

$$A_2 = 1 + \frac{1}{2}\left(\frac{\pi d}{\lambda}\right)^2 \left(\frac{11}{4} - \ln\frac{p}{\pi d}\right) + \frac{1}{24}\left(\frac{\pi d}{p}\right)^2 - \left(\frac{\pi d}{p}\right)^2 \sum_{m=1}^{\infty}\left[m - \frac{1}{2m}\left(\frac{p}{\lambda}\right)^2 - C_m\right] \tag{C.11}$$

$$C_m = \left[m^2 - \left(\frac{p}{\lambda} \right)^2 \right]^{1/2} \tag{C.12}$$

$$\frac{Z_c}{Z_0} = i f_c(p, d, \lambda) \tag{C.13}$$

$$\frac{Z_d}{Z_0} = -i f_d(p, d, \lambda) \tag{C.14}$$

$$f_c(p, d, \lambda) = \frac{p}{\lambda} \left[\ln \frac{p}{\pi d} + \sum_{m=1}^{\infty} \left(\frac{1}{C_m} - \frac{1}{m} \right) \right] \tag{C.15}$$

$$f_d(p, d, \lambda) = \frac{p}{\lambda} \left(\frac{\pi d}{p} \right)^2 , \tag{C.16}$$

where p is the grating period, d is the diameter of the grating wires, λ is the wavelength of the incident radiation, $i = \sqrt{-1}$ and Z_0 is the impedance of free space ($\sqrt{\mu/\epsilon}$). Empirically, 20 is a good approximation for ∞ in the summations.

Appendix D

Hardware Drawings

This appendix contains dimensioned drawings of all the custom hardware for distributed photomixer testing.

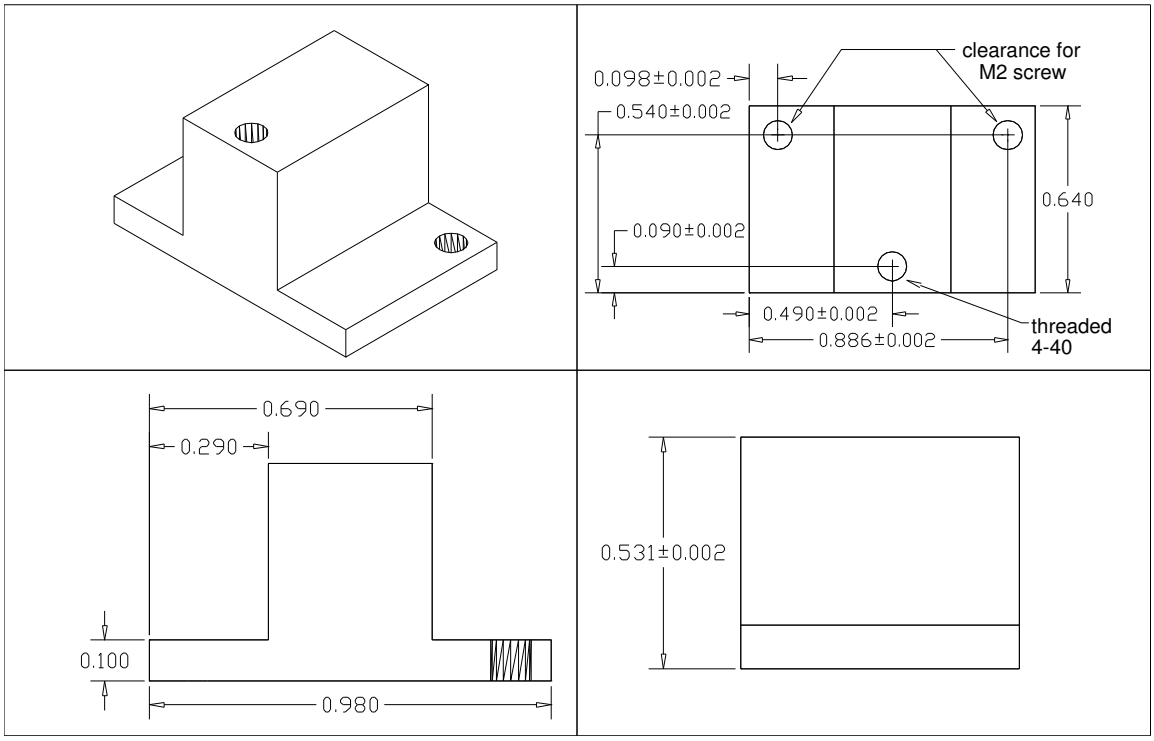

Figure D-1: Adapter between goniometer and beamsplitter. Dimensions are in inches.

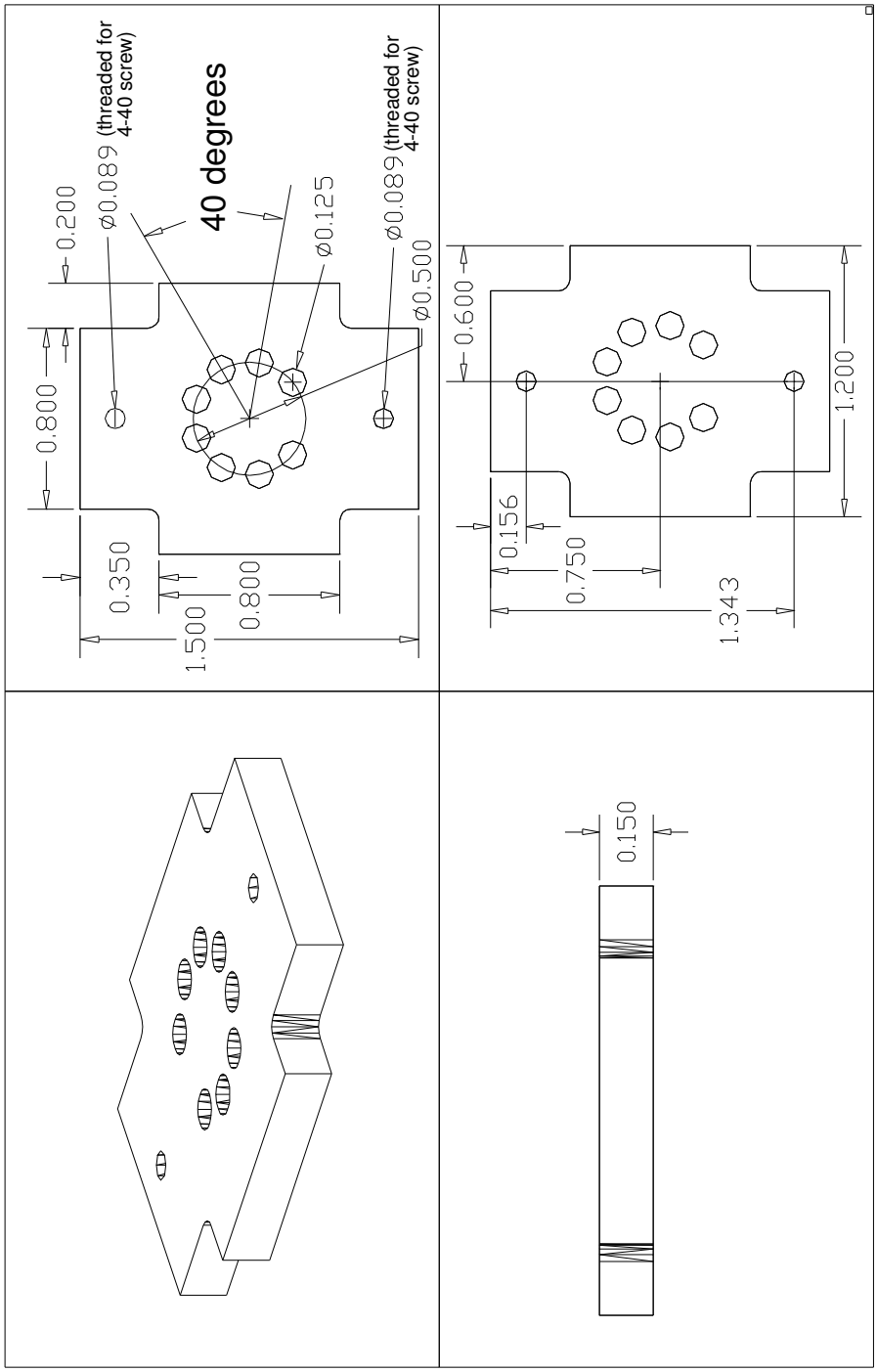

Figure D-2: Dimensioned adapter for TO3 laser package. Dimensions are in inches.

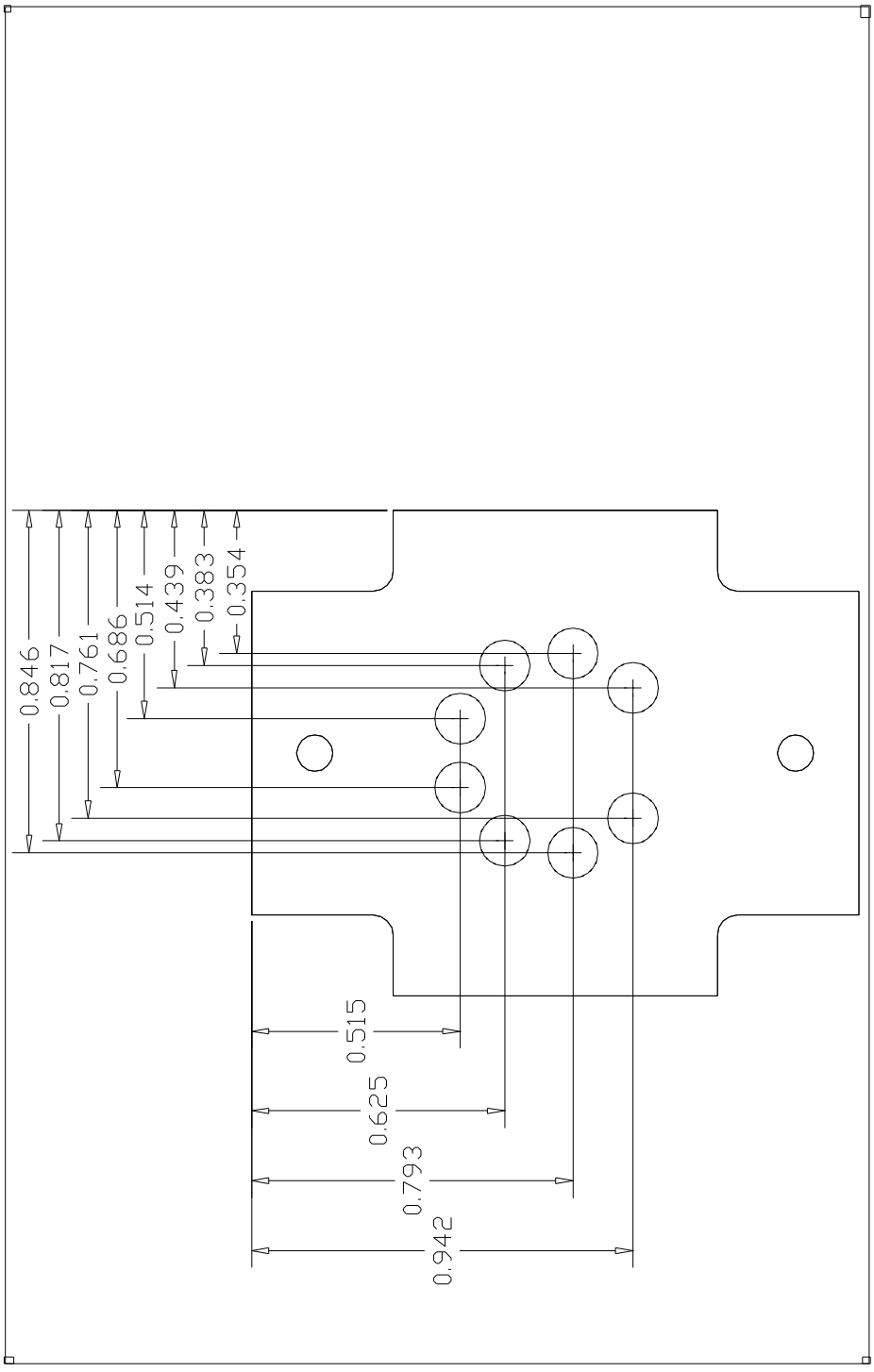

Figure D-3: Dimensioned adapter for TO3 laser package. Dimensions are in inches.

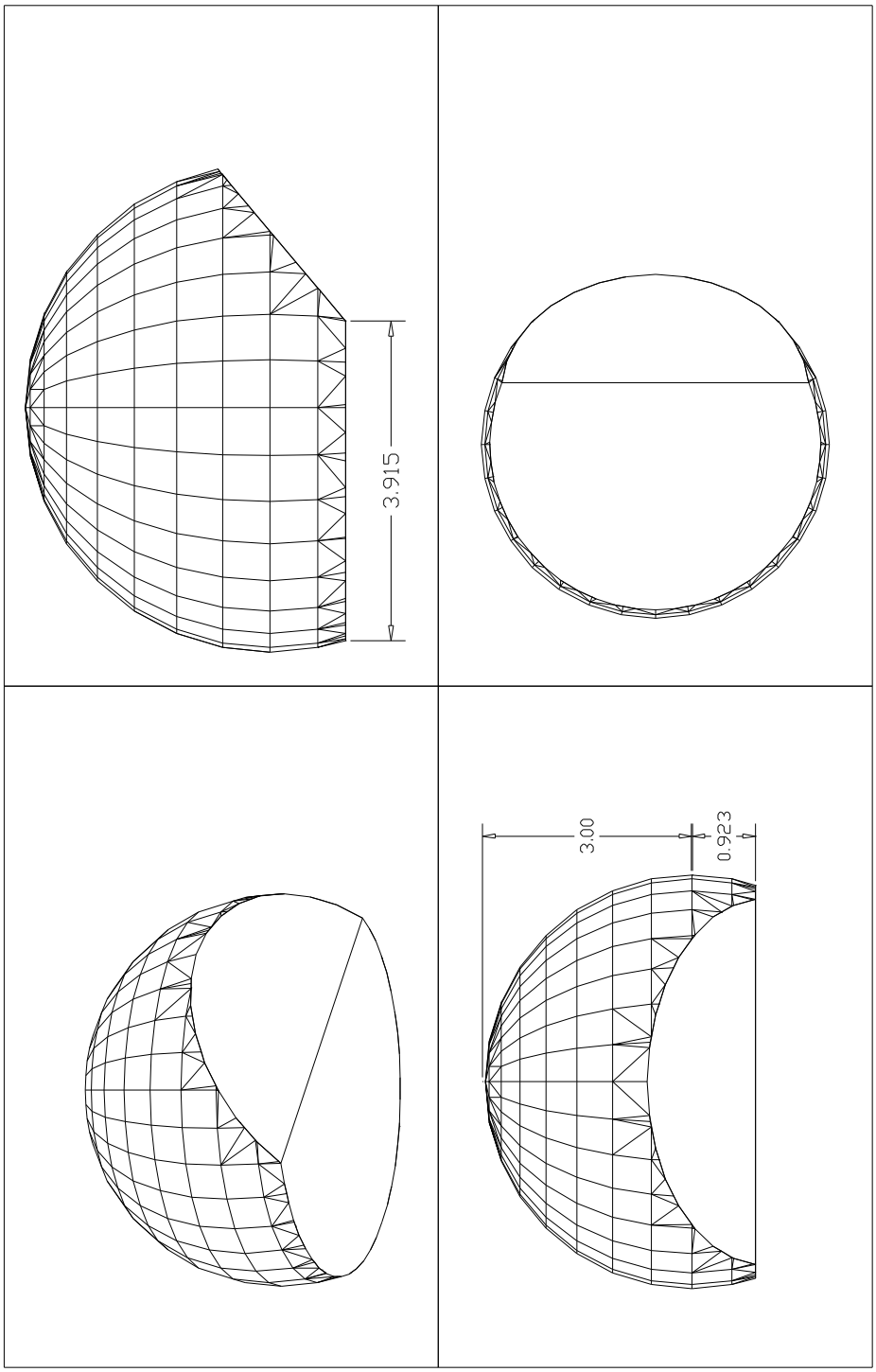

Figure D-4: Dimensioned Silicon hyperhemispherical lens. Dimensions are in millimeters.

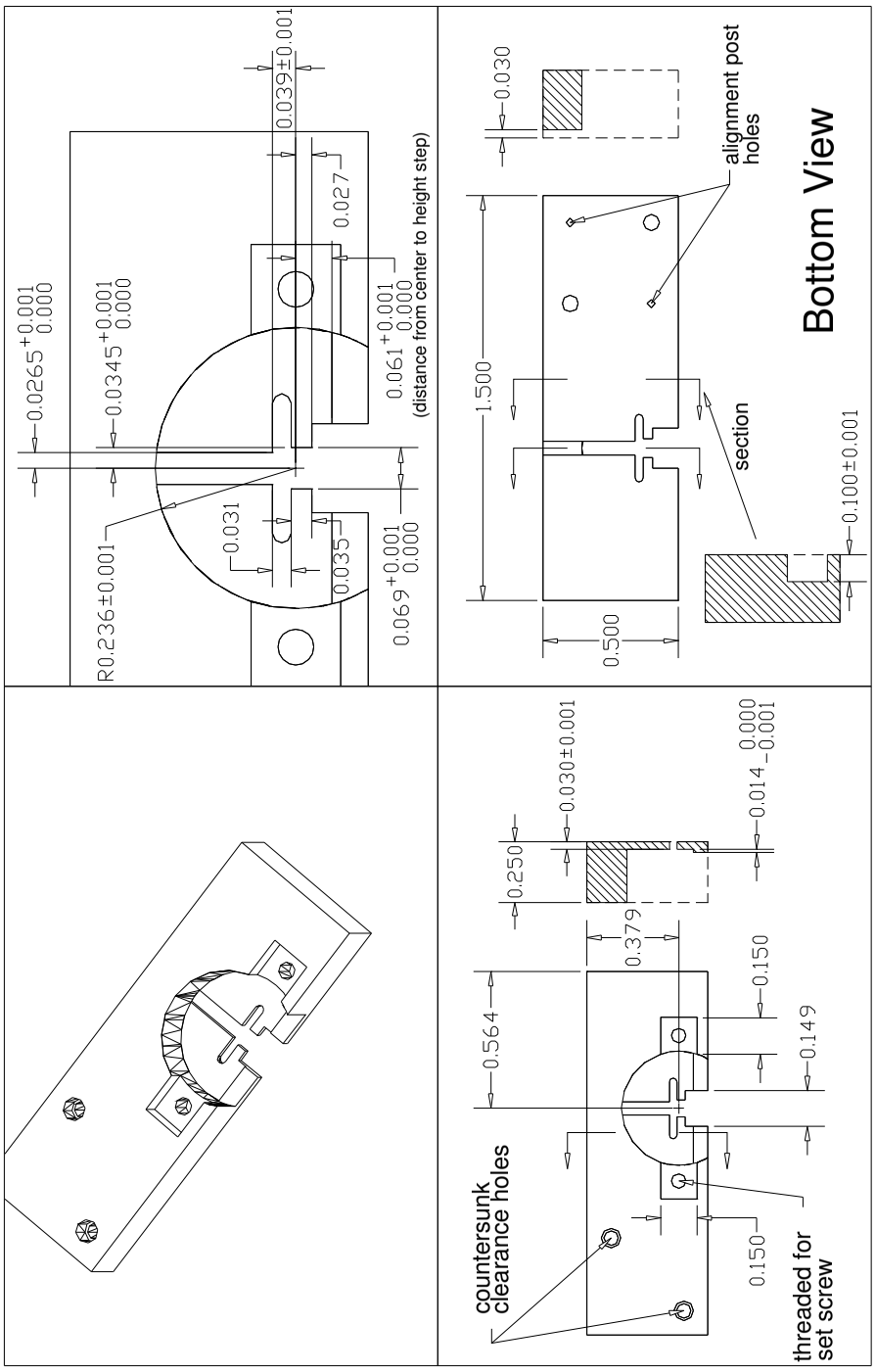

Figure D-5: Dimensioned upper part of mount for hyperhemispherical lens. Dimensions are in inches.

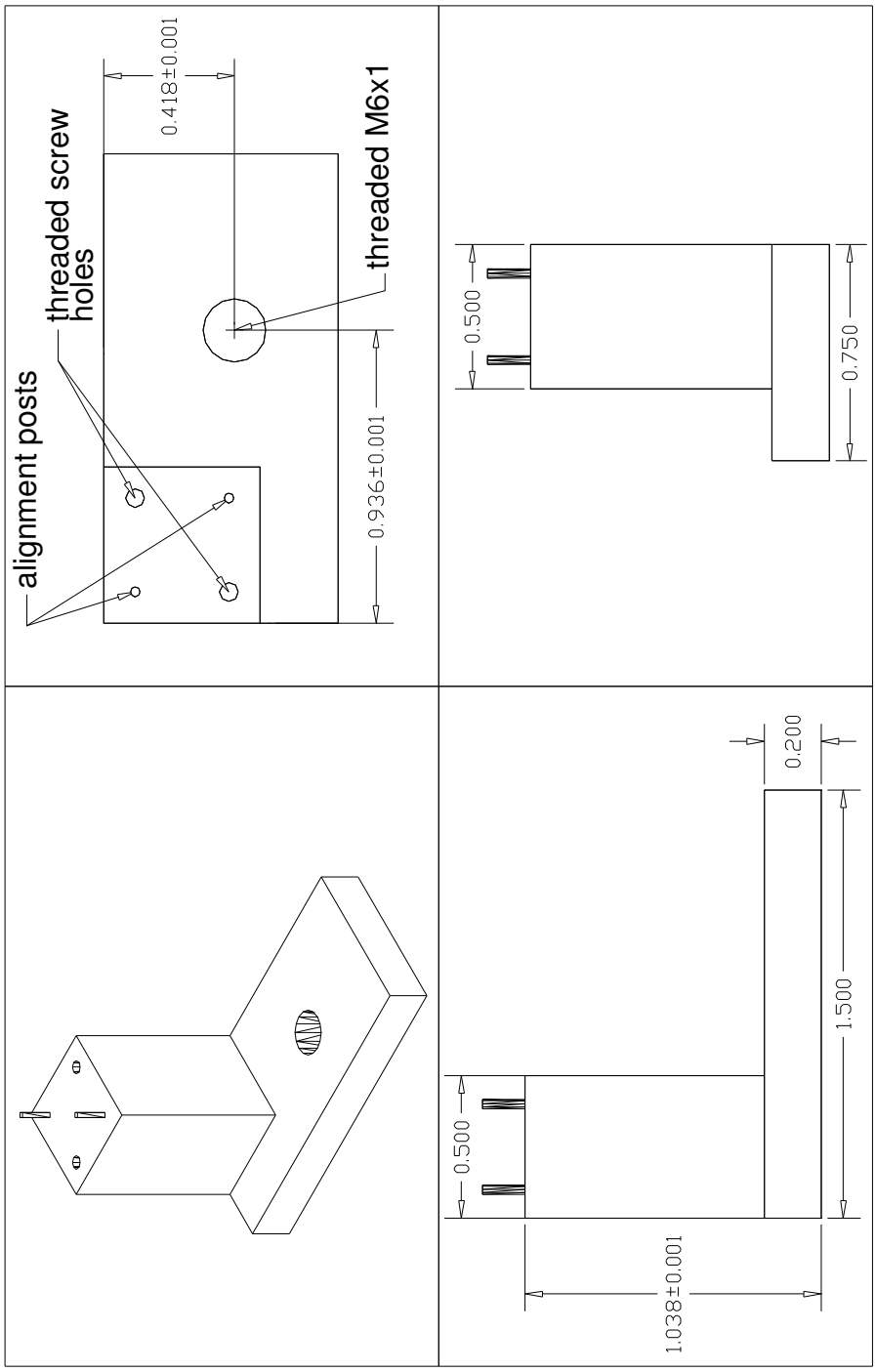

Figure D-6: Dimensioned base of mount for hyperhemispherical lens. Dimensions are in inches.

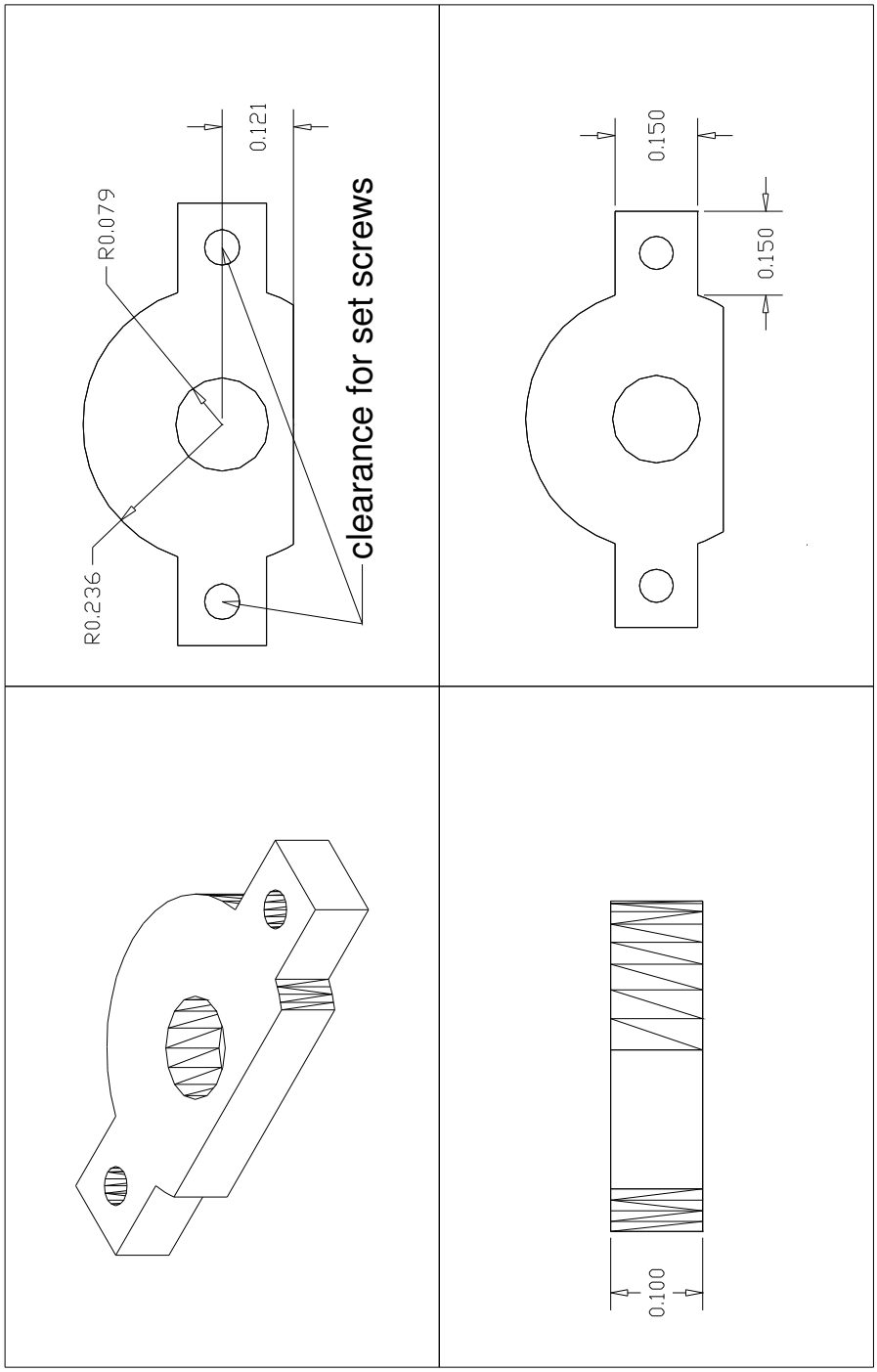

Figure D-7: Dimensioned holder for hyperhemispherical lens. Dimensions are in inches.

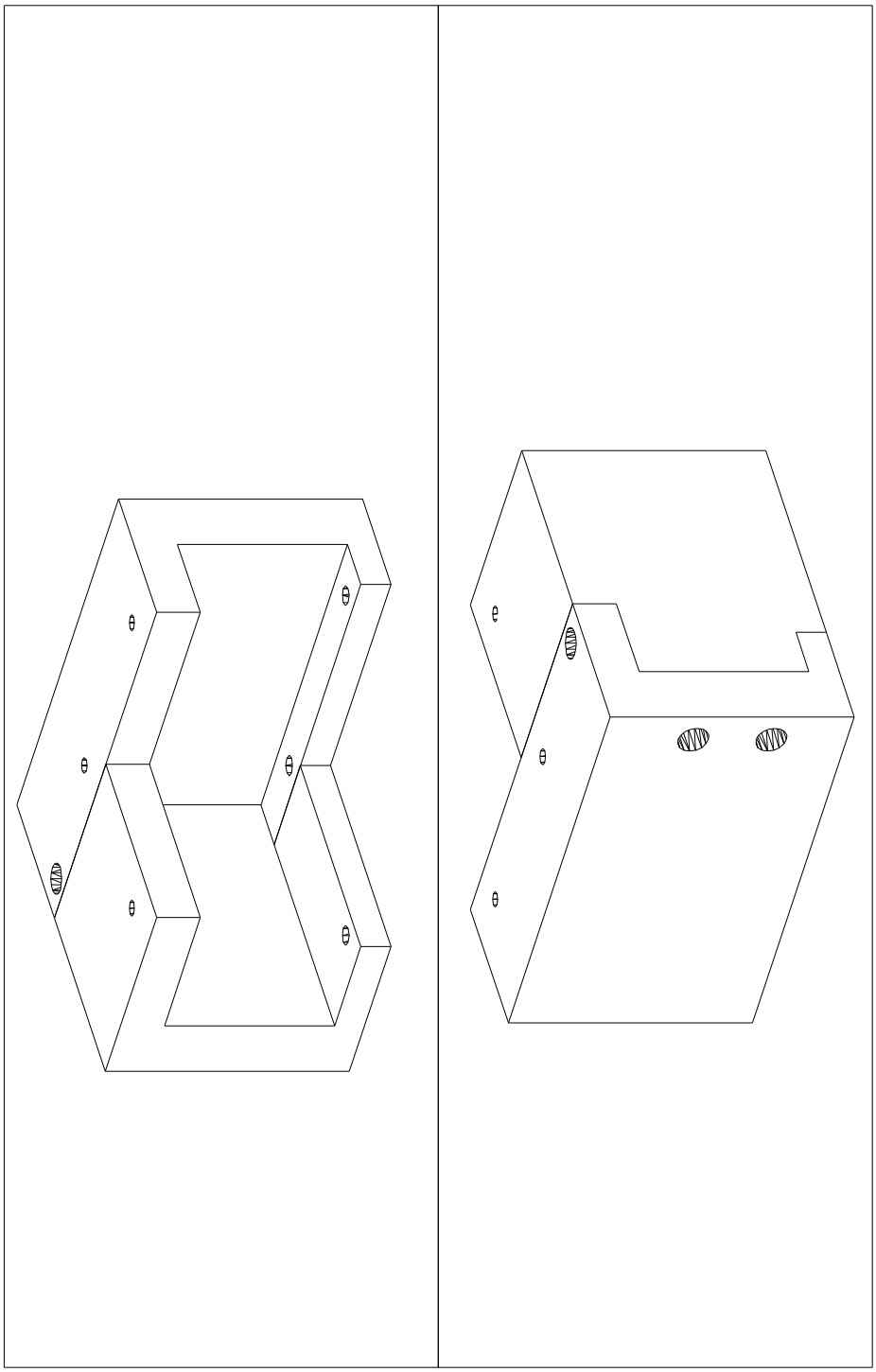

Figure D-8: Views of bracket for beamsplitter positioning hardware.

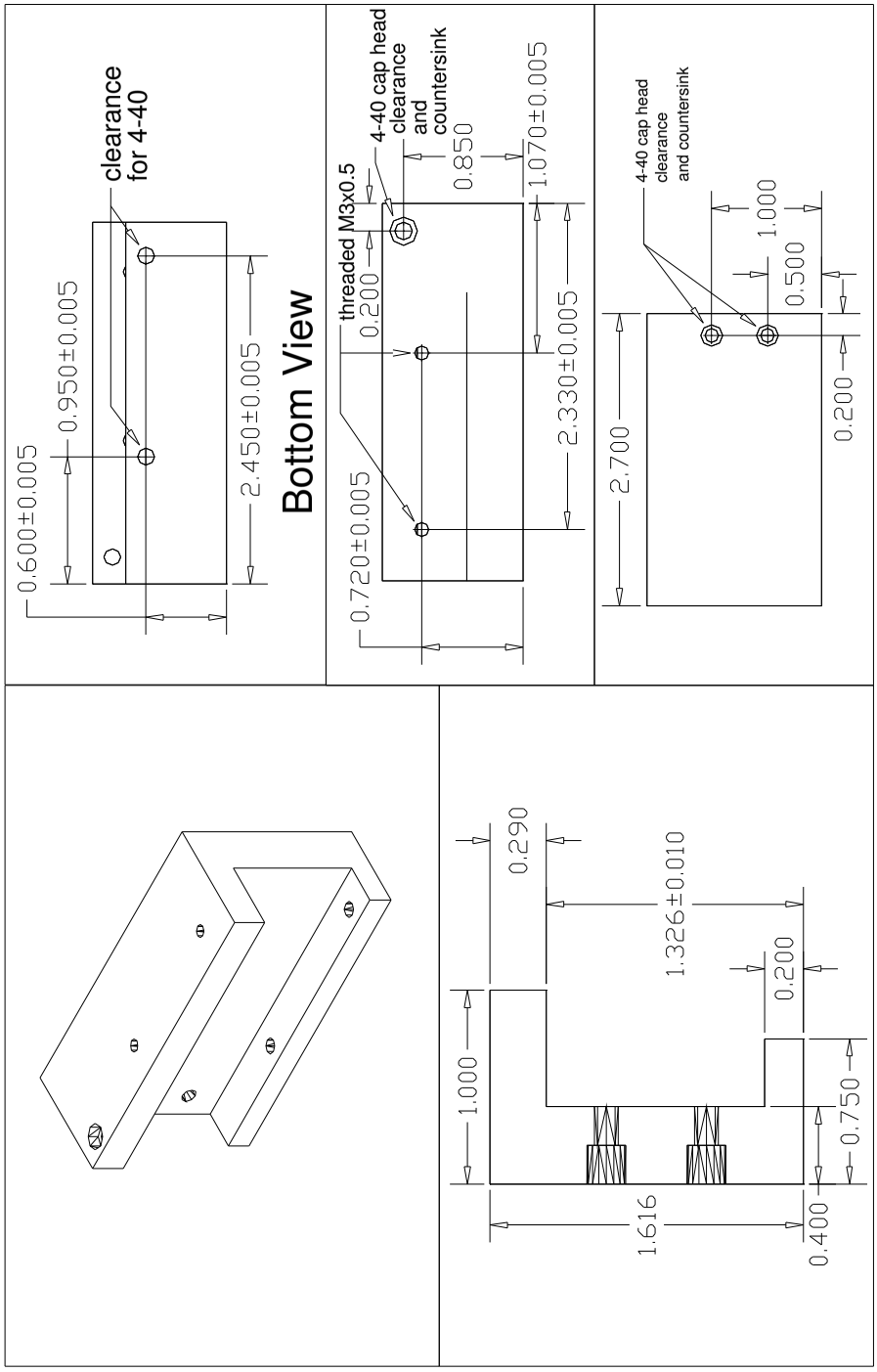

Figure D-9: Dimensioned bracket for beamsplitter positioning hardware (long side). Dimensions are in inches.

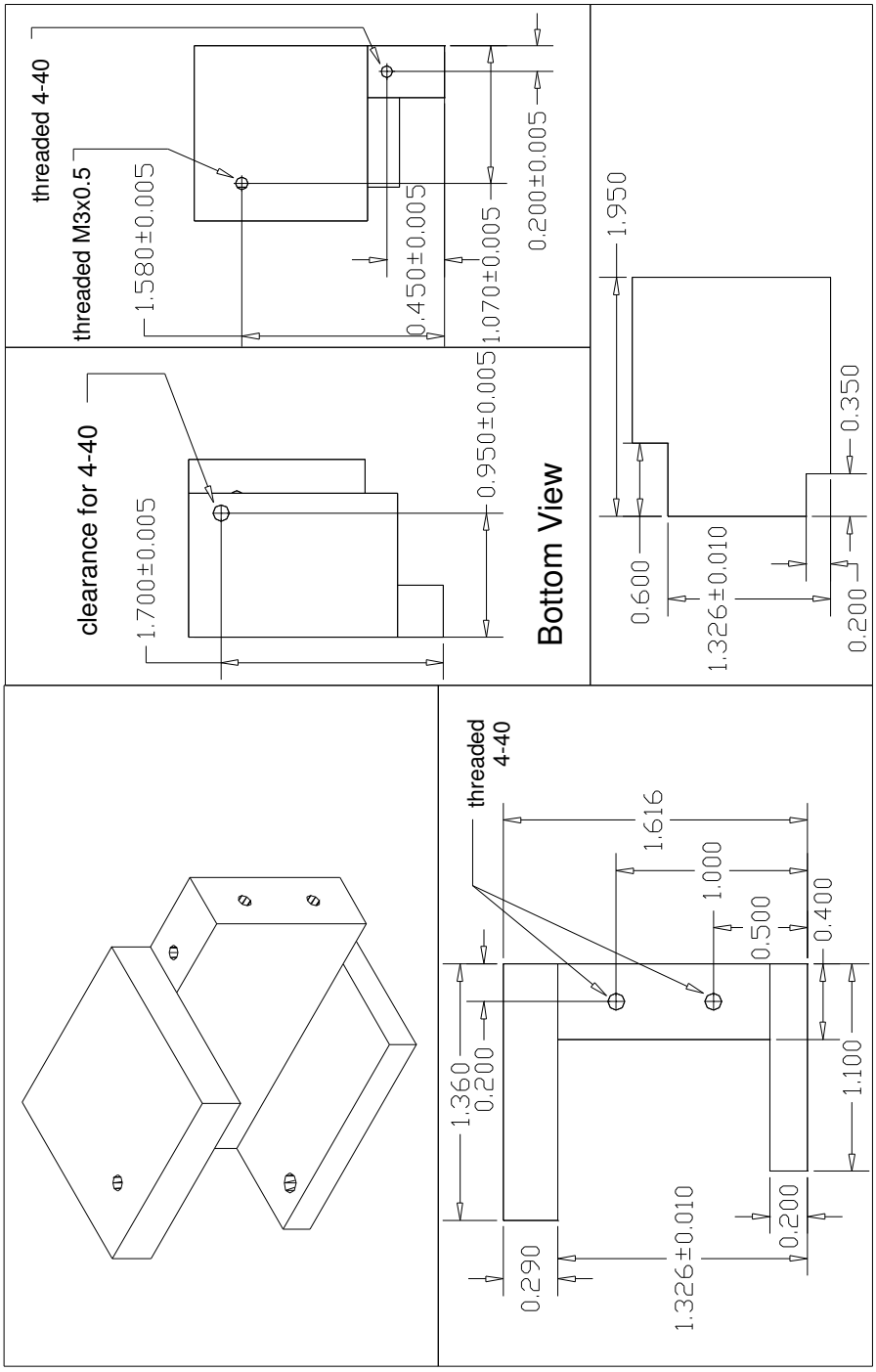

Figure D-10: Dimensioned bracket for beamsplitter positioning hardware (short side). Dimensions are in inches.

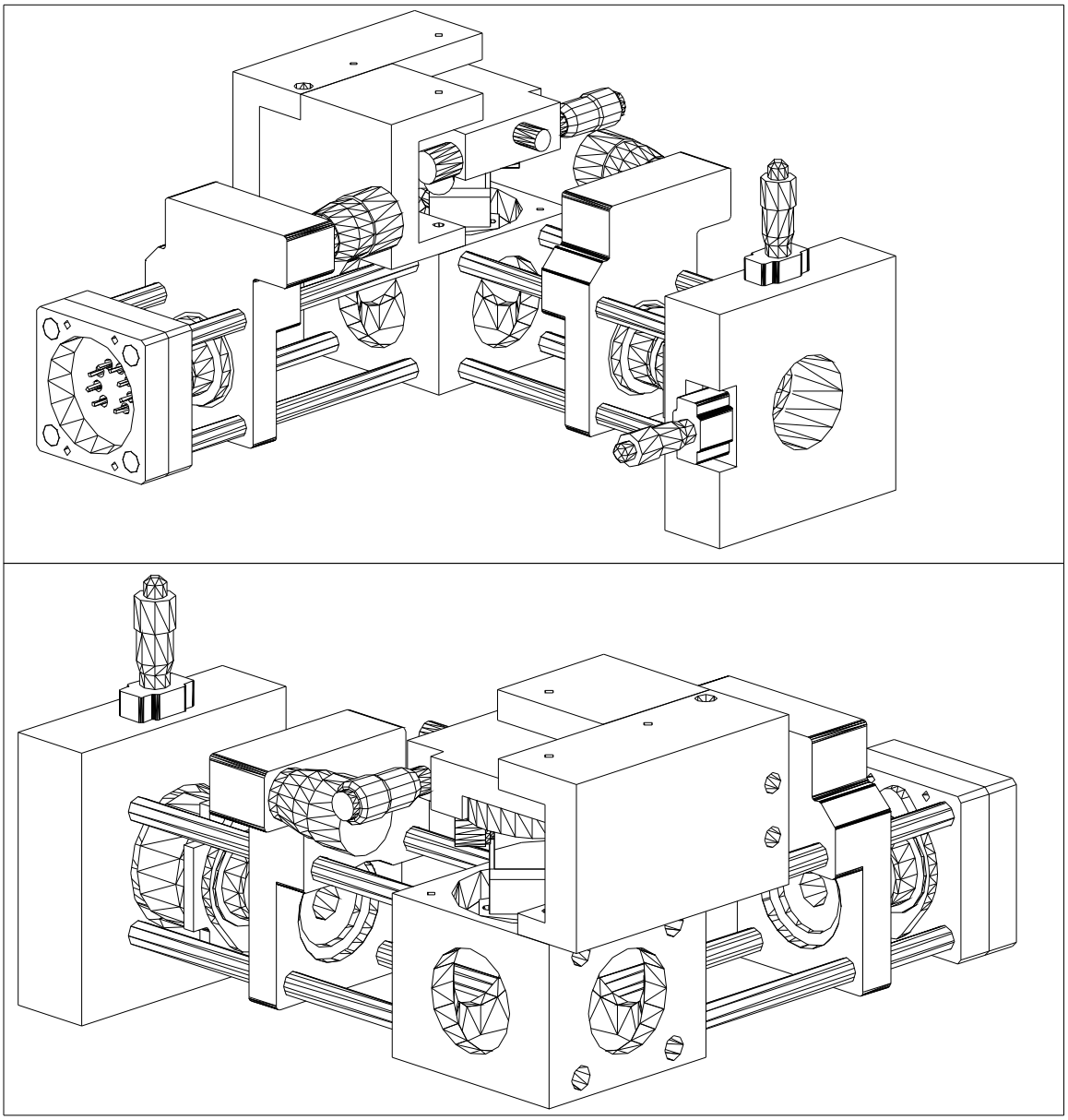

Figure D-11: Views of beam combiner assembly.

Bibliography

[1] P. H. Siegel. Terahertz technology. *IEEE Transactions on Microwave Theory and Technique*, 50(3):910–28, March 2002.

[2] K. A. McIntosh, E. R. Brown, K. B. Nichols, O. B. McMahon, W. F. DiNatale, and T. M. Lyszczarz. Terahertz photomixing with diode lasers in low-temperature-grown GaAs. *Applied Physics Letters*, 67(26):3844–6, December 1995.

[3] S. Verghese, K. A. McIntosh, and E. R. Brown. Highly tunable fiber-coupled photomixers with coherent terahertz output power. *IEEE Transactions on Microwave Theory and Techniques*, 45(8):1301–9, August 1997.

[4] R. K. Lai, Hwang Juinn-Ren, T. B. Norris, and J. F. Whitaker. A photoconductive, miniature terahertz source. *Applied Physics Letters*, 72(24):3100–2, June 1998.

[5] S. Verghese, K. A. McIntosh, S. M. Duffy, and E. K. Duerr. Continuous-wave terahertz generation using photomixers. In R. E. Miles, P. Harrison, and D. Lippens, editors, *Terahertz Sources and Systems*, number 27 in NATO Science Series, pages 145–65. Kluwer Academic Publishers, Boston, MA, 2001.

[6] K. J. Siebert, H. Quast, R. Leonhardt, T. Löffler, and M. Thomson. Continuous-wave all-optoelectronic terahertz imaging. *Applied Physics Letters*, 80(16):3003–5, April 2002.

[7] J. Zhiping, X. G. Xu, and X.-C. Zhang. Improvement of terahertz imaging with a dynamic subtraction technique. *Applied Optics*, 39(17):2982–7, June 2000.

[8] P. Chen, G. A. Blake, M. C. Gaidis, E. R. Brown, K. A. McIntosh, S. Y. Chou, M. I. Nahan, and F. Williamson. Spectroscopic applications and frequency locking of THz photomixing with distributed-bragg-reflector diode lasers in low-temperature-grown GaAs. *Applied Physics Letters*, 71(12):1601–3, 1997.

[9] S. Matsuura, M. Tani, H. Abe, K. Sakai, H. Ozeki, and S. Saito. High-resolution terahertz spectroscopy by a compact radiation source based on photomixing with diode lasers in a photoconductive antenna. *Journal of Molecular Spectroscopy*, 187(1):97–101, January 1998.

[10] A. S. Pine, R. D. Suenram, E. R. Brown, and K. A. McIntosh. A terahertz photomixing spectrometer: Application to SO_2 self broadening. *Journal of Molecular Spectroscopy*, 175:37–47, 1996.

[11] S. Verghese, K. A. McIntosh, S. Calawa, W. F. DiNatale, E. K. Duerr, and L. H. Mahoney. The photomixer transceiver. In *Proceedings of the SPIE*, volume 3617, pages 7–13, 1999.

[12] S. Verghese, K. A. McIntosh, S. Calawa, W. F. Dinatale, E. K. Duerr, and K. A. Molvar. Generation and detection of coherent terahertz waves using two photomixers. *Applied Physics Letters*, 73(26):3824–6, 1998.

[13] T. G. Phillips and J. Keene. Submillimeter astronomy. *Proceedings of the IEEE*, 80(11):1662–78, November 1992.

[14] E. K. Duerr, K. A. McIntosh, S. M. Duffy, S. D. Calawa, S. Verghese, C.-Y. E. Tong, R. Kimberk, and R. Blundell. Demonstration of a 630-GHz photomixer used as a local oscillator. In Mehran Matloubian, editor, *1999 IEEE MTT-S International Microwave Symposium Digest*, number 1, pages 127–130, Anaheim, CA, June 1999. IEEE.

[15] Submillimeter Wave Astronomy Satellite. http://cfa-www.harvard.edu/swas/.

[16] Herschel. http://sci.esa.int/home/first/.

[17] Heterodyne Instrument for the Far Infrared. http://www.sron.nl/divisions/lea/hifi/.

[18] Aura Atmospheric Chemistry. http://eos-aura.gsfc.nasa.gov/.

[19] J. W. Waters. Submillimeter-wavelength heterodyne spectroscopy and remote sensing fo the upper atmosphere. *Proceedings of the IEEE*, 801(11):1679–701, November 1992.

[20] E. R. Mueller, Jr. W. E. Robotham, R. P. Meisner, R. A. Hart, J. Kennedy, and L. A. Newman. 2.5 THz laser local oscillator for the eos chem 1 satellite. In *Proceedings of the Ninth International Space Terahertz Technology Symposium*, pages 563–572, Pasadena, CA, Mar. 17–19 1998.

[21] Caltech Submillimeter Observatory. http://www.submm.caltech.edu/cso/.

[22] Atacama Large Millimeter Array. http://www.alma.nrao.edu/.

[23] R. Blundell and C.-Y. E. Tong. Submillimeter receivers for radio astronomy. *Proceedings of the IEEE*, 80(11):1702–20, November 1992.

[24] T. W. Crowe, R. J. Mattauch, H. P. Röser, W. L. Bishop, W. C. B. Peatman, and X. Liu. GaAs schottky diodes for THz mixing applications. *Proceedings of the IEEE*, 80(11):1827–41, November 1992.

[25] K. Hui, J. L. Hesler, D. S. Kurtz, W. L. Bishop, and T. W. Crowe. A micromachined 585 GHz schottky mixer. *IEEE Microwave and Guided Wave Letters*, 10(9):374–6, September 2000.

[26] K. H. Gundlach and M. Schicke. SIS and bolometer mixers for terahertz frequencies. *Superconductor Science Technology*, 13:R171–R187, 2000.

[27] M. J. Wengler. Submillimeter-wave detection with superconducting tunnel diodes. *Proceedings of the IEEE*, 80(11):1810–26, November 1992.

[28] A. D. Semenov, H.-W. Hübers, J. Schubert, G. N. Gol'tsman, A. I. Elantiev, B. M. Voronov, and E. M. Gershenzon. Design and performance of the lattice-cooled hot-electron terahertz mixer. *Journal of Applied Physics*, 88(11):6758–67, December 2000.

[29] E. Gerecht, C. F. Musante, Y. Zhuang, K. S. Yngvesson, T. Goyette, J. C. Dickinson, J. Waldman, P. A. Yagoubov, G. N. Gol'tsman, B. M. Voronov, and E. M. Gershenzon. NbN hot electron bolometric mixers — a new technology for low-noise THz receivers. *IEEE Transactions on Microwave Theory and Techniques*, 47(12):2519–27, December 1999.

[30] K. S. Yngvesson, E. Gerecht, C. F. Musante, Y. Zhuang, M. Ji, T. Goyette, and J. Waldman. New results on THz HEB low-noise recievers and focal plane arrays. In *Proceedings of the SPIE*, volume 4111, pages 152–62, 2000.

[31] E. Gerecht, C. D. Reintsema, E. N. Grossman, A. L. Betz, and R. T. Boreiko. Noise temperature results for Nb DHEB mixer receiver for far-infrared spectroscopy. In *Proceedings of the Thirteenth International Space Terahertz Technology Symposium*, Cambridge, MA, Mar. 26–28 2002. Paper 7.3.

[32] N. Erickson. 1.5 THz all-planar multiplied source. In *Proceedings of the Thirteenth International Space Terahertz Technology Symposium*, Cambridge, MA, Mar. 26–28 2002. Paper 5.2.

[33] S. Komiyama, O. Astafiev, V. Antonov, H. Hirai, and T. Kutsuwa. A single-photon detector in the far-infrared range. *Nature*, 405:405–7, January 2000.

[34] K. S. Yngvesson, J. Nicholson, Y. Zhuang, F. Rodriguez, X. Zhao, D. Gu, R. Zannoni, E. Gerecht, M. Coulombe, J. DIckinson, T. Goyette, J. Waldman, C. K. Walker, A. Stark, and A. Lane. Progress on TREND — a low noise reciever user instrument at 1.25THz to 1.5THz for AST/RO at the south pole. In *Proceedings of the Thirteenth International Space Terahertz Technology Symposium*, Cambridge, MA, Mar. 26–28 2002. Paper 8.23.

[35] A. F. Krupnov, M.-Yu Tretvakov, V. N. Markov, E. N. Karyakin, G.-Yu Golubyatnikov, V. V. Parshin, S. A. Volokhov, A. M. Schitov, V. V. Bychkov, and I. J. Leonov. Precise measurements in millimeter and submillimeter-wave range based on phase-locked primary radiation sources. In *Physics and Engineering of Millimeter and Submillimeter Waves MSMW 98 Symposium Proceedings*, volume 1, pages 115–20. IEEE, 1998.

[36] B. S. Williams, B. Xu, Q. Hu, and M. R. Melloch. Narrow-linewidth terahertz intersubband emission from three-level systems. *Applied Physics Letters*, 75(19):2927–9, November 1999.

[37] B. S. Williams and Q. Hu. Optimized energy separation for phonon scattering in three-level terahertz intersubband lasers. *Journal of Applied Physics*, 90(11):5504–11, December 2001.

[38] J. Faist, F. Capasso, D. L. Sivco, C. Sirtori, A. L. Hutchinson, and A. Y. Cho. Quantum cascade laser. *Science*, 30(11):865–6, May 1994.

[39] M. Rochat, J. Faist, M. Beck, U. Oesterle, and M. Ilegems. Far-infrared ($\lambda = 88\ \mu$m) electroluminescence in a quantum cascade structure. *Applied Physics Letters*, 73(25):3724–6, December 1998.

[40] R. Köhler, A. Tredicucci, F. Beltram, H. E. Beere, E. H. Linfield, A. G. Davies, D. A. Ritchie, R. C. Iotti, and F. Rossi. Terahertz semiconductor-heterostructure laser. *Nature*, 417:156–9, May 2002.

[41] Benjamin Williams, *private communication*.

[42] K. Kawase, T. Hatanaka, H. Takahashi, K. Nakamura, and T. Taniuchi. Tunable terahertz-wave generation from DAST crystal by dual signal-wave parametric oscillation of periodically poled lithium niobate. *Optics Letters*, 25(23):1714–6, December 2000.

[43] Y. S. Lee, T. Meade, T. B. Norris, and A. Galvanauskas. Tunable narrow-band terahertz generation from periodically poled lithium niobate. *Applied Physics Letters*, 78(23):3583–5, June 2001.

[44] A. V. Räisänen. Frequency multipliers for millimeter and submillimeter wavelngths. *Proceedings of the IEEE*, 80(11):1842–52, November 1992.

[45] I. Mehdi, E. Schlecht, A. Arzumanyan, J. Bruston, P. Siegel, R. P. Smith, J. Pearson, S. Martin, and D. Porterfield. Development of millimeter and submillimeter-wave local oscillator circuits for a space telescope. In *Proceedings of the SPIE*, volume 3795, pages 329–37, 1999.

[46] A. Maestrini, G. Chattopadhyay, E. Schlecht, and I. Mehdi. 1400–1900 ghz membrane based schottky diode triplers. In *Proceedings of the Thirteenth International Space Terahertz Technology Symposium*, Cambridge, MA, Mar. 26–28 2002. Paper 5.1.

[47] E. Schlecht, G. Chattopadhyay, A. Maestrini, D. Pukala, J. Gill, and I. Mehdi. Harmonic balance optimization of terahertz schottky diode multipliers using an advanced bevice model. In *Proceedings of the Thirteenth International Space Terahertz Technology Symposium*, Cambridge, MA, Mar. 26–28 2002. Paper 5.3.

[48] C. E. Tong, R. Blundell, D. C. Papa, M. Smith, J. Kawamura, G. Gol'tsman, E. Gershenzon, and B. Voronov. An all solid-state superconducting heterodyne receiver at terahertz frequencies. *IEEE Microwave and Guided Wave Letters*, 9(9):366–8, September 1999.

[49] J. E. Oswald, T. Koch, I. Mehdi, A. Pease, R. J. Dengler, T. H. Lee, D. A. Humphrey, M. Kim, P. H. Siegel, M. A. Frerking, and N. R. Erickson. Planar diode solid-state receiver for 557 GHz with state-of-the-art performance. *IEEE Microwave and Guided Wave Letters*, 8(6):232–4, June 1998.

[50] A. T. Forrester, R. A. Gudmundsen, and P. O. Johnson. Photoelectric mixing in incoherent light. *Physical Review*, 99(6):1691–700, September 1955.

[51] E. R. Brown, F. W. Smith, and K. A. McIntosh. Coherent millimeter-wave generation by heterodyne conversion in low-temperature-grown GaAs photoconductors. *Journal of Applied Physics*, 73(3):1480–4, February 1993.

[52] J. K. Luo, H. Thomas, and D. V. Morgan. Transport properties of GaAs layers grown by molecular beam epitaxy at low temperature and the effects of annealing. *Journal of Applied Physics*, 79(7):3622–9, April 1996.

[53] A. J. Lochtefeld, M. R. Melloch, J. C. P. Chang, and E. S. Harmon. The role of point defects and arsenic precipitates in carrier trapping and recombination in low-temperature grown GaAs. *Applied Physics Letters*, 69(10):1465–7, September 1996.

[54] E. S. Harmon, M. R. Melloch, J. M. Woodall, D. D. Nolte, N. Otsuka, and C. L. Chang. Carrier lifetime versus anneal in low temperature growth GaAs. *Applied Physics Letters*, 63(16):2248–50, October 1993.

[55] K. A. MacIntosh, K. B. Nichols, S. Verghese, and E. R. Brown. Investigation of ultrashort photocarrier relaxation times in low-temperature-grown GaAs. *Applied Physics Letters*, 70(3):354–6, 1997.

[56] N. Zamdmer, Q. Hu, K. A. McIntosh, and S. Verghese. Increase in response time of low-temperature-grown GaAs photoconductive switches at high voltage bias. *Applied Physics Letters*, 75(15):2313–5, October 1999.

[57] A. W. Jackson. *Low-Temperature-Grown GaAs Photomixers Designed for Increased Terahertz output Power*. PhD dissertation, University of California, Santa Barbara, Material Engineering, October 1999.

[58] E. R. Brown. A photoconductive model for superior GaAs THz photomixers. *Applied Physics Letters*, 75(6):769–71, August 1999.

[59] C. Kadow, A. W. Jackson, A. C. Gossard, J. E. Bowers, S. Matsuura, and G. A. Blake. Self-assembled eras islands in GaAs for THz applications. *Physica E*, 7:97–100, 2000.

[60] S. M. Duffy, S. Verghese, K. A. McIntosh, A. Jackson, A. C. Gossard, and S. Matsuura. Accurate modeling of dual dipole and slot elements used with photomixers for coherent terahertz output power. *IEEE Transactions on Microwave Theory and Techniques*, 49(6):1032–8, June 2001.

[61] S. Matsuura, G. A. Blake, R. A. Wyss, J. C. Pearson, C. Kadow, A. W. Jackson, and A. C. Gossard. Design and characterization fo optical-thz phase-matched traveling-wave photomixers. In *Proceedings of the SPIE*, volume 3795, pages 484–92, 1999.

[62] E. K. Duerr and K. A. McIntosh. Distributed photomixers. In *Conference on Lasers and Electro-Optics Technical Digest*, pages 382–3, San Francisco, CA, 2000.

[63] K. S. Giboney, M. J. W. Rodwell, and J. E. Bowers. Traveling-wave photodetector design and measurements. *IEEE Journal of Selected Topics in Quantum Electronics*, 2(3):622–9, September 1996.

[64] K. S. Giboney, M. J. W. Rodwell, and J. E. Bowers. Traveling-wave photodetector theory. *IEEE Transactions on Microwave Theory and Techniques*, 45(8):1310–9, August 1997.

[65] V. M. Hietala, G. A. Vawter, T. M. Brennan, and B. E. Hammons. Traveling-wave photodetectors for high-power, large bandwidth applications. *IEEE Transactions on Microwave Theory and Techniques*, 43(9):2291–8, September 1995.

[66] L. Y. Lin, M. C. Wu, T. Itoh, T. A. Vang, R. E. Muller, D. L. Sivco, and A. Y. Cho. High-power high-speed photodetectors–design, analysis and experimental demonstration. *IEEE Transactions on Microwave Theory and Techniques*, 45(8):1320–31, August 1997.

[67] J.-W. Shi, K-G Gan, Y-J Chiu, Y-H Chen, C-K Sun, Y-J Yang, and J E Bowers. Metal-semiconductor-metal traveling-wave photodetectors. *IEEE Photonics Technology Letters*, 16(6):623–5, June 2001.

[68] J-W Shi and C-K Sun. Design and analysis of long absorption-length traveling-wave photodetectors. *Journal of Lightwave Technology*, 18(12):2176–87, December 2000.

[69] Y-J Chiu, S. B. Fleischer, and J. E. Bowers. High-speed low-temperature-grown GaAs p-i-n traveling-wave photodetector. *IEEE Photonics Technology Letters*, 10(7):1012–4, July 1998.

[70] Y. J. Chiu. PhD dissertation, University of California, Santa Barbara, 1999.

[71] H. P. Zappe. *Introduction to Semiconductor Integrated Optics*. Artech House, Inc., Boston, MA, 1995.

[72] FIMMWAVE (waveguide mode solver) from Photon Design. 34 Leopold Street, Oxford OX4 1TW United Kingdom. http://www.photond.com.

[73] R. G. Hunsperger. *Integrated Optics: Theory and Technology*. Springer-Verlag, Berlin, third edition, 1991.

[74] S. Adachi. GaAs, AlAs, and $\mathrm{Al}_x\mathrm{Ga}_{1-x}\mathrm{As}$: Material parameters for use in research and device applications. *Journal of Applied Physics*, 58(3):R1–R29, August 1985.

[75] A. B. Djurišić, A. D. Rakić, P. C. K. Kwok, E. H. Li, M. L. Majewski, and J. M. Elazar. Modeling the optical constants of $\mathrm{Al}_x\mathrm{Ga}_{1-x}\mathrm{As}$ alloys. *Journal of Applied Physics*, 86(1):445–51, July 1999.

[76] S. Adachi. *Properties of Aluminium Gallium Arsenide*. INSPEC, the Institution of Electrical Engineers, London, UK, 1993.

[77] K. C. Gupta, R. Garg, I. Bahl, and P. Bhartia. *Microstrip Lines and Slotlines*, chapter 7. Artech House, Boston, Massachusetts, second edition, 1996.

[78] D. B. Rutledge, D. P. Niekirk, and D. P. Kasilingam. Integrated-circuit antennas. In K. J. Button, editor, *Millimeter Components and Techniques, Part II*, number 10 in Infrared and Millimeter Waves, chapter 1, pages 1–90. Academic Press, Inc., New York, NY, 1983.

[79] G. Hasnain, A. Dienes, and J. R. Whinnery. Dispersion of picosecond pulses in coplanar transmission lines. *IEEE Transactions on Microwave Theory and Techniques*, 34(6):738–41, June 1986.

[80] D. Grischkowsky, I. N. Duling, J. C. Chen, and C.-C. Chi. Electromagnetic shock waves from transmission lines. *Physical Review Letters*, 59(15):1663–6, October 1987.

[81] D. S. Phatak and A. P. Defonzo. Dispersion charateristics of optically excited coplanar striplines: Pulse propagation. *IEEE Transactions on Microwave Theory and Techniques*, 38(5):654–61, May 1990.

[82] M. Y. Frankel, S. Gupta, J. A. Valdamis, and G. A. Mourou. Terahertz attenuation and dispersion characteristics of coplanar transmission lines. *IEEE Transactions on Microwave Theory and Techniques*, 39(6):910–6, 1991.

[83] Y. C. Lim and R. A. Moore. Properties of alternately charged coplanar parallel strips by conformal mappings. *IEEE Transactions on Electron Devices*, ED-15(3):173–80, 1968.

[84] Momentum, Planar EM Simulator. Agilent EEsof division, 5301 Stevens Creek Blvd., Santa Clara, CA 95052-8059.

[85] G. H. Brown and Jr. O. M. Woodard. Experimentally determined radiation characteristics of conical and triangular antennas. *RCA Review*, 13:425–52, December 1952.

[86] R. C. Compton, R. C. McPhedran, Z. Popović, G. M. Rebeiz, P. P. Tong, and D. B. Rutledge. Bow-tie antennas on a dielectric half-space: Theory and experiment. *IEEE Transactions on Antennas and Propagation*, 35(6):622–31, June 1987.

[87] M. Kominami, D. M. Pozar, and D. H. Schaubert. Dipole and slot elements on semi-infinite substrates. *IEEE Transactions on Antennas and Propagation*, 33(6):600–7, June 1985.

[88] K. R. Carver and J. W. Mink. Microstrip antenna technology. *IEEE Transactions on Antennas and Propagation*, 29(1):2–24, January 1981.

[89] L. Zhu and K. Wu. Model-based characterization of cps-fed printed dipole for innovative design of uniplanar integrated antenna. *IEEE Microwave and Guided Wave Letters*, 9(9):342–4, September 1999.

[90] Leonard Mahoney, *private communication*.

[91] S. Duffy, S. Verghese, and K. A. McIntosh. Photomixers for continuous-wave terahertz generation. In D. Mittleman, editor, *Sensing with Terahertz Radiation*. Springer-Verlag, 2002.

[92] S. Verghese, N. Zamdmer, Q. Hu, E. R. Brown, and A. Förster. An optical correlator using a low-temperature-grown GaAs photoconductor. *Applied Physics Letters*, 69(6):842–4, August 1996.

[93] K. G. Eyink, M. A. Capano, S. D. Walck, T. W. Haas, and B. G. Streetman. *In situ* and *ex situ* spectroscopic investigation of low temperature grown gallium arsenide by molecular beam epitaxy. *Journal of Vacuum Science Technology B*, 14(3):2278–81, May/Jun 1996.

[94] S. U. Dankowski, P. Kiesel, M. Ruff, D. Streb, S. Tautz, U. D. Keil, C. B. Sørenson, B. Knüpfer, M. Kneissl, and G. H. Döhler. Optical and eletro-optical investigation of low-temperature grown GaAs. *Materials Science & Engineering B*, 44:316–9, 1997.

[95] U. D. Keil, J. M. Hvam, S. Tuatz, S. U. Dankowski, P. Kiesel, and G. H. Döhler. Femtosecond differential transmission measurements on low temperature GaAs metal-semiconductor-metal structures. *Applied Physics Letters*, 70(1):72–4, January 1997.

[96] H. S. Loka, S. D. Benjamin, and P. W. E. Smith. Influence of material growth and annealing conditions on recombination processes in low-temperature-grown GaAs. *Optics Communications*, 161:232–5, March 1999.

[97] D. Streb, M. Ruff, S. U. Dankowski, P. Kiesel, M. Kneissl, S. Malzer, U. D. Keil, and G. H. Döhler. Optical characterization of low temperature grown GaAs by transmission measurements above the band gap. *Journal of Vacuum Science Technology B*, 14(3):2275–7, May/Jun 1996.

[98] Newport Corporation. 1791 Deere Avenue, Irvine, CA 92606. http://www.newport.com.

[99] S. D. Calawa, *private communication*.

[100] P. G. Snyder, M. C. Rost, G. H. Bu-Abbud, and J. A. Woollam. Variable angle of incidence spectroscopic ellipsometry: Application to GaAs-$Al_xGa_{1-x}As$ multiple heterostructures. *Journal of Applied Physics*, 60(9):3293–301, November 1986.

[101] R. Loudon. *The quantum theory of light*. Clarendon Press, Oxford, UK, second edition, 1985.

[102] F. W. Smith. *The Device Applications and Characterization of Nonstoichiometric* GaAs *grown by Molecular Beam Epitaxy*. PhD dissertation, Massachusetts Institute of Technology, Department of Electrical Engineering and Computer Science, April 1990.

[103] N. Marcuvitz. *Waveguide Handbook*, volume 21 of *IEE Electromagnetic Waves Series*. Peter Peregrinus, Ltd., London, UK, second edition, December 1985.

[104] A. Blanco, S. Fonti, and A. Piacente. Transmission coefficients of free-standing wire grids in the far infrared: A theoretical approach for easy computation. *Infrared Physics*, 26(6):357–63, 1986.

[105] J. Y. Suratteau and R. Petit. Numerical study of perfectly conducting wire gratings in the resonance domain. *International Journal of Infrared and Millimeter Waves*, 6(9):831–65, 1985.

[106] R. C. Compton, L. B. Whitbourn, and R. C. McPhedran. Strip gratings at a dielectric interface and application of babinet's principle. *Applied Optics*, 23(18):3236–42, September 1984.

[107] L. B. Whitbourn and R. C. Compton. Equivalent-circuit formulas for metal grid reflectors at a dielectric boundary. *Applied Optics*, 24(2):217–20, January 1985.

[108] J. P. Ibbetson and U. K. Mishra. Space-charge-limited currents in nonstoichiometric GaAs. *Applied Physics Letters*, 68(26):3781–3, June 1996.

[109] N. Zamdmer. *The Design and Testing of Integrated Circuits for Submillimeter-wave Spectroscopy*. PhD dissertation, Massachusetts Institute of Technology, Department of Electrical Engineering and Computer Science, June 1999.

[110] D. M. Pozar. *Microwave Engineering*. John Wiley & Sons, Inc., New York, NY, second edition, 1998.

[111] Dr. Jeffrey Hesler, *private communication*.

[112] D. Grischkowsky, Søren Keiding, M. van Exter, and Ch. Fattinger. Far-infrared time-domain spectroscopy with terahertz beams of dielectrics and semiconductors. *Journal of the Optical Society of America B*, 7(10):2006–15, October 1990.

[113] E. D. Palik. Gallium arsenide (GaAs). In E. D. Palik, editor, *Handbook of Optical Constants of Solids*, Academic Press Handbook Series, pages 429–43. Academic Press, Inc., New York, NY, 1985.

[114] O. J. Glembocki and K. Takarabe. Aluminum gallium arsenide ($\mathrm{Al}_x\mathrm{Ga}_{1-x}\mathrm{As}$). In E. D. Palik, editor, *Handbook of Optical Constants of Solids II*, Academic Press Handbook Series, pages 513–58. Academic Press, Inc., New York, NY, 1991.

[115] Dr. Joseph Donnelly, *private communication*.

[116] G. M. Rebeiz. Millimeter-wave and terahertz integrated circuit antennas. *Proceedings of the IEEE*, 80(11):1748–70, November 1992.

[117] D. F. Filipovic, S. S. Gearhart, and G. M. Rebeiz. Double-slot antennas on extended hemispherical and elliptical silicon dielectric lenses. *IEEE Transactions on Microwave Theory and Techniques*, 41(10):1738–49, October 1993.

[118] D. F. Filipovic. *Analysis and Design of Dielectric-Lens Antennas and Planar Multiplier Circuits for Millimeter-wave Applications*. PhD dissertation, The University of Michigan, Department of Electrical Engineering and Computer Science, August 1995.

[119] S. Matsuura, P. Chen, G. A. Blake, J. C. Pearson, and H. M. Pickett. Simultaneous amplification of terahertz difference frequencies by an injection-seeded semiconductor laser amplifier at 850 nm. *International Journal of Infrared and Millimeter Waves*, 19(6):849–58, June 1998.

[120] S. Matsuura, P. Chen, G. A. Blake, J. C. Pearson, and H. M. Pickett. A tunable cavity-locked diode laser source for terahertz photomixing. *IEEE Transactions on Microwave Theory and Techniques*, 48(3):380–7, March 2000.

[121] Thorlabs, Inc. 435 Route 206, P.O. Box 366, Newton, NJ 07860-0366. http://www.thorlabs.com.

[122] Melles Griot, Inc. 2051 Palomar Airport Road 200, Carlsbad, CA 92009. http://www.mellesgriot.com.

[123] OptoSigma Corporation. 2001 Deere Avenue, Santa Ana, CA, 92705. http://www.optosigma.com.

[124] CVI Laser Corporation. CVI East, 111 Highland Drive, Putnam, CT 06260-3010. http://www.cvilaser.com.

[125] Semiconductor Device Lab (now JDS Uniphase). JDS Uniphase Corporation, 1768 Automation Parkway, San Jose, CA 95131. http://www.sdli.com.

[126] P. F. Goldsmith. *Quasioptical Systems: Gaussian Beam Quasioptical Propagation and Applications*. IEEE Press/Chapman & Hall Publishers Series on Microwave Technology and RF. IEEE Press, New York, NY, 1998.

[127] Dr. Simon Verghese and K. Alex McIntosh, *private communication*.

[128] J. N. Walpole, J. P. Donnelly, P. J. Taylor, L. J. Missaggia, C. T. Harris, R. J. Bailey, A. Napoleone, S. H. Groves, S. R. Chinn, R. Huang, and J. Plant. Slab-coupled 1.3-μm semiconductor laser with single-spatial, large-diameter mode. *IEEE Photonics Technology Letters*, 14(6):756–8, June 2002.

[129] M. Born and E. Wolf. *Principles of Optics*. Pergamon Press, New York, NY, sixth edition, 1984.

[130] R. E. Collin. *Foundations for Microwave Engineering*. McGraw-Hill Series in Electrical Engineering. McGraw-Hill, Inc., New York, NY, second edition, 1992.

[131] T. Larsen. A survey of the theory of wire grids. *IRE Transactions on Microwave Theory and Techniques*, pages 191–201, May 1962.